

AD-A055 937

ILLINOIS INST OF TECH CHICAGO DEPT OF MECHANICS MECH--ETC F/G 14/2
ON TEMPERATURE AND YAW DEPENDENCE OF HOT-WIRES.(U)

AUG 77 R E DRUBKA, H M NAGIB, J TAN-ATICHAT F44620-76-C-0062

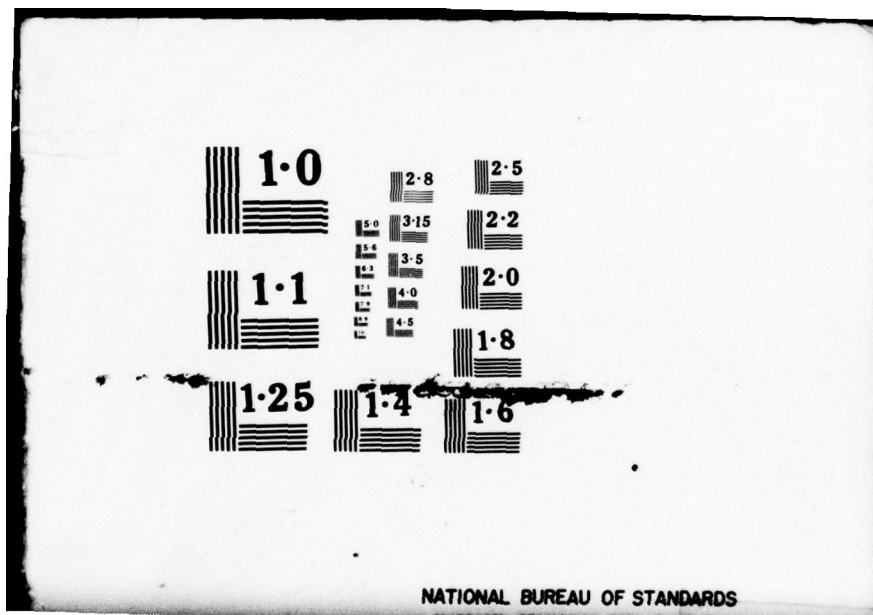
UNCLASSIFIED

IIT-FLUIDS/HEAT TRANS-R77 ARO-12290.9-E

NL

1 OF 3
ADA
065937





AD A 055937

FOR FURTHER TRAN

ARO. 12290. 9-E

12

S

Illinois Institute of Technology, Chicago, Illinois 60616

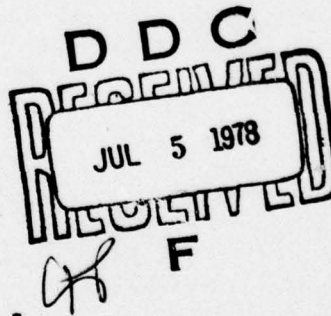
ON TEMPERATURE AND YAW DEPENDENCE
OF HOT-WIRES

By

R. E. Drubka, H. M. Nagib and J. Tan-atichat

IIT-Fluids & Heat Transfer Report R77-1

August, 1977



Supported under ARO Grant DAHC04-74-G-0160, NSF Grant ENG76-04112,
and AFOSR Contract F44620-76-C-0062
APPROVED FOR PUBLIC RELEASE; DISTRIBUTION UNLIMITED

78 07 03 056

AD No. /
DDC FILE COPY

The findings in this report are not to be construed as an official Department of the Army position, unless so designated by other authorized documents.

Qualified requestors may obtain additional copies from the Defense Documentation Center, all others should apply to the National Technical Information Service.

Conditions of Reproduction

Reproduction, translation, publication, use and disposal in whole or in part by or for the United States Government is permitted.

UNCLASSIFIED

SECURITY CLASSIFICATION OF THIS PAGE (When Data Entered)

REPORT DOCUMENTATION PAGE		READ INSTRUCTIONS BEFORE COMPLETING FORM
1. REPORT NUMBER IIT-FMT-R77-1	2. GOVT ACCESSION NO.	3. RECIPIENT'S CATALOG NUMBER
4. TITLE (and Subtitle) ON TEMPERATURE AND YAW DEPENDENCE OF HOT-WIRES.		5. TYPE OF REPORT & PERIOD COVERED Technical rept.
7. AUTHOR(s) R. E. Drubka, H. M. Nagib and J. Tan-aticat		6. PERFORMING ORG. REPORT NUMBER
9. PERFORMING ORGANIZATION NAME AND ADDRESS Illinois Institute of Technology Mechanics & Mechanical & Aerospace Engineering Chicago, Illinois 60616		8. CONTRACT OR GRANT NUMBER(s) ARO Grant DAHC04-74-G-0160, NOT Grant ENC76-04112, AFOSR Contract F44620-76-C-0062
11. CONTROLLING OFFICE NAME AND ADDRESS U.S. Army Research Office Box CM, Duke Station Durham, North Carolina 27706		10. PROGRAM ELEMENT, PROJECT, TASK AREA & WORK UNIT NUMBERS F44620-76-C-0062, DAHC04-74-G-0160
14. MONITORING AGENCY NAME & ADDRESS (if different from Controlling Office) IIT-FLUIDS/HEAT TRANS-R77-1		12. REPORT DATE Aug 77
		13. NUMBER OF PAGES 267p.
		15. SECURITY CLASS. (of this report) UNCLASSIFIED
16. DISTRIBUTION STATEMENT (of this Report) Approved for public release, distribution unlimited.		15. DECLASSIFICATION/DOWNGRADING SCHEDULE
17. DISTRIBUTION STATEMENT (of the abstract entered in Block 20, if different from Report)		
18. SUPPLEMENTARY NOTES		
19. KEY WORDS (Continue on reverse side if necessary and identify by block number) Hot-Wires; Hot-films; Velocity Calibration; Temperature Variation Effects; Temperature Compensation; Temperature Calibration; Compensating Circuits; Yaw Sensitivity; Yaw Response; X-Probe; Yaw Calibration; Inclined Sensors; Velocity Correlation; Reynolds Stress; Yaw Relation; Turbulence Intensity; CONTINUED		
20. ABSTRACT (Continue on reverse side if necessary and identify by block number) A scheme utilizing a temperature probe immersed in the working fluid to compensate for the dependence of hot-wire velocity calibration on ambient temperature variations was analyzed. One needs only to know the properties of the anemometer bridge and the velocity and temperature probes to achieve the compensation. Hence the scheme provides means for incorporating the temperature compensation a priori to conducting the experiments without any need for temperature calibration. Estimates of the errors introduced through the non-ideal CONTINUED		

DD FORM 1473 1 JAN 73

EDITION OF 1 NOV 68 IS OBSOLETE

UNCLASSIFIED

SECURITY CLASSIFICATION OF THIS PAGE (When Data Entered)

400 437

CL

UNCLASSIFIED

SECURITY CLASSIFICATION OF THIS PAGE(When Data Entered)

19. KEY WORDS - Continued

Effect of Reynolds's Number; Effect of Sensor Length; Effect of Overheat Ratio; Turbulence Correction Factor

20. ABSTRACT - Continued

behavior of the compensating circuits have been derived and indicate that the error is proportional to the square of the temperature variation. For typical probes with an ambient temperature increase of 40°C, maximum errors in the indicated velocity of -1% or less can be achieved.

Measurements in many complex flowfields, such as in swirling flows or near bluff bodies, require the knowledge of the yaw sensitivity of an X-wire probe to a high degree of accuracy. The yaw relation $U_e/U_1 = [1 - b(1 - \cos^m \alpha)]^2$ is proposed and investigated analytically and experimentally. In the derivation of the response equation of inclined cylindrical sensors in steady and fluctuating velocity fields, previous analyses have been extended for the present yaw relation to include X-probes with dissimilar sensors as well as mean velocities at an angle γ to the line of symmetry of the X-wires.

For mean velocity measurements, with sensors that have yaw dependence which does not closely follow the cosine law, neither the simple nor an approximate weighted sum and difference technique applies when $\gamma \neq 0$. This makes analog processing to obtain accurate mean velocities extremely difficult if not impossible. However, for cases where the mean streamline is aligned with the probe axis of symmetry, the errors introduced were found to be less than 5%. In low level turbulence, time dependent velocity components can always be obtained with comparable accuracy using a weighted sum and difference technique once the mean flow angle is determined. However, the weighting must take into account deviations from the cosine law. For a typical sensor whose yaw data has a standard deviation from the cosine law of 0.5%, and when $\gamma = 0$, the estimates of errors in u' , v' and \overline{uv} are approximately 3%, 11% and 8%, respectively. The error in \overline{uv} increases substantially as γ deviates from zero. These errors are essentially proportional to the standard deviation from the cosine law, σ , as it increases above its value in this example. Even when the sensor closely follows the cosine law, i.e., $\sigma \approx 0.1\%$, errors in these quantities as large as 3% can exist. Discrepancies were also found between different yaw relations in calculated values of turbulence velocity correlations which are derived from the same data. These discrepancies depend on the mean flow angle, the distribution of the turbulence energy between the velocity components and the accuracy to which the mean flow calibration data fits the yaw function.

The effect of various parameters on the yaw sensitivity of hot-wires has been experimentally determined. In all cases, the present yaw relation fits the calibration data to a higher degree of accuracy than the cosine law or the Friehe and Schwarz relation, where $m = 0.5$. The ratio of improvement over either relation is smaller for the very short sensors ($l/d \approx 100$) than for the long sensors ($l/d \approx 1000$). The trend of the yaw parameters with either sensor l/d or Reynolds number does not seem to approach the cosine law but rather it seems to overshoot it without any observed asymptotic values. Values of the transverse sensitivity coefficient calculated from a yaw sensitivity function, taking into account deviations from the cosine law, yield a higher degree of accuracy than those obtained directly from the data. Based on the Reynolds number dependency of the yaw coefficients, one should use different yaw calibration coefficients for different velocities. If a single set of parameters is to be used, the accuracy achieved by a simple relation like the cosine law is as good as one may expect. However, after the data has been gathered, the results must be corrected for the large errors introduced into the mean and rms velocity components. Each new sensor mounted on a probe must be calibrated, even if the new sensor is identical to the one being replaced.

UNCLASSIFIED

SECURITY CLASSIFICATION OF THIS PAGE(When Data Entered)

ACKNOWLEDGEMENT

The authors would like to thank John L. Way for his advice in regard to the unsteady calibration experiment and for his help with the digital processing of the data. We are also grateful to Tom Corke for his help in preparing the figures and to Richard Wlezien for writing the contour plotting routine at a time when it was most needed. A note of thanks is due John Foss of Michigan State University for providing some of his yaw calibration data, and Frank Champagne of University of California at San Diego for discussions on the yaw sensitivity of hot wires.

The authors also have great appreciation for Roberta Corke, who exersized much care and concern in typing the manuscript.

Research in this report was partially supported under U.S. Army Research Office Grant DAHC04-G-0160, NSF Grant ENG76-04112, and AFOSR Contract F44620-76-C-0062.

R. E. D., H. M. N. and J. T.

ACCESSION for	
NTIS	White Section <input checked="" type="checkbox"/>
DOC	Buff Section <input type="checkbox"/>
UNANNOUNCED	<input checked="" type="checkbox"/>
JUSTIFICATION	
BY	
DISTRIBUTION/AVAILABILITY CODES	
Dist.	SPECIAL
A	

TABLE OF CONTENTS

	Page
ACKNOWLEDGEMENT	iii
LIST OF TABLES	viii
LIST OF FIGURES	ix
NOTATION	xviii
ABSTRACT	xxiv
 CHAPTER	
I. INTRODUCTION	1
Background	1
Relevant Literature	5
Objectives	9
 II. ANALYSIS OF TEMPERATURE COMPENSATING CIRCUITS FOR USE WITH HOT WIRES OR HOT FILMS	
Analysis	12
Case A: Constant Overheat Ratio	
Case B: Constant Overheat Resistance Difference	
Case C: Constant Bridge Output Voltage	
Case D: Constant Linearized Output Voltage	
Compensating Circuit 1	
Compensating Circuit 2	
Compensating Circuit 3	
Selection of A Compensating Probe	23
Error Estimates.	24
Case C: Non-Linear Output Voltage A Sample Estimate	

CHAPTER		PAGE
III.	RESPONSE EQUATIONS OF INCLINED CYLINDRICAL SENSORS IN STEADY AND FLUCTUATING VELOCITY FIELDS	32
	Time-Mean Velocity Field	32
	Cosine Law	
	Further Generalization of Cosine Law	
	Time-Dependent Velocity Field	41
	Streamwise Coordinate System	
	x-y Coordinate System	
	Discrepancies Between Different Yaw Relations in Calculated Values of Turbulence Velocity Correlations	47
	Response of Sensors to Velocity Fluctuations	52
IV.	EXPERIMENTAL FACILITIES AND TECHNIQUES . . .	56
	Experimental Facilities	56
	Environmental Wind Tunnel	
	Calibration Tunnel	
	Angularity Chuck	
	Velocity Sensors	
	Angularity Measurements	59
	Steady Velocity Calibration	
	Fluctuating Velocity Calibration	
	Data Processing.	62

CHAPTER	PAGE
V. YAW CALIBRATION FOR STEADY VELOCITIES	66
Single-Wire Probes	68
Effect of Probe Misalignment	
Effect of Reynolds Number	
Effect of Sensor l/d	
Combined Effects of Reynolds Number	
and Sensor l/d	
Application of Yaw Relations Over	
Reynolds Number Range	
Effect of Overheat Ratio	
Effect of Angular Range of Data	
X-Wire Probe	82
Determination of Transverse and Longi-	
tudinal Sensitivity Coefficients	
VI. YAW CALIBRATION FOR FLUCTUATING VELOCITIES . . .	88
Establishment of Fluctuating Velocity Field .	88
Single-Wire Probe	92
X-Wire Probe	95
VII. DISCUSSION	97
Temperature Dependence	97
Yaw Dependence	98
VIII. CONCLUSIONS AND RECOMMENDATIONS	113
Conclusions	113
Recommendations	120

APPENDIX

LIST OF TABLES

PAGE

A. INITIAL ERROR ESTIMATES FOR TEMPERATURE COMPENSATING CIRCUITS	122
B. EXPERIMENTS ON TEMPERATURE COMPENSATION	125
C. YAW CALIBRATION RESULTS FROM HOT-FILMS IN WATER	131
D. YAW CALIBRATION RESULTS FROM X-WIRE PROBES; DATA COURTESY OF MSU	134
E. FIGURES	138
BIBLIOGRAPHY	235

LIST OF TABLES

TABLE

- | | Page |
|--|------|
| 1. Sample Error Estimates for Typical Velocity
and Temperature Probes in Circuits 1 and 2 . | 28 |

LIST OF FIGURES

Figure	Page
1. Effect on Present Yaw Relation of Changing Coefficient b While Holding Exponent m Constant	139
2. Effect on Present Yaw Relation of Changing Exponent m While Holding Coefficient b Constant	140
3. Schematic of Circuits Utilized in Schemes to Compensate for Ambient Temperature Variations	141
4. Non-dimensional Charts for Selecting Parallel and Series Resistances of Compensating Circuit 1	142
5. Non-dimensional Charts for Selecting Series and Parallel Resistances of Compensating Circuit 2	143
6. Schematic of an X-Probe in a Low Intensity Turbulent Field	144
7. Turbulence Correction Factor, g/h , as a Function of b and m for $\gamma=0$	145
8. Side-View Schematic of High-Speed Test Section of Environmental Wind Tunnel	146
9. Outside View of Wind Tunnel Test Section Showing Single-Sensor Probe Mounted in Angularity Chuck, and Photograph of Calibration Tunnel with Probe in Position for Calibration Along with Instrumentation for Mean Yaw Calibration	147
10. Top-View Schematic of Calibration Tunnel, Modified to Superimpose Periodic Fluctuations on Mean Free-Stream	148
11. Photographs of Calibration Tunnel, Modified to Produce Streamwise Periodic Fluctuations, with Single-Sensor Probe Mounted in Angularity Chuck, and Instrumentation for Unsteady Yaw Calibration	149
12. Photographs of Single-Sensor Probe, and Side and Top Views of X-Probe; All Wires have $\ell/d=580$	150

Figure		Page
13.	Instrumentation Schematic for Mean Velocity Yaw Calibration	151
14.	Instrumentation Schematic for Unsteady Yaw Calibration Utilizing a Single Wire Probe	152
15.	Instrumentation Schematic for Unsteady Yaw Calibration Utilizing an X-Wire Probe . . .	153
16.	Sample Yaw Calibration Data Prior to Initial Shifting to Determine Mean Flow Direction; Dashed Line Indicates Angle Corresponding to Mean Flow Normal to Wire	154
17.	Typical Variation with Offset Angle of Stan- dard Deviation, from Present Relation, of Mean Yaw Calibration Data Indicating that Initially Shifted Data is not Properly Centered.	155
18.	Typical Variation with Offset Angle of Stan- dard Deviation, from Present Relation, of Mean Yaw Calibration Data for Properly Shifted Data	156
19.	Typical Variation of Standard Deviation of Mean Yaw Calibration Data with Probe Mis- alignment Using Three Different Yaw Relations	157
20.	Deviation from Cosine Law for a Standard- length Single Wire Probe; $l/d=580$	158
21.	Contours of Constant Standard Deviation in b-m Plane for a Single Wire Probe at a Fixed Reynolds Number; $l/d=250$ and $Re_d=1.8$	159
22.	Contours of Constant Standard Deviation in b-m Plane for a Standard-length Single Wire Probe at a Fixed Reynolds Number; $l/d=580$ and $Re_d=1.8$	160
23.	Variation with Reynolds Number of Region of a Minimum Standard Deviation in b-m Plane for a Single Wire Probe; $l/d=250$	161
24.	Variation with Free Stream Velocity of Region of Minimum Standard Deviation for X-Wire Data from MSU and a Standard-length Single Wire Probe	162

Figure	Page
25. Effect of Probe Misalignment and Reynolds Number on Standard Deviation, from Cosine Law, of Mean Yaw Calibration Data for a Single Wire Probe; $l/d=250$	163
26. Effect of Probe Misalignment and Reynolds Number on Standard Deviation, from Friehe and Schwarz Relation, of Mean Yaw Calibration Data for a Single Wire Probe; $l/d=250$	164
27. Effect of Probe Misalignment and Reynolds Number on Standard Deviation, from Present Relation, of Mean Yaw Calibration Data for a Single Wire Probe; $l/d=250$	165
28. Effect of Probe Misalignment and Reynolds Number on Best Fit Coefficient Determined from Friehe and Schwarz Relation for a Single Wire Probe; $l/d=250$	166
29. Effect of Probe Misalignment and Reynolds Number on Best Fit Coefficient Determined from Present Relation for a Single Wire Probe; $l/d=250$	167
30. Effect of Probe Misalignment and Reynolds Number on Standard Deviation, from Friehe and Schwarz Relation, of Mean Yaw Calibration Data for a Standard-length Single Wire Probe; $l/d=580$	168
31. Effect of Probe Misalignment and Reynolds Number on Standard Deviation, from Present Relation, of Mean Yaw Calibration Data for a Standard-length Single Wire Probe; $l/d=580$	169
32. Effect of Probe Misalignment and Reynolds Number on Best Fit Coefficient Determined from Friehe and Schwarz Relation for a Standard-length Single Wire Probe; $l/d=580$	170
33. Effect of Probe Misalignment and Reynolds Number on Best Fit Coefficient Determined from Present Relation for a Standard-length Single Wire Probe; $l/d=580$	171
34. Effect of Probe Misalignment and Reynolds Number on Best Fit Exponent Determined from Present Relation for a Standard-length Single Wire Probe $l/d = 580$	172

Figure	Page
35. Effect of Probe Misalignment and Reynolds Number on Turbulence Correction Factor Determined from Present Relation for a Standard-length Single Wire Probe; $l/d=580$	173
36. Effect of Reynolds Number on Ratio of Standard Deviation Improvement Between Cosine, Friehe and Schwarz and Present Relations for $l/d=75$ and 1000	174
37. Variation with Reynolds Number of Best Fit Coefficients Determined from Friehe and Schwarz and Present Relations for $l/d=1000$	175
38. Variation of Hot-Wire Velocity Calibration Constants with l/d	176
39. Variation of Ratio of Standard Deviation Improvement Between Cosine and Present Relations with Sensor l/d at a Fixed Reynolds Number; $Re_d=1.8$	177
40. Variation of Ratio of Standard Deviation Improvement Between Friehe and Schwarz and Present Relations with Sensor l/d at a Fixed Reynolds Number; $Re_d=1.8$	178
41. Variation of Best Fit Coefficient Determined from Friehe and Schwarz Relation with Sensor l/d at a Fixed Reynolds Number; $Re_d=1.8$	179
42. Variation of Best Fit Coefficient Determined from Present Relation with Sensor l/d at a Fixed Reynolds Number; $Re_d=1.8$	180
43. Variation of Best Fit Exponent Determined from Present Relation with Sensor l/d at a Fixed Reynolds Number; $Re_d=1.8$	181
44. Variation of Turbulence Correction Factors, as Determined from Friehe and Schwarz and Present Relations, with Sensor l/d at a Fixed Reynolds Number; $Re_d=1.8$	182
45. Combined Effect of Reynolds Number and Sensor l/d on Ratio of Standard Deviation Improvement Between Friehe and Schwarz and Present Relations	183

Figure		Page
46.	Combined Effect of Reynolds Number and Sensor ℓ/d on Best Fit Coefficient Determined from Friehe and Schwarz Relation	184
47.	Combined Effect of Reynolds Number and Sensor ℓ/d on Best Fit Coefficient Determined from Present Relation	185
48.	Combined Effect of Reynolds Number and Sensor ℓ/d on Best Fit Exponent Determined from Present Relation	186
49.	Combined Effect of Reynolds Number and Sensor ℓ/d on Turbulence Correction Factor Determined from Friehe and Schwarz Relation . . .	187
50.	Combined Effect of Reynolds Number and Sensor ℓ/d on Turbulence Correction Factor Determined from Present Relation	188
51.	Contours in b - m Plane of Constant Effective Standard Deviation over Range of Reynolds Numbers for a Single Wire Probe; $\ell/d=250$, $0.9 \leq Re_d \leq 3.6$	189
52.	Contours in b - m Plane of Constant Effective Standard Deviation over Range of Reynolds Numbers for a Standard-length Single Wire Probe; $\ell/d=580$, $0.9 \leq Re_d \leq 3.6$	190
53.	Variation with Overheat Ratio of Turbulence Correction Factor and Ratio of Standard Deviation Improvement Between Friehe and Schwarz and Present Relations for a Standard-length Single Wire Probe; $\ell/d = 580$. . .	191
54.	Variation of Best Fit Coefficients and Exponent Determined from Friehe and Schwarz and Present Relations with Overheat Ratios for a Standard-length Probe; $\ell/d=580$. . .	192
55.	Variation of Turbulence Correction Factor and Ratio of Standard Deviation Improvement Between Friehe and Schwarz and Present Relations with Angular Range of Calibration; $\ell/d=145$	193
56.	Variation of Best Fit Coefficients and Exponent Determined from Friehe and Schwarz and Present Relations with Angular Range of Calibration; $\ell/d=145$	194

Figure		Page
57.	Variation of Turbulence Correction Factor and Ratio of Standard Deviation Improvement, Between Friehe and Schwarz and Present Relations, with Angular Range of Calibration for a Standard-length Single Wire Probe; $\ell/d = 580$195
58.	Variation of Best Fit Coefficients and Exponent Determined from Friehe and Schwarz and Present Relations with Angular Range of Calibration for a Standard-length Single Wire Probe; $\ell/d = 580$196
59.	Comparison Between Experimentally Determined X-Probe Sensitivity Term and Those Calculated Using Cosine, Friehe and Schwarz and Present Relations for Wire 1 and $Q_S = 12.5$ ft/sec.197
60.	Comparison Between Experimentally Determined X-Probe Velocity Sensitivity Term and Those Calculated Using Cosine, Friehe and Schwarz and Present Relations for Wire 1 and $Q_S = 25$ and 37.5 ft/sec.198
61.	Comparison Between Experimentally Determined X-Probe Velocity Sensitivity Term and Those Calculated Using Cosine, Friehe and Schwarz and Present Relations for Wire 1 and $Q_S = 50$ ft/sec.	199
62.	Comparison Between Experimentally Determined X-Probe Velocity Sensitivity Term and Those Calculated Using Friehe and Schwarz and Present Relations for Wire 2 and $Q_S = 12.5$ and 25 ft/sec.200
63.	Comparison Between Experimentally Determined X-Probe Velocity Sensitivity Term and Those Calculated Using Friehe and Schwarz and Present Relations for Wire 2 and $Q_S = 37.5$ and 50 ft/sec.201
64.	Variation, Due to Change of Yaw Angle, of Effective rms Velocity with Mean Effective Velocity for a Single Wire Probe202
65.	Variation of Normalized Effective Turbulence Intensity with Angle of Yaw for Single Wire Probe203

Figure	Page
66. Effect of Free-Stream Fluctuations of Different Frequencies and Intensities on Best Fit Coefficient Determined from Friehe and Schwarz Relation for a Constant Free-Stream Velocity, $U_{\infty}=12$ ft/sec.204
67. Variation of Normalized Effective Turbulence Intensity with Angle of Incidence for an X-Probe at $U_{\infty}=12.5$ ft/sec.205
68. Variation of Normalized Effective Turbulence Intensity with Angle of Incidence for an X-Probe at $U_{\infty}=15$ ft/sec.206
69. Comparison of X-Probe Velocity Sensitivity Term Calculated from Mean Velocity Yaw Calibration Data with that Calculated from Fluctuating Velocity Yaw Calibration Data207
70. Variation of Best Fit Coefficient Determined from Friehe and Schwarz Relation with Sensor l/d for Different Reynolds Numbers.208
71. Variation of Equivalent Coefficient Determined from Hinze-Champagne Relation with Sensor l/d , for Different Reynolds Numbers209
72. Variation of Best Fit Coefficient Determined Using Present Relation with Sensor l/d for Single Wires, X-Wires and Hot-Film Probes210
73. Variation of Best Fit Exponent Determined Using Present Relation with Sensor l/d for Single Wires, X-Wires and Hot-Film Probes211
74. Variation of Turbulence Correction Factor Determined Using Present Relation with Sensor l/d for Single Wires, X-Wires and Hot-Film Probes212
75. Correlation Between Best Fit Coefficients and Exponents Determined Using Present Relation for Single Wires, X-Wires and Hot-Film Probes213
76. Combined Effect of Reynolds Number and Sensor l/d on Region of "Significant" Improvement over Friehe and Schwarz Relation by use of Present Relation214
77. Combined Effect of Reynolds Number and Sensor l/d on Regions where Turbulence Correction Factor follows "Cosine-Like" Behavior215

Figure	Page
78. Overall Improvement by Present Relation over Cosine Law and Friehe and Schwarz Relations when Using Best Coefficients and Exponents Averaged over a Reynolds Number Range; $0.9 \leq Re_d \leq 3.6$	216
79. Typical Variation with Mean Flow Angle of Computed Differences in v' and $\bar{u}v$ Obtained Using Different Yaw Relations for a Sensor with Large Deviations from Cosine Law	217
80. Typical Variation with Mean Flow Angle of Computed Differences in U and u' Intensity Obtained Using Different Yaw Relations for a Sensor with Large Deviation from Cosine Law	218
81. Typical Variation with Mean Flow Angle of Computed Turbulence Velocities Obtained Using Different Yaw Relations for a Standard-length Single Wire Probe	219
82. Schematic of Experimental Facility for Velocity Calibration in Air at Different Ambient Temperatures	220
83. Effect of Air Temperature on Output of Anemometer for Different Overheat Ratios Including Operation in Constant Overheat Ratio and Constant Overheat Resistance Difference Modes at Several Fixed Velocities	221
84. Variation with Air Temperature of Overheat Ratio and Resistance Difference for Constant Output Voltage Operation at Several Fixed Velocities	222
85. Typical Temperature Dependence of Resistance Ratio τ for Hot-Wires in Air at Several Fixed Velocities	223
86. Temperature Dependence of Hot-Wire Velocity Calibration Coefficients for Different Overheat Ratios	224
87. Temperature Dependence of King's Law Coefficients for Different Overheat Ratios.	225
88. Deviations from Cosine Law as Determined by Friehe and Schwarz	226

Figure		Page
89.	Deviations from Cosine Law for Hot-Films in Water	227
90.	Contours of Constant Standard Deviation of $f(\alpha)$ in b-m Plane for a Hot-Film in Water at $U_\infty=0.07$ ft/sec.	228
91.	Contours of Constant Standard Deviation of $f(\alpha)$ in b-m Plane for a Hot-Film in Water at $U_\infty=1.0$ ft/sec.	229
92.	Dependence of Region of Minimum Standard Deviation in b-m Plane on Reynolds Number for Hot-Films in Water	230
93.	Variation of Hot-Wire Velocity Calibration Coefficients with Yaw Angle for an X-Probe.	231
94.	Contours in b-m Plane of Constant Standard Deviation for MSU Data at $U_\infty=25$ ft/sec.	232
95.	Variation with Reynolds Number of Best Fit Coefficient Determined from Friehe and Schwarz Relation, and Ratio of Standard Deviation Improvement Between Friehe and Schwarz and Present Relations for MSU Data	233
96.	Variation with Reynolds Number of Best Fit Coefficient and Exponent Determined From Present Relation for MSU Data	234

NOTATION

Symbol	Definition
A	Coefficient in King's Law
A'	Hot-wire velocity calibration constant
a'	Constant relating series resistance ratios of compensating circuit 3
B	Coefficient in King's Law
B', B' _α	Hot-wire velocity calibration constant
b, b*, $\overline{b^*}$	Coefficient, best fit coefficient and best fit coefficient averaged over a range of Reynolds numbers, respectively, in present relation for yaw dependence of hot-wires or hot-films
b'	Constant relating parallel resistance ratios of compensating circuit 3
b _f , b _f [*] , $\overline{b_f^*}$	Coefficient, best fit coefficient and best fit coefficient averaged over a range of Reynolds numbers, respectively, in Friehe and Schwarz relation for yaw dependence of hot-wires or hot-films
c _{1u} c _{2u} c _{3u}	Coefficients relating difference between calculated values of u ² determined using cosine law and present relation
c _{1uv} c _{2uv} c _{3uv}	Coefficients relating differences between calculated values of \overline{uv} , by subtracting mean squared output voltages, determined using cosine law and present relation
c _{1uv} [*] c _{2uv} [*] c _{3uv} [*]	Coefficients relating differences between calculated values of \overline{uv} , by time averaging instantaneous quantity, determined using cosine law and present relation
c _{1v} c _{2v} c _{3v}	Coefficients relating difference between calculated values of v ² determined using cosine law and present relation
d	Wire diameter
E _b	Anemometer bridge output voltage

Symbol	Definition
E_L	Linearized anemometer output voltage
\bar{E}_1, \bar{E}_2	Time-mean output voltages of sensors 1 and 2 of an X-probe, respectively
e_1, e_2	Time-dependent part of output voltages of sensors 1 and 2 of an X-probe, respectively
f^2	Function used to relate effective velocity to incident velocity and yaw angle
g	Weighting function taking into account deviations from cosine law
H	Function used to relate effective velocity to sensor output voltage
h	Weighting function taking into account deviations from cosine law
I	Integral related to non-ideal behavior of temperature compensating circuits
I^*	Integrand of I
I_P	Current passing through velocity sensor
\tilde{K}_1	Temperature dependent linearization constant of velocity calibration used in temperature compensation analysis of Chapter II and Appendix A
K_1, K_2	Linearization constants for sensors 1 and 2 of an X-probe, respectively
ℓ	Sensor length
$m, m^*, \overline{m^*}$	Exponent, best fit exponent and best fit exponent averaged over a range of Reynolds numbers, respectively, in present relation for yaw dependence of hot-wires or hot-films
n	Exponent in probe velocity calibration and King's law
P_r	Parallel resistance ratio = R_P/R_T
Q_e	Instantaneous effective cooling velocity

Symbol	Definition
\bar{Q}_e	Time-mean effective cooling velocity
Q_i	Instantaneous velocity incident on X-probe
Q_s	Mean value of streamwise velocity
q_e	Time-dependent part of effective cooling velocity
q_s, q_n	Fluctuating velocities in a Cartesian coordinate system along and normal to mean streamline, respectively
q'_s, q'_e	RMS value of q_s and q_e , respectively
R_C	Resistance of velocity sensor
R_{Co}	Resistance of velocity sensor at reference temperature T_o
Re_d	Reynolds number based on wire diameter = $Q_s d / \nu$
R_H	Operating resistance of velocity sensor
R_P, R_{P1}, R_{P2}	Parallel resistances in temperature compensating circuits
R_S, R_{S1}, R_{S2}	Series resistances in temperature compensating circuits
R_T	Resistance of temperature compensator
R_{To}	Resistance of temperature compensator at reference temperature T_o
R_1, R_2	Fixed resistances in anemometer bridge
R_3	Equivalent resistance of temperature compensating circuit
r_o	Overheat ratio = R_H / R_C
S_r	Series resistance ratio = R_S / R_T
$S_{1u}, S_{1v}, S_{2u}, S_{2v}$	X-probe velocity sensitivity coefficients which are functions of γ
T	Ambient temperature

Symbol	Definition
T_o	Ambient reference temperature
U, V	Time-mean velocity components in Cartesian coordinate system x and y , respectively
U_{eff}	Time-mean effective cooling velocity
u, v	Time-dependent part of velocity components in Cartesian coordinate system x and y , respectively
x_c, x_f, x_p	A quantity x calculated using cosine law, Friehe and Schwarz and present relations, respectively
z_1, z_2, z_3, z_4, z_5	Non-dimensional resistance groups used in the solution of temperature compensating circuit number 3
α_1, α_2	Angle between mean flow and direction normal to sensors 1 and 2, respectively
α_C	Temperature coefficient of resistance for velocity sensor
α_r	Ratio of temperature coefficients for compensator and velocity sensor = α_T/α_C
α_T	Temperature coefficient of resistance for compensator probe
α_o	Angle indicating line of symmetry of mean yaw calibration data
$\hat{\alpha}_i$	Time dependent component of instantaneous incident angle β_i ; $\beta_i = \alpha_i + \hat{\alpha}_i$
β	Probes resistance ratio = R_T/R_C
β_o	Probes resistance ratio at reference temperature T_o
β_1, β_2	Angle between instantaneous velocity and direction normal to sensor 1 and 2, respectively
γ	Angle of inclination of mean velocity with respect to axis of an X-probe

Symbol	Definition
Δ	Determinant formed from weighting functions of velocity components for each sensor of X-probe
$\Delta\alpha$	Angular range over which yaw calibration data was obtained
λ	Weighting function of angle of mean velocity = $\cos \gamma + \sin \gamma$
ξ	Weighting function of angle of mean velocity = $\cos \gamma - \sin \gamma$
ρ_u	Ratio of mean square values of v to that of u as calculated using cosine law = $(v^2/u^2)_c$
ρ_{uv}	Ratio of Reynolds stress, \overline{uv} , to $\overline{u^2}$ calculated using cosine law = $(\overline{uv})_c / (\overline{u^2})_c$
ϵ_x	Percentage difference in a quantity x as calculated by Friehe and Schwarz relation and by present relation
$\tilde{\epsilon}_x$	Percentage difference in a quantity x as calculated by cosine law and by present relation
$(\tilde{\epsilon}_x)_f$	Percentage difference in a quantity x as calculated by cosine law and by Friehe and Schwarz relation
Σ_p	Effective standard deviation of $f^2(\alpha)$ determined using present relation = $\hat{\sigma}_p + \hat{\sigma}_p$
$\Sigma_c^*, \Sigma_f^*, \Sigma_p^*$	Minimum effective standard deviation of $f^2(\alpha)$ determined using cosine, Friehe and Schwarz and present relations, respective
$\bar{\sigma}_p$	Standard deviation of $f^2(\alpha)$ determined using present relation and normalized with value at $\alpha = 0$
$\sigma_c^*, \sigma_f^*, \sigma_p^*$	Minimum standard deviation of $f^2(\alpha)$ using cosine, Friehe and Schwarz and present relations, respectively
$\overline{\sigma_c^*}, \overline{\sigma_f^*}, \overline{\sigma_p^*}$	Minimum standard deviation of $f^2(\alpha)$, averaged over a Reynolds number range, using cosine, Friehe and Schwarz and present relations, respectively

Symbol	Definition
$\hat{\sigma}_p$	Standard deviation associated with calculating $\bar{\sigma}_p$ from several $\bar{\sigma}_p$'s at different Reynolds numbers
$\hat{\sigma}_c, \hat{\sigma}_f, \hat{\sigma}_p$	Standard deviation associated with $\bar{\sigma}_c^*$, $\bar{\sigma}_f^*$ and $\bar{\sigma}_p^*$, respectively
σ'	Standard deviation of $f(\alpha)$ using present relation
θ_1, θ_2	Angle of inclination of sensors 1 and 2 of an X-probe with respect to x direction
η	General temperature function defined by Equation (II-28)
ν	Kinematic viscosity
τ	Resistive function for constant bridge and linearized output voltages defined by Equation (II-22)
ϕ_1	Left hand side of Equation (II-60) which is related to bridge relation
ϕ_2	Left hand side of Equation (II-61) which is related to temperature relation

ABSTRACT

A scheme utilizing a temperature probe immersed in the working fluid to compensate for the dependence of hot-wire velocity calibration on ambient temperature variations was analyzed. One needs only to know the properties of the anemometer bridge and the velocity and temperature probes to achieve the compensation. Hence, the scheme provides means for incorporating the temperature compensation a priori to conducting the experiments without any need for temperature calibration. Estimates of the errors introduced through the non-ideal behavior of the compensating circuits have been derived and indicate that the error is proportional to the square of the temperature variation. For typical probes with an ambient temperature increase of 40°C, maximum errors in the indicated velocity of -1% or less can be achieved.

Measurements in many complex flowfields, such as in swirling flows or near bluff bodies, require the knowledge of the yaw sensitivity of an X-wire probe to a high degree of accuracy. The yaw relation $U_e/U_i = [1 - b(1 - \cos^m \alpha)]^2$ is proposed and investigated analytically and experimentally. In the derivation of the response equations of inclined cylindrical sensors in steady and fluctuating velocity fields, previous analyses have been extended for the present yaw relation to include X-probes with dissimilar sensors as well as mean velocities at an angle γ to the line of symmetry of the X-wires.

For mean velocity measurements, with sensors that have yaw dependence which does not closely follow the cosine law, neither the simple nor an approximate weighted sum and difference technique applies when $\gamma \neq 0$. This makes analog processing to obtain accurate mean velocities extremely difficult if not impossible. However, for cases where the mean streamline is aligned with the probe axis of symmetry, the errors introduced were found to be less than 5%. In low level turbulence, time dependent velocity components can always be obtained with comparable accuracy using a weighted sum and difference technique once the mean flow angle is determined. However, the weighting must take into account deviations from the cosine law. For a typical sensor whose yaw data has a standard deviation from the cosine law of 0.5%, and when $\gamma = 0$, the estimates of errors in u' , v' and \overline{uv} are approximately 3%, 11% and 8%, respectively. The error in \overline{uv} increases substantially as γ deviates from zero. These errors are essentially proportional to the standard deviation from the cosine law, σ , as it increases above its value in this example. Even when the sensor closely follows the cosine law, i.e., $\sigma \approx 0.1\%$, errors in these quantities can exist. Discrepancies were also found between different yaw relations in calculated values of turbulence velocity correlations which are derived from the same data. These discrepancies depend on the mean flow angle, the distribution of the turbulence energy between the velocity components and the accuracy to which the mean flow calibration data fits the particular yaw function.

The effect of various parameters on the yaw sensitivity of hot-wires has been experimentally determined. In all cases, the present yaw relation fits the calibration data to a higher degree of accuracy than the cosine law or the Friehe and Schwarz relation, where $m = 0.5$. The ratio of improvement over either relation is smaller for the very short sensors ($l/d \approx 100$) than for the long sensors ($l/d \approx 1000$). The trend of the yaw parameters with either sensor l/d or Reynolds number does not seem to approach the cosine law but rather it seems to overshoot it without any observed asymptotic values. Values of the transverse sensitivity coefficient calculated from a yaw sensitivity function, taking into account deviations from the cosine law, yield a higher degree of accuracy than those obtained directly from the data. Based on the Reynolds number dependency of the yaw coefficients, one should use different yaw calibration coefficients for different velocities. If a single set of parameters is to be used, the accuracy achieved by a simple relation like the cosine law is as good as one may expect. However, after the data has been gathered, the results must be corrected for the large errors introduced into the mean and rms velocity components. Each new sensor mounted on a probe must be calibrated, even if the new sensor is identical to the one being replaced.

The parameters of the yaw relation are affected by the presence of unsteady velocities in the flowfield and depend on the frequency of these fluctuations. While dynamic

yaw calibration of the probes is not necessary, the mean
yaw sensitivity of the probe should be obtained in the pres-
ence of some velocity fluctuations, e.g., in the presence of
some background turbulence of similar spectral content to
the flow under consideration.

CHAPTER I

INTRODUCTION

Background

Hot-wire sensors are probably the most commonly used measuring instrument in experimental fluid mechanics. In conjunction with a constant temperature anemometer unit, they provide unique capabilities which to date are only rivaled by the laser doppler velocimeter. Because of various limitations, such as very high cost, ambiguities related to the scattering particles and errors introduced by continuous tracking signal processing units, hot-wire anemometers will most likely remain a primary instrument for velocity measurements. The hot-wire does, however, have many of its own limitations, some of which will always remain; e.g., need for the sensor and its support to be located in the flowfield and the nonlinearity of the anemometer output. Numerous studies have been carried out to develop the instrument to its present stage. In particular, several of these studies have been devoted to removing some of the limitations.

The temperature of the working fluid in many of the flow facilities does not remain constant for the entire duration of the experiment. These temperature changes may be deliberate, because of some aspect of the experiment, or incidental, e.g., due to the energy losses from the fan or pump providing the flow in the facility. In industrial applications of hot-wires, such temperature variations are

unavoidable. Since the hot-wire sensor is not only sensitive to the flow velocity but also to the fluid temperature, density and viscosity, such variations lead in many occasions to substantial errors in the indicated velocity. A simple and inexpensive method of temperature compensation which would require no extensive additional calibration of the anemometer would be ideal. For example, an acceptable method would be one which can be accurately used once basic properties of the probes are known. The accuracy of the method is of course measured by the errors introduced during temperature variations. Hence, an estimate of these errors is an essential part of the development and documentation of the method.

In turbulent or complex flowfields various arrays of hot-wire sensors are needed in order to resolve the various components and correlations of the velocity field. Various types have been used over the last three or four decades, the most common being the X-wire probe. In order for any hot-wire array to resolve velocity components in directions other than the streamwise direction or to provide information on the components of velocity in more than one direction, the dependence of the anemometer output on the yaw or pitch of the probe must be known. If fluctuating velocities or their correlations are to be measured, this dependence must be known to a very high degree of accuracy, since the derivatives of the output with respect to the yaw or pitch angle are required in order to infer these quantities from

the anemometer signals.

In the case of the X-probe, the dependence or sensitivity of the output signal from both sensors must be known as a function of the yaw angle, measured for example from the axis of symmetry of the X-wires. When the mean streamlines of the flow are not parallel to this axis during the entire traverse of the probe in the flowfield, the mean velocity vector will not be aligned with the X-wire axis of symmetry at all times. In such cases the yaw dependence of the probe must be known to the high degree of accuracy over a wider range of angles. Many practical and complex flowfields are included in these cases. The one class of flows which motivated this work and is of particular interest here can be described in general as "swirling flows". Such flows arise in many problems as, for example, can be seen from the Introduction to Nagib's work [1].* Measurements in such flows or near bluff bodies, in particular in the presence of turbulence, require the information described above.

The present study was initiated in response to needs which arose in connection with the recent work by Wigeland et al. [2,3] and aims at providing its results to future extensions of their investigations. To obtain the measurements presented in their papers [2,3] Wigeland, Ahmed and Nagib utilized X-wire probes. They used well known methods

*Numbers in brackets refer to numbered references in the Bibliography.

to calibrate the probes and to process the signal with the aid of analog circuitry. Several such methods, which rely on different approaches, have been used by many investigators and only some of them are documented in the literature. In particular, some of the approaches not documented in the literature rely on digital processing techniques which have been recently introduced to experimental fluid mechanics research, but seem to be gaining considerable ground over analog signal processing systems. At I.I.T. we believe that both analog and digital techniques should be available to the experimenter so that they may be utilized in the various stages of diagnostics and final data collection of the experiment. Therefore, in our opinion a most essential ingredient required in an approach for dealing with the calibration and utilization of X-wire, as well as multiple sensor probes, is their adaptability to both signal processing techniques.

Almost all of the methods used with X-wires rely at one stage on describing the yaw calibration data by some analytical function. These vary from simple cosine functions to high order polynomials. In a few cases the discrete calibration data are used in the method. However, these suffer from the difficulties involved in obtaining derivatives of the anemometer output with respect to yaw angle.

Many of these methods and comparisons between them are discussed in the following chapters. In the remainder of this chapter, some of the results in the literature of

importance to the two aspects of the present study, i.e., yaw and temperature dependence of hot-wires, are briefly discussed.

Relevant Literature

Extensive work has been done in the areas of temperature and yaw dependence of hot-wires. In regard to the temperature dependence, semi-empirical heat-transfer laws have been developed by Collis and Williams [4], Davies and Fisher [5] and Bradbury and Castro [6]. With the aid of these relations, a number of schemes to measure and/or compensate for the ambient temperature variations are described both in the literature and through commercially available compensators.

Burchill and Jones [7] proposed a scheme in which the resistance in the anemometer bridge that controls the wire temperature is manually adjusted as the fluid temperature changes, the adjustment being based on calibration curves obtained earlier at different ambient temperatures. The amount of time wasted during an experiment is the major objection to this scheme. Other techniques developed by Chevray and Tutu [8] and similarly by Ali [9] involve a complex compensating scheme which is applied to the signal from the bridge, after it has been linearized, through the linearizer constants. Rose [10] determined a method by which values read from the anemometer were corrected through the use of a correction factor which was a function of temperature. His method was found to give 3% errors in

indicated velocity due to only a 12°F change of temperature. Methods like those of Chevray and Tutu [8] and of Ali [9] are particularly suited when high frequency temperature changes are present in the flowfield. Their methods as well as Rose's can be also adapted to digital signal processing techniques.

A number of compensating units are sold by the hot-wire anemometer manufacturers. However cost is prohibitive in many cases and these units can be interfaced only with the newer anemometer models. Nagib [1] and Tan-atichat et al. [11] employed a simple compensating scheme that consisted of a temperature sensing probe together with a resistive network which was used as the leg in the bridge of a constant temperature anemometer opposite the velocity sensor. Using this scheme they were able to compensate to better than 1% change in indicated velocity over a 20°C change in water temperature. However to determine the values of resistances in the network required a long and tedious iterative procedure. Nevertheless, this was by far the simplest scheme which attained the desired accuracy, as long as the frequency response of the temperature probe was higher than the frequency of temperature changes.

In regard to the yaw dependence, Prandtl [12], Struminsky [13] and Jones [14] determined that for an infinite heated cylinder only the velocity component normal to it was effective in the cooling. In this case the yaw sensitivity function is given by

$$f^2(\alpha) = \cos \alpha \quad (\text{I-1})$$

where α is the angle between the incident velocity and the normal to the wire. The effective velocity, U_e ; is therefore related to the incident velocity, U_i , by:

$$U_e = U_i f^2(\alpha) \quad (\text{I-2})$$

Hinze [15], Webster [16] and Champagne [17] have found that finite length hot-wires produce deviations from the cosine law and suggested the following for the directional sensitivity,

$$f^2(\alpha) = (\cos^2 \alpha + k^2 \sin^2 \alpha)^{1/2} \quad (\text{I-3})$$

where k is a small parameter accounting for the axial component of the velocity. All of them report that k varies with sensor ℓ/d although considerable amount of scatter is evident when comparing their data. Hinze [15], Bruun [18], and Kjellström et al. [19] have determined that k decreases with increasing velocity, which Horvatin [20] suggests may be due to the axial temperature profile of the wire becoming more isothermal at the higher velocities.

Other yaw relations have been proposed by Bruun [18], by Fujita and Kovasznay [21], and by Friehe and Schwarz [22] where in their case,

$$f^2(\alpha) = [1 - b(1 - \cos^k \alpha)]^2 \quad (\text{I-4})$$

The Friehe and Schwarz relation appears to fit most yaw calibration data to a greater degree of accuracy than any of the previous yaw relations examined. However, their data [22] indicate that hot-films which have small ℓ/d 's seem to deviate less from the cosine law as compared to hot wires which have much larger ℓ/d 's.

In an attempt to explain these trends, and to examine the conditions in water, Roberts et al. [23,24] generalized the Friehe and Schwarz relation to

$$f^2(\alpha) = [1 - b(1 - \cos^m \alpha)]^2 \quad (I-5)$$

and investigated the yaw dependence of commercially available hot-film probes in water. This generalization was based on observed trends in the data which indicated that a combination of the behaviors depicted in Figures 1 and 2 is more suitable than either one separately. It is quite clear from these two figures that the behavior in the two cases is significantly different at large yaw angles. It should also be noted that the behavior of Figure 1 is that of the Friehe and Schwarz relation while Equation (I-5) combines the trends shown in both figures. Roberts et al. [23,24] determined that the accuracy in fitting the calibration data using this relation, which is called the present relation in the following chapters, was superior to the Friehe and Schwarz relation. However, the trends they sought to explain still remained unresolved after their studies.

Champagne et al. [25] and later Friehe and Schwarz,

each using their own yaw sensitivity relation, have determined corrections to low intensity turbulence measurements using an ideal linearized X-probe for the case where the mean velocity is along the axis of symmetry of the X-wires. These corrections have not been determined yet in complex flows where the mean velocity cannot be aligned with the X-probe, nor has a comparison been made between the various turbulence correlations as would be obtained from the same data using different yaw relations.

Morrison et al. [26] show that dynamic calibration of X-probes yields significantly different results than those obtained by static calibration. Bruun [17] has demonstrated that part of this difference is caused by poor approximation of the static calibration. Bruun's data however, reveals that a difference does still exist which he attributes to experimental error.

From the literature cited above it seems that there is considerable disagreement and uncertainty in the interpretation of signals from and use of X-wire probes. This study aims to clarify some of these problems.

Objectives

The objective of this work can be divided into two groups; one relating to the temperature dependence of hot-wires, and the other to their yaw dependence.

In regard to the temperature dependence, the objective is to analyze the compensating scheme proposed by Nagib [1] to obtain, whenever possible, exact solutions of the values

of the resistances in the compensating network, and to derive estimates of the errors introduced by the technique during typical temperature variations. It is considered desirable to be able to perform all of these knowing only the temperature dependence of the velocity sensor and compensating probes and their resistances, which are usually specified by the manufacturer. If these objectives are accomplished the desired compensation can be achieved and the expected errors estimated a priori to making any flow measurements and without the need for temperature calibration.

In regard to the yaw dependence of hot-wires, the first objective is to do a careful study of the effect of various parameters on the yaw sensitivity as described by the cosine law, the Friehe and Schwarz relation and the present relation. These parameters include Reynolds number, probe misalignment and length to diameter ratio of the sensor, l/d . Two possible methods of varying the sensor l/d were considered during the planning stages. The first is based on varying the active portion of the sensor while keeping the ratio between the prong spacing and the active length constant. Another method is to keep the prong spacing constant while changing the sensor l/d . The latter was selected for several reasons, although the former appeared attractive for other reasons. While the length of the active sensor is easily changed during fabrication the prong spacing is usually not readily altered. The separation of the prongs

is often dictated by the size of the experimental setup and requirements of minimum probe interference. On the other hand the length of the active sensor may be varied to suit the flow conditions, including the scales of the velocity gradients and turbulence field.

The second objective is to extend the analysis of Champagne [17] and Friehe and Schwarz [22] to cases when an X-probe, with sensors having different yaw sensitivities, is used in flows where the mean velocity is not along the line of symmetry of the X-wires. In conjunction with this, a comparison of the differences between the values of the turbulence velocity correlations computed from the cosine law, Friehe and Schwarz and the present relation can be made.

The third objective is to examine the effect of free-stream fluctuations on the yaw sensitivity of hot-wires. Since hot wires are calibrated for yaw sensitivity under static conditions with very low turbulence levels, i.e. calibration conditions, operating them under conditions where larger fluctuations are present may have an effect on the various sensitivities.

CHAPTER II

ANALYSIS OF TEMPERATURE COMPENSATING CIRCUITS

FOR USE WITH HOT-WIRES OR HOT-FILMS

A number of temperature compensating schemes have been proposed by the hot-film manufacturers. Several of these schemes depend on a temperature sensing probe which can be used in the anemometer bridge shown in Figure 3 in place of the bridge resistance R_3 . The ideal probe for this purpose should have the following properties:

1. Its resistance R_T should be given by

$$R_T = r_o M R_C = M R_H$$

where M is the bridge ratio and r_o is the overheat ratio.

2. The dependence of R_T on temperature should be identical to that of the velocity probe operating resistance R_H .

3. The size of the probe should be sufficiently large so as not to be heated by the bridge current.

The latter requirement assures that the probe resistance is independent of the fluid velocity.

Such a probe is of course almost impossible to manufacture and even if it could be selected from a large statistical sample it could only be used with the one matched velocity probe. Fortunately most of the hot-film and hot-wire probes furnished by a manufacturer are quite similar in properties with their resistances falling within a limited range. A temperature compensating circuit similar to those outlined in Figure 3 can therefore be

used, at least over some range of ambient temperature variation. A complete analysis for the determination of the series and parallel resistances of compensating circuits 1, 2 and 3 are presented.

Analysis

Based on the bridge balance condition of the anemometer circuit in Figure 3,

$$R_1/R_2 = R_H/R_3 \equiv M \quad (\text{II-1})$$

where M is the bridge ratio and R_3 is the equivalent resistance of the temperature compensating network

Considering only the first coefficient of the temperature dependence of R_C and R_T (i.e., ignoring second and higher order terms of temperature changes) we write

$$\frac{dR_T}{dT} = R_{T0} \alpha_T \quad (\text{II-2})$$

and

$$\frac{dR_C}{dT} = R_{C0} \alpha_C \quad (\text{II-3})$$

Or that

$$R_T = R_{T0} [1 + \alpha_T (T - T_0)] \quad (\text{II-4})$$

and

$$R_C = R_{C0} [1 + \alpha_C (T - T_0)] \quad (\text{II-5})$$

where R_{T0} and R_{C0} are the resistances of the temperature compensating probe and the cold resistance of the velocity probe, respectively, when the ambient temperature, T , is equal to the probe reference temperature T_0 .

Assuming that α_r is independent of temperature, where

$$\alpha_r \equiv \frac{\alpha_T}{\alpha_C} \quad \text{and} \quad \alpha_r > 0 \quad (\text{II-6})$$

we define a probe resistance ratio as follows

$$\beta \equiv \frac{R_T}{R_C} \quad (\text{II-7})$$

The resistance ratio β is dependent on temperature and its value at the original reference temperature T_0 , (usually room temperature) is

$$\beta_0 = \left[\frac{R_T}{R_C} \right]_{T=T_0} \quad (\text{II-8})$$

We denote the operating resistance of the velocity sensor by R_H , i.e.,

$$R_H = R_C r_0(T) \quad \text{and} \quad r_0(T) > 1 \quad (\text{II-9})$$

where r_0 is the overheat ratio. Since R_H is related to the temperature compensating circuit resistance through the bridge relation, it is also a function of the ambient temperature. First, we consider compensating circuit 1, where

$$R_3 = R_S + \frac{R_P R_T}{R_P + R_T} \quad (\text{II-10})$$

From the bridge balance condition, we write

$$R_H = M \left[R_S + \frac{R_P R_T}{R_P + R_T} \right] \quad (\text{II-11})$$

Using Equations (II-5) and (II-7) and defining non-dimensional series and parallel resistances, S_r and P_r respectively, where

$$S_r \equiv \frac{R_S}{R_T} \quad \text{and} \quad S_r > 0 \quad (\text{II-12})$$

and

$$P_r \equiv \frac{R_P}{R_T} \quad \text{and} \quad P_r > 0 \quad (\text{II-13})$$

we obtain the nondimensional bridge balance condition,

$$S_r + \left(1 + \frac{1}{P_r}\right)^{-1} = \frac{r_o}{\beta M} \quad (\text{II-14})$$

The governing equation for the velocity sensor (King's Law) can be written as

$$\frac{I_P^2 R_H}{R_H - R_C} = A + BU^n \quad (\text{II-15})$$

where U is the fluid velocity and I_P is the current through the probe; A , B and n are nearly constant. Based on this relation and since for constant temperature operation the anemometer servo-amplifier maintains the probe temperature and hence its resistance R_H constant, one may conclude that two possible modes may be useful for keeping the output voltage constant, i.e., independent of ambient temperature. One can either maintain a constant overheat ratio or maintain a constant resistance difference.

Another possible mode exists if we rewrite King's Law in terms of the bridge output voltage and determine the condition necessary to keep the output independent of ambient temperature.

Case A: Constant Overheat Ratio. In this case we set

$$r_o = \text{constant}$$

Since

$$M = \frac{R_H}{R_3} = \frac{r_o R_C}{R_3} \quad (\text{II-16})$$

and the anemometer bridge ratio M is constant, then

$$\frac{M}{r_o} = \frac{R_C(T)}{R_3(T)} = \text{constant}$$

and

$$\frac{d}{dT} \left[\frac{R_C}{R_3} \right] = 0$$

so that using Equations (II-2,3,4) we obtain

$$\frac{dR_3}{dT} = \frac{R_{Co} \alpha_C r_o}{M} \quad (\text{II-17})$$

Case B: Constant Overheat Resistance Difference. In this case we set

$$R_H - R_C = \text{constant}$$

so that

$$\frac{d}{dT} [R_H - R_C] = 0$$

Using Equations (II-1) and (II-4), we obtain

$$\frac{dR_3}{dT} = \frac{R_{Co} \alpha_C}{M} \quad (\text{II-18})$$

Case C: Constant Bridge Output Voltage. In this case referring to Figure 3, and using the bridge balance condition, the non-linear governing Equation (II-15) may be rewritten as

$$E_b^2 = \left(1 - \frac{R_C}{R_H} \right) (R_1 + R_H)^2 (A + BU^n) \quad (\text{II-19})$$

(note that if the ambient temperature remains constant,

this reduces to the form $E_b^2 = A' + B'U^n$). Assuming that the coefficients A, B, and n are insensitive to temperature variations relative to the changes in R_C and R_H with ambient temperature (the validity of this assumption is examined in Appendix B), we set

$$\left(\frac{\partial}{\partial T} E_b \right)_U = 0 \quad (\text{II-20})$$

Using Equations (II-1), (II-4) and (II-19), we obtain

$$\frac{dR_3}{dT} = \frac{R_{Co} \alpha_C \tau(T)}{M} \quad (\text{II-21})$$

where

$$\tau(T) = \frac{1 + \frac{R_1}{R_H}}{2 + \frac{R_C}{R_H} \left[\frac{R_1}{R_H} - 1 \right]} \quad (\text{II-22})$$

Let us now consider one final case. In this case we determine the condition necessary to keep the output voltage constant as the ambient temperature varies if the anemometer output is linearized.

Case D: Constant Linearized Output Voltage. From Equation (II-19) we can write

$$E_L = \tilde{K}_1(T) U \quad (\text{II-23})$$

where E_L is the linearized output voltage and the linearization constant \tilde{K}_1 is a function of T given by

$$\tilde{K}_1(T) = k_o \left[B \left(1 + \frac{R_C}{R_H} \right) (R_1 + R_H)^2 \right]^{1/n} \quad (\text{II-24})$$

For the output to be independent of temperature variations, we set

$$\left(\frac{\partial E_L}{\partial T} \right)_U = 0 \quad (\text{II-25})$$

that is,

$$\frac{d\tilde{K}_1}{dT} = 0 \quad (\text{II-26})$$

Using Equations (II-1), (II-4), (II-24) and (II-26) we obtain

$$\frac{dR_3}{dT} = \frac{R_{Co} \alpha_C \tau(T)}{M}$$

Comparing this with Equation (II-21), we find that temperature compensation does not depend upon whether the anemometer output voltage is linearized or not.

We now combine all of the above cases into a single equation which specifies the functional dependence of the compensating circuit with temperature. This equation can be written as

$$\frac{dR_3}{dT} = \frac{R_{Co} \alpha_C}{M\eta} \quad (\text{II-27})$$

where

$$\eta = \begin{cases} \frac{1}{r_o} & \text{for Case A} \\ 1 & \text{for Case B} \\ \frac{1}{\tau(T)} & \text{for Cases C and D} \end{cases} \quad (\text{II-28})$$

The solution of Equation (II-27) along with the non-dimensional bridge relation for each circuit will yield values of the series and parallel resistances for each circuit.

Compensating Circuit 1. Substitution of Equation (II-10) into Equation (II-27) and using Equations (II-12) and (II-13) leads to the solution for the parallel resistance directly

$$P_r = (\sqrt{\alpha_r M \eta} \beta_o - 1)^{-1} \quad (\text{II-29})$$

or

$$R_p = [R_T (\sqrt{\alpha_r M \eta} \beta_o - 1)^{-1}]_{T=T_o} \quad (\text{II-30})$$

then substitution of Equation (II-29) into Equation (II-14) leads to

$$R_s = \left[R_T \left(\frac{r_o}{\beta M} - \frac{1}{\sqrt{\alpha_r M \eta} \beta_o} \right) \right]_{T=T_o} \quad (\text{II-31})$$

Here, the values of R_s and R_p are evaluated at the initial reference temperature T_o .

Compensating Circuit 2. Referring to Figure 3, we obtain

$$R_3 = \frac{R_p (R_s + R_T)}{R_p + R_s + R_T} \quad (\text{II-32})$$

Use of Equations (II-1), (II-12) and (II-13) leads to the non-dimensional bridge balance condition,

$$S_r + 1 - P_r \left[\frac{\beta M}{r_o} (S_r + 1) - 1 \right] = 0 \quad (\text{II-33})$$

Substitution of Equation (II-32) into Equation (II-27) yields a non-dimensional form

$$S_r = P_r [\sqrt{\alpha_r M \eta} \beta_o - 1] - 1 \quad (\text{II-34})$$

The solution of Equations (II-33) and (II-34) for the series and parallel resistances results in the resistances

$$R_P = \left[\frac{R_T r_O \sqrt{\alpha_r M \eta \beta_O}}{\beta M (\sqrt{\alpha_r M \eta \beta_O} - 1)} \right]_{T=T_O} \quad (\text{II-35})$$

and

$$R_S = \left[R_T \left(\frac{r_O}{\beta M} \sqrt{\alpha_r M \eta \beta_O} - 1 \right) \right]_{T=T_O} \quad (\text{II-36})$$

Operating charts for the selection of the series and parallel resistances for circuits 1 and 2 are also plotted in Figures 4 and 5, respectively. These charts, or the equations given above, can be used by the reader to design or adjust either of the two compensating circuits. One needs only to know the properties of the anemometer bridge and the velocity and temperature probes, i.e., their resistances and their temperature dependence coefficients, in order to achieve the compensation, without any need for temperature calibration.

Compensating Circuit 3. Circuit 3 is slightly different than the previous two circuits presented in that there are four unknown resistances to determine. Since we are working with two relationships, it would seem that at this point two of the resistances can be selected arbitrarily. It will be shown later that some constraints on the other two resistances exist. However, initially we will proceed as if there are no constraints in order to generate a family of solutions.

From Figure 3, the equivalent resistance is

$$R_3 = \frac{(R_{S1} + R_{P1} + R_T) R_{P2} R_{S2} + R_{P1} R_{P2} (R_{S1} + R_T)}{(R_{S1} + R_{P1} + R_T) (R_{P2} + R_{S2}) + R_{P1} (R_{S1} + R_T)} \quad (\text{II-37})$$

Using the previous methods, the non-dimensional bridge relation becomes

$$(S_{r1} + P_{r1} + 1) (P_{r2} + S_{r2}) + P_{r1} (S_{r1} + 1) - \frac{\beta M}{r_o} [(S_{r1} + P_{r1} + 1) P_{r2} S_{r2} + P_{r1} P_{r2} (S_{r1} + 1)] = 0 \quad (\text{II-38})$$

Substitution of Equation (II-37) into Equation (II-27) yields the non-dimensional form

$$(S_{r1} + P_{r1} + 1) (P_{r2} + S_{r2}) + P_{r1} (S_{r1} + 1) = P_{r1} P_{r2} \sqrt{\alpha_r M \eta \beta_o} \quad (\text{II-39})$$

Since two of the resistances will be arbitrary we define

$$S_{r2} \equiv a' S_{r1} \quad \text{and} \quad a' \geq 0 \quad (\text{II-40})$$

$$P_{r2} \equiv b' P_{r1} \quad \text{and} \quad b' > 0 \quad (\text{II-41})$$

where a' and b' are constants to be determined.

We also define the following quantities,

$$Z_1 \equiv S_{r1} (S_{r1} + P_{r1} + 1) \quad (\text{II-42a})$$

$$Z_2 \equiv P_{r1} (S_{r1} + 1) \quad (\text{II-42b})$$

$$Z_3 \equiv \frac{\beta M}{r_o} P_{r1} S_{r1} (S_{r1} + P_{r1} + 1) \quad (\text{II-42c})$$

$$Z_4 \equiv \frac{\beta M}{r_o} P_{r1}^2 (S_{r1} + 1) - P_{r1} (S_{r1} + P_{r1} + 1) \quad (\text{II-42d})$$

Substitution of Equations (II-40) and (II-41) into Equation (II-38) along with Equation (II-42) leads to

$$b' = \frac{a'z_1 + z_2}{a'z_3 + z_4} \quad (\text{II-43})$$

Substitution of Equation (II-40) and Equation (II-41) into Equation (II-39) leads to

$$b' = \frac{a'z_1 + z_2}{z_5} \quad (\text{II-44})$$

where

$$z_5 \equiv p_{r1}^2 \sqrt{\alpha_r M \eta \beta_o} - p_{r1}(s_{r1} + p_{r1} + 1)$$

Solving for a' and b' in Equations (II-43) and (II-44), we obtain

$$a' = \frac{z_5 - z_4}{z_3} \quad (\text{II-45})$$

and

$$b' = \frac{z_1(z_5 - z_4) + z_2 z_3}{z_5 z_3} \quad (\text{II-46})$$

Since $a' \geq 0$ we find from Equation (II-45) that

$$z_5 > z_4$$

This leads to

$$0 \leq s_{r1} \leq \frac{r_o}{\beta M} \sqrt{\alpha_r M \eta \beta_o} - 1 \quad (\text{II-47})$$

The condition on the coefficient b' is that $b' > 0$ which implies that

$$z_5 > 0$$

and hence

$$p_{r1} > \frac{s_{r1} + 1}{\sqrt{\alpha_r M \eta \beta_o} - 1} \quad (\text{II-48})$$

Having selected S_{r1} and P_{r1} based on Equations (II-47) and (II-48), P_{r2} and S_{r2} can be determined from Equations (II-40) and (II-41).

Putting the solution in dimensional form we have the following:

- (1) Select R_{S1} such that

$$0 \leq R_{S1} \leq \left[R_T \left(\frac{r_O}{\beta M} \sqrt{\alpha_r M \eta \beta_O} - 1 \right) \right]_{T=T_O} \quad (\text{II-49})$$

- (2) Select R_{P1} such that

$$R_{P1} > \left[\frac{R_T + R_{S1}}{\sqrt{\alpha_r M \eta \beta_O} - 1} \right]_{T=T_O} \quad (\text{II-50})$$

- (3) Determine R_{S2} from

$$R_{S2} = \left[\frac{R_{P1}}{(R_{S1} + R_{P1} + R_T)} \left(\frac{R_T r_O \sqrt{\alpha_r M \eta \beta_O}}{\beta M} - R_{S1} - R_T \right) \right]_{T=T_O} \quad (\text{II-51})$$

- and (4) R_{P2} is given by

$$R_{P2} = \left\{ \frac{R_{P1} \sqrt{\alpha_r M \eta \beta_O}}{\beta M [R_{P1} \sqrt{\alpha_r M \eta \beta_O} - (R_{S1} + R_{P1} + R_T)]} \right\}_{T=T_O} \quad (\text{II-52})$$

Selection of A Compensating Probe

Ideally, it would be desirable to have one temperature compensating probe for all velocity probes. For typical probes this is not always possible. However, knowing the range of resistances of the velocity probes and their temperature coefficients, a temperature probe may be carefully selected for use in most of the cases. Based on the solution of compensating circuits 1, 2 and 3, and

requiring that a real solution exist, the following inequality involving the parameters of both probes must hold:

$$\frac{R_{Co}}{M\alpha_r\eta(T_o)} < R_{To} \leq \frac{R_{Co}r_o^2\alpha_r\eta(T_o)}{M} \quad (II-53)$$

With a knowledge of the properties of available velocity sensors, operating overheat ratios, anemometer bridge ratio and operation mode of the compensating circuit, a suitable temperature compensator may either be fabricated or purchased from a manufacturer based on this inequality.

Besides this restriction, the compensating probe must not be influenced by the electrical current passing through it. This results in temperature probes sensitive to velocity, which is not only an undesirable feature but also affects the calibration curve of the velocity probe as discussed by Tan-atichat et al.[11]. The compensating circuit also has a frequency response to temperature variations which depends on the thermal time constant of the temperature probe (up to several cycles per second can be obtained using commercially available probes).

Error Estimates

We do not expect "perfect" compensation from the proposed circuit configurations. This is true since Equation (II-27) prescribes the dependence of R_3 on ambient temperature for ideal compensation, while the introduction of a proposed circuit and a temperature probe forces a set

function of temperature on R_3 . Therefore, the error will be related to the difference between the two.

Case C: Non-Linear Output Voltage. As before,

$$E_b = (R_1 + R_H) \sqrt{\left(1 - \frac{R_C}{R_H}\right)} (A + BU^n)$$

Then, with the assumption that A, B and n are not functions of temperature,

$$\begin{aligned} \frac{1}{E_b} \frac{\partial E_b}{\partial T} = & \frac{1}{2} (R_1 + R_H)^{-1} \left(1 - \frac{R_C}{R_H}\right)^{-1} \left[M \frac{\partial R_3}{\partial T} \left(2 - \frac{R_C}{R_H} + \frac{R_1 R_C}{R_H^2}\right) \right. \\ & \left. - \alpha_C R_{Co} \left(1 + \frac{R_1}{R_H}\right) \right] \end{aligned} \quad (\text{II-54})$$

If R_3 behaves ideally then the terms in the brackets would vanish and Equation (II-27) would arise. Since this is not necessarily true, we integrate Equation (II-54) from the initial reference temperature T_o to some ambient temperature T to obtain

$$E_b(T) = E_b(T_o) e^{I/2} \quad (\text{II-55})$$

where

$$I \equiv \int_{T_o}^T \frac{M \frac{\partial R_3}{\partial T} \left(2 - \frac{R_C}{MR_3} + \frac{R_1 R_C}{M^2 R_3^2}\right) - \alpha_C R_{Co} \left(1 + \frac{R_1}{MR_3}\right)}{\left(1 - \frac{R_C}{MR_3}\right) (R_1 + MR_3)} dT \quad (\text{II-56})$$

Since I is a function of $R_3(T)$ which is a function of the particular compensating circuit used, the magnitude of the change in the output voltage with temperature will be a function of the circuit configuration employed.

Once the velocity sensor is calibrated at the reference temperature, i.e.

$$E_b^2 = A' + B'U^n,$$

then the error in the indicated velocity will be

$$\frac{U(T) - U(T_o)}{U(T_o)} = \left[\frac{E_b^2(T_o)e^I - A'}{E_b^2(T_o) - A'} \right]^{1/n} - 1 \quad (\text{II-57})$$

In the case of the linearized output voltage, following a similar procedure, we find that

$$E_L(T) = E_L(T_o)e^{I/n} \quad (\text{II-58})$$

and the corresponding error in the indicated velocity is given as

$$\frac{U(T) - U(T_o)}{U(T_o)} = e^{I/n} - 1 \quad (\text{II-59})$$

A Sample Estimate. We now consider a typical hot-wire and compensator combination to obtain an indication of the quality of the compensation using the proposed scheme. Assume we are using a tungsten hot-wire whose resistance at room temperature is 10Ω and whose temperature coefficient, α_C , is $0.0048/^\circ\text{C}$. From Equation (II-53) we determine that a compensator made from nickel whose resistance at room temperature is 15Ω and whose temperature coefficient, α_T , is $0.0067/^\circ\text{C}$ is suitable.

Using the analysis described, the values of the resistances for circuit 1 are

$$R_P = 49.68\Omega$$

$$R_S = 6.48\Omega,$$

and for compensating circuit 2 are

$$R_P = 77.61\Omega$$

$$R_S = 8.44 \Omega.$$

Using these values we can determine $R_3(T)$ and dR_3/dT and thus evaluate Equations (II-55) and (II-59) for different ambient temperature changes for circuits 1 and 2. The results are shown in Table 1.

The estimates presented in Table 1 indicate that the proposed compensating circuits will tend to slightly under-compensate for ambient temperature changes. The use of compensating circuit 1 with a temperature change of 40°C produces a 2% change in the indicated velocity, while utilizing circuit 2 would reduce this error to 1% for the same temperature change. Over the range of temperature changes examined the error is approximately proportional to the square of the temperature difference.

Next, we ask the following question: by changing from circuit 1 to circuit 2, the error was reduced by a factor of 2; can we then minimize the error by going to circuit 3?

At the reference temperature, the compensating circuit must satisfy constraint equations as derived previously.

It must satisfy the bridge relation, i.e.,

$$\phi_1 \equiv \left[R_3 - \frac{r_O R_C}{M} \right]_{T=T_O} = 0, \quad (\text{II-60})$$

Table 1. Sample Error Estimates for Typical Velocity and Temperature Probes in Circuits 1 and 2.

	$T - T_o (^{\circ}\text{C})$				
	0	10	20	30	40
$R_C(T) (\Omega)$	10.00	10.48	10.96	11.44	11.92
$R_T(T) (\Omega)$	15.00	16.01	17.01	18.02	19.02

Circuit 1

$R_3(T) (\Omega)$	18.00	18.59	19.15	19.70	20.23
$\frac{dR_3}{dT} \left(\frac{\Omega}{^{\circ}\text{C}} \right)$	0.0593	0.0575	0.0557	0.0541	0.0525
$\frac{E_b(T) - E_b(T_o)}{E_b(T_o)} (\%)$	0	-0.03	-0.11	-0.25	-0.44
$\frac{E_L(T) - E_L(T_o)}{E_L(T_o)} (\%)$	0*	-0.13*	-0.52*	-1.17*	-2.05*

Circuit 2

$R_3(T) (\Omega)$	18.00	18.59	19.17	19.73	20.28
$\frac{dR_3}{dT} \left(\frac{\Omega}{^{\circ}\text{C}} \right)$	0.0593	0.0581	0.0570	0.0559	0.0548
$\frac{E_b(T) - E_b(T_o)}{E_b(T_o)} (\%)$	0	-0.01	-0.05	-0.12	-0.25
$\frac{E_L(T) - E_L(T_o)}{E_L(T_o)} (\%)$	0*	-0.06*	-0.23*	-0.53*	-0.94*

* $n = 0.43$

and the temperature relation, Equation (II-21), i.e.,

$$\phi_2 \equiv \left[\frac{dR_3}{dT} - \frac{\alpha_C R_{Co} \tau(T)}{M} \right]_{T=T_0} = 0, \quad (\text{II-61})$$

for the constant output voltage modes. The error involved is related to I which is defined by Equation (II-56).

Since in circuits 1 and 2 there are only two adjustable resistances, I is fixed, i.e., the error is unique. Circuit 3, however, has four undetermined resistances so that I can be minimized subject to the two constraints.

For a prescribed temperature difference, $T_f - T_0$, which one wishes to compensate over,

$$I = f(R_{S1}, R_{S2}, R_{P1}, R_{P2}) \quad (\text{II-62})$$

where

$$f(R_{S1}, R_{S2}, R_{P1}, R_{P2}) = \int_{T_0}^{T_f} I^* dT \quad (\text{II-63})$$

and where I^* is a known function of temperature, namely,

$$I^* = \frac{\frac{MdR_3}{dT} \left[2 - \frac{R_C}{MR_3} + \frac{R_1 R_C}{M^2 R_3^2} \right] - R_{Co} \alpha_C \left[1 + \frac{R_1}{MR_3} \right]}{\left(1 - \frac{R_C}{MR_3} \right) (R_1 + MR_3)} \quad (\text{II-64})$$

A necessary condition that I has a minimum value is that

$$dI = \frac{\partial f}{\partial R_{S1}} dR_{S1} + \frac{\partial f}{\partial R_{S2}} dR_{S2} + \frac{\partial f}{\partial R_{P1}} dR_{P1} + \frac{\partial f}{\partial R_{P2}} dR_{P2} = 0 \quad (\text{II-65})$$

subject to two constraints

$$\phi_1 = 0$$

and

$$\phi_2 = 0$$

where ϕ_1 and ϕ_2 are defined in Equations (II-60) and (II-61). Using the method of Lagrange multipliers, we obtain six equations in six unknowns, R_{S1} , R_{S2} , R_{P1} , R_{P2} , λ_1 and λ_2 , where λ_1 and λ_2 are the Lagrange multipliers. The six equations are:

$$\frac{\partial}{\partial R_{S1}} \int_{T_0}^{T_f} I^* dT + \frac{\lambda_1 \partial R_3}{\partial R_{S1}} + \frac{\lambda_2 \partial^2 R_3}{\partial T \partial R_{S1}} = 0 \quad (\text{II-66a})$$

$$\frac{\partial}{\partial R_{S2}} \int_{T_0}^{T_f} I^* dT + \frac{\lambda_1 \partial R_3}{\partial R_{S2}} + \frac{\lambda_2 \partial^2 R_3}{\partial T \partial R_{S2}} = 0 \quad (\text{II-66b})$$

$$\frac{\partial}{\partial R_{P1}} \int_{T_0}^{T_f} I^* dT + \frac{\lambda_1 \partial R_3}{\partial R_{P1}} + \frac{\lambda_2 \partial^2 R_3}{\partial T \partial R_{P1}} = 0 \quad (\text{II-66c})$$

$$\frac{\partial}{\partial R_{P2}} \int_{T_0}^{T_f} I^* dT + \frac{\lambda_1 \partial R_3}{\partial R_{P2}} + \frac{\lambda_2 \partial^2 R_3}{\partial T \partial R_{P2}} = 0 \quad (\text{II-66d})$$

$$\left[R_3 - \frac{r_{OC}}{M} \right]_{T=T_0} = 0 \quad (\text{II-66e})$$

$$\left[\frac{\partial R_3}{\partial T} - \frac{\alpha_C R_{CO} \tau(T)}{M} \right]_{T=T_0} = 0 \quad (\text{II-66f})$$

In the above equations R_3 is given by Equation (II-37). Solution of the above system of equations will lead to values of resistances which make circuit 3 the optimized circuit configuration. The solution of this system of equations has not yet been attempted. However, in principle

they can be solved numerically.

The performance of the constant output voltage mode was based upon the assumption that the coefficients in King's Law were independent of temperature. From the experimental results in Appendix B, we see that all of the coefficients are weak functions of ambient temperature. However, data for the different operating modes indicates that the anemometer output voltage drift is independent of the fluid velocity for measurements in air. Therefore the variations of B and n with temperature may be ignored.

The analysis can be modified to take into account the variation of the coefficient A with temperature. However, the variation of A would have to either be assumed or experimentally determined. In this case, the compensating circuits could not be set a priori to making any velocity measurements and the experimenter would have to calibrate his probe for both velocity and temperature. The error introduced, however, by making this assumption should be small and will be experimentally determined in future extensions of the present investigation.

CHAPTER III

RESPONSE EQUATIONS OF INCLINED CYLINDRICAL SENSORS IN STEADY AND FLUCTUATING VELOCITY FIELDS

In this chapter, the X-probe array of Figure 6 is considered to be immersed in a flow field described at any instant of time by an instantaneous velocity Q_1 . This flow field can be decomposed into a mean velocity Q_s which is inclined at an angle γ with respect to the x-axis, and the time dependent velocities q_s and q_n aligned with the mean streamline and the direction normal to it, respectively. Throughout this report the effect of fluctuations which are normal to both q_s and q_n is not considered. The response of the X-probe array to this low turbulence intensity velocity field will be determined utilizing various relations for the yaw sensitivity to determine the differences between them in calculating the flow field characteristics.

Time-Mean Velocity Field

Only the effect of Q_s on the time averaged output of the X-probe is examined here. As will be shown later this is only true for cases of low turbulence intensity. Referring to Figure 6, the mean effective cooling velocity that each sensor is subjected to can be related to the mean streamwise velocity through the equation

$$\bar{Q}_{e,1} = Q_s f^2(\theta_1 - \gamma) \quad (\text{III-1})$$

for sensor 1 and

$$\bar{Q}_{e,2} = Q_s f^2(\theta_2 + \gamma) \quad (\text{III-2})$$

for sensor 2. The function $f^2(\theta)$ is determined from the yaw sensitivity relation utilized. The mean effective cooling velocity is related to the mean output voltage of the sensor by

$$\bar{Q}_{e,i} = H(\bar{E}_i) \quad i = 1, 2 \quad (\text{III-3})$$

Where $H(\bar{E}_i)$ can take many forms. Two of these forms are given by

$$H(\bar{E}_i) = \begin{cases} \frac{\bar{E}_i}{K_i} & (\text{III-4a}) \\ \left[\frac{\bar{E}_i^2 - A_i}{B_i} \right]^{1/n_i} & (\text{III-4b}) \end{cases}$$

Where K_i is the calibration constant for a linearized sensor and A_i , B_i and n_i are the calibration constants for a non-linearized sensor. In each case calibration is carried out when the sensor is normal to the free-stream velocity.

Cosine Law. The angle of inclination γ and the mean U and V velocity components, aligned with the x and y axes, respectively, are to be extracted from Equations (III-1) and (III-2). If one is fortunate enough to have sensors which obey the cosine law, then Equations (III-1) and (III-2) are linear in U and V and lead to

$$U = (\cot \theta_1 + \cot \theta_2)^{-1} \left[\frac{H(\bar{E}_1)}{\sin \theta_1} + \frac{H(\bar{E}_2)}{\sin \theta_2} \right] \quad (\text{III-5})$$

$$V = (\tan \theta_1 + \tan \theta_2)^{-1} \left[\frac{H(\bar{E}_1)}{\cos \theta_1} - \frac{H(\bar{E}_2)}{\cos \theta_2} \right] \quad (\text{III-6})$$

where

$$\gamma = \tan^{-1} \left[\frac{V}{U} \right] \quad (\text{III-7})$$

When the hot-wire signals are linearized, Equations (III-5) and (III-6) represent a simple weighted sum and difference technique and are therefore, very attractive for use with analog processing.

As Champagne et. al. [25] have shown, nearly all sensors deviate from the cosine law and the magnitude of this deviation is a function of probe characteristics. In order to correct for these deviations more sophisticated yaw sensitivity relations have been proposed. These relations introduce nonlinearities in such a manner that a simple weighted sum and difference technique as in Equations (III-5) and (III-6) is usually not feasible. To determine the mean velocity components, the angle of mean flow, γ , may first be determined from an iteration scheme using

$$\frac{f^2(\theta_1 - \gamma)}{f^2(\theta_2 + \gamma)} = \frac{H(\bar{E}_1)}{H(\bar{E}_2)} \quad (\text{III-8})$$

The mean streamwise velocity can then be determined using Equation (III-1) or (III-2) with Equation (III-3). A simple decomposition of this mean velocity then yields the mean U and V components of velocity.

In general, proper schemes for determining the mean components when taking into account deviations from the cosine law do not readily lend themselves to analog processing techniques. How large an error then does one make in the determination of the mean velocity if one assumes the cosine law to take advantage of the simplicity previously

described? For ease of interpreting the results we assume that $\theta_1 = \theta_2 = 45^\circ$ and that both sensors have identical yaw sensitivity. Let γ , Q_s , U and V be quantities determined utilizing a yaw sensitivity function taking into account the deviations from the cosine law, and γ_c , $(Q_s)_c$, U_c , V_c be those quantities calculated from the same data utilizing the cosine law. It can then be shown that

$$\gamma_c = \tan^{-1} \left[\frac{f^2(45^\circ - \gamma) - f^2(45^\circ + \gamma)}{f^2(45^\circ - \gamma) + f^2(45^\circ + \gamma)} \right] \quad (\text{III-9})$$

$$\frac{U_c}{U} = \frac{(Q_s)_c}{Q_s} \left[\frac{\cos \gamma_c}{\cos \gamma} \right] \quad (\text{III-10})$$

$$\frac{V_c}{V} = \frac{(Q_s)_c}{Q_s} \left[\frac{\sin \gamma_c}{\sin \gamma} \right] \quad (\text{III-11})$$

where

$$\frac{(Q_s)_c}{Q_s} = \sqrt{[f^2(45^\circ - \gamma)]^2 + [f^2(45^\circ + \gamma)]^2} \quad (\text{III-12})$$

Examining Equations (III-9) through (III-12), one observes that as the response of the sensors deviates from the cosine law the magnitude of the errors introduced increases. These errors will be significant particularly in the angle of the mean flow and the V component.

It was pointed out in Chapter I that there are many yaw sensitivity functions in the literature which take into account the deviations from the cosine law. For mean velocity measurements when $\gamma=0$, there is no significant difference in accuracy among them. In the next few chapters it will be

shown that this is definitely not the case for time dependent velocity measurements. It will also be demonstrated that the present relation yields the highest accuracy in all cases. Thus, for the purpose of examining the errors introduced when using Equations (III-5) and (III-6), we assume here that $f(\alpha)$ is given either by the present relation or the Friehe and Schwarz relation.

Since we will be examining the difference in a quantity x as calculated by the present relation and by the cosine law, we define a relative error in x by

$$\epsilon_x = \frac{x_p - x_c}{x_c} \quad (\text{III-13})$$

where p and c denote the present and cosine relations, respectively. Similarly, the difference in the same quantity x as calculated by the Friehe and Schwarz relation and by the cosine law can be written as

$$(\epsilon_x)_f = \epsilon_x \bigg|_{\substack{b=b_f \\ m=0.5}} \quad (\text{III-14})$$

For comparison, the difference between the present relation and the Friehe and Schwarz relation is denoted by ϵ_x .

An ideal X-probe whose sensors have identical yaw response and are inclined at $\pm 45^\circ$ to the x -axis will now be considered. When the mean streamwise velocity is aligned with the x -axis, using Equations (III-10), (III-12) and (III-13) it can be shown that

$$\varepsilon_U \Big|_{\gamma=0} = \frac{1}{\sqrt{2} [1-b(1-2^{-m/2})]^2} - 1 \quad (\text{III-15})$$

and

$$\varepsilon_U \Big|_{\gamma=0} = \left[\frac{1-.159 b_f}{1-b(1-2^{-m/2})} \right]^2 - 1 \quad (\text{III-16})$$

For all cases within the scope of this work it was found that $\varepsilon_U|_{\gamma=0} < 5\%$. Thus, whenever $\gamma=0$ the cosine law is quite adequate in determining the mean velocity irrespective of the sensor being used. However, the magnitude of this error will be shown to depend on a number of parameters.

For the cases where $\gamma \neq 0$, sensors whose response is close to the cosine law are first considered. Next, sensors whose response is far from the cosine law will be discussed. As an example of the former case, we assume that $b=1.046$ and that $m=0.487$ (details of these results can be found in Chapter V). Using Equations (III-9) through (III-12) one then finds that for $\gamma \leq 25^\circ$

$$\varepsilon_\gamma \approx 2.5\%$$

$$\varepsilon_U \approx 1.3\%$$

$$\varepsilon_V \approx -2\%$$

Therefore, for sensors that do not show a marked deviation from the cosine law, mean velocity measurements are not significantly altered by employing a "more sophisticated" yaw relation and the simple sum and difference technique of the cosine law is quite adequate.

For the latter case we take $b=0.534$ and $m=0.868$. Using

these parameters in Equations (III-9) through (III-12) one obtains for $\gamma=5^\circ$

$$\epsilon_\gamma = 20\%$$

$$\epsilon_U = -5\%$$

$$\epsilon_V = 20\%$$

As the angle of the mean flow increases these errors also increase. Thus, for sensors which show a noticeable deviation from the cosine law, the simple sum and difference technique does not apply for cases where $\gamma \neq 0$, making analog processing extremely difficult if not impossible.

Furthur Generalization of Cosine Law. For sensors which exhibit small deviations from the cosine law it was shown that utilizing the cosine law leads to quite accurate results. An approximate method which may result in even more accurate results is based on the use of a weighted sum and difference technique utilizing a "more sophisticated" yaw relation. Here it is assumed that the mean effective cooling velocity can be decomposed in the manner similar to the cosine law.

$$\bar{Q}_{e,1} = U_{ap} f^2(\theta_1) + V_{ap} f^2(90-\theta_1) \quad (\text{III-17a})$$

and

$$\bar{Q}_{e,2} = U_{ap} f^2(\theta_2) - V_{ap} f^2(90-\theta_2) \quad (\text{III-17b})$$

The function $f^2(\theta_1)$ once again refers to the yaw relation utilized and the subscript ap refers to quantities calculated using this approximate method. Since the angle of inclination of the sensors is known, then once the sensors are

calibrated for yaw sensitivity, the weighting coefficients are determined. Solving Equations (III-17) for U_{ap} and V_{ap} one obtains

$$U_{ap} = \frac{\left[\frac{H(\bar{E}_1)}{f^2(90^\circ - \theta_1)} + \frac{H(\bar{E}_2)}{f^2(90^\circ - \theta_2)} \right]}{\left[\frac{f^2(\theta_1)}{f^2(90^\circ - \theta_1)} + \frac{f^2(\theta_2)}{f^2(90^\circ - \theta_2)} \right]} \quad (\text{III-18a})$$

and

$$V_{ap} = \frac{\left[\frac{H(\bar{E}_1)}{f^2(\theta_1)} - \frac{H(\bar{E}_2)}{f^2(\theta_2)} \right]}{\left[\frac{f^2(90^\circ - \theta_1)}{f^2(\theta_1)} + \frac{f^2(90^\circ - \theta_2)}{f^2(\theta_2)} \right]} \quad (\text{III-18b})$$

The errors introduced using this scheme can be calculated in a manner similar to that used for Equations (III-9) through (III-12). It then follows that

$$\tan \gamma_{ap} = \left\{ \frac{\frac{f^2(\theta_1 - \gamma)}{f^2(\theta_1)} - \frac{f^2(\theta_2 + \gamma)}{f^2(\theta_2)}}{\frac{f^2(\theta_1 - \gamma)}{f^2(90^\circ - \theta_1)} + \frac{f^2(\theta_2 + \gamma)}{f^2(90^\circ - \theta_2)}} \right\} \left\{ \frac{\frac{f^2(\theta_1)}{f^2(90^\circ - \theta_1)} - \frac{f^2(\theta_2)}{f^2(90^\circ - \theta_2)}}{\frac{f^2(\theta_1)}{f^2(90^\circ - \theta_1)} + \frac{f^2(\theta_2)}{f^2(90^\circ - \theta_2)}} \right\} \quad (\text{III-19a})$$

$$\frac{U_{ap}}{U} = \frac{\left[\frac{f^2(\theta_1 - \gamma)}{f^2(90^\circ - \theta_1)} + \frac{f^2(\theta_2 + \gamma)}{f^2(90^\circ - \theta_2)} \right]}{\left[\frac{f^2(\theta_1)}{f^2(90^\circ - \theta_1)} + \frac{f^2(\theta_2)}{f^2(90^\circ - \theta_2)} \right]} \left[\frac{1}{\cos \gamma} \right] \quad (\text{III-19b})$$

and

$$\frac{v_{ap}}{v} = \frac{\left[\frac{f^2(\theta_1 - \gamma)}{f^2(\theta_1)} - \frac{f^2(\theta_2 + \gamma)}{f^2(\theta_2)} \right]}{\left[\frac{f^2(90^\circ - \theta_1)}{f^2(\theta_1)} + \frac{f^2(90^\circ - \theta_2)}{f^2(\theta_2)} \right]} \left[\frac{1}{\sin \gamma} \right] \quad (\text{III-19c})$$

This approximate technique is a function of the sensors angle of inclination and its yaw sensitivity response. It is not possible in general to state that the approximate technique will lead to more accurate results than those based on the cosine law. The errors introduced should be checked in both cases to determine which method is more applicable.

Lastly, there may be times when mean velocity data are to be corrected for deviations from the cosine law after the data has been taken. Since all one wants to do is to "adjust" the experimental values for the deviations from the cosine law, one would not necessarily want to go through the iteration scheme previously mentioned. Utilizing Equations (III-10) and (III-11), the corrections can easily be calculated once the true angle of the mean flow with respect to the probe axis is known. From Equation (III-9) one can write for an ideal X-probe

$$\tan \gamma_c = f^*(\gamma) \quad (\text{III-20})$$

where

$$f^*(\gamma) = \frac{f^2(45^\circ - \gamma) - f^2(45^\circ + \gamma)}{f^2(45^\circ - \gamma) + f^2(45^\circ + \gamma)} \quad (\text{III-21})$$

Expanding $f^*(\gamma)$ in a Taylor series around γ_c one can also write

$$\tan \gamma_c = f^*(\gamma_c) + \frac{d}{d\gamma} \left[f^*(\gamma) \right]_{\gamma=\gamma_c} (\gamma - \gamma_c) + \dots \quad (\text{III-22})$$

The mean flow angle can then be computed from

$$\gamma = \gamma_c + \frac{\tan \gamma_c - f^*(\gamma_c)}{\frac{d}{d\gamma} \left[f^*(\gamma) \right]_{\gamma=\gamma_c}} \quad (\text{III-23})$$

Normally the first order correction should lead to accurate results. For sensors which show large deviations from the cosine law a second order correction term must be added to Equation (III-22). Utilizing Equations (III-10), (III-11) and (III-23) corrections for mean velocity measurements can be made after the data has been taken if the yaw sensitivity of the wire is known.

Time-Dependent Velocity Field

In this section, expressions for the turbulence velocity correlations will be developed for an ideal X-probe in a low-intensity turbulent flow. Figure 6 shows an X-probe array aligned with the x-axis and the mean velocity inclined at an angle γ with respect to this axis. Here the notation of references [17] and [22] have been used. Using the assumption of low-intensity turbulence, second and higher order terms in the velocity correlations are neglected and the instantaneous velocity can be written in the form

$$Q_i = Q_s \left(1 + \frac{q_s}{Q_s} \right) \quad (\text{III-24})$$

For sensor 1, we obtain the expression for the instantaneous angle of incidence, assuming an ideal X-probe, $\theta_1 = \theta_2 = 45^\circ$

and $K_1 = K_2 = K$, to be

$$\cos \beta_1 = \frac{\lambda\sqrt{2}}{2} \left(1 + \frac{\xi}{\lambda} \frac{q_n}{Q_s} \right) \quad (\text{III-25})$$

where

$$\lambda \equiv \cos \gamma + \sin \gamma \quad (\text{III-26})$$

and

$$\xi \equiv \cos \gamma - \sin \gamma \quad (\text{III-27})$$

Similarly, it can be shown that for sensor 2

$$\cos \beta_2 = \frac{\xi\sqrt{2}}{2} \left(1 - \frac{\lambda}{\xi} \frac{q_n}{Q_s} \right)$$

The effective instantaneous velocity is given by

$$Q_{e,j} = Q_i f^2(\beta_j) \quad j=1,2 \quad (\text{III-29})$$

where

$$f^2(\beta_j) = [1 - b_j (1 - \cos^{m_j} \beta_j)]^2$$

Assuming that the sensor output voltage is linear in the effective cooling velocity, i.e.,

$$E_j = K Q_{ej}$$

one can write

$$E_j = K(Q_s + q_s) f^2(\beta_j) \quad (\text{III-30})$$

Expanding $f^2(\beta_j)$ in a power series and keeping only first order terms, one obtains

$$E_1 = K g(b_1, m_1, \lambda) Q_s + K q_s g(b_1, m_1, \lambda) + K \xi q_n h(b_1, m_1, \lambda) \quad (\text{III-31})$$

and

$$E_2 = K g(b_2, m_2, \xi) Q_s + K q_s g(b_2, m_2, \xi) - K \lambda q_n h(b_2, m_2, \xi) \quad (\text{III-32})$$

where

$$g(b_1, m_1, \lambda) = [1 + (2^{-\frac{m_1}{2}} \lambda^{m_1-1} b_1)]^2 \quad (\text{III-33a})$$

$$g(b_2, m_2, \xi) = [1 + (2^{-\frac{m_2}{2}} \xi^{m_2-1} b_2)]^2 \quad (\text{III-33b})$$

$$h(b_1, m_1, \lambda) = 2^{1-\frac{m_1}{2}} \lambda^{m_1-1} b_1 m_1 [1 + (2^{-\frac{m_1}{2}} \lambda^{m_1-1} b_1)] \quad (\text{III-33c})$$

and

$$h(b_2, m_2, \xi) = 2^{1-\frac{m_2}{2}} \xi^{m_2-1} b_2 m_2 [1 + (2^{-\frac{m_2}{2}} \xi^{m_2-1} b_2)] \quad (\text{III-33d})$$

The sensor output voltage can be decomposed into a mean and a fluctuating component, that is

$$E_j = \bar{E}_j + e_j ; \quad j=1,2 \quad (\text{III-34})$$

With this, the response of the x-probe to the velocity fluctuations becomes

$$e_1 = Kq_s g(b_1, m_1, \lambda) + K\xi q_n h(b_1, m_1, \lambda) \quad (\text{III-35})$$

$$e_2 = Kq_s g(b_2, m_2, \xi) - K\lambda q_n h(b_2, m_2, \xi) \quad (\text{III-36})$$

In the remainder of this section the turbulence velocity correlations are determined in two different coordinate systems: (1) one whose axes are along and normal to the mean velocity vector and (2) one which is along and normal to the x and y axes of Figure 6.

Streamwise Coordinate System. From Equations (III-35) and (III-36) and defining

$$\Delta \equiv \lambda h(b_2, m_2, \xi) g(b_1, m_1, \lambda) + \xi h(b_1, m_1, \lambda) g(b_2, m_2, \xi) \quad (\text{III-37})$$

we obtain the following expressions for the instantaneous values of the fluctuating streamwise and normal velocity components:

$$q_s = K^{-1} \Delta^{-1} [\lambda h(b_2, m_2, \xi) e_1 + \xi h(b_1, m_1, \lambda) e_2] \quad (\text{III-38})$$

and

$$q_n = K^{-1} \Delta^{-1} [g(b_2, m_2, \xi) e_1 - g(b_1, m_1, \lambda) e_2] \quad (\text{III-39})$$

Taking the time average of Equations (III-31) and (III-32) one arrives at the following expressions for the mean velocity

$$\bar{E}_1 = K Q_s g(b_1, m_1, \lambda) \quad (\text{III-40})$$

$$\bar{E}_2 = K Q_s g(b_2, m_2, \xi) \quad (\text{III-41})$$

Squaring and time averaging Equation (III-38) and normalizing by the mean velocity we obtain the streamwise velocity correlation

$$\frac{\overline{q_s^2}}{Q_s^2} = \left[1 + \frac{\xi}{\lambda} \frac{g(b_2, m_2, \xi) h(b_1, m_1, \lambda)}{g(b_1, m_1, \lambda) h(b_2, m_2, \xi)} \right]^{-2} \left\{ \frac{\left[e_1 + \frac{\xi h(b_1, m_1, \lambda)}{\lambda h(b_2, m_2, \xi)} e_2 \right]^2}{\bar{E}_1^2} \right\} \quad (\text{III-42})$$

Following a similar procedure, the following normal velocity correlation was derived:

$$\frac{\overline{q_n^2}}{Q_s^2} = \left[\frac{\lambda h(b_2, m_2, \xi)}{g(b_2, m_2, \xi)} + \frac{\xi h(b_1, m_1, \lambda)}{g(b_1, m_1, \lambda)} \right]^{-2} \left\{ \frac{\left[e_1 - \frac{g(b_1, m_1, \lambda)}{g(b_2, m_2, \xi)} e_2 \right]^2}{\bar{E}_1^2} \right\} \quad (\text{III-43})$$

Squaring and time averaging Equations (III-35) and (III-36) then subtracting them leads to the following relation for the bi-normal turbulence velocity correlation

$$\begin{aligned}
\frac{\overline{q_s q_n}}{\overline{Q_s^2}} = & \frac{1}{2} \left[\frac{\xi g(b_1, m_1, \lambda) h(b_1, m_1, \lambda)}{g^2(b_2, m_2, \xi)} + \frac{\lambda h(b_1, m_1, \xi)}{g(b_2, m_2, \xi)} \right]^{-1} \left\{ \frac{\overline{e_1^2 - e_2^2}}{\overline{E^2}} \right. \\
& + \left[1 - \frac{g^2(b_1, m_1, \lambda)}{g^2(b_2, m_2, \xi)} \right] \left[\frac{\overline{q_s^2}}{\overline{Q_s^2}} \right] + \left[\frac{\lambda^2 h^2(b_2, m_2, \xi)}{g^2(b_2, m_2, \xi)} \right. \\
& \left. \left. - \frac{\xi^2 h^2(b_1, m_1, \lambda)}{g^2(b_2, m_2, \xi)} \right] \left[\frac{\overline{q_n^2}}{\overline{Q_s^2}} \right] \right\} \quad (\text{III-44})
\end{aligned}$$

In the special case when $\gamma=0$, $b_1=b_2$ and $m_1=m_2$, these expressions reduce to the forms presented by Champagne [17] and Friehe and Schwarz [22], i.e.,

$$\frac{\overline{q_s^2}}{\overline{Q_s^2}} = \frac{1}{4} \frac{(\overline{e_1 + e_2})^2}{\overline{E^2}} \quad (\text{III-45})$$

$$\frac{\overline{q_n^2}}{\overline{Q_s^2}} = \frac{1}{4} \left[\frac{g(b, m)}{h(b, m)} \right]^2 \frac{(\overline{e_1 - e_2})^2}{\overline{E^2}} \quad (\text{III-46})$$

$$\frac{\overline{q_s q_n}}{\overline{Q_s^2}} = \frac{1}{4} \left[\frac{g(b, m)}{h(b, m)} \right] \frac{\overline{e_1^2 - e_2^2}}{\overline{E^2}} \quad (\text{III-47})$$

When the X-probe is non-ideal, i.e., when each sensor has a slightly different yaw response, there is a correction factor in the streamwise velocity correlation, even in the case when $\gamma=0$. In this case, the Reynolds stress cannot be determined using the above scheme without prior determination of the streamwise and normal velocity correlations. When the mean flow angle is not zero, in order to determine

the velocity correlations using analog techniques, a weighted sum and difference may be used. The magnitude of the weighting functions depends on the yaw sensitivity coefficients of both sensors of the probe as well as the mean flow angle.

x-y Coordinate System. In most cases where the mean velocity is at an angle γ with respect to an x-y coordinate system the fluid mechanics experimenter is not interested in determining the local streamwise and normal fluctuations but rather he is interested in the u & v fluctuations along the x and y axes respectively. The streamwise and normal fluctuating velocities can be decomposed into components along the x and y axes by the following transformation,

$$q_s = u \cos \gamma + v \sin \gamma \quad (\text{III-48})$$

$$q_n = -u \sin \gamma + v \cos \gamma \quad (\text{III-49})$$

Substitution into Equations (III-35) and (III-36) yields the response for the fluctuating output voltage. This can be written as

$$e_1 = KS_{1u}(\gamma)u + KS_{1v}(\gamma)v \quad (\text{III-50})$$

and

$$e_2 = KS_{2u}(\gamma)u - KS_{2v}(\gamma)v \quad (\text{III-51})$$

where the velocity sensitivity coefficients are given by

$$S_{1u}(\gamma) = g(b_1, m_1, \lambda) \cos \gamma - \xi h(b_1, m_1, \lambda) \sin \gamma \quad (\text{III-52})$$

$$S_{1v}(\gamma) = g(b_1, m_1, \lambda) \sin \gamma + \xi h(b_1, m_1, \lambda) \cos \gamma \quad (\text{III-53})$$

$$S_{2u}(\gamma) = g(b_2, m_2, \xi) \cos \gamma + \lambda h(b_2, m_2, \xi) \sin \gamma \quad (\text{III-54})$$

and

$$S_{2v}(\gamma) = -g(b_2, m_2, \xi) \sin \gamma + \lambda h(b_2, m_2, \xi) \cos \gamma \quad (\text{III-55})$$

Solving Equations (III-50) and (III-51) for the instantaneous velocity components, we obtain

$$u = K^{-1} \Delta^{-1} [S_{2v}(\gamma) e_1 + S_{1v}(\gamma) e_2] \quad (\text{III-56})$$

$$v = K^{-1} \Delta^{-1} [S_{2u}(\gamma) e_1 - S_{1u}(\gamma) e_2] \quad (\text{III-57})$$

which again is a simple weighted sum or difference of the output voltages. It should be pointed out that the mean velocity components must be determined, in order to evaluate the angle of incidence γ , before Equations (III-56) and (III-57) can be used.

In the case of an ideal x-probe and $\gamma=0$, the deviations from the cosine law in the computed turbulence velocity correlations would appear in the correction terms $(g/h)^2$ and (g/h) for the normal and bi-normal turbulence intensities as given by Equations (III-45 through 47). A plot of various constant g/h 's as a function of b and m is shown in Figure 7. With this plot, one can determine the difference between these calculated values assuming either the cosine law, the Friehe and Schwarz relation or the present relation.

Discrepancies Between Different Yaw Relations in Calculated Values of Turbulence Velocity Correlations. In many complex flows one is faced with cases in which $\gamma \neq 0$. How then do these three relations compare in the computed velocity correlations?

Squaring and time averaging Equation (III-56) we obtain

$$(\overline{u^2})_p = K^{-2} \Delta^{-2} [S_{2v}(\gamma)e_1 + S_{1v}(\gamma)e_2]^2 \quad (\text{III-58})$$

If one assumes the cosine law for yaw sensitivity, (i.e., $b=1$ and $m=0.5$) Equations (III-50) and (III-51) become

$$e_1 = K2^{-\frac{1}{2}}(u_c + v_c) \quad (\text{III-59})$$

$$e_2 = K2^{-\frac{1}{2}}(u_c - v_c) \quad (\text{III-60})$$

where u_c and v_c are the time dependent velocities determined using the cosine law. Note that employing the cosine law results in no explicit dependence on γ . Substitution into Equation (III-58), with the aid of Equation (III-20a), yields

$$\tilde{\epsilon}_{\overline{u^2}} = c_{1u} + c_{2u}\rho_u + c_{3u}\rho_{uv} \quad (\text{III-61})$$

where

$$c_{1u} = \frac{\Delta^{-2}}{2} [S_{2v}(\gamma) + S_{1v}(\gamma)]^2 - 1 \quad (\text{III-62a})$$

$$c_{2u} = \frac{\Delta^{-2}}{2} [S_{2v}(\gamma) - S_{1v}(\gamma)]^2 \quad (\text{III-62b})$$

and

$$c_{3u} = \frac{\Delta^{-2}}{2} [S_{2v}^2(\gamma) - S_{1v}^2(\gamma)] \quad (\text{III-62c})$$

The ratios ρ_u and ρ_{uv} , which represent the distribution of turbulence energy in the different directions and their interaction, are defined as

$$\rho_u \equiv \frac{(\overline{v^2})_c}{(\overline{u^2})_c} \quad (\text{III-63a})$$

$$\rho_{uv} \equiv \frac{(\overline{uv})_c}{(\overline{u^2})_c} \quad (\text{III-63b})$$

Equation (III-61) represents the difference in the mean square of the u component velocity fluctuations as would be computed by the present relation and by the cosine law. It is a function of the coefficients of the present relation, the angle of incidence, γ , and the distribution of the turbulence as would be computed with the cosine law.

In many cases the difference in the rms fluctuations is of more interest. It can be calculated by

$$\tilde{\epsilon}_{u'} = \sqrt{\tilde{\epsilon}_{\frac{u^2}{u^2}} + 1} - 1 \quad (\text{III-64})$$

where u' is the root mean square of the u component fluctuations.

Following a similar procedure, the difference between the mean square of the v component fluctuations computed using the present relation and that obtained by the cosine law becomes

$$\tilde{\epsilon}_{\frac{v^2}{v^2}} = c_{1v} + \frac{c_{2v}}{\rho_u} + c_{3v} \frac{\rho_{uv}}{\rho_u} \quad (\text{III-65})$$

where

$$c_{1v} = \frac{\Delta^{-2}}{2} [S_{2u}(\gamma) + S_{1u}(\gamma)]^2 - 1 \quad (\text{III-66a})$$

$$c_{2v} = \frac{\Delta^{-2}}{2} [S_{2u}(\gamma) - S_{1u}(\gamma)]^2 \quad (\text{III-66b})$$

and

$$c_{3v} = \Delta^{-2} [S_{2u}^2(\gamma) - S_{1u}^2(\gamma)]^2 \quad (\text{III-66c})$$

For the rms fluctuations we obtain

$$\tilde{\epsilon}_{v'} = \sqrt{\tilde{\epsilon}_{\frac{u}{v}} + 1} - 1 \quad (\text{III-67})$$

Next, we examine the difference in the computed values of the Reynolds stress \overline{uv} as obtained by two different methods. The first method is based upon the subtraction of the mean square of the linearized fluctuating output voltages of the two sensors. For this case one obtains

$$\tilde{\epsilon}_{\frac{u}{v}} = c_{1uv} + c_{2uv} \frac{(\tilde{\epsilon}_{\frac{u}{v}} + 1)}{\rho_{uv}} + c_{3uv} (\tilde{\epsilon}_{\frac{u}{v}} + 1) \frac{\rho_u}{\rho_{uv}} \quad (\text{III-68})$$

where

$$c_{1uv} = [S_{1u}(\gamma)S_{1v}(\gamma) + S_{2u}(\gamma)S_{2v}(\gamma)]^{-1} - 1 \quad (\text{III-69a})$$

$$c_{2uv} = \frac{[S_{2u}^2(\gamma) - S_{1u}^2(\gamma)]}{2(c_{1uv} + 1)^{-1}} \quad (\text{III-69b})$$

and

$$c_{3uv} = \frac{[S_{2v}^2(\gamma) - S_{1v}^2(\gamma)]}{2(c_{1uv} + 1)^{-1}} \quad (\text{III-69c})$$

Computation of the Reynolds stress in this manner can introduce large discrepancies since it is sensitive to the differences in the computation of the other velocity correlations.

Using analog or digital techniques, the instantaneous values of u and v can be determined from Equations (III-56) and (III-57). Since for analog signal processing squaring circuits are more readily available than multipliers, we

determine the instantaneous value of uv from the relation

$$uv = \frac{1}{4} [(u+v)^2 - (u-v)^2] \quad (\text{III-70})$$

and then time average the signal.

Using this approach the difference in the values of \overline{uv} , computed by the present relation and by the cosine law, is given by

$$\tilde{\epsilon}_{uv}^* = c_{1uv}^* + \frac{c_{2uv}^*}{\rho_{uv}} + c_{2uv}^* \frac{\rho_u}{\rho_{uv}} \quad (\text{III-71})$$

where

$$\tilde{\epsilon}_{uv}^* \equiv \left[\frac{(\overline{uv})_p - (\overline{uv})_c}{(\overline{uv})_c} \right] \quad \text{Equation (III-70)}$$

The coefficients can be calculated from

$$c_{1uv}^* = \Delta^{-2} [S_{2v}(\gamma)S_{2u}(\gamma) + S_{1v}(\gamma)S_{1u}(\gamma)] - 1 \quad (\text{III-72a})$$

and

$$c_{2uv}^* = 2^{-1} \Delta^{-2} [S_{2v}(\gamma)S_{2u}(\gamma) + S_{1v}(\gamma)S_{1u}(\gamma) - S_{2u}(\gamma)S_{1v}(\gamma) + S_{2v}(\gamma)S_{1u}(\gamma)] \quad (\text{III-72b})$$

In each of the previous cases, the differences between the Friehe and Schwarz relation and the cosine law can be computed from

$$(\tilde{\epsilon}_x)_f = \tilde{\epsilon}_x \Big|_{\substack{b=b_f \\ m=0.5}}$$

This is true since when the present relation is evaluated using an exponent of 0.5 and the best coefficient corresponding to it, the yaw dependence becomes that proposed

by Friehe and Schwarz. The difference then between the Friehe and Schwarz relation and the present relation in computing a quantity x is

$$\epsilon_x = \frac{\tilde{\epsilon}_x - (\tilde{\epsilon}_x)_f}{(\tilde{\epsilon}_x)_f + 1} \quad (\text{III-73})$$

Using the previous definitions the differences in computing the velocity correlations can be determined as will be presented in Chapter VII.

Response of Sensor To Velocity Fluctuations

In all of the previous derivations, we have assumed that the instantaneous effective velocity, Q_e , was related to the instantaneous velocity, Q_i , through the yaw relation, i.e., Equation (III-29) or

$$Q_e = Q_i f^2(\beta)$$

where β is the instantaneous angle between Q_i and the direction normal to the sensor. Although this relation is assumed, only the yaw dependence of the mean velocity is measured when calibrating a probe for its yaw characteristics. The calibration does not give any information about the yaw dependence of the time-dependent velocities, e.g., the rms of the fluctuations.

Since Q_e , Q_i and β are instantaneous values, they can be decomposed into time-mean and fluctuating components and written in the form

$$Q_e = \bar{Q}_e + q_e \quad (\text{III-74})$$

$$\beta = \alpha + \hat{\alpha} \quad (\text{III-75})$$

where α is the mean yaw angle and \bar{Q}_e is the time average of Q_e . Assuming low intensity turbulence, the relation

$$Q_i = Q_s + q_s + \frac{q_n^2}{2Q_s} \quad (\text{III-76})$$

may be utilized. Expanding $f^2(\beta)$ using Equation (III-16) and noting that

$$\hat{\alpha} \approx -\frac{q_n}{Q_s} \quad (\text{III-77})$$

one obtains

$$\begin{aligned} f^2(\beta) \approx & f^2(\alpha) + \frac{d[f^2(\alpha)]}{d\alpha} \frac{q_n}{Q_s} \\ & + p(\alpha) \frac{q_n^2}{Q_s^2} - \frac{d}{d\alpha} [f^2(\alpha)] \frac{q_s q_n}{Q_s^2} + O\left(\frac{q_n^3}{Q_s^3}\right) \end{aligned}$$

where

$$p(\alpha) = b^2 m^2 \cos^{2m} \alpha \tan^2 \alpha + 2f(\alpha) \left[\frac{bm(m-1)}{2} \tan^2 \alpha - \frac{bm}{2} \right] \cos^m \alpha \quad (\text{III-78})$$

Applying this relation, the time average of Equation (III-29) becomes

$$\bar{Q}_e = Q_s f^2(\alpha) + [p(\alpha) + \frac{f^2(\alpha)}{2}] \frac{\overline{q_n^2}}{Q_s} \quad (\text{III-79})$$

Under normal calibration conditions the second term will always be negligible compared to the first so that the calibration for mean velocity becomes

$$\bar{Q}_e = Q_s f^2(\alpha) \quad (\text{III-80})$$

Squaring and time averaging Equation (III-29), keeping up to second order terms, and utilizing Equation (III-79) leads to

$$\overline{q_e^2} = \overline{q_s^2} f^4(\alpha) + \left(\frac{d}{d\alpha} [f^2(\alpha)] \right)^2 \overline{q_n^2} - 2f^2(\alpha) \left(\frac{d}{d\alpha} [f^2(\alpha)] \right)^2 \overline{q_s q_n} \quad (\text{III-81})$$

This equation relates the contributions of the streamwise, normal and bi-normal turbulence intensities to the effective fluctuating velocity, i.e., the time dependent cooling to which the sensor responds. Two special cases of Equation (III-81) are significant. The general case arises for flows in which the correlation between the streamwise and normal velocity fluctuations can not be ignored. In this case, the effective rms velocity which the sensor indicates has contributions from the streamwise, normal and bi-normal turbulence stresses and is described by Equation (III-81).

For the special cases where the streamwise and normal velocity fluctuations are uncorrelated, $\overline{q_s q_n} = 0$, the sensor is only sensitive to the streamwise and normal intensities. The first case arises when periodic streamwise fluctuations are superimposed on the calibration flow, i.e., a very low turbulence intensity flow. With this stipulation, $\overline{q_s q_n} = 0$ and $\overline{q_n^2} \ll \overline{q_s^2}$ so that Equation (III-81) reduces to

$$q_e' = q_s' f^2(\alpha) \quad (\text{III-82})$$

where q_e' and q_s' are rms values. Combining this with Equation (III-80) one obtains

$$\frac{q'_e}{Q_e} = \frac{q'_s}{Q_s} = \text{constant} \quad (\text{III-83})$$

This equality states that the effective local turbulence intensity, measured at any yaw angle, remains constant.

This result will be experimentally examined in Chapter V.

The last special case of Equation (III-81) also results in contributions to the effective rms velocity from fluctuations other than those in the streamwise direction. When such contributions are not negligible Equation (III-82) will not hold, i.e.,

$$\frac{q'_e}{Q_e} \neq f^2(\alpha) \quad (\text{III-84})$$

Contrasting Equations (III-80) and (III-84) one observes that yaw relations of hot-wires and hot-films obtained from calibration in a steady velocity field may only be applied to mean and instantaneous velocities measured in a turbulent flow. They can not be used for the rms of the velocity fluctuations. A discussion of the implications of the above results on the present experimental work, as well as on previous ones, e.g., Morrison et al. [26] and Bruun [27], is presented in Chapter VI.

CHAPTER IV

EXPERIMENTAL FACILITIES AND TECHNIQUES

Experimental Facilities

Two main facilities were utilized during the course of the experimental part of the present study: the I.I.T. Environmental Wind Tunnel and the I.I.T. Calibration Tunnel.

Environmental Wind Tunnel. The I.I.T. Environmental Wind Tunnel operates in a closed return mode thus permitting use of two test sections. The present experiments utilized the high-speed test section. The dimensions of this section are 2 ft. deep, 3 ft. high and 10 ft. long, and the free stream velocity can be controlled at any speed up to 65 ft/sec. Through the use of turbulence manipulators [28], a turbulence level much less than 0.1% is maintained throughout the test section. A schematic showing the side view of the tunnel from the high-speed side is shown in Figure 8. For a more detailed description of the wind tunnel the reader is referred to the report by Tan-atichat and Nagib [29].

Calibration Tunnel. The I.I.T. Calibration Tunnel was utilized in two modes during the course of the investigation. In the experiments of Chapter V it was used in its standard configuration for velocity calibration of the hot-wire probes. It was also used in Chapter VI in another configuration to produce a flowfield with periodic

velocity fluctuations superimposed on the mean streamwise velocity. In both tunnel configurations, compressed air enters an acoustically baffled plenum chamber and flows through a bellmouth into a 3 in. diameter plexiglass duct.

In the calibration mode, a nozzle is attached to the end of the duct to produce a laminar free jet flowfield. The probes are placed in the core of the one-inch diameter jet as shown in the bottom photograph of Figure 9. Detailed information regarding the construction and calibration of the tunnel, and on the turbulence manipulators used in this configuration are presented by Loehrke and Nagib [28].

A schematic of the tunnel in the second flow configuration is shown in Figure 10. To produce the desired flow conditions, a screen, two perforated plates and two honeycombs are used as turbulence manipulators in two straight sections of the duct. The straight ducts are connected with a plexiglass "T" section as shown in the top photograph of Figure 11. One end of the "T" section is connected to a conical contraction from a 15 in. speaker which produces the periodic forcing of the flow. The other end of the duct is open to the laboratory. The first utilization of the tunnel in this mode is described by Marcichow et al. [30].

Angularity Chuck. A special angularity chuck designed and built by Roberts [23] was utilized throughout the course of this investigation. The chuck can accurately

position the probes at various angles of yaw to within $\pm 0.04^\circ$. The chuck is shown attached to the side of the Environmental Wind Tunnel in the top photograph of Figure 9, and positioned in the traversing mechanism next to the Calibration Tunnel in Figure 11. In conjunction with the angularity chuck, a specially designed probe support system was used to attach the probes. It allowed the velocity probes to be rotated either about the midpoint of the sensor or about any point along the length of the probe body. In acquiring mean yaw calibration data, the probe was rotated about the midpoint of the probe body (as shown in Figure 9), while for the unsteady yaw calibration it was rotated about the midpoint of the sensor. The arrangement of the support system for the latter case is visible in the photograph of Figure 11.

Velocity Sensors. The single- and X-wire probes used were designed based on the work of Comte-Bellot et al. [31] and Strohl et al. [32] to minimize the aerodynamic interference on the sensors. In each case, the probe body was constructed from 0.25 inch O.D. stainless steel tubing 18 inches in length. The prongs of the single-wire probes are 1 inch long, 0.016 inch in mean diameter and the spacing between their tips is equal to 0.20 in. The prongs of the X-wire are 0.75 in. long, and 0.016 in. in mean diameter with a spacing of 0.12 in. between prongs at the point where the wires are soldered. The separation distance between the wires is 0.04 in.

The sensors used in all measurements are made of 0.00015 in. diameter tungsten wire. The sensor l/d was varied from 75 to 1000 for single sensor probes, while a standard-length sensor ($l/d=580$) was used for all X-wire measurements. The active, i.e., heated, length of the wire was controlled by changing the length of the segments of the wire coated with copper. The wires are soldered to the prongs with the active length centered between them. Photographs of some of the probes are shown in Figure 12.

Angularity Measurements

Steady Velocity Calibration. Mean-velocity yaw calibration for single- and X-wire probes was performed in the Environmental Wind Tunnel. However, the probes were first connected to a DISA 55D01 constant temperature anemometer and velocity calibration data were obtained by placing them in the jet of the Calibration Tunnel positioned next to the Environmental Wind Tunnel; see Figure 9. Using the angularity jig shown in the bottom photograph of Figure 9, X-probes were rotated to orient each of the wires normal to the flow direction during its calibration. Next, the probes were connected to the angularity chuck attached to the side of the wind tunnel. The probes were supported at the midpoint of the body and aligned such that the prongs remained in the same vertical plane throughout as much of the rotation as possible. The probe was then connected to the same DISA 55D01 constant temperature anemometer using

the same overheat ratio utilized in the velocity calibration.

At any constant tunnel velocity, the ambient temperature remained constant to within $\pm 0.5^{\circ}\text{F}$. However, the tunnel air temperature varied with tunnel velocity so that the output was manually adjusted at each free stream velocity to yield the output voltage calculated from the calibration curve. The adjustment was provided by the variable bridge resistance in the anemometer. The accuracy of this scheme of compensation of the anemometer output for variation in the tunnel air temperature is verified in Chapter II and Appendix B. The anemometer output was then displayed on a Tektronix 564 oscilloscope, time averaged for 10 sec. with a Heath multimeter and also recorded on an H.P. Mosley strip chart recorder. A photograph and a schematic of the instrumentation for these measurements are shown in Figures 9 and 13 respectively.

To measure the mean tunnel velocity a Validyne DP-45 pressure transducer connected to a pitot static probe was employed. This transducer was powered by a CD-15 carrier demodulator and its gain set to obtain the value calibrated by Corke et al. [33] of 405.28 volts/psid. The voltage proportional to the differential pressure was connected to the analog averaging circuit of Figure 13, which has a time constant of 4 seconds. The averaged output was then monitored on a Dana Model 3300A digital multimeter and displayed on Channel 2 of the oscilloscope. For further

details of the pressure transducer system and its calibration, the reader is referred to Corke et al. [33].

Fluctuating Velocity Calibration. For this portion of the investigation, the modified calibration tunnel was used and the velocity fluctuations were produced via a 15 inch, 25 watt Altec Biflex speaker. The probe was attached to the angularity chuck using special attachments so that the probe rotated about the midpoint of the sensor and the entire sensor remained in the test volume shown in Figure 10. The angularity chuck was attached to a milling machine indexing head so that four degrees of freedom were available (three translational and one rotational). Both single and X-probe measurements were made and the schematics of the instrumentation employed are shown in Figures 14 and 15. The bottom photograph of Figure 11 also depicts the setup of the instrumentation. In either case, the output of a sensor was fed to a DISA 55D01 Constant Temperature Anemometer, utilizing an overheat ratio of 1.8, and then linearized by a DISA 55D10 Linearizer. This signal which is proportional to the velocity, was time averaged with a Heath Digital Instrument model EU805 for 10 seconds. The accuracy of the linearized velocity, i.e., $\pm 1\%$, was comparable but not as good as that achieved with the non-linearized operation discussed in the next section. To obtain the rms of the signal, the linearized output was fed into a DISA RMS meter, Model 55D35, and its output read using an H.P. 3440A Digital Voltmeter. The

output of a Brüel and Kjaer 1022 Beat Frequency Oscillator powered the speaker and served as a reference signal to the PAR Waveform Eductor and to the Acton Labs 329B Phasemeter. To obtain the rms of the periodic fluctuations, the linearized signal was connected to the Eductor. The Waveform Eductor serves as a periodic averaging device triggered by the signal producing the velocity fluctuations. The educted output, which only contained the part of the signal correlated to the periodic fluctuation, was then fed to the RMS meter to determine its level. At each forcing frequency examined, the phasemeter was used to measure the phase differences between the reference signal and the educted sensor signal. The phasemeter output was monitored while traversing the probe across the test section to insure that the periodic forcing was planar over the test volume.

Data Processing

Data from the experiments were reduced utilizing a UNIVAC 1108 computer and a digital data acquisition and processing system [34]. Velocity calibration data, with the sensors normal to the flow, were fit to the following equation:

$$E^2 = A' + B' U^n \quad (IV-1)$$

The values of A' , B' and n were obtained by minimizing the standard deviation of the data from the associated

fit. The equation was fit for a range of velocities from 10 to 50 ft/sec. The normalized standard deviation of the calculated velocity from the data for all sensors was approximately 0.4%. This normalized standard deviation is defined as

$$\sqrt{\frac{1}{N} \sum_{i=1}^N \left[1 - \frac{U_{\text{calculated}}}{U_{\text{measured}}} \right]^2}$$

At the four free-stream velocities of 12.5, 25, 37.5 and 50 ft/sec, calibration data were obtained for the yaw angles $-70^\circ \leq \alpha \leq 70^\circ$. At each position for the yaw angles the anemometer output voltage and the angle of yaw with respect to the flow direction were recorded. The flow direction was initially determined by maximizing the anemometer output. The wire output voltage was then plotted versus yaw angle for α values in the range $\pm 30^\circ$ to determine the angle at which the mean flow was normal to the sensor, i.e., $\alpha_0 = 0$. In order to perform accurate comparisons between the different yaw relations, the angle α_0 was redetermined to a higher degree of precision in the data reduction routine as will be discussed in Chapter V. The yaw data were obtained at increments of three degrees in all cases and every one degree in some cases.

Wire output voltages were then converted to mean velocities via Equation (IV-1) and normalized by the velocity calculated when $\alpha = \alpha_0$, i.e., U_∞ . The data was then fit to the following relation

$$\sqrt{\frac{U_e}{U_\infty}} = a + b \cos^m \alpha \quad (\text{IV-2})$$

to obtain the values of the coefficients a , b and m which minimize the standard deviation of the fit. These values are denoted by b^* and m^* . The coefficient a can be replaced in Equation (IV-2) by $1-b$, since $a+b$ must equal to one to satisfy the conditions when $\alpha = 0$. Therefore, we can rewrite Equation (IV-2) as a two parameter yaw relation,

$$\frac{U_e}{U_\infty} = [1 - b(1 - \cos^m \alpha)]^2 = f^2(\alpha) \quad (\text{IV-3})$$

For the rest of this report this equation will be referred to as the present yaw relation.

A grid of b and m values was then specified and at each grid point, the standard deviation of U_e/U_∞ from the present relation was determined. The standard deviation, σ_p , is defined as

$$\sigma_p = \sqrt{\frac{1}{N} \sum_{i=1}^N \left[f^2(\alpha_i) - \frac{U_{e,i}}{U_\infty} \right]^2} \quad (\text{IV-4})$$

where N is the number of data points. When the value of the exponent $m = 0.5$, then $\sigma_p = \sigma_f$, where σ_f is the standard deviation of the data from the Friehe and Schwarz relation [22]. For the case when the coefficient $b=1$ and $m=0.5$, $\sigma_p = \sigma_c^*$, where σ_c^* is the standard deviation of the fit using the cosine law.

These values were then written onto magnetic tape and processed on the PDP 11-10 utilizing a contour plotting routine in the Data Acquisition and Processing System Library. This contour plotting routine was written by Richard Wlezien during the course of the present investigation.

CHAPTER V

YAW CALIBRATION FOR STEADY VELOCITIES

This chapter examines the influence of various parameters on the yaw calibration of single sensors and X-wire probes utilizing three different relations for the yaw sensitivity; the cosine law, the Friehe and Schwarz relation and the present relation; see Chapter I for details.

As discussed in the previous chapter, the mean yaw calibration data was initially centered graphically to determine the mean flow direction which corresponds to $\alpha_0 = 0$. An example of this is shown in Figure 16, where the anemometer output voltage is plotted versus angle of yaw. The distance between the curve and the initial line of symmetry was measured at different heights and used to calculate the average shift in the center line. The values measured in the example of Figure 16 are shown on the graph. This process was carried out for every run to ensure that there was no slippage of the probe in the angularity chuck. Such a procedure is sufficient for angularity calibration for normal experimental work. However, for the purpose of doing an accurate comparison of the standard deviations determined from the three yaw relations as influenced by different parameters this was not sufficient. The reason behind this is found in Figure 17.

Using the initially shifted data, the offset angle, α_0 , was varied from -9° to $+9^\circ$ in equal increments and the minimum standard deviation, σ_p^* , corresponding to each

value of α_0 was found using the present relation. The deviation of symmetric data from an even yaw relation, as calculated in this approach, should be symmetric about the true mean flow direction. As demonstrated graphically in Figure 17, the true line of symmetry appears to be -0.18° away from that determined from centering the data by the procedure of Figure 16. Using this corrected value, the typical variation of σ_p^* with offset angle (i.e. probe misalignment) is shown in Figure 18. At $\alpha_0=0$, σ_p^* achieves its minimum value of 0.15% and increases linearly with offset angle. In all cases examined, the variation of σ_p^* with α_0 over this range was independent of sensor l/d or Re_d and equal to 0.8% per degree of misalignment. The data processing program included a subroutine which automatically performed this accurate alignment of the data and assigned the corrected yaw angles to all data points.

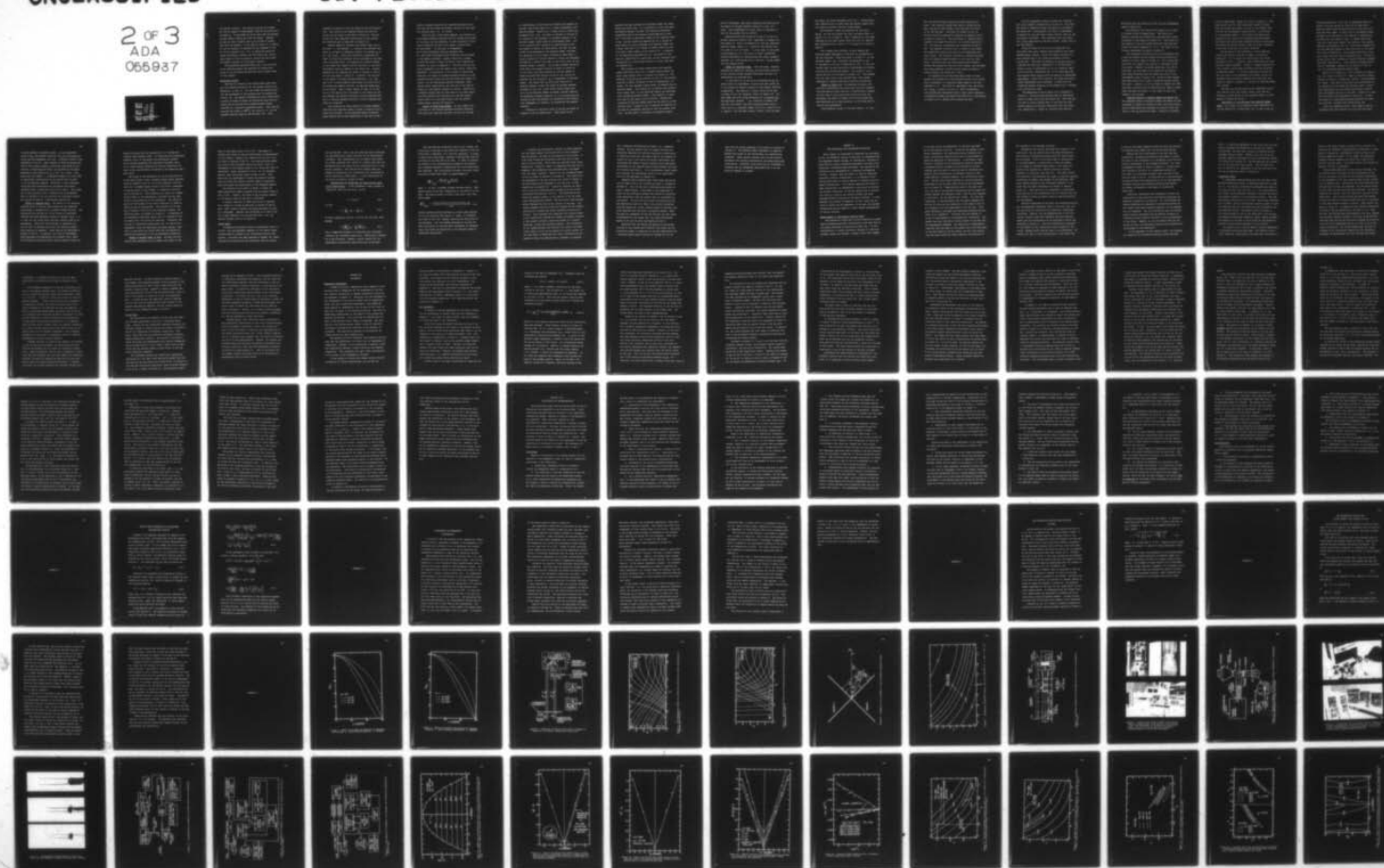
Using this technique to determine the true mean flow angle, the variations of the minimum standard deviations determined using the cosine law, Friehe and Schwarz's and the present relation were examined. A typical result is shown in Figure 19 for a sensor l/d of 250 and a free stream velocity of 37.5 ft/sec. If the probe was properly aligned, an error of 1.8% in the normalized velocity, U_e/U_∞ , would be the minimum achievable with the cosine law. This value, which indicates the goodness of the fit, was typically equal to 0.5% if the Friehe and Schwarz relation was used. It was reduced to approximately 0.1% by using

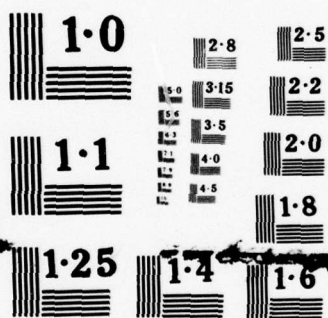
UNCLASSIFIED

IIT-FLUIDS/HEAT TRANS-R77 ARO-12290.9-E

NL

2 OF 3
ADA
065937





NATIONAL BUREAU OF STANDARDS
MICROCOPY RESOLUTION TEST CHART

the present relation. The values of σ_p^* and σ_f^* increase by 0.8% per degree of misalignment from the accurately determined α_0 . If the probe is off by more than two degrees σ_c^* also varies linearly by 0.85% per degree. However, σ_c^* does not vary linearly with α_0 for values of offset less than two degrees. In the case of Figure 19, a factor of four in accuracy, as measured by the goodness of the fit of the relation (i.e., σ^*), is gained by using the Friehe and Schwarz relation over the cosine law, and another factor of five is gained in going from the Friehe and Schwarz relation to the present relation.

The procedures described above and in the last part of the previous chapter are employed for single-wire probes in the following sections and with X-probes later in this chapter.

Single-Wire Probes

The best fit values of the coefficients which minimize the standard deviation for the present relation are denoted by b^* and m^* . For the Friehe and Schwarz relation b_f^* corresponds to the minimum value of standard deviation, σ_f^* . One method of determining these coefficients is shown in Figure 20 where the deviations away from the cosine law are plotted for a standard-length sensor ($l/d=580$) as a function of Reynolds number. Since the deviations are linear in $\cos^{m^*} \alpha$, the value of b^* can be computed from the slope of the straight line. This

approach is similar to the one used by Friehe and Schwarz [22]. Both positive and negative deviations from the cosine law are found in the data of Figure 20. This behavior will have important implications on the various yaw relations and is discussed in Chapter VII.

Another method to indicate the regions where the coefficient b and exponent m minimize the standard deviation σ_p is based on examining contours of constant σ_p in the b - m plane. Using this technique a comparison between all three yaw relations can be performed at the same time, since when $m=0.5$ the present yaw relation reduces to the Friehe and Schwarz relation and when $b=1$ and $m=0.5$ the present relation reduces to the cosine law. Typical examples of this approach are shown in Figures 21 and 22. For the case shown in Figure 21 ($\ell/d=250$), the position of the region of minimum standard deviation, i.e. less than 0.5%, is quite removed from either the cosine law or the Friehe and Schwarz relation as depicted graphically on the figure. When a longer sensor is used, as in Figure 22, this region will lie closer to the cosine law and pass through the Friehe and Schwarz relation, although the point of minimum standard deviation is still removed from these yaw relations.

The variations of these regions of minimum standard deviation with Reynolds number is shown in Figure 23 for a sensor with $\ell/d=250$. As the Reynolds number increases, these regions tend to move upward and to the left of the

figure, although remaining far removed from both the cosine law and the Friehe and Schwarz relation at the highest velocity used, i.e. 50 ft/sec.

Since in many of the cases examined the position of the minimum standard deviation was far removed from either of the other two yaw relations, we were concerned if this type of behavior was due to the manner of fabrication of the probes. To this end, an independent set of yaw calibration data was obtained from Dr. John Foss of Michigan State University and processed in the manner described. Sample results for a sensor $l/d=200$ are shown in Figure 24 while a more complete description is given in Appendix D. From this and the figures in Appendix D one can observe that similar trends are exhibited. In particular, at low values of free-stream velocity, the region of minimum standard deviation is far removed from the cosine law and the Friehe and Schwarz relation. As the free-stream velocity increases, these regions shift upward and to the left and in the case of Figure 24, they display regions of overlap. Results for a standard-length wire are also shown in the same figure. This data exhibits more similarity to the MSU results (shown above it on the same figure) than the shorter length sensor contours of Figure 23.

Effect of Probe Misalignment. We next examine the variations of the minimum standard deviations obtained from using the three yaw relations, as well as the best

fit coefficients in the Friehe and Schwarz and present relations, with offset angle (i.e., probe misalignment) and Reynolds number. Results for a sensor with an $\ell/d=250$ are presented first and are shown in Figures 25 through 29 as contours of the parameter or variable examined in the Reynolds number versus angle of misalignment plane. Figure 25 indicates that σ_c^* varies by approximately 0.85% per degree of offset, as found before, and that the magnitude of σ_c^* decreases as the Reynolds number increases. The variation of σ_f^* is shown in Figure 26 where again it varies linearly by 0.8% per degree of offset and decreases, although at a smaller rate than in the cosine case, as the Reynolds number increases. The minimum standard deviation found using the present relation is shown in Figure 27. In this case, σ_p^* varies linearly by 0.8% per degree of offset as found from Figures 18 and 19, but unlike the previous two yaw relations, σ_p^* is independent of Reynolds number. The reason that σ_c^* and σ_f^* are functions of Reynolds numbers is that the region of minimum standard deviation in the b-m plane shifts toward these relations as the Reynolds number increases, thereby reducing the difference between relations. It is of course more desirable to have the accuracy of representing the calibration independent of velocity, as achieved by the present relation.

Variations in b_f^* and b^* with α_o and Re_d are shown in Figures 28 and 29 respectively. From Figure 28 one

observes that b_f^* increases with Reynolds number and tends toward the cosine law. It is important to note that small differences between the mean flow direction determined graphically and by the accurate method depicted in Figure 17 will have a negligible effect on the computed value of b_f^* . Similar trends are observed for b^* in Figure 29, where again its value increases with Reynolds number and a small (less than 0.2°) change in offset angle will usually have a small effect on the value of b^* . In general, if the probe was misaligned by 0.5° , the effect of the best fit coefficients is equivalent to that resulting from calibration at a free stream velocity 3 ft/sec less than the desired one.

The variation of these coefficients with Reynolds number and offset angle for a standard-length sensor are shown using similar plots in Figures 30 through 35. The behavior of σ_f^* and σ_p^* are similar to that of the previous case and is shown in Figures 30 and 31, respectively, although for this standard length probe, σ_f^* depends less on Reynolds number. From Figure 32, we observe that b_f^* has a value larger than 1 at low Reynolds numbers and decreases with increasing Reynolds number. This behavior is opposite that of the sensor with an $l/d=250$. However, the variations of b_f^* with offset angle are the same as in the previous case. Figures 33 and 34 examine the behavior of the best fit parameters determined from the present relation. We note that b^* increases with Reynolds number

while m^* decreases, once again indicating the shifting of the region of minimum standard deviation in the b - m plane. Their dependence on offset angle is identical to that for the sensor with an $l/d=250$.

Associated with the values of b^* and m^* is the turbulence correction factor $(g/h)^*$ described in Chapter III. From Figure 35, $(g/h)^*$ increases by 5% over the indicated Reynolds number range (i.e., values of free-stream velocity from 12.5 to 50 ft/sec). In this case, if the probe is misaligned by 0.5° , the value of $(g/h)^*$ determined would be equivalent to recalibrating the probe, properly centered, in a free-stream with a velocity 3 ft/sec higher than the desired value.

Effect of Reynolds Number. With the probe properly centered the effects of changing the free-stream velocity on the various minimum standard deviations and best fit coefficients are examined next.

If the values of σ_c^* and σ_f^* are normalized by σ_p^* , we obtain ratios of improvement in going from the cosine law or the Friehe and Schwarz relation to the present relation, respectively. The behavior of these ratios can be seen in Figure 36 for two different values of sensor l/d . For both cases the ratio σ_c^*/σ_p^* decreases with increasing Re_d . The magnitude, however, is a function of sensor l/d . With the long sensor ($l/d=1000$), σ_c^*/σ_p^* decreases from a value of 25 at a Reynolds number of 0.9 to a value of 3 at a $Re_d=3.6$. For the short sensor ($l/d=75$), over the same

Re_d range, the ratio decreases from 9 to 3. Surprisingly, this indicates that in some cases the shorter sensor fits the cosine law better than the longer sensor.

Two different trends are observed for the ratio σ_f^*/σ_p^* . For the long sensor the ratio increases from 1 at $Re_d=0.9$ to 1.75 at $Re_d=3.6$. This is opposite to the trend observed for the short sensor where the ratio of improvement decreases from a value of 3.5 at $Re_d=0.9$ to unity at $Re_d=3.6$.

For a sensor with $l/d=1000$, we next examine the Reynolds number dependency of the best fit parameters of the yaw relations. These are shown in Figure 37. As the Reynolds number, Re_d , increases, b_f^* decreases by 10%, b^* decreases by 15% and m^* decreases by 10%. In this particular case, the yaw sensitivity coefficients are strong functions of the Reynolds number. This behavior is expected and will be discussed in Chapter VII. This dependence can also lead to many problems when using analog techniques to measure turbulence velocity correlations.

Effect of Sensor l/d . By changing the sensor l/d , previous investigators have found that the axial temperature distribution along the wire is significantly altered. This may lead to large deviations from the cosine law. Therefore, the effect of sensor l/d on the minimum standard deviation and on the parameters in the three yaw relations was investigated.

Five different values of l/d were tested: 75, 145,

250, 580 and 1000 while keeping the prong spacing constant. Two identical probes were used in collecting the data, and one of them (Probe 1) was used with the l/d 's of 75, 580 and 1000. The effect of sensor l/d on the hot-wire velocity calibration constants of Equation (IV-1) is shown in Figure 38. The coefficient B' remains fairly constant with sensor l/d while A' is a strong function of l/d . The exponent n decreases with decreasing values of l/d . The exponent of King's law, n , seems to tend toward the theoretical value of one half as l/d approaches very large values. The velocity calibration constants obtained from the standard length sensors of the X-wire are also shown. Recalling that the prong spacing was different between the single-wire and the X-wire probes, one concludes that probe geometry, including prong shape and spacing, greatly affects the values of B' and n .

To separate out any Reynolds number effect we next examine the results for a free stream velocity of 25 ft/sec, which corresponds to a Reynolds number based on the wire diameter of 1.8. The ratio of improvement over the cosine law, σ_c^*/σ_p^* , is shown in Figure 39, where intermediate value points were determined using a three point Lagrangian interpolation scheme (available with HP97 and 67 calculators) in order to fit a smooth curve through the data.

For the intermediate range of sensor l/d ($l/d \approx 250$), this ratio reaches a maximum value of over 20. This maximum value is reduced by either increasing or decreasing the sensor l/d . Surprisingly, the ratio of improvement is smaller for the very short sensor ($l/d=75$) than for the long sensor ($l/d=1000$). This indicates that the cosine law is more applicable to the short sensor, rather than to the long sensor!

Figure 40 shows the variation of σ_f^*/σ_p^* with l/d . Once again this ratio reaches large values for the intermediate sensor lengths. Since the present relation is a more complex form of the Friehe and Schwarz relation, one may ask: when does the benefits of greater accuracy outweigh the additional complexity? If we arbitrarily assign a ratio of improvement of two as a marginal additional accuracy, remembering that in all cases $\sigma_p^* \approx 0.15\%$, then regions where $\sigma_f^*/\sigma_p^* > 2$ would be regions of significant improvement. Using this criterion, one finds that significant improvement can be obtained in going from the Friehe and Schwarz relation to the present one, if sensors with l/d 's < 550 are used.

The dependence of b_f^* on sensor l/d is examined in Figure 41. The variation indicates that no significant range of sensor l/d 's fits the cosine law. Note that b_f^* can take on values greater than or less than one indicating negative and positive deviations from the cosine law, respectively. Figure 41 indicates that positive

deviations from the cosine law occur for the intermediate range of sensor l/d .

The variation of b^* and m^* with sensor l/d is shown in Figures 42 and 43, respectively. The value of b^* reaches a minimum for $l/d=250$ and increases while either increasing or decreasing the sensor l/d . From Figure 43, the exponent m^* has the largest deviation away from the Friehe and Schwarz exponent of 0.5 in the region of significant improvement as shown in Figure 40.

The turbulence correction factor, as determined from Friehe and Schwarz and the present relation, plotted as a function of l/d , is shown in Figure 44. This figure indicates that all sensors will require a turbulence correction factor. However, by proper selection, this can be minimized. We note again as in Figures 39 through 43, that large deviations from the cosine law exist in the intermediate range of sensor l/d . Figure 44 also reveals that there exists only a small difference between $(g/h)_f^*$ and $(g/h)^*$. However, it will be shown in Chapter VII that this small deviation will be magnified many times in cases where the mean flow angle γ is not equal to zero with respect to an X-probe.

Combined Effects of Reynolds Number and Sensor l/d .

The combined effects of Reynolds number and sensor l/d are presented in Figures 45 through 50 where the various parameters investigated are displayed as constant value contours in the Re_d versus l/d plane. Contours of constant

ratio of improvement, σ_f^*/σ_p^* , are shown in Figure 44. This again points out the large improvement gained in going from the Friehe and Schwarz relation to the present relation for the intermediate length sensors, in particular at low Reynolds numbers. This figure also depicts the decrease of this ratio with increasing Reynolds number, indicating that the minimum standard deviation found using the Friehe and Schwarz relation does not remain constant, unlike that found from the present relation.

The variation of the parameters in the Friehe and Schwarz and present relations is shown in Figures 46 through 48. In all cases, the coefficients are strong functions of l/d . In general, these coefficients are also Reynolds number dependent. However it appears possible to find a probe in which these constants are weak functions of Reynolds number. It is most significant to point out that the trend of the parameters with either of the two variables does not seem to approach the cosine law, but rather it seems to overshoot it without any observed asymptotic values.

The same can also be said for the turbulence correction factors $(g/h)^*$ and $(g/h)_f^*$, namely, that they are functions of both sensor l/d and Reynolds number, as displayed in Figures 49 and 50.

Application of Yaw Relations Over Reynolds Number Range. As a result of the Reynolds number dependence of the yaw sensitivity coefficients, one is lead to ask the

following questions: does a set of parameters exist for either of the yaw relations, which can be used over a Reynolds number range and which would give the best accuracy over this range? If such a set of parameters exists, how good is the accuracy of the relation in representing the data over this range of Re_d ? To answer these questions for a particular sensor, the values of the standard deviation calculated in the b - m plane were averaged over the four Reynolds numbers at each grid point in the plane. This value is denoted $\bar{\sigma}_p$. The standard deviation of the four values from this value is denoted by $\hat{\sigma}_p$. The sum of $\bar{\sigma}_p$ and $\hat{\sigma}_p$ will then indicate an overall effective standard deviation, denoted by Σ_p . This effective standard deviation is considered a measure of the quality of the fit over the prescribed Reynolds number range.

Contours of constant Σ_p 's for an $\ell/d=250$ are shown in the b - m plane of Figure 51. These curves have a shape similar to those at a single Re_d , however the magnitudes are larger. Once again we see that the minimum region is far removed from the cosine law although there is negligible improvement over the Friehe and Schwarz relation when the present relation is utilized. Results for a sensor with $\ell/d=580$ are reproduced in Figure 52. In this case there is a negligible difference between all three yaw relations including the simple cosine law.

This is an expected result, since based on the experimental data the variation of U_e/U_∞ with yaw angle

strongly depends on Reynolds number. At any prescribed value of Re_d , the present relations will most accurately describe the yaw dependence, but with different values of the parameters b^* and m^* . Small changes in these parameters may lead to very large changes in the errors introduced by the relation in describing the data, as indicated by the sharp gradients in the contours of σ_p in the b - m plane. Averaging over any number, n , of Reynolds numbers will then lead to significant contributions to the errors from at least $n-1$ of the Reynolds numbers. Therefore, if the turbulence velocities and correlations are calculated using these averaged values, significant errors will result. This leads one to the conclusion that a different set of parameters must be utilized in the yaw relation for each mean velocity the X-probe is used at; a most severe restriction.

Effect of Overheat Ratio. The effect of the operating overheat ratio on the yaw coefficients was also examined using Probe 2, equipped with a standard length hot-wire. Yaw calibration was carried out at two values of freestream velocity and three different values of overheat ratio: 1.4, 1.6 and 1.8, the latter being the most commonly used by experimenters. (Note that this resulted in repeating two runs at the 1.8 overheat ratio with two identical probes using similar l/d sensors). These results are described in Figures 53 and 54. In general, the ratio of improvement σ_f^*/σ_p^* decreases with decreasing the overheat ratio, while the turbulence correction factor remains constant within 2%.

Figure 54 proves that the parameters b^* , m^* and b_f^* vary slightly with overheat ratio: b^* decreasing with decreasing overheat ratio; m^* increasing with decreasing overheat ratio; and b_f^* increasing with decreasing overheat ratio. All of these results indicate that the yaw sensitivity of wires is not significantly influenced by the operating overheat ratio.

The values of the parameters of the yaw relations obtained using Probe 2 with a standard length sensor operated using an overheat ratio of 1.8 can be compared to the results for a standard length sensor using Probe 1 presented in earlier parts of this chapter in connection with Figures 46 through 48. This comparison can serve as a repeatability check on the experimental procedure and may shed light on the generality of the parameters. The values of b_f^* and m^* from Figure 54 are nearly identical to those in Figure 46 and 48 respectively. The variation of b^* with Re_d in Figures 47 and 54 is also identical, however the values are about 15% higher in Figure 54. A comparison of the turbulence correction factor $(g/h)^*$ in Figures 50 and 53 reveals that the values are identical. Therefore, the two sets of experiments demonstrate that the results are repeatable using the same probe and sensor design. However, at this point one cannot reach any conclusions regarding the generality of the yaw dependence parameters.

Effect of Angular Range of Data. The mean yaw calibration data discussed in this chapter were taken in the

range of yaw angles from -70° to $+70^\circ$. The effect of changing this range on the yaw coefficients is demonstrated in this section. Results for a sensor with an ℓ/d of 145 are shown in Figures 55 and 56. For this particular probe the value of the turbulence correction factor $(g/h)^*$ is independent of the angular range of fit, while the ratio of improvement, σ_f^*/σ_p^* , decreases to unity for all Reynolds numbers when the angular range of data is $\pm 45^\circ$. This means that the improvement in using the present relation over the Friehe and Schwarz relation comes at relatively large yaw angles and particularly at low Reynolds numbers.

The variation of b^* and m^* is shown in Figure 56. These coefficients remain constant from an angular range of $\pm 50^\circ$ to $\pm 70^\circ$. However, the value of b_f^* increases linearly as the angular range of the data is decreased.

A similar variation in these quantities is observed for a sensor of $\ell/d=580$ as depicted in Figures 57 and 58. Here, $(g/h)^*$ remains constant and σ_f^*/σ_p^* decreases to unity as $\Delta\alpha$ decreases. However, the variations of b^* and m^* are not as well defined as in the previous case: e.g., b_f^* remains constant with $\Delta\alpha$ to within 1%.

X-Wire Probe

In measuring turbulence velocity correlations using an X-probe, the time dependent component of the sensor output voltages must be related to the fluctuating velocity components. One method has been examined in Chapter III, where expressions accounting for the deviations from the cosine

law are derived. Thus, once the probe has been calibrated for yaw sensitivity, these relations can be analytically evaluated. Many investigators do not employ this method but rather calibrate the X-probe in a manner such that the deviations from the cosine law are accounted for in a calibration constant. This section will compare these two methods of determining the longitudinal and transverse velocity sensitivity coefficients. A brief description of the direct calibration method follows.

Determination of Transverse and Longitudinal Sensitivity Coefficients. If the anemometer output voltage is linearized, then one can write, [22,35]

$$E = E(Q_i, \beta) \quad (V-1)$$

so that

$$e = \frac{\partial E}{\partial Q_i} dQ_i + \frac{\partial E}{\partial \beta} d\beta \quad (V-2)$$

By use of Equations (III-24), (III-75) and (III-78), this becomes

$$e = \left[\frac{\partial \bar{E}}{\partial Q_s} \right] q_s - \frac{1}{Q_s} \left[\frac{\partial \bar{E}}{\partial \alpha} \right] q_n \quad (V-3)$$

Only a comparison between the calculated and calibrated values of the transverse sensitivity, $(\partial \bar{E} / \partial \alpha) / Q_s$, is attempted in the following. However, similar results for the longitudinal sensitivity coefficients can be obtained.

From the mean yaw calibration data of the X-probe, the velocity as a function of yaw angle was computed so that the coefficient in Equation (V-3) could be evaluated. In order to obtain this coefficient, methods of determining local derivatives of the data had to be used. In order to minimize any effects of the differentiation scheme on the results, four different methods of determining the local derivatives were employed. The first method utilized a two point local derivative scheme where $\partial \bar{E} / \partial \alpha$ is approximated by

$$\left. \frac{\partial \bar{E}}{\partial \alpha} \right|_{\alpha=\alpha_i} = \frac{\bar{E}(\alpha_i+h) - \bar{E}(\alpha_i-h)}{2h} \quad (V-4)$$

where h is the α increment between the data points. This method should be the most susceptible to the scatter in the data. The second method utilized a four point local derivative where

$$\left. \frac{\partial \bar{E}}{\partial \alpha} \right|_{\alpha=\alpha_i} = \frac{8 [\bar{E}(\alpha_i+h) - \bar{E}(\alpha_i-h)] - \bar{E}(\alpha_i+2h) + \bar{E}(\alpha_i-2h)}{12h} \quad (V-5)$$

Another method involved performing a linear least squared fit on five adjacent data points, 1° apart, to determine the slope of the line, thereby obtaining the derivative at the mid-point. The last method consisted of fitting the same five points to a second order polynomial of Chebyshev type, from which the derivative at the midpoint could be determined analytically.

A complete yaw calibration, similar to those presented for the single sensor, was carried out at four different mean velocities for each of the sensors of the X-probe. A finer grid of data was collected around the axis of symmetry of the X-wires. While data were obtained every three degrees for $-70^\circ \leq \alpha \leq 70^\circ$, where α is measured from the axis of symmetry, the calibration was performed every one degree over the range $-10^\circ \leq \alpha \leq 10^\circ$. Results for the transverse sensitivity are shown in Figures 59 through 63. The results for the parameters of the yaw relation are listed in tables in the same figures and discussed in the last part of this chapter and in Chapter VII. Figure 59 compares the variation of the four differentiation schemes with the values calculated from Equation (III-35). The method which produces the largest scatter in the results is the two point local differentiation method. The five point least squares method averages out most of the scatter in the data. The values computed from the Friehe and Schwarz and the present relations lie through the values obtained by direct calibration. This indicates that computing the velocity sensitivity coefficients through the Friehe and Schwarz relation or the present relation, using the present or a similar technique, yields more accurate results. The utilization of any "sophisticated" yaw relation will lead to the same result since it will not be sensitive to small scatter in the data which is magnified when local differentiation is applied or when the experimenter's judgement is required

for a different differentiation scheme, e.g., graphical methods. We also observe that the cosine law does not accurately describe the velocity sensitivity coefficients. It should be noted that the sensor used in the example of Figure 59 lies in the region of minimum improvement over the Friehe and Schwarz relation thereby giving negligible differences in the computed sensitivities between the present relation and their's. If an intermediate length sensor was utilized, the differences would be more significant. This will be discussed in Chapter VII.

Examples using different mean free-stream velocities and the other wire in the X-probe are shown in Figures 60 through 63. Only the two point differentiation method is used in these figures since based on the comparison of Figure 59 the difference between the methods of obtaining local derivatives from the present data is considered insignificant. In each case the values calculated from the yaw sensitivity function, taking into account deviations from the cosine law, yield a higher degree of accuracy than those obtained from the direct calibration method. When the best fit parameters of the yaw relation are near those corresponding to the cosine law, the cosine derivatives appear to be just as good; see Figures 60 and 61.

Recalling that the design and spacing of the prongs utilized in the X-probe were different than those for the single-wire probe, a comparison of the yaw coefficients for a standard length sensor (Figures 46 through 48) can be

made with the values presented in the tables of Figures 59 through 63. The Reynolds number dependency is identical. However, the values of the coefficients are substantially different. These results indicate that the yaw relation parameters are strongly influenced by the probe design and construction. Therefore, each probe must be calibrated to determine the yaw parameters associated with it at the Reynolds numbers of interest.

Establishment of Fluctuating Velocity Field

The calibration tunnel was initially modified to superimpose extraneous periodic fluctuations on the mean flow in the manner described by Hartschow and Way (30). In this configuration, a linear contraction leading to a one-inch diameter nozzle was attached through a short duct segment

CHAPTER VI

YAW CALIBRATION FOR FLUCTUATING VELOCITIES

When a sensor is calibrated to determine its yaw sensitivity, the effective cooling of the wire, as represented by the anemometer output voltage, is recorded as a function of angle during a static calibration procedure utilizing a low turbulence, calibration-type flowfield. The results of the calibration are represented by a relation like Equation (III-80). However, when the sensor is used for measuring turbulence velocity correlations, it is exposed to fluctuating velocities of varying degrees of intensity and frequency distributions. This chapter examines the effect of such fluctuations, as represented in particular by controlled periodic velocities, on the yaw sensitivity of the sensor, which is given by the relation between the time-averaged effective cooling and the mean flowfield. It also examines the validity of Equation (III-83), which was derived to relate the yaw dependence of the mean and unsteady fluctuations and was based on a quasi-steady approximation of the yaw relation.

Establishment of Fluctuating Velocity Field

The calibration tunnel was initially modified to superimpose streamwise periodic fluctuations on the mean flow in the manner described by Marcichow and Way [30]. In this configuration, a linear contraction leading to a one-inch diameter nozzle was attached through a short duct segment

to the open end of the plexiglass "T" section (see Chapter IV and Figures 9 and 10). Driven by the speaker at different frequencies, the resulting free-jet flowfield provided a fluctuating velocity field with a controllable air speed and amplitude of fluctuations. In particular, high levels of intensity of the fluctuations could be achieved. A standard hot-wire attached to the angularity jig and indexing head was used to carefully map the flowfield produced by this configuration at different values of free stream velocity, forcing frequency and fluctuations intensity. Vertical and lateral profiles at various positions downstream of the jet were taken utilizing the instrumentation of Figure 14. These profiles were of the mean velocity, the rms of the educted fluctuations and the phase difference between the reference signal, from the beat frequency oscillator, and the educted wire signal. For this configuration, it was determined that the phase changed by as much as 40° from the jet centerline to the edge of the jet at a position 0.25 inch downstream of the jet exit. This phase difference increased with downstream distance and was found to be asymmetric. Initially this was thought to be due to misalignment of the speaker-duct connection. The speaker was then inclined at various angles to the duct and the measurements repeated. The second set of measurements indicated that the angle of the speaker had little influence on the flow field out of the nozzle, and that the contraction and nozzle were the likely component contributing to

the skewness of the unsteady flowfield.

Considering the size of the probe with respect to the nozzle exit, one can surmise that such phase differences would lead to fluctuations incident upon the sensor which are not planar. This in turn would lead to inaccuracies in the measurements, in particular at large yaw angles. In an attempt to minimize these effects, the linear contraction was replaced by a smooth contraction section leading to an identical size free jet. (The same contraction section is utilized when the tunnel is used for velocity calibration of probes; see Chapter IV and Reference [28]). After careful mapping of the flowfields produced, it was found that the phase difference was reduced to approximately 20° . This was still not acceptable, in particular since the rms of the fluctuations was not constant over the test volume in which the sensor would be positioned during yaw calibration.

The main advantages of the above two configurations are the low background turbulence level in the free jets, and the wide range of velocities and fluctuation intensities achievable. However, the two-dimensionality of the fluctuating velocity field was considered the most important aspect and the configuration of the Calibration Tunnel was modified to achieve it. The final modification consisted of the removal of the contraction section leading to the nozzle, thereby having the duct open to the laboratory. By mapping the flow in this configuration, it was found that

as long as the sensor remained within the duct, the velocity fluctuations were planar over the entire cross section.

Assured that the fluctuations in the duct were two dimensional, turbulence manipulators were added to reduce the level of the turbulence to an acceptable level but with minimum interference to the unsteady flowfield. The final arrangement of these is shown in Figure 10. Without periodic forcing of the flow, at a freestream velocity of 12 ft/sec, the turbulence intensity near the exit of the duct was found to be 2%. For more details on the flow manipulators and the flow characteristics at the test position, including velocity and turbulence profiles and spectra, the reader is directed to the report of Loehrke and Nagib [29].

Additional experiments were conducted to select the combinations of mean velocity, fluctuations amplitude and frequency suitable for calibration. All the selected conditions exhibited two dimensional fluctuations across the test section and simple harmonic character of the unsteady velocity component. The only limitations were the maximum steady velocity achievable and the maximum intensity of fluctuations which could be obtained in this configuration of the tunnel. However, as will be evident from the following sections, the available conditions were adequate for the purposes of the experiments.

In the remainder of this chapter, single and X-probes are tested in the fluctuating velocity field described

above. It should be emphasized at this point that the sensors are exposed simultaneously to periodic and random fluctuations and that their cooling is affected by both unsteady velocity fields. However, with the aid of the periodic sampling techniques utilizing the Waveform Eductor (for details see Chapter IV), one can separate the periodic part of the hot-wire output signal. This periodic part will be useful in the comparison of the yaw relations with the aid of equations given in Chapter III.

Single-Wire Probe

A linearized standard-length hot wire was used in the modified Calibration Tunnel as described above and in Chapter IV. The velocity fluctuations presented here refer to the educted signal from the wire, i.e., the linearized hot-wire output was periodically averaged to provide the rms of the periodic component of the measured velocity. With the free-stream velocity set at 12 ft/sec, the forcing frequency set at 1000Hz and the fluctuations intensity equal to 3.8%, the effective mean and rms velocities were recorded as the yaw angle was varied. The results shown in Figure 64, for various angles of yaw in the range $\pm 48^\circ$, indicate that the effective turbulence intensity, u'_e/U'_e , remains constant. The behavior of the data in this figure is represented by Equation (III-83) which testifies to its validity.

To examine this in greater detail, forcing frequencies of different intensities were used. The effective turbulence intensity, normalized by its value when the sensor is

normal to the flow, is shown in Figure 65 as a function of yaw angle for different frequencies and intensities. A wide range of frequencies encompassing a major portion of the hot-wire spectrum is used. In all cases, the turbulence intensity remains constant and within 2% or less of its value at zero yaw angle. With these results the validity of Equation (III-83) is confirmed.

Having established that at any forcing frequency, the yaw sensitivity for the mean and rms fluctuations of the flow are the same, the effect of the velocity fluctuations on the parameters of the yaw relation based on mean calibration is examined next. Maintaining the free-stream velocity constant while varying the frequency, the yaw sensitivities for both mean and rms velocities were obtained. For ease of comparing the results, only the variation in b_f^* will be presented here. This is done because the Friehe and Schwarz relation has only one variable coefficient and its variation in this case should be easier to follow. These results are shown in Figure 66. In absence of the velocity fluctuations, the value of b_f^* was determined to be equal to 1.0. When periodic fluctuations were superimposed on the flow, keeping the time-mean velocity constant, the values of b_f^* obtained from both mean and rms yaw calibration changed by as much as 3% at the lower frequencies and by as little as 1% at the higher frequencies. The figure displays b_f^* , obtained in presence of the fluctuation, decreasing with increasing frequency and approaching the value obtained from static

calibration. It should be pointed out that the same amplitudes of fluctuations were used in Figures 65 and 66.

This frequency dependence of the yaw coefficients will cause a discrepancy between static and dynamic calibration for the X-probe sensitivity coefficients described in Equation (III-35). In addition, Figure 66 brings out other important problems. If mean velocities are to be measured in an essentially laminar flow using inclined wires, only a static calibration will describe its true yaw behavior. In order to accurately measure mean velocities with an X-wire in a turbulent flow the probe should be calibrated in a fluctuating flowfield of similar intensities and frequencies. In cases where fluctuating velocities are to be measured using inclined wires, neither static nor dynamic calibration will yield accurate results since the sensitivities for inclined wires will be frequency dependent. This frequency dependence can also lead to substantial errors in spectral measurements utilizing inclined sensors.

Although the data of Figure 66 are based on the periodic part of the hot-wire signal, the results may be influenced by the presence of the random 2% turbulence fluctuations. Based on Equation (III-79) and in presence of turbulence Reynolds stresses, \overline{uv} , one would expect the difference, depicted in Figure 66, between the mean-velocity yaw calibration with and without fluctuations present. A similar conclusion can be made regarding the unsteady velocity from

Equation (III-81). In the calibration condition used in this chapter such Reynolds stresses could be present in the random fluctuations or due to their interaction with the periodic velocity field. However it remains somewhat puzzling that Equation (III-83) was verified earlier, while in view of the results of Figure 66 it may not necessarily hold. It could be that the additional terms in Equation (III-79) and (III-81) balanced each other leading to the behavior described by Equation (III-83) without having to satisfy all the assumptions made to derive it.

X-Wire Probe

The applicability of Equation (III-83) was also examined through measurements utilizing a linearized X-wire probe. Results for the normalized turbulence intensity for different ranges of angular position are shown in Figures 67 and 68 for frequencies of different intensities. Once again, these show that the effective turbulence intensity remains essentially constant. The scatter in the data in Figure 68 arises from measurements with forcing frequencies having intensities of 1 to 2%, where a small error in measuring the rms velocity leads to large errors in the measured turbulence intensity.

The transverse sensitivity coefficient, numerically calculated by a two point local derivative method (for further details see the section of "X-Wire Probe" in Chapter V), for mean and fluctuating velocities, using a forcing frequency of 40 Hz, is shown in Figure 69. These should be equal

through use of Equation (III-83). The transverse sensitivity coefficient determined from Equation (III-35) using the yaw coefficients obtained from yaw calibration in the absence of periodic velocity variations, is also shown on the same figure. A significant difference in the calculated sensitivity coefficients exists between static and dynamic calibration. The reason for this lies in the frequency dependence of the yaw coefficients as described in Figure 66. Although reasonable agreement is demonstrated between the three curves of Figure 69, other data did not yield as good an agreement. However, in all cases larger discrepancies were found between the static and dynamic calibration for the yaw dependence of mean velocities.

Morrison et al. [26] found that large differences in both sensitivity coefficients of the X-wire existed between static and dynamic calibration. Bruun [27] argues that part of this difference is caused by poor approximation of the static calibration data over a large velocity range by use of a constant power exponent law, and seems to attribute all of it to this approximation. However, his results consistently show the statically determined longitudinal sensitivity coefficient less than that determined by dynamic calibration by approximately 2%. This is consistent with the present results and hence could not be attributed to experimental error as Bruun states.

CHAPTER VII

DISCUSSION

Temperature Dependence

A scheme utilizing a temperature probe immersed in the working fluid to compensate for the dependence of the hot-wire velocity calibration on ambient temperature variations was examined in Chapter II. Requiring only the knowledge of the resistances of the velocity sensor and the temperature probe, and their temperature dependence, this scheme was found capable of compensation over as much as 40°C with as small as a 1% error in the indicated velocity (The error is essentially proportional to the square of the maximum temperature variations). This error may be reduced even further if the optimum circuit design is employed. The analysis for this optimum design yields a range of solutions from which a minimum error condition can be derived, in principle. This derivation requires an optimization approach and has not been completed yet.

The analysis and error estimates were based on the premise that the coefficient A in King's law is independent of temperature. However, it was determined in Appendix B that this coefficient exhibits a slight variation with ambient temperature. This variation will add a small contribution to the errors in the compensation attained.

If one wishes to utilize this scheme without velocity calibration at various temperatures, one may use the

analysis based on the constant A assumption. However, if one uses the scheme after such velocity calibration has been performed, the analysis can be modified slightly to take into account the variation of A with temperature. The errors can be determined from the data presented in Appendix B. They will be calculated by comparing the values based on the experimental data of dR_3/dT , i.e., the values required for a constant anemometer output at a fixed velocity with varying temperature, with those derived by the analysis of Chapter II.

Yaw Dependence

In regard to the yaw dependence of hot-wires, results for yaw calibration in steady velocities are presented in Chapter V. As a check on these results, they are compared to those available in the literature.

Since the Friehe and Schwarz relation was one of the yaw relations examined in the course of the present investigation, the yaw coefficients determined when using it can be compared to the results of Friehe and Schwarz [22]. This comparison is summarized in Figure 70. Although there is a fair amount of scatter, due to the Reynolds number dependence, a general trend is drawn. The data of Friehe and Schwarz [22] fall along this trend indicating that the results are consistent. However, the present data, having cases when $b_f^* > 1$, i.e. negative deviations from the cosine law, reveals one aspect which they did not report.

Another check on the data is performed by comparing the

results to the data of Champagne [17]. Champagne used the following yaw relation

$$f^2(\alpha) = (\cos^2 \alpha + k^2 \sin^2 \alpha)^{1/2} \quad (\text{VII-1})$$

where k is a small parameter accounting for the axial cooling of the wire. The variation of k with sensor l/d at velocities approximately equal to 110 ft/sec was reported in his work [17,25]. Data from the present relation were converted to an equivalent average value of k^2 through the following relation

$$k^2 = \frac{1}{2\Delta\alpha} \int_0^{\Delta\alpha} \frac{[1 - b^*(1 - \cos^{m^*} \alpha)]^4 - \cos^2 \alpha}{\sin^2 \alpha} d\alpha \quad (\text{VII-2})$$

where $\Delta\alpha$ is the angular range over which the yaw calibration data were obtained. These results, plotted in Figure 71, indicate that k^2 is a strong function of Reynolds Number, i.e., decreasing with increasing Re_d ; a result which is also supported by Kjellström and Hedberg [19]. In spite of this Reynolds number dependence, a general trend with sensor l/d can be also drawn in this figure. For intermediate sensor lengths, k^2 is positive. However, it becomes negative for shorter sensors (i.e. $l/d < 150$) and for longer sensors (i.e. $l/d > 600$), a result not determined by Champagne. In all cases one observes that Champagne's data follows the trend of the present results. Again, as for $b_f^* > 1$, the negative values of k^2 represent effective cooling of the

sensor less than that described by the cosine law. Figure 71 is plotted using k^2 instead of k to avoid introducing imaginary values in the coefficients of the yaw relations. However, if one is to use Equation (VII-1) to represent experimental data, the present results indicate that one should either use k^2 as the parameter or should allow k to be imaginary if it is to be utilized directly. In Figure 71 each of the present data sets is represented twice: once based on its fit to the present relation, and the other based on the best correlation of the data by the Friehe and Schwarz relation. The standard deviation of the two fits is different and is always smaller in the former case. The trends remain the same in both representations.

Based on the results of Chapter V and in Figures 70 and 71, it is evident that as the velocity over the sensor changes, its yaw sensitivity is altered. At any velocity, for a constant temperature anemometer, the conduction from the wire to the prongs is constant. However, as the velocity increases, the convection increases thereby changing the ratio between convection and conduction, which in turn will alter the axial temperature profile of the wire. Horvatin [36] concludes that as this ratio increases (in his case by decreasing the conduction effects) the temperature profile becomes more uniform along the entire length of the wire. This can be also calculated directly through use of the analysis presented by Sandborn et al. [37]. Therefore, one would expect that at higher velocities, where th

temperature profile becomes more uniform, that the sensors' yaw response should be closer to the cosine law approximation.

The variation of the yaw coefficients obtained from the present relation are shown in Figures 72 and 73. At any l/d , there is a wide range of scatter of the coefficients with Reynolds number and type of probe used. The calibration data obtained by an independent source over a wider range of Reynolds numbers and data from hot-films calibrated in water are all included in these and the following figure. Figures 72 and 73 indicate that the yaw coefficients obtained for any probe are strong functions of probe design and construction. Therefore, each probe must be calibrated separately for yaw sensitivity. Similar results for the turbulence correction factor are presented in Figure 74, indicating again that no typical values of the yaw parameters can be found for any of the l/d 's shown. In particular, the figure displays the wide range of correction factors of the turbulence intensity correlations which may be encountered for typical probes.

Included in Figures 72, 73 and 74 are the data from the different overheat ratios, the different angular ranges of calibration, and the X-wire calibration. The X-probe data brings out a most significant result. Comparing the values of b_f^* , b^* and m^* for Wire 1, listed in the tables of Figures 59, 60 and 61, to those for Wire 2, given in Figures 62 and 63, one notes the substantial difference between them. As

illustrated by the photographs of Figure 12, the two wires of the X-probe were made as identical as one can expect them to be. The photograph proves that they appear identical and symmetric to the naked eye even with the enlargement of the pictures. In addition, the two wires were made from the same stock using the identical technique. After careful examination under the microscope and while using an optical comparator, it was found that Wire 2, which exhibited the larger deviation from the cosine law, had a slight double curvature along its length.

The above results lead us to believe that not only each probe but also each new sensor mounted on the probe must be calibrated even if the new sensor is identical to the one being replaced.

An interesting correlation between b^* and m^* is shown in Figure 75 where b^* varies approximately as $(2m^*)^{-1}$. If this correlation is used, the present yaw relation can be reduced to a one parameter relation. This would still give a more accurate description of the data than the Friehe and Schwarz relation but will no longer give the minimum errors which can be achieved with the two parameter relation. Again, data from MSU and from hot-films in water are included in this figure. The small scatter about the correlation is surprising in view of the variety of the data included.

Considering the added complexity introduced by a two parameter relation over the various one coefficient relations, it is important to find out when a more complex

relation is most needed. The most obvious comparison is between the present and the Friehe and Schwarz relations. Taking into account the effect of l/d and the Reynolds number, the regions where a substantial improvement in the accuracy is gained by using the present relation are shown in Figure 76. "Significant" improvement is indicated where the ratio σ_f^*/σ_p^* is larger than two as described in Chapter V. This figure can then be used as an operating chart to determine which of the two yaw relations is more "suitable" for a particular l/d .

Considering 5% deviations from unity in the value of the correction factor of the turbulence correlations to be small, sensors which behave like the cosine law can be identified (Note that unity corresponds to the cosine relation). The cross hatched regions of Figure 77 encompass all the conditions found to fall under this definition. The results are somewhat surprising in that the short sensors should have a non-uniform axial temperature distribution which some investigators suggest causes deviation from the cosine law. However the reason that the longer sensors show some deviation from the cosine law may be explained by the method used to change l/d . In all l/d cases, the spacing between the hot-wire prongs is kept constant so that as the sensor l/d increases, the active portion of the sensor will be closer to the prongs thereby increasing the conduction and aerodynamic interference effects. These increased effects are probably only significant for $l/d=1000$.

If one uses a probe similar to that used in this investigation, Figures 45 and 76 can be utilized as operating charts to determine which sensor would be most applicable. From these, one observes that going to a very short sensor, e.g., $\ell/d=100$, would be most advantageous. With this sensor, the effects of gradients in mean velocity on the wire sensitivity as described by Gessner and Moller [38] would be minimized. The short sensor would also be more suitable for measurement of turbulence quantities, as described by Frenkiel [39].

In Chapter V, the idea of finding the best values of the yaw relation parameters over a range of Reynolds numbers, i.e., velocities, is introduced. Such values would be useful when X-probes are utilized to obtain the various profiles of the velocity components and their correlations. This is particularly true in connection with analog signal processing. The selection of the best values of the parameters is based on an effective standard deviation of the data from the yaw relation, over the desired range of Reynolds numbers. As demonstrated in Figures 51 and 52, employing the various yaw relations will lead to different effective standard deviations. The effective overall ratio of improvement gained by changing from one relation to another can be calculated for the range of Reynolds numbers under investigation by dividing the values of the best effective standard deviations found from the different yaw relations. This improvement ratio is given in Figure 78 for

a comparison between the present relation and both the cosine law and the Friehe and Schwarz relation. A negligible improvement is achieved by using the present instead of the Friehe and Schwarz relation. A small improvement is made by substituting the present relation for the cosine law.

However, these results must be interpreted with some care. The magnitude of Σ_p^* is typically an order of magnitude larger than that of σ_p^* , which indicates the large errors introduced by trying to represent a range of Reynolds numbers by a single set of yaw relation parameters. The present exercise, therefore, indicates that one should use different yaw calibration coefficients for different Reynolds numbers, or velocities. Based on the results of the exercise one can also surmise that if a single set of parameters is to be used, the accuracy achieved by a simple relation like that of Friehe and Schwarz is as good as one may expect. In fact for most sensor l/d 's, using the cosine law is just as good. Therefore, it can be stated that for analog signal processing one may just as well use the simplest yaw relation, i.e., the cosine law. However, after the data has been gathered, the results must be corrected for the large errors introduced by the cosine law. These errors are present in all of the mean and rms velocity components measured by the X-probe and, of course, in their correlations. The correction factors must be obtained with the aid of the yaw calibration data of the wires and most likely they are functions of the velocity, i.e., Reynolds

number.

Such correction factors have been derived by Champagne et al. [25] based on his yaw relation for the case when the mean flow is aligned with the axis of symmetry of the X-wires. They also demonstrate that a simple summing and differencing technique can be used to determine the various turbulence intensities and Reynolds stresses. Bruun[40] presents an approximate method which he argues can be used to determine these quantities when the mean flow angle is not aligned with the probe. His approximate method again relies on simple sum and difference techniques. However, based on the present analysis, his approximation will lead to large errors in some cases. In Chapter III, it was shown that to first order, an X-probe can be used with the same degree of accuracy in flows where the mean flow angle is not aligned with the probe as when the mean flow angle is zero. The approach of Chapter III is based on simple weighted summing and differencing of the signals from the sensors. The weighting functions depend on the yaw coefficients and the mean flow angle. Having shown in Chapter VI that dynamic calibration, as for example used by Perry et al. [41], or that calibration in a turbulent flow may be necessary, one ascertains that the method proposed in Chapter III is much more suitable. In particular, since it has no restrictions on the type of flowfield it is calibrated in. This method will also express the accuracy of the relation representing the calibration data by the

quantity σ_p .

To demonstrate the importance of knowing the standard deviation of the yaw data, σ_i , and how even small differences in σ_i can cause substantial discrepancies in the computed turbulence intensities for different mean flow angles, Figures 79 through 81 are presented. In order to determine these discrepancies, the distribution of energy between the different components of the turbulence, as calculated by the cosine law must be known. Sample results are shown for two different flow conditions, one typical of the outer region of a turbulent boundary layer, the other typical of the inner region. Data for these flow conditions were based on the measurements of Klebanoff [42]. While only very small mean flow angles with respect to the X-probe, γ , are present in the boundary layer, Klebanoff's data is used here for $0^\circ \leq \gamma \leq 25^\circ$ to illustrate the trends and to give the reader a feeling for the magnitudes of the errors involved.

The yaw parameters used in Figures 79 and 80 are for the case where the largest deviations were observed between the three yaw relations, i.e., the worst case expected based on the probes tested here.

In Figures 79, 80 and 81 the differences between values computed by the cosine law and those computed by either the present relation or the Friehe and Schwarz relation are represented by $\tilde{\epsilon}_i$ and $(\tilde{\epsilon}_i)_f$, respectively. The subscript i denotes the turbulence velocity correlation computed. For

example, an $\tilde{\epsilon}$ of 0.1 indicates a 10% difference between the values computed by the two relations in question based on the same output signals from the X-wire and the same yaw calibration data. The differences between the present and the Friehe and Schwarz relation can be obtained by the difference between $(\tilde{\epsilon}_i)_f$ and $(\tilde{\epsilon}_i)$; see Equation (III-73).

In Figure 79, when the mean flow angle, γ , is zero, a 4.5% difference in computed values of v' exist between the Friehe and Schwarz relation and the present relation even though only less than 0.5% difference in fitting the mean velocity is observed in Figure 80. This difference in v' increases to 10% as γ increases. The major effect appears in the Reynolds stress \overline{uv} where a difference of over 70% exists between the Friehe and Schwarz and the present relations for increasing values of γ , while the difference in \overline{uv} between the cosine law and Friehe and Schwarz varies between 9 and 16%. When $\gamma = 0$, the minimum difference of 5.5% in the calculated \overline{uv} is found between the present and the Friehe and Schwarz relations.

The distribution of the turbulence does have some effect on the differences in the computed values of v' , however it plays a larger role in the determination of the Reynolds stress. As the magnitude of the v component of the fluctuations approaches that of the u fluctuations, the difference in \overline{uv} computed by the present relation and Friehe and Schwarz' relation substantially increases. At the same time the difference between the Friehe and Schwarz relation

and the cosine law increases only by approximately 7% at the large γ 's.

Differences in mean and streamwise fluctuating velocities for the same case appear in Figure 80. Although small differences in u' are found when $\gamma = 0$, these differences grow to 12% as γ increases. For $\gamma = 0$ the difference in the computed value of u' is identical to the difference in mean velocity. Therefore the ratio of these, i.e., the streamwise turbulence intensity, remains the same in all three cases. This is true in the case of an ideal X-probe. However once a typical X-probe in which each sensor has a slightly different yaw sensitivity is used, there will be differences in the computed turbulence intensities. The results of the analysis demonstrate that the longitudinal turbulence intensity is the only quantity that can be measured exactly, even then only with an ideal probe with matched sensors at equal angles to the mean flow direction. It is ironic that this quantity can be measured just as accurately by the much simpler method of one hot-wire perpendicular to the flow direction.

It should be noted that in all cases, when $\gamma = 0$, the differences between the computed values reduce to those given by Equations (III-45) through (III-47) and are in agreement with the results of Friehe and Schwarz [22] and of Roberts et al. [23, 24]. While the present analysis is limited to small turbulence intensities, by extending it to the cases $\gamma \neq 0$, one is able to get an indication of the

trends at high intensities. Under large turbulence conditions the instantaneous value of the angle, i.e., β , can achieve very large values. If the heat transfer from the wire behaves in a somewhat quasi-steady fashion, the $\gamma \neq 0$ results may give good indications of the errors introduced by the simpler yaw relations.

The case for an X-probe constructed of standard-length hot-wires corresponding to the region of negligible improvement between the three relations, is shown in Figure 81 for the same flow conditions as those of Figures 79 and 80. The differences in the computed values of u' and v' are negligible between the Friehe and Schwarz and the present relations while the differences in \overline{uv} are only as large as 4%. The typical differences for such an ideal probe are of the order of 1%. The difference between σ_p for Friehe and Schwarz and the present data in this case is 0.01%.

The results of Figure 81 demonstrate that large differences in the computed turbulence velocity correlations can exist even for insignificant differences (i.e., 0.01%) in fitting the mean yaw calibration data. In addition, the magnitude of the standard deviation of the yaw calibration fit must be very small. The data of Figures 79 and 80 show that a value of σ_f of approximately 0.7% is certainly not small enough, a most surprising conclusion. Reducing this value by a factor of about 4.8, i.e., to a $\sigma_p \approx 0.15\%$, leads to very significant reductions in the errors in measuring the various turbulence quantities. The errors in the most

critical of these quantities, namely \overline{uv} , are reduced by 6 to 70% depending on the inclination of the X-wires with respect to the mean flow direction (or depending on the intensity of the turbulence). Therefore, a very high degree of accuracy in fitting the mean yaw calibration data is needed to attain accurate results.

The sample results presented in Figures 79, 80 and 81 utilized information on the distribution of the turbulence energy, i.e., ρ_u and ρ_{uv} , based on the classical experiments of Klebanoff [42]. In practice, the correction factors must be derived based on the data obtained from the experiment in addition to the yaw calibration parameters. Such corrections can be made a posteriori if analog signal processing is used or can be incorporated in a subroutine to the digital data processing program. In the former case the analog system would be set based on the cosine relation because of the discussion on the accuracies achieved over a Reynolds number range presented earlier in this section. If the Reynolds number of the probe remains unchanged during the experiment, the corrections can be included a priori to the experiments. They would be automatically incorporated in the weighted sums and differences of the output signal based on the yaw calibration parameters corresponding to the operating Reynolds number. The details of this approach are given in Chapter III.

In regard to the effects of velocity fluctuations on the yaw calibration of hot wires, the results obtained in

this study are presented and discussed in Chapter VI. However the main thrust of the findings will now be summarized.

Various sensors from single- and X-probes were calibrated under steady conditions as well as in the presence of velocity fluctuations. The results indicate that while dynamic yaw calibration of the probes is not necessary, the mean yaw sensitivity of the probe should be obtained in the presence of some velocity fluctuations, e.g., in the presence of some background turbulence. These results also suggest that the velocity calibration of the probe may follow the same trends. This of course is contradictory to the common practice of using calibration flow conditions with the minimum possible turbulence intensity. However, they are not necessarily surprising in view of the changes which may be induced by unsteady velocities in the boundary layers and in the flow around the sensor and prongs as well as in other aspects of the convective heat transfer from the wire.

CHAPTER VIII

CONCLUSIONS AND RECOMMENDATIONS

The conclusions drawn from the various parts of the investigation are presented in the following order: first, conclusions obtained from the analysis of the temperature compensating scheme, examined in Chapter II and Appendix A, are presented. Next, the main findings of the experiments on temperature compensation, reported in Appendix B, are summarized. The major conclusions drawn from the analysis describing the yaw response of hot-wires in steady and fluctuating velocity fields are presented next. This analysis is given in detail in Chapter III. Finally, conclusions based on the results of the experiments on the yaw sensitivity of hot-wires are listed. The discussion of these results is included in Chapters VII, VI and V.

Conclusions

Based on the analysis of the scheme proposed for compensation of the anemometer output for ambient temperature variations, it was found that:

1. Temperature compensation does not depend on whether the anemometer output is linearized or not.
2. One needs only to know the properties of the anemometer bridge and the velocity and temperature probes (i.e., their resistance and temperature dependence coefficients) in order to achieve the compensation, without any need for temperature calibration. Hence, the scheme

provides means for incorporating the temperature compensation a priori to conducting the experiments.

3. Constraints on the parameters of the temperature compensating probe, valid for all three circuit configurations, were derived. With this and the knowledge of the properties of available velocity sensors, operating overheat ratios, anemometer bridge ratio and operating mode, a suitable temperature compensating probe may either be fabricated or purchased.

4. Exact solutions for temperature compensating circuits 1 and 2 were obtained for three different operating modes; i.e., constant overheat ratio, constant overheat difference and constant output voltage. Operating charts are provided (Figures 4 and 5) for the selection and adjustment of the resistances in the circuits.

5. When no constraints are imposed, a family of solutions exist for compensating circuit 3. Constraints to minimize the non-ideal behavior are being derived for this circuit making it the optimum circuit configuration.

6. Estimates for the errors introduced through the non-ideal behavior of the compensating circuits have been derived and indicate that the error is proportional to the square of the temperature variation.

7. For a typical hot-wire, temperature compensator pair, it was determined that circuit 1 with an ambient temperature increase of 40°C produces a -2% change in the indicated velocity, while utilizing circuit 2 reduces the

error to -1%. This error can be further reduced if the optimized configuration of circuit 3 is employed.

8. The temperature dependence of the coefficient A in King's Law, which was found from the experiments, was ignored in the analysis and error estimates. Its variation with temperature will add a small contribution to the errors in the compensation attained. In order to account for the temperature dependence of this or the other coefficients in King's Law, i.e., n and B , the a priori setting of the scheme and estimating of the errors will not be possible without velocity calibration at different temperatures.

Based on the experiments on temperature compensation conducted in air, the following conclusions were drawn:

1. For a constant velocity, if the ambient temperature changes, operating in a constant overheat mode overcompensates but seems to approach the ideal compensation to a greater degree of accuracy as compared to the constant difference mode of operation, which undercompensates.

2. The effective temperature compensation of all operating modes was found to be independent of fluid velocity and initial overheat ratio.

In the derivation of the response equations of inclined cylindrical sensors in steady and fluctuating velocity fields, previous analyses have been extended for the present yaw relation to include X-probes with dissimilar sensors as well as mean velocities at an angle γ to the line of symmetry of the X-wires. The following conclusions are based on the results of the analysis.

1. For sensors with yaw dependence that does not closely follow the cosine law, neither the simple nor an approximate weighted sum and difference technique applies when $\gamma \neq 0$. This makes analog processing to obtain accurate mean velocities extremely difficult if not impossible. However, for cases where the mean streamline is aligned with the probe axis of symmetry, the errors introduced are usually less than 5%.

2. In low-level turbulence, time dependent velocity components can be obtained using a weighted sum and difference technique once the mean flow angle is known.

3. By extending the analysis to cases where $\gamma \neq 0$, while using low intensity assumptions, one is able to get an indication of the trends at high intensities for which the instantaneous flow angle can assume very large values.

4. The correction factors derived for the measured mean and turbulence quantities must be based on the data obtained from the experiment in addition to the yaw calibration parameters. Such corrections can be made a posteriori if analog signal processing is used or can be incorporated in a subroutine to the digital data processing program.

5. Discrepancies exist between different yaw relations in calculated values of turbulence velocity correlations which are derived from the same data. These discrepancies depend on the mean flow angle, the distribution of the turbulence energy between the velocity components and the accuracy to which the mean flow calibration data fits the particular yaw function. For differences in this accuracy of

0.5%, discrepancies as large as 10% and 70% may exist in the computation of v' and \overline{uv} , respectively. Differences in fitting mean calibration data of 0.01% produce discrepancies in turbulence quantities of the order of 1% when $\gamma = 0$ and as large as 4%, in the Reynolds stress, at large γ 's.

6. The longitudinal turbulence intensity is the only quantity that can be measured exactly, even then only with an ideal probe having matched sensors at equal angles to the mean flow direction.

7. Measurements in many complex flowfields such as "swirling flows" or near bluff bodies, in particular in the presence of turbulence, require that the yaw sensitivity of both sensors of an X-probe must be known to a high degree of accuracy.

Conclusions based on the experiments on yaw sensitivity in steady and fluctuating velocities are listed in the following:

1. Unlike the cosine law or the Friehe and Schwarz relation, the standard deviation of fitting the yaw calibration data by the present relation is independent of the Reynolds number and the length of the sensor, i.e., l/d .

2. In all cases examined, including hot-films in water and data from an independent source, the present relation fit the yaw calibration data to a higher degree of accuracy than the cosine law or the Friehe and Schwarz relation. The improvement in the accuracy over the cosine law can be as large as a factor of 25, while that over the Friehe and

Schwarz relation can only be as large as 5. This improvement, however, is dependent on probe design and Reynolds number.

3. The ratio of improvement over either the cosine law or the Fricke and Schwarz relation is smaller for the very short sensors ($l/d \approx 100$) than for the long sensor ($l/d = 1000$). This indicates that the cosine law is more applicable to the short sensors, rather than to the long ones! The variation of the yaw parameters was not found to be monotonic with sensor l/d and did agree with previously reported results.

4. The improvement in using the present relation over the Fricke and Schwarz relation comes at relatively large yaw angles (i.e., larger than 50°) and particularly at low Reynolds numbers. The yaw coefficients determined from the present relation are independent of the angular range of data between $\pm 50^\circ$ and $\pm 70^\circ$.

5. A good yaw relation must account for both higher and lower effective cooling rates than that determined by the cosine law.

6. The yaw sensitivity of hot wires is not significantly influenced by the operating overheat ratio in the range between 1.4 and 1.8.

7. The trend of the yaw parameters with either sensor l/d or Reynolds number does not seem to approach the cosine law, but rather it seems to overshoot it without any observed asymptotic values.

8. In general, if an X-probe is misaligned by 0.5° , the effect on the yaw coefficients is equivalent to that resulting from recalibrating the probe, properly centered, at a freestream velocity 3 ft/sec lower than the desired one.

9. An approximate correlation can be used to reduce the present two parameter yaw function to a single parameter relation and is given by $b^* = 1/2m^*$. Employing this relation would still yield a more accurate description of the yaw calibration data but will no longer give the minimum possible errors.

10. For all cases examined, values of the transverse sensitivity coefficient calculated from a yaw sensitivity function, taking into account deviations from the cosine law, yield a higher degree of accuracy than those obtained directly from the data.

11. All sensors require a turbulence correction factor to take into account deviations from the cosine law. However, by proper design and selection, the magnitude of this correction factor can be minimized.

12. One should use different yaw calibration coefficients for different velocities. If a single set of parameters is to be used, the accuracy achieved by a simple relation like the cosine law is as good as one may expect. However, after the data has been gathered, the results must be corrected for the large errors introduced into the mean and rms velocity components.

13. The yaw parameters are influenced by the probe design and construction. Therefore, each probe must be calibrated to determine the yaw parameters associated with it at the Reynolds numbers of interest. The results lead us to believe that not only each probe but also each new sensor mounted on the probe, must be calibrated, even if the new sensor is identical to the one being replaced.

14. The parameters of the yaw relation are affected by the presence of unsteady velocities in the flowfield and depend on the frequency of these fluctuations.

15. While dynamic yaw calibration of the probes is not necessary, the mean yaw sensitivity of the probe should be obtained in the presence of some velocity fluctuations, e.g., in the presence of some background turbulence of similar spectral content to the flow under consideration.

Recommendations

The following items are recommended for future investigations in connection with the proposed temperature compensation scheme:

1. The optimization analysis of compensating circuit 3 should be completed.

2. The analysis of the compensating scheme should be extended to incorporate the variations of the coefficients A and B in King's Law with ambient temperature; this should include estimates of the errors involved. The variation of A with temperature is important in air while the variation of B with temperature will probably be important in water.

3. The errors can be calculated exactly from the experimental data presented in Appendix B. They should be found by comparing the values based on the experimental data of dR_3/dT , i.e., the values required for a constant anemometer output at a fixed velocity with varying temperature, with those derived by the analysis of Chapter II.

4. Experiments using real compensating probes should be performed to verify the analysis of Chapter II.

The following items are recommended to develop further insight into the yaw dependence of hot-wires.

1. The analysis can be extended to account for the effect of small lateral velocity fluctuations, i.e., w , on the various turbulence correlations.

2. The analysis can also be extended to determine the variation of the measured u' and v' as functions of γ .

3. Experiments on yaw calibration in fluctuating velocity fields should be modified to also include controlled periodic velocity fluctuations in the transverse direction.

3. The errors can be calculated exactly from the experimental data presented in Appendix B. They should be found by comparing the values based on the experimental data of $\delta\gamma/\delta T$, i.e., the values required for a constant anemometer output at a fixed velocity with varying temperature, with those derived by the analysis of Chapter II.

4. Experiments using real compensating probes should be performed to verify the analysis of Chapter II.

The following items are recommended to develop further insight into the yaw dependence of hot-wires:

1. The analysis can be extended to account for the effect of small lateral velocity fluctuations, i.e., w , on the various turbulence correlations.

APPENDIX A

2. The analysis can also be extended to determine the variation of the measured u' and v' as functions of y .

3. Experiments on yaw calibration in fluctuating velocity fields should be modified to also include controlled periodic velocity fluctuations in the transverse direction.

INITIAL ERROR ESTIMATES FOR TEMPERATURE COMPENSATING CIRCUITS

Instead of the approach presented in Chapter II for determining the errors introduced when using the temperature compensating circuits, the following approximate method was initially used. If one assumes that over a reasonable range of ambient temperature variations (e.g., for a temperature change of 40°C in air) the equivalent resistance R_3 varies linearly, the operating velocity probe resistance R_H will also be linear due to the bridge balance condition. The resistance R_H can then be written as:

$$R_H \approx R_{H0} [1 + \alpha_H (T - T_0)] \quad (A-1)$$

Operating the anemometer and compensating circuit in the constant bridge output voltage mode, we assume that the temperature function $\tau(T)$, which is defined in Chapter II, can be approximated by

$$\tau(T) \approx \tau(T_0) - m(T - T_0) \quad (A-2)$$

where $\tau(T_0)$ is a constant evaluated at the reference temperature and $m(T - T_0)$ is a small variation away from this constant value. Here, the coefficient m can be determined once $R_C(T)$ and $R_3(T)$ are known.

Using Equation (A-2) with Equation (II-21) one observes that $\partial E_b / \partial T \neq 0$. The resulting variation of bridge output voltage with ambient temperature can be given as

$$\begin{aligned}
\frac{E_b(T) - E_b(T_o)}{E_b(T_o)} &\approx \frac{R_{Co} \alpha_C m(T - T_o)}{R_1 + R_{Ho}} \\
&+ \frac{R_{Co}^2 \alpha_C^2 m(T - T_o)}{2 \alpha_H (\alpha_H - \alpha_C) R_{Ho} (R_{Ho} - R_{Co})} + \frac{R_{Co} \alpha_C m(T - T_o)}{2} \left[\frac{\alpha_H - \alpha_C}{\alpha_H^2 R_{Ho}} \right. \\
&\left. - \frac{1}{(\alpha_H - \alpha_C) (R_{Ho} - R_{Co})} \right] \quad (A-3)
\end{aligned}$$

If the anemometer output voltage is linearized, following a similar procedure one finds that

$$\begin{aligned}
E_L^n(T) - E_L^n(T_o) &\approx \alpha_C R_{Co} k_o B U^n m \left[(T - T_o)^2 / 2 \right. \\
&+ \frac{R_{Co} \alpha_C R_1 (T - T_o)}{\alpha_H^2 R_{Ho}^2} + R_1 \left(\frac{R_{Co}}{\alpha_H^2 R_{Ho}^2} \right. \\
&\left. - \frac{2 \alpha_C R_{Co}}{3 \alpha_H^2 R_H} \right) \ln[1 + \alpha_H (T - T_o)] \\
&\left. + R_1 \left(\frac{\alpha_C R_{Co}}{\alpha_H^2 R_{Ho}^2} - \frac{R_{Co}}{\alpha_H^2 R_{Ho}^2} \right) \frac{(T - T_o)}{1 + \alpha_H (T - T_o)} \right] \quad (A-4)
\end{aligned}$$

With available information on the temperature dependence of the compensating probe and the velocity probe, Equation (A-3) or (A-4) may be used to estimate the drift in output voltage. The accuracy of this method solely depends upon the accuracy of Equation (A-1) which can be experimentally determined.

EXPERIMENTS ON TEMPERATURE

COMPENSATION

is parallel with the analysis of the temperature compensation circuitry presented in Chapter II and Appendix A. Experiments were conducted in air to determine the validity of several of the assumptions made and to determine the temperature dependence of some of the parameters derived. Measurements were carried out utilizing the I.I.T. compressed-air driven hot-wire calibration tunnel. Dry air was heated by a 4.5 kw "Chromalox" Model GCH3405 heater prior to entering the plenum chamber of the calibration tunnel. The air temperature was varied by regulating the current to the heater via a 3-phase voltage control unit. Air temperature was monitored in the test section of the calibration tunnel by a specially constructed circuit utilizing a thermistor. A digital voltmeter indicated the temperature in $^{\circ}\text{C}$ directly and the accuracy and repeatability of the readings were within 0.5°C over the range from 10 to 60°C . At high velocities a thermistor near the upstream end of the test section was used, while at low velocities, the temperature was monitored approximately 3 cm. downstream of the hot-wire to reduce errors due to heat loss to the surroundings. The flow rate was controlled by a Watts Model 110 pressure regulator in line with and ahead of the air heater. A schematic

EXPERIMENTS ON TEMPERATURE COMPENSATION

In parallel with the analysis of the temperature compensating circuits presented in Chapter II and Appendix A, experiments were conducted in air to determine the validity of several of the assumptions made and to determine the temperature dependence of some of the parameters derived.

Measurements were carried out utilizing the I.I.T. compressed-air driven hot-wire calibration tunnel. Dry air was heated by a 4.5 kw "Chromalox" Model GCH3405 heater prior to entering the plenum chamber of the calibration tunnel. The air temperature was varied by regulating the current to the heater via a 3-phase voltage control unit. Air temperature was monitored in the test section of the calibration tunnel by a specially constructed circuit utilizing a thermistor. A digital voltmeter indicated the temperature in $^{\circ}\text{C}$ directly and the accuracy and repeatability of the readings were within 0.5°C over the range from 20 to 60°C . At high velocities a thermistor near the upstream end of the test section was used, while at low velocities, the temperature was monitored approximately 2 cm. downstream of the hot-wire to reduce errors due to heat loss to the surroundings. The flow rate was controlled by a Watts Model 110 pressure regulator in line with and ahead of the air heater. A schematic

of the entire setup is shown in Figure 82.

The temperature coefficient of resistance of two compensating probes and a standard length hot-wire ($l/d=580$) were obtained by exposing the probes to heated air streams of known temperature. Probe resistance was measured using the bridge of a Disa 55D01 anemometer unit to within $\pm 0.005 \Omega$. The temperature was varied and measurements taken throughout the range from 20 to 60°C. Graphs of probe resistance versus temperature were plotted and the temperature coefficients of resistance determined from the slope of the curve. The temperature dependence of all probe resistances was found to be linear for the range of temperature variation.

Guided by the analysis, three different operating modes were examined. The first kept the operating overheat ratio constant by manually adjusting the decade resistance on the anemometer at each temperature where data was taken. The second mode kept the operating resistance difference, $R_H - R_C$, constant by manually adjusting the decade resistance at each temperature. The third mode of operation involved adjusting the decade resistance on the anemometer to achieve constant output voltage at each fixed velocity as the air temperature was varied. The operating resistance as a function of ambient temperature, required to maintain the bridge output constant, was found from the latter approach.

Results from this portion of the experiment are shown in Figures 83 through 85. Figure 83 demonstrates that without compensation, the non-dimensional bridge voltage

decreases linearly with increasing temperature while maintaining the velocity constant. This result was found to be independent of flow velocity from 3.5 to 30 m/s. This drop in the bridge output voltage is dependent on the overheat ratio used and is largest for low overheats. Three overheats were used: 1.4, 1.6 and 1.8, the latter being the most common value employed by various experimenters.

Holding the resistance difference constant, again while maintaining a constant velocity, the drop in output voltage was found to decrease. Ideally, the bridge output voltage for a velocity sensor should remain constant for a constant velocity if the ambient temperature changes. The constant overheat mode over-compensates but seems to approach the ideal compensation to a greater degree of accuracy than the constant difference mode. Both of these operating modes are found to be independent of fluid velocity and initial overheat ratio.

If the bridge output is forced to remain constant at a given velocity, i.e., the third mode of operation described above, the variation in the overheat ratio and resistance difference can be determined as shown in Figure 84. The resistance difference has to increase substantially while the overheat ratio must drop slightly as the temperature increases in order to achieve ideal compensation. This tends to suggest that compensation using a constant overheat mode would give better results as compared to the constant

difference mode, a result which is in agreement with Figure 83. Each of these cases, normalized in the proper way, is independent of fluid velocity and initial overheat ratio.

The variation of the function τ with ambient temperature is shown in Figure 85. Use of this figure permits the evaluation of the coefficient m , discussed in Appendix A, which is needed for the approximate estimate of the errors of the compensating circuits. The linear variation of τ with temperature substantiates the assumptions made in Appendix A.

The hot-wire used in these measurements was calibrated for velocity over a range of overheat ratios and ambient temperatures. The summary of the results is shown in Figure 86. Both of the coefficients A' and B' are found to be dependent on the ambient temperature and initial overheat ratio. A' increases with temperature and with overheat ratio while the coefficient B' decreased with overheat ratio and with ambient temperature. The exponent n was found to be the least sensitive to temperature, varying only within 4% of its mean value for all cases.

The parameters A and B in King's Law can be extracted from these results with the aid of Equation (II-19). The calculated values are plotted in Figure 87. The curves indicate that the coefficient A has a slight temperature dependence while the coefficient B remains almost the same for all cases.

The analysis of the constant output voltage mode in

Chapter II was based upon the assumption that the parameters in King's law, i.e., A , B and n , are independent of temperature. Based on Figures 83 and 87 one can conclude that the variation in B and n may be neglected. However, the temperature dependence of A will introduce a small error in the resistances computed for proper compensation. The magnitude of this error can be calculated from the experimental data.

VAPORIZATION RESULTS FROM HOT FILMS

IN WATER

Initial work on the present vaporization was done by I.I.T. by E. A. Roberts [11] using hot films in water. In an attempt to explain some of the trends shown in Fig. 4, data presented by Ertel and Roberts [12] has been reproduced in this figure using their method of measurement. The data indicates that hot films, which have small L/D 's, tend to deviate less from the curve law as compared to the hot wires which have much larger L/D 's. Although for each of the films or the wires measured L/D decreases the deviation from the curve relation, the behavior of the data in Figure 4 is somewhat different after the studies of Ertel and Roberts [12] and of Roberts [11].

The majority of Roberts' data is presented in this appendix and in Figure 5 through 7 since his conditions were so generally available to the reader. His data, for a hot film with $L/D=12$, are plotted in a similar fashion to those of Ertel and Roberts in Figure 4. The Reynolds number dependence of the heat flux coefficients in the least squares sense, as determined from the present relation, demonstrates the importance of studying vaporization over a range of Reynolds numbers. To date we have not been able to find many such studies in the literature.

Contours in the h - T plane of constant standard deviation of the data from the present relation are shown in

YAW CALIBRATION RESULTS FROM HOT-FILMS
IN WATER

Initial work on the present yaw relation was done at I.I.T. by F. A. Roberts [23] using hot-films in water in an attempt to explain some of the trends shown in Figure 88. Data presented by Friehe and Schwarz [22] has been reproduced in this figure using their method of presentation. The data indicates that hot-films, which have small l/d 's, seem to deviate less from the cosine law as compared to the hot-wires which have much larger l/d 's. Although for each of the films or the wires increasing l/d decreases the deviation from the cosine relation, the behavior of the data in Figure 88 remained unexplained after the studies of Friehe and Schwarz [22] and of Roberts [23].

The summary of Roberts' data is presented in this appendix and in Figures 72 through 75 since his original work is not readily available to the reader. His data, for a hot-film with $l/d=18$, are plotted in a similar fashion to those of Friehe and Schwarz in Figure 89. The Reynolds number dependence of the best fit yaw coefficients (in the least squares sense) as determined from the present relation demonstrates the importance of studying yaw relations over a range of Reynolds numbers. To date we have not been able to find many such studies in the literature.

Contours in the $b-m$ plane of constant standard deviation of the data from the present relation are shown in

Figures 90 through 92 for the same sensor. It should be noted here that the definition of σ' differs from that of σ_p in Chapter V. Here σ' is the standard deviation of $f(\alpha)$, namely,

$$\sigma' = \sqrt{\frac{1}{N} \sum_{i=1}^N \left[f(\alpha_i) - \sqrt{\frac{U_{e,i}}{U_\infty}} \right]^2} \quad (C-1)$$

where $|\alpha|$ varied from 0° to 70° . Figures 90 and 91 show trends of constant σ' similar to those described in Chapter V.

Figure 92 shows the dependence of the minimum regions of constant standard deviation on Reynolds number for a standard commercial hot-film in a typical range of velocities. The movement of these regions is not consistent with the trends observed in Chapter V for hot-wires in air. This may suggest that even though both types of velocity sensors obey the present relation, their variation with parameters examined in the present work may be vastly different.

Figures 30 through 32 for the same reason. It should be noted here that the definition of σ differs from that of σ_p in Chapter V. Here σ is the standard deviation of $\hat{f}(t)$, namely,

$$\sigma^2 = \frac{1}{T} \int_0^T \left[\hat{f}(t) - \bar{\hat{f}} \right]^2 dt \quad (C-1)$$

where $\hat{f}(t)$ varied from 0 to 10. Figures 30 and 31 show trends of constant σ similar to those described in Chapter V.

Figures 32 show the dependence of the minimum variance of constant standard deviation on Reynolds number for a standard commercial hot-film in a velocity range of velocity. The minimum of the variance is not constant with the trends observed in Chapter V for hot-wires in air. This may suggest that even though both types of velocity sensors obey the present relation, their variation with Reynolds number examined in the present work may be vastly different.

APPENDIX D

YAW CALIBRATION RESULTS FROM X-WIRE PROBES; DATA COURTESY OF MSU

In an attempt to verify the behavior of the hot wires used at I.I.T. as typical, two independent sets of yaw calibration data were made available by Dr. John Foss of Michigan State University.

Both sets of calibration data were obtained using an X-wire probe with sensors having an $\ell/d=200$. Each set was obtained through different calibration procedures. The initial X-wire data, called Set 1, consisted of a free-stream velocity calibration of each sensor at various angles of yaw.

In his analysis of similar data, Foss [43] used the Friehe and Schwarz yaw relation and assumed that the velocity calibration equation at any angle of yaw can be written as

$$E_b^2 = A' + B' U_e^n \quad (D-1)$$

Since U_e and U_∞ are related by $f^2(\alpha)$, Equation (D-1) can be rewritten as

$$E_b^2 = A' + B' [f(\alpha)]^{2n} U_\infty^n$$

or

$$E_b^2 = A' + B'_\alpha U_\infty^n \quad (D-2)$$

where the coefficient B'_α will depend on the angle of yaw. Both A' and n are assumed to remain constant for all α 's.

At each angle of yaw, the hot-wire velocity calibration constants were determined by fitting the data from Set 1 to Equation (D-2) while minimizing the deviation of the data from the equation. The results, shown in Figure 93, indicate that the coefficient B'_α decreases with increasing angle of yaw as was expected from Equation (D-2). On the other hand the coefficients A' and exponent n increase with increasing angle of yaw. The effect of forcing A' and n to remain constant on the standard deviation of fitting the data has not as yet been examined. However, based on the available results it is likely that the errors introduced by this scheme would be larger than those achieved by the present approach and discussed in the following part and in earlier chapters.

A second set of calibration data was requested from MSU and Dr. Foss obtained the data using the same calibration procedures employed in the present work. First, he performed a velocity calibration of each sensor when it was normal to the flow. Next, at each free stream velocity, he varied the yaw angle of the probe to obtain readings of effective velocities through the use of Equation (IV-1).

The velocity range of Set 1 was between 10 ft/sec. and 110 ft/sec. while the second set varied from 15 ft/sec. to 55 ft/sec. For Set 1, once a free stream velocity was chosen, the corresponding output voltages were calculated using Equation (D-2) at each yaw angle. Using the coefficients obtained when the probe was nearly normal to the

flow, the same equation was utilized to calculate the effective velocities. Both sets of data were then analyzed in the manner described in Chapter IV and some of the resulting correlations are shown in Figures 94 through 96.

Sample contours of constant standard deviation in the b-m plane for one velocity of the yaw calibration data taken from Set 2 are shown in Figure 94. A comparison with Figures 21 and 22 reveals the similar trends with nearly the same values for the standard deviation contours. The variations with Reynolds number of the ratio of improvement in the fit of the data, σ_f^*/σ_p^* , and the yaw coefficients from Friehe and Schwarz and the present relation for both sets of data are shown in Figures 95 and 96. The coefficients b_f^* and b^* increase with Reynolds number while m^* and the ratio of improvement decrease with Reynolds number. Considering the l/d of the sensor ($l/d=200$), these trends can be compared to those presented in Figures 45 through 48. Such comparison indicates that in each case, the trends are identical although there is a fair amount of scatter in the magnitudes of the coefficients.

These results indicate that the behavior of the wires used at I.I.T. are typical. The MSU data also reaffirms the fact that the yaw coefficients depend strongly on the probe design and construction.

APPENDIX E

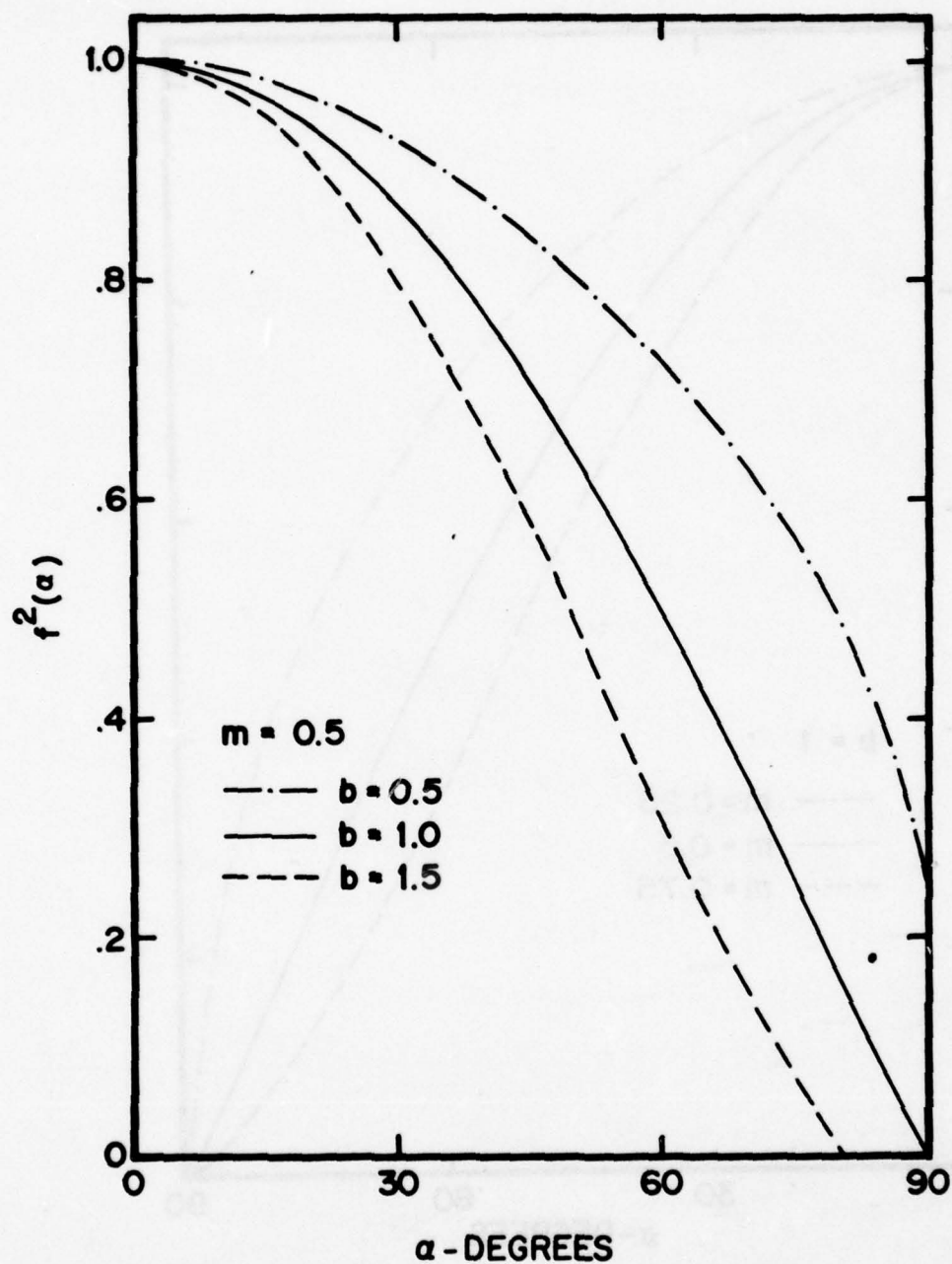


Figure 1. Effect on Present Yaw Relation of Changing Coefficient b While Holding Exponent m Constant

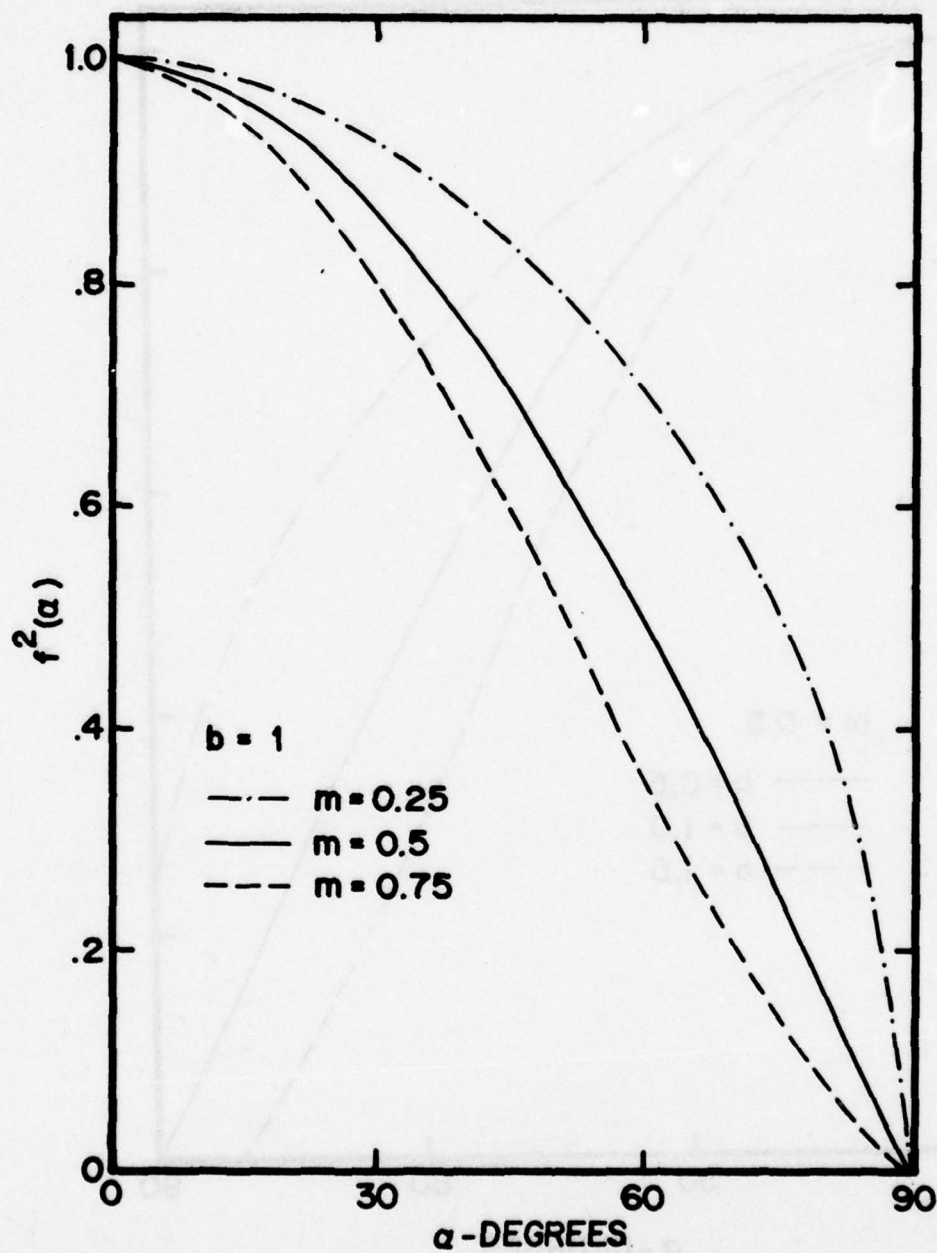


Figure 2. Effect on Present Yaw Relation of Changing Exponent m While Holding Coefficient b Constant

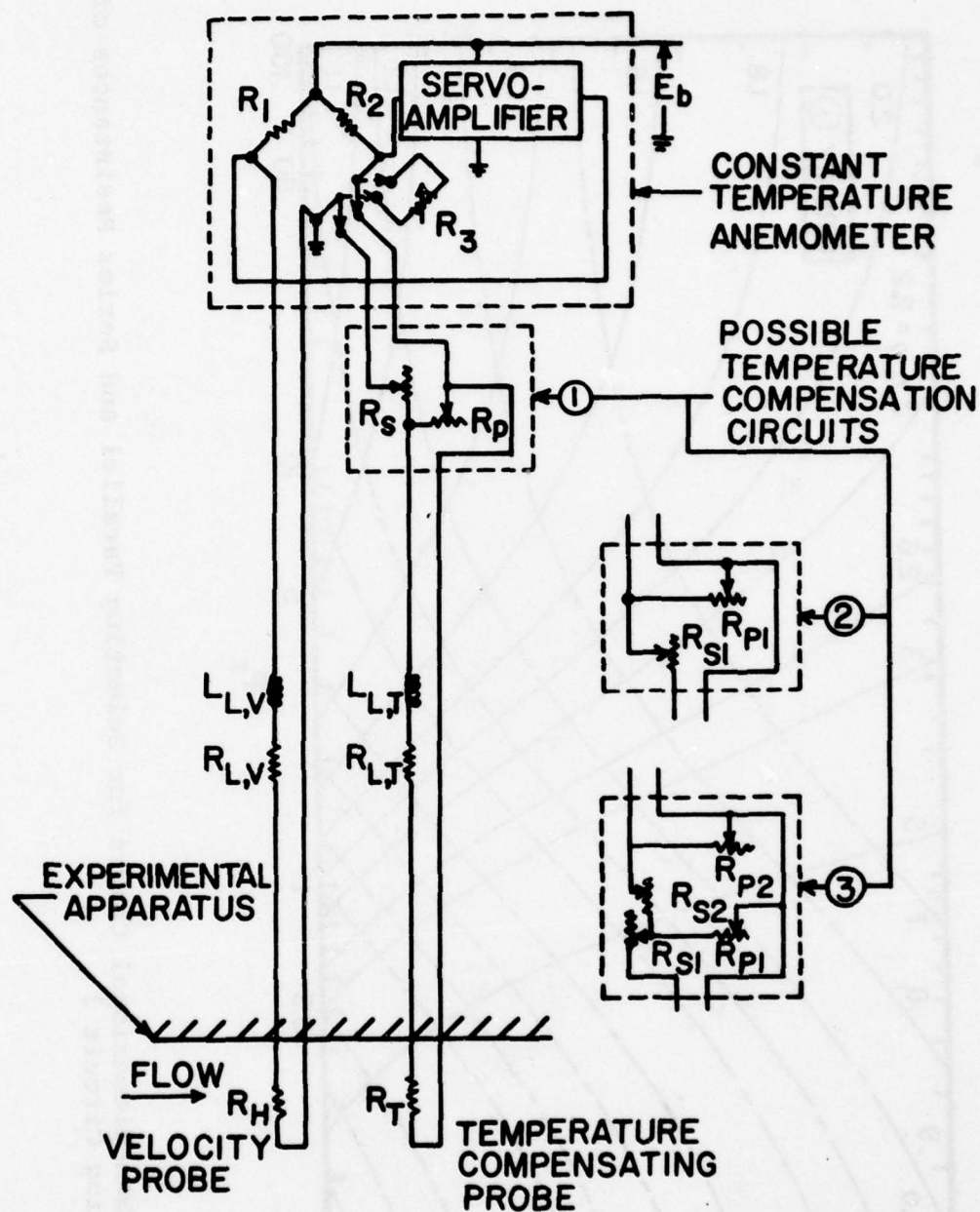


Figure 3. Schematic of Circuits Utilized in Schemes to Compensate for Ambient Temperature Variations

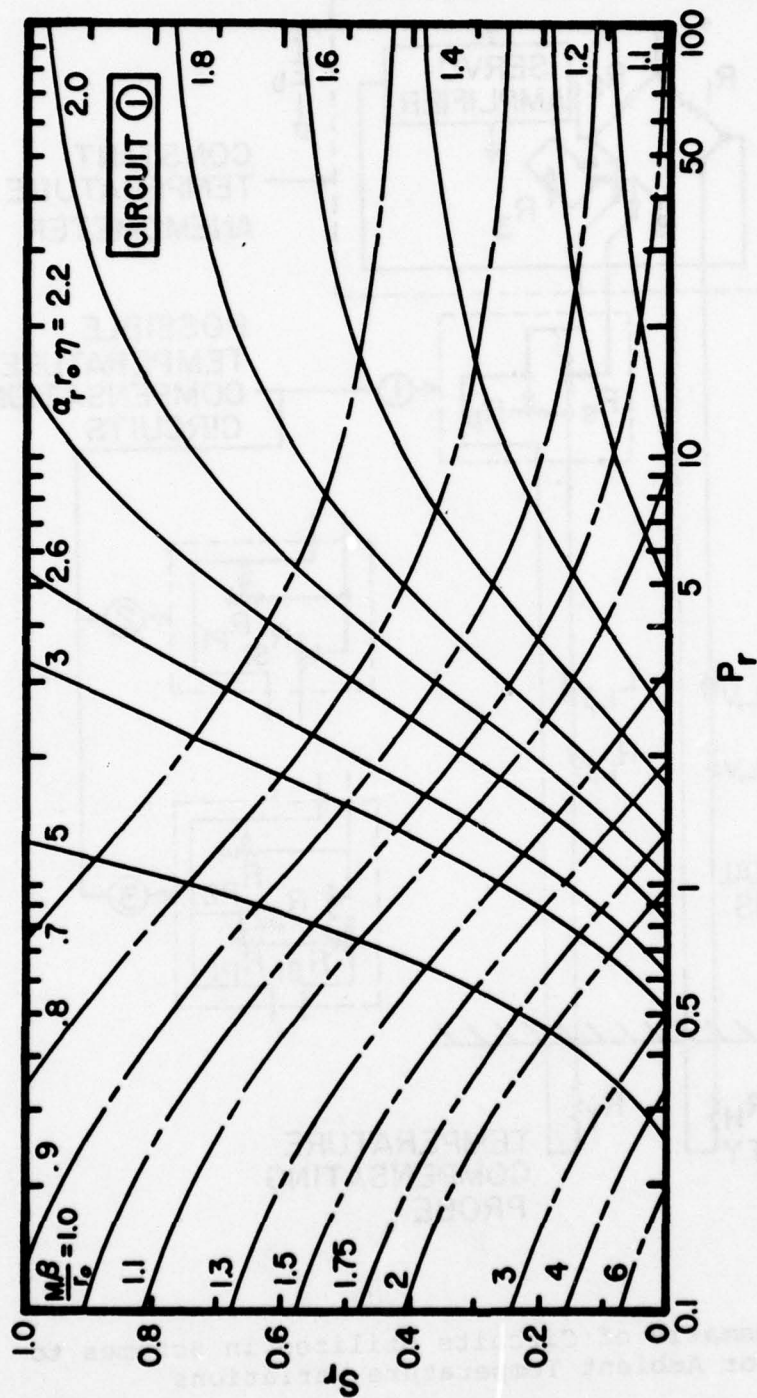


Figure 4. Non-dimensional Charts for Selecting Parallel and Series Resistances of Compensating Circuit 1

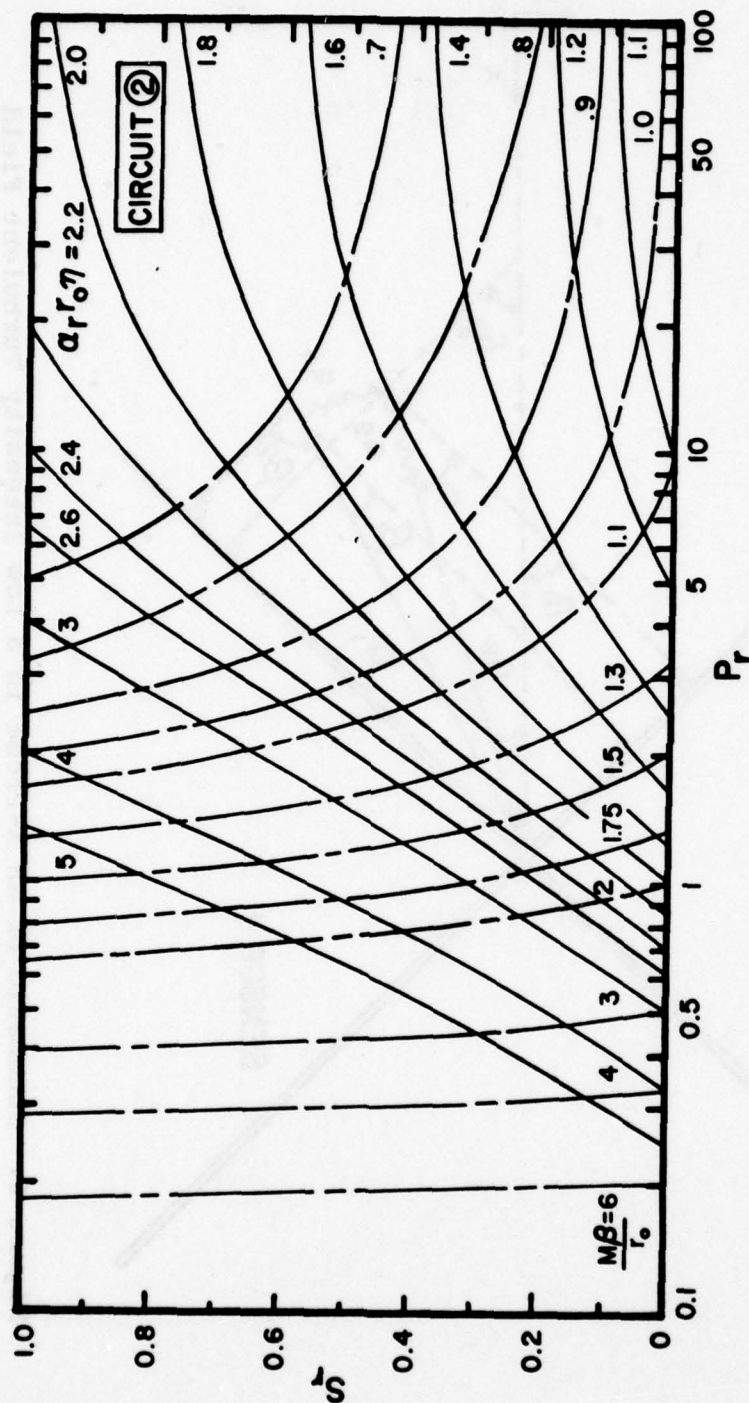


Figure 5. Non-dimensional Charts for Selecting Series and Parallel Resistances of Compensating Circuit 2

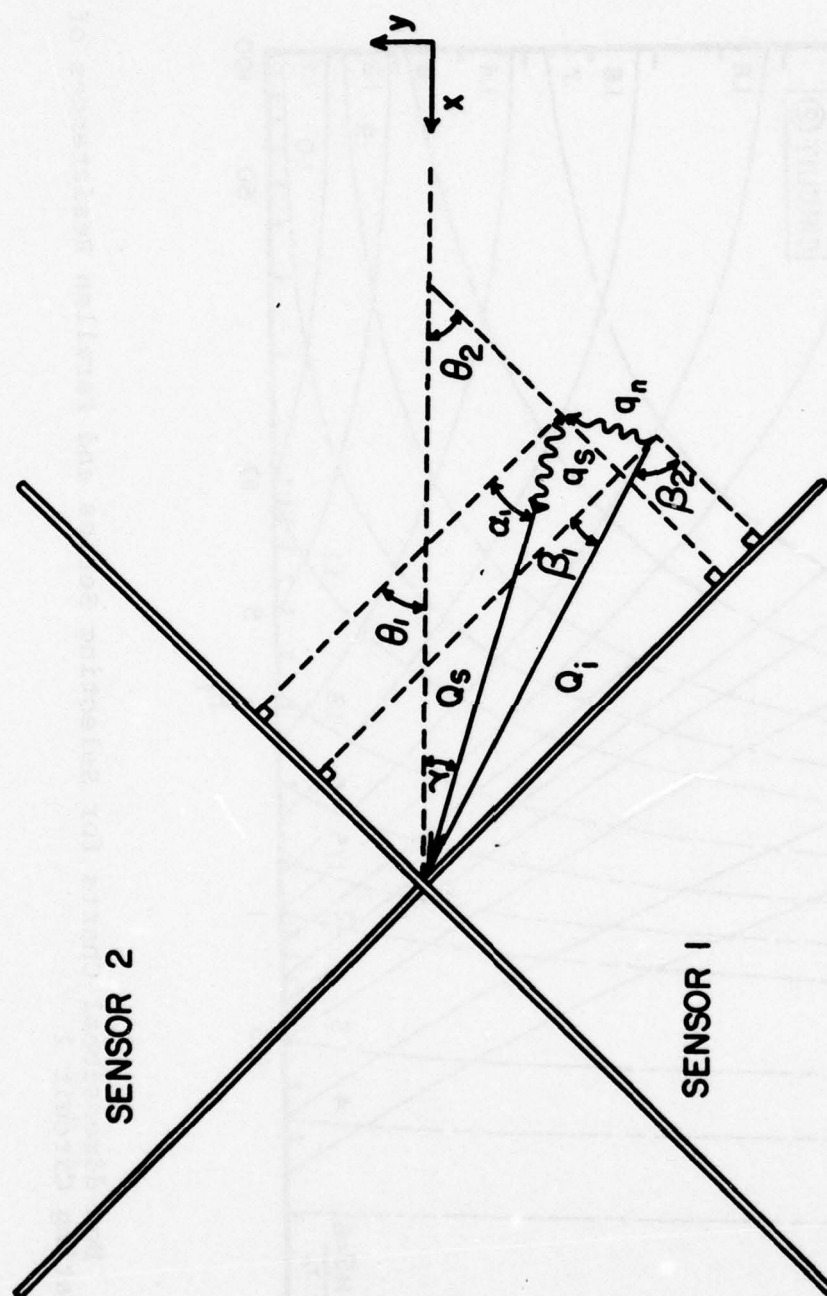


Figure 6. Schematic of an X-Probe in a Low Intensity Turbulent Field

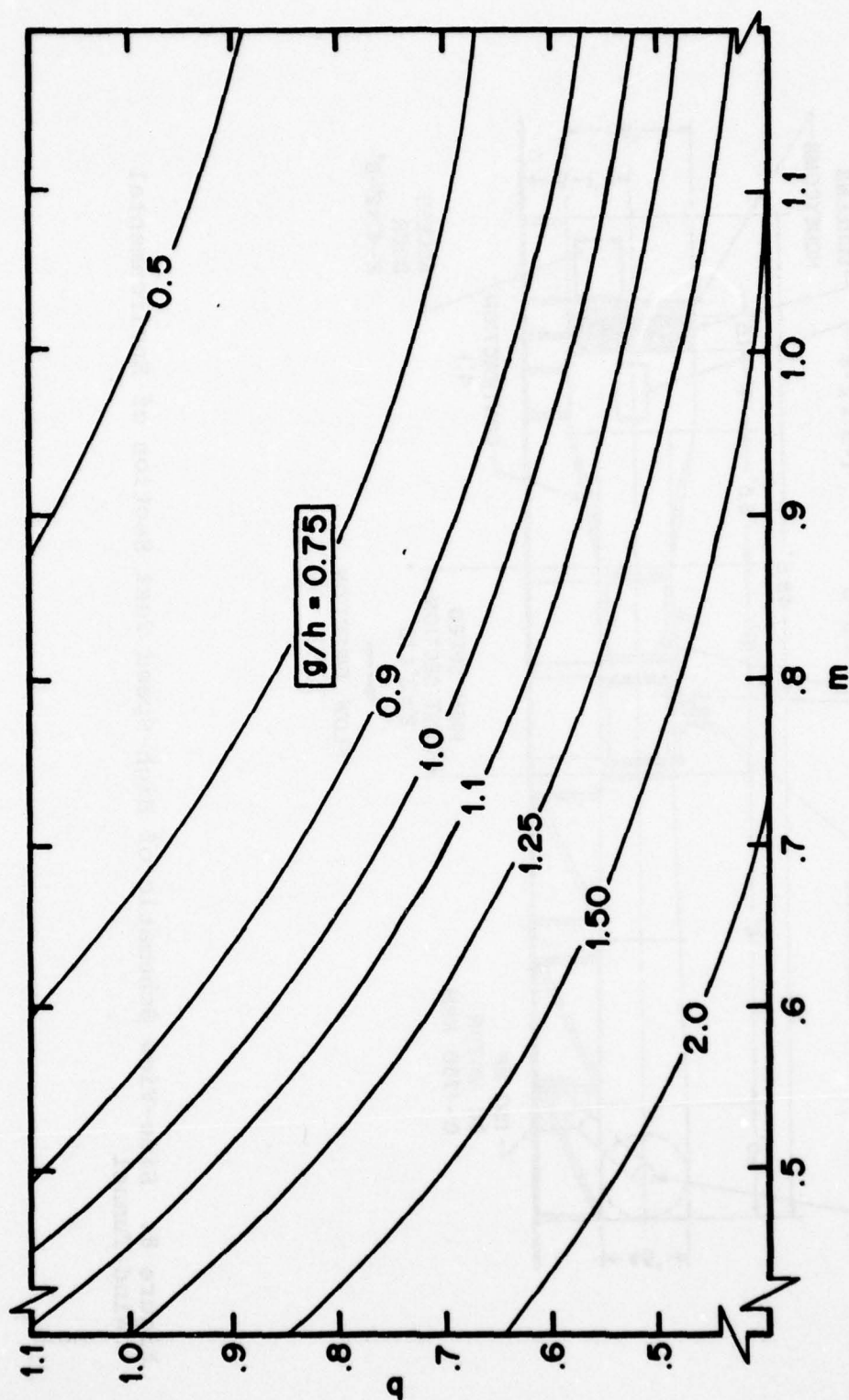


Figure 7. Turbulence Correction Factor, g/h , as a Function of b and m for $\gamma=0$

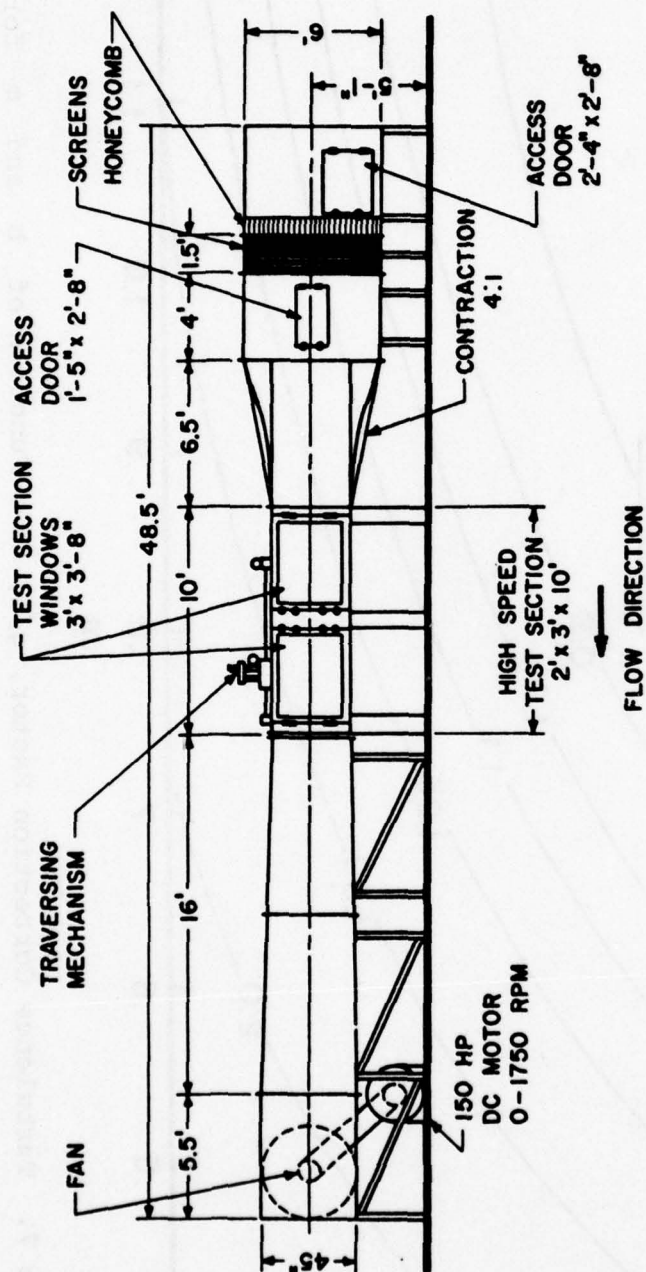


Figure 8. Side-View Schematic of High-Speed Test Section of Environmental Wind Tunnel

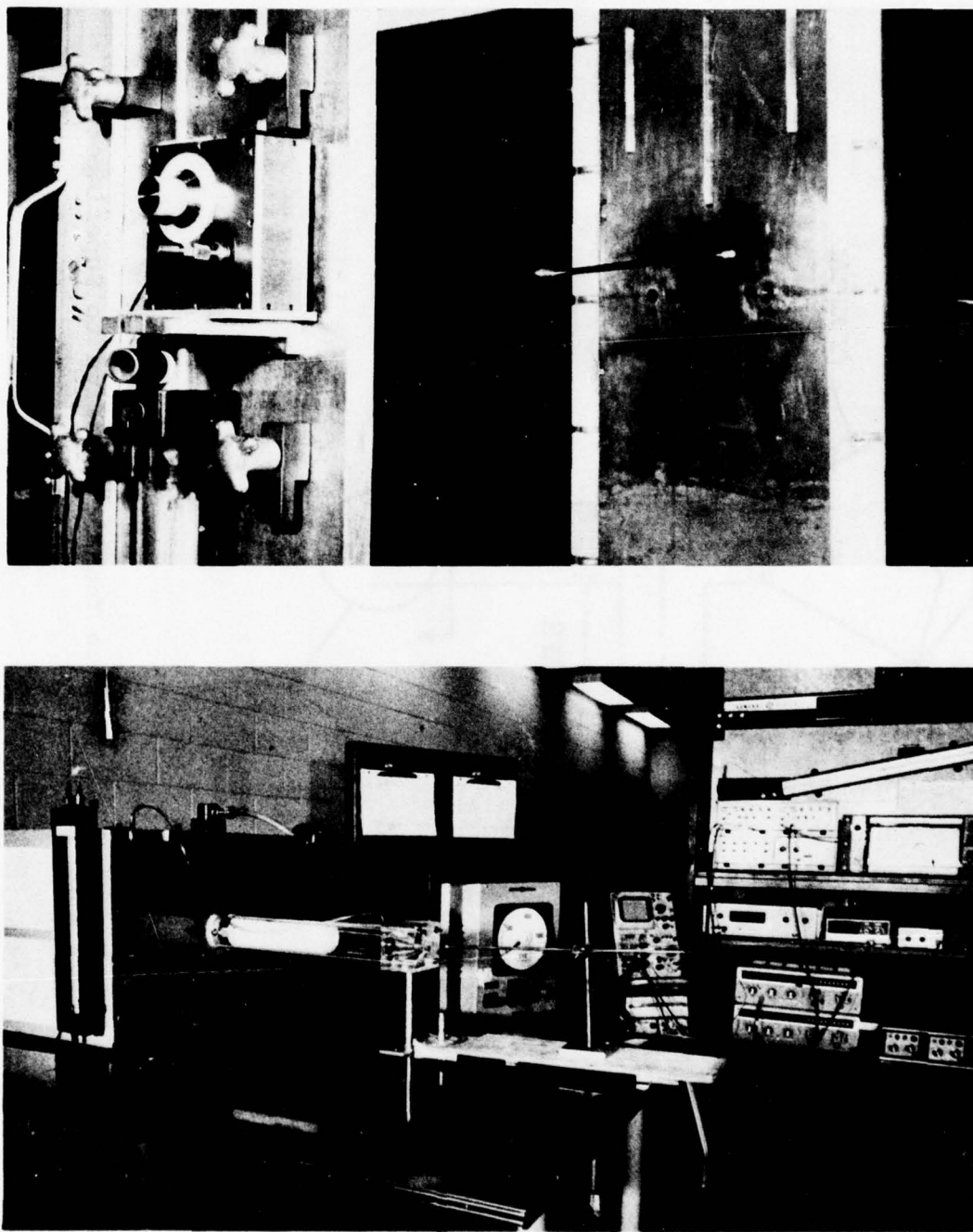


Figure 9. Outside View of Wind Tunnel Test Section Showing Single-Sensor Probe Mounted in Angularity Chuck, and Photograph of Calibration Tunnel with Probe in Position for Calibration Along with Instrumentation for Mean Yaw Calibration

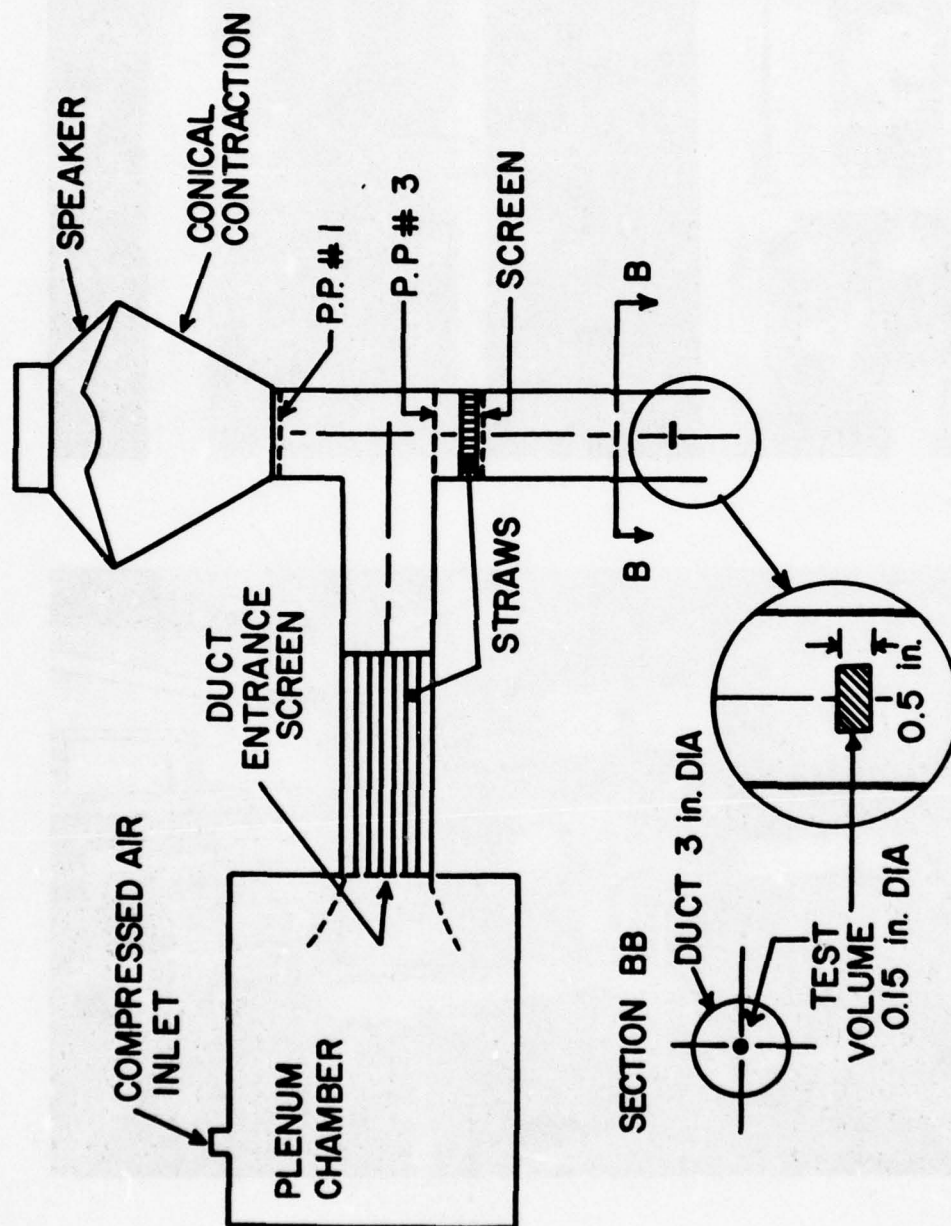


Figure 10. Top-View Schematic of Calibration Tunnel, Modified to Superimpose Periodic Fluctuations of Mean Free-Stream

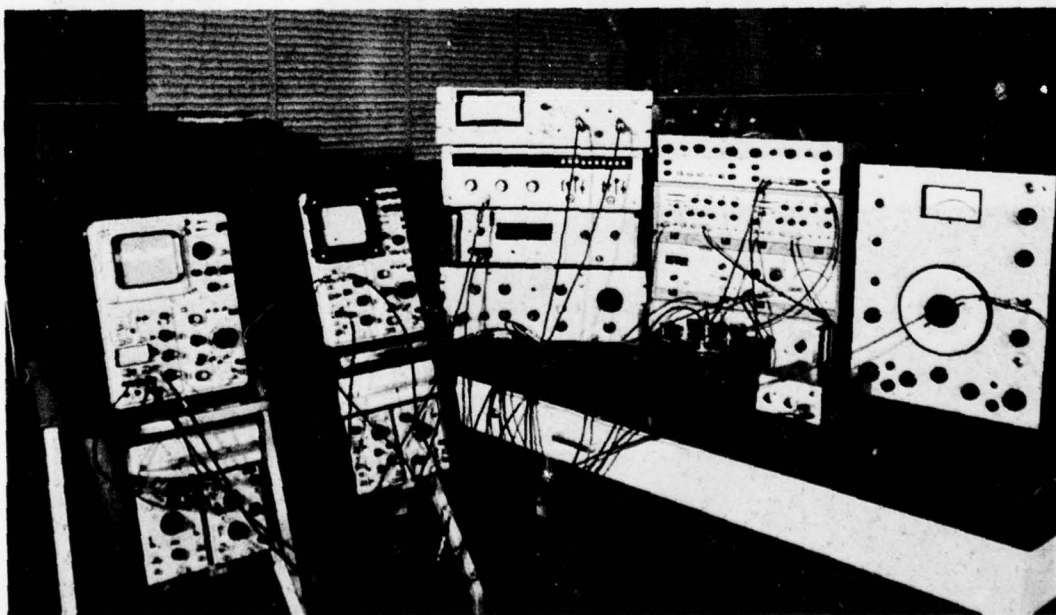
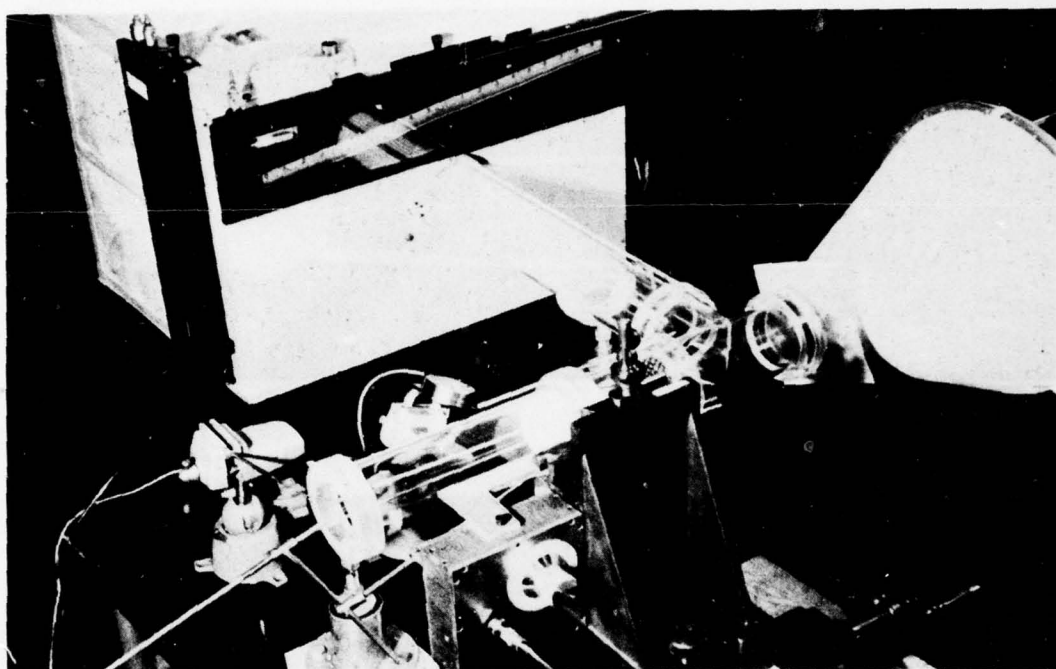


Figure 11. Photographs of Calibration Tunnel, Modified to Produce Streamwise Periodic Fluctuations, with Single Sensor Probe Mounted in Angularity Chuck, and Instrumentation for Unsteady Yaw Calibration

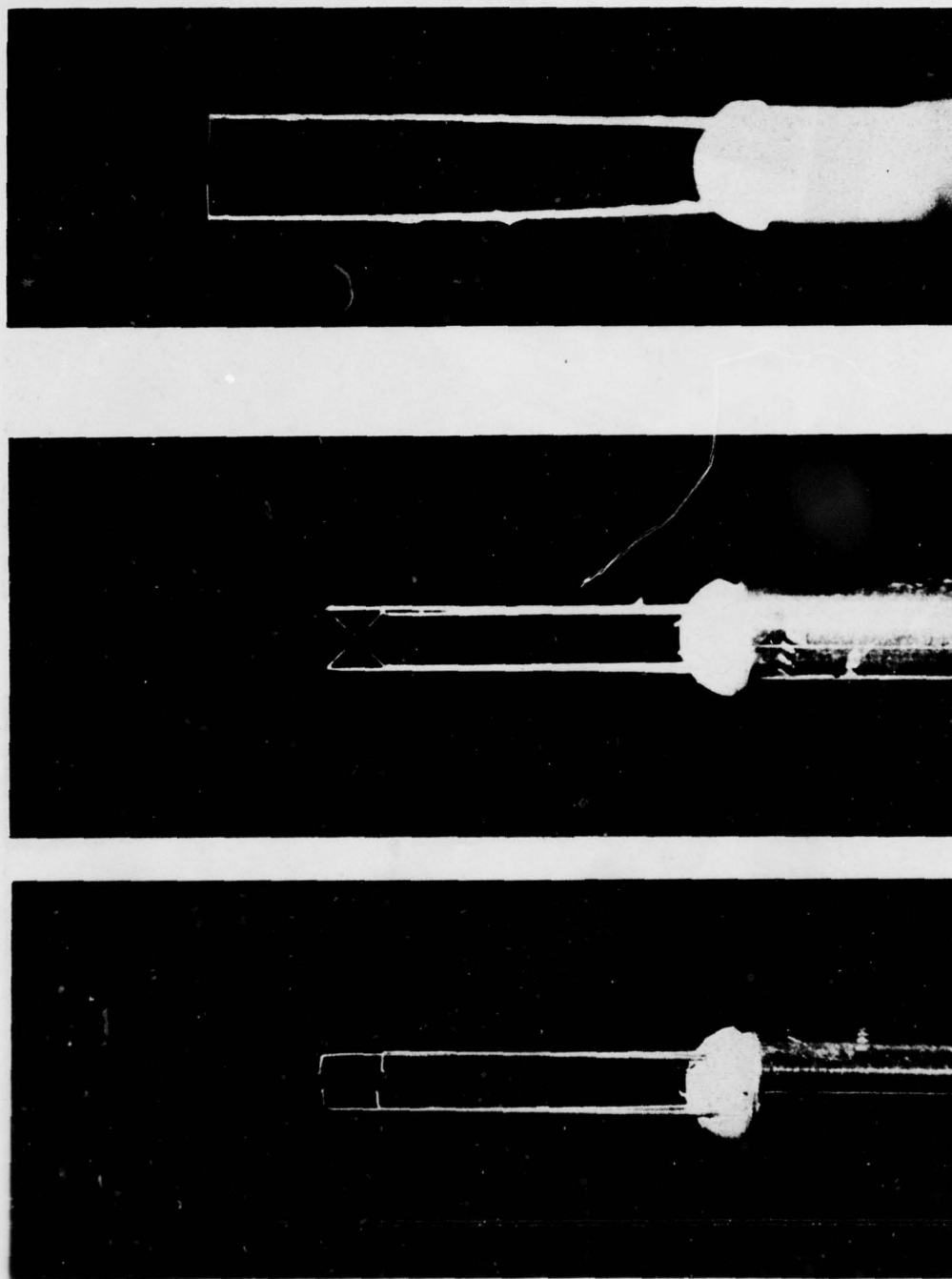


Figure 12. Photographs of Single-Sensor Probe, and
Side and Top Views of X-Probe; All Wires have $l/d=580$

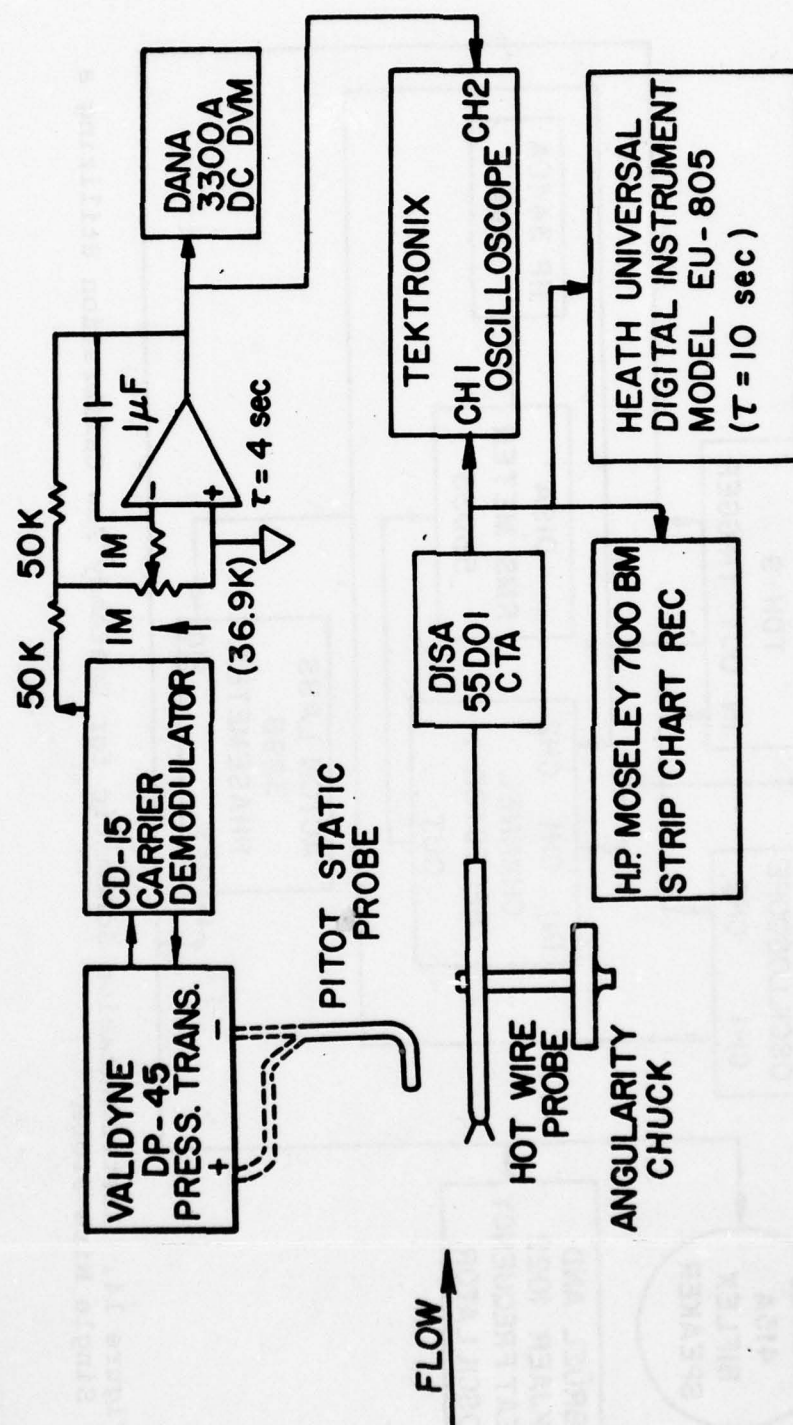


Figure 13. Instrumentation Schematic for Mean Velocity Yaw Calibration

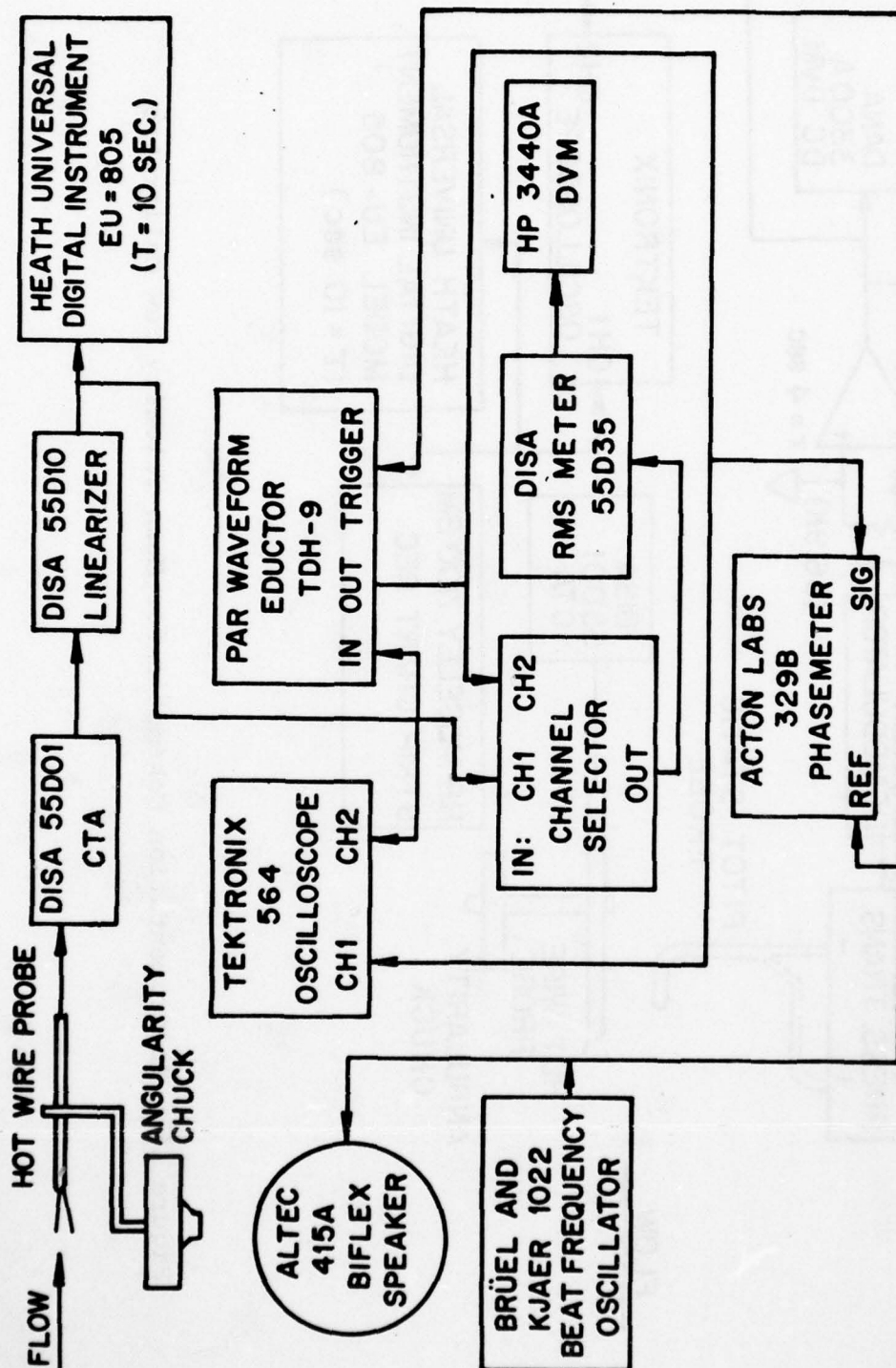


Figure 14. Instrumentation Schematic for Unsteady Yaw Calibration Utilizing a Single Wire Probe

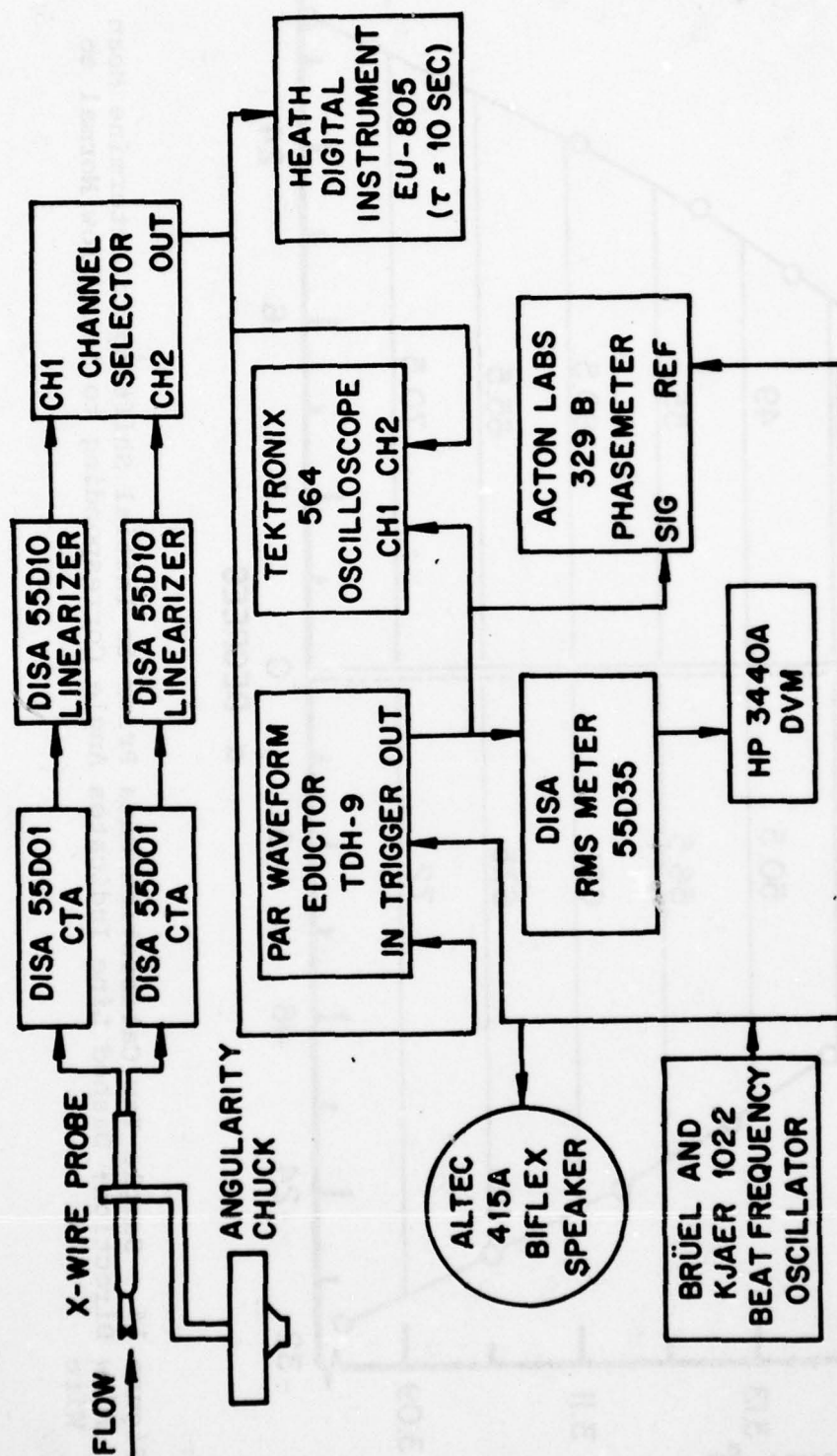


Figure 15. Instrumentation Schematic for Unsteady Yaw Calibration Utilizing an X-Wire Probe

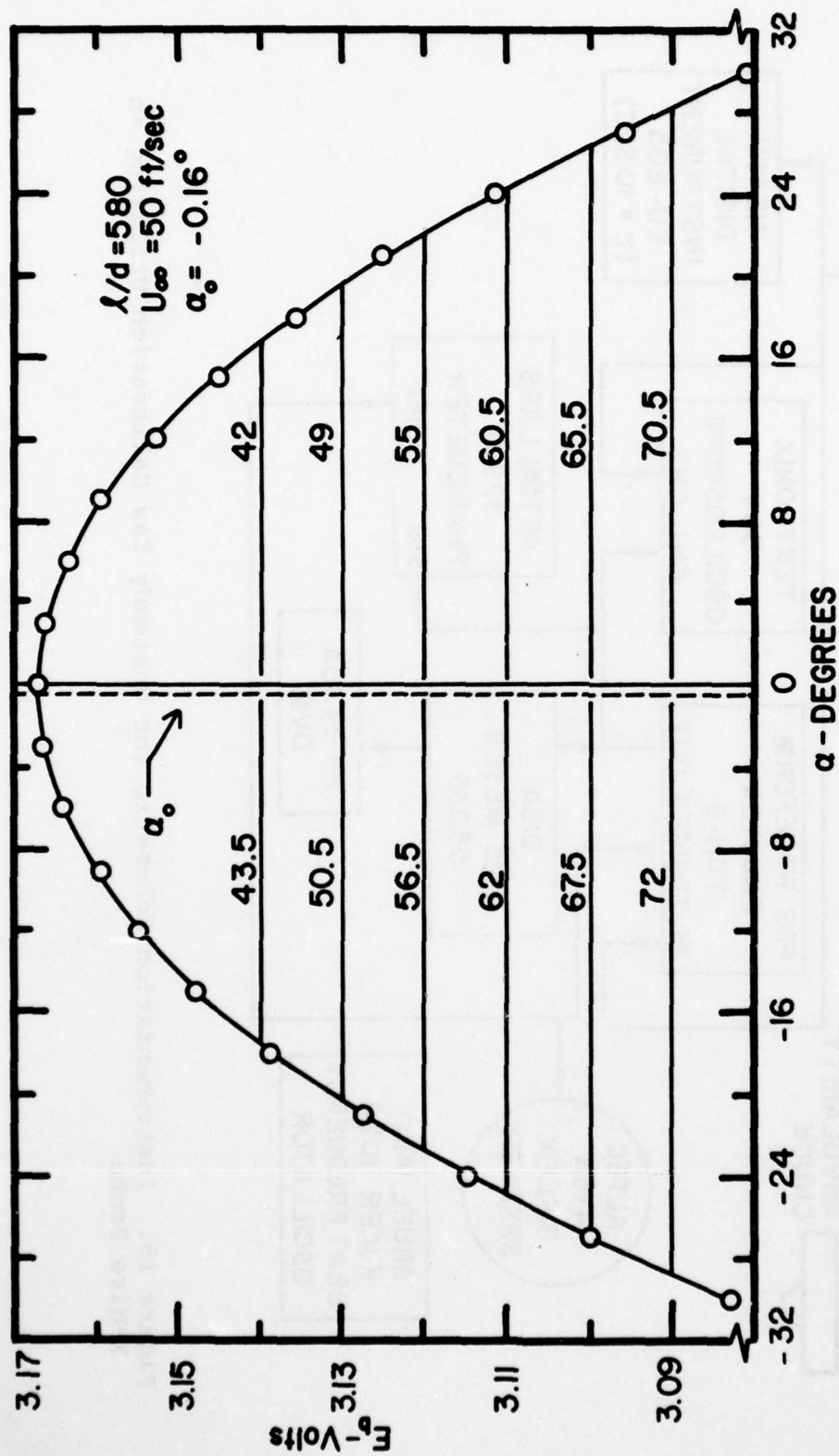


Figure 16. Sample Yaw Calibration Data Prior to Initial Shifting to Determine Mean Flow Direction; Dashed Line Indicates Angle Corresponding to Mean Flow Normal to Wire

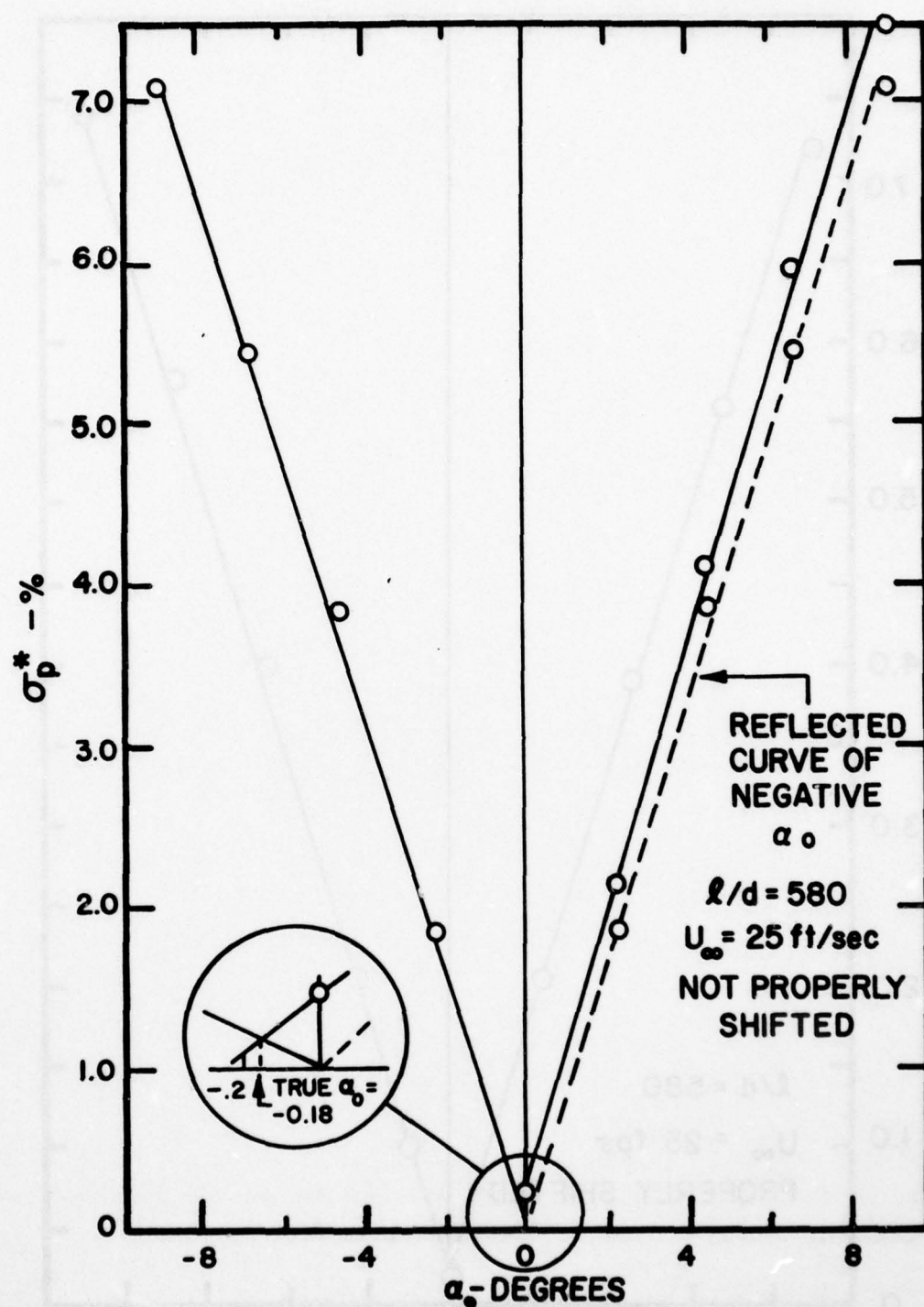


Figure 17. Typical Variation with Offset Angle of Standard Deviation, from Present Relation, of Mean Yaw Calibration Data Indicating that Initially Shifted Data is Not Properly Centered

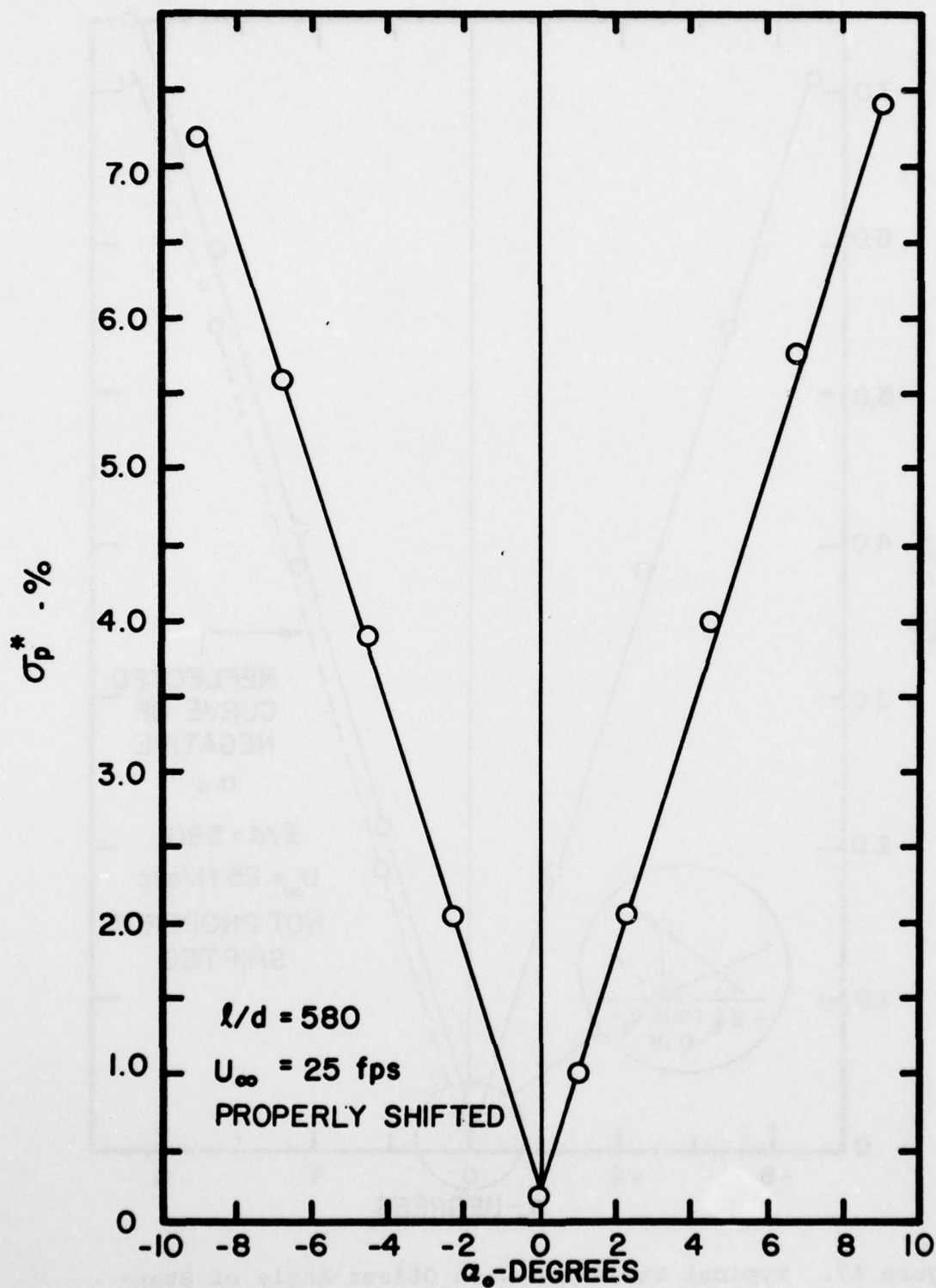


Figure 18. Typical Variation with Offset Angle of Standard Deviation, from Present Relation, of Mean Yaw Calibration Data for Properly Shifted Data

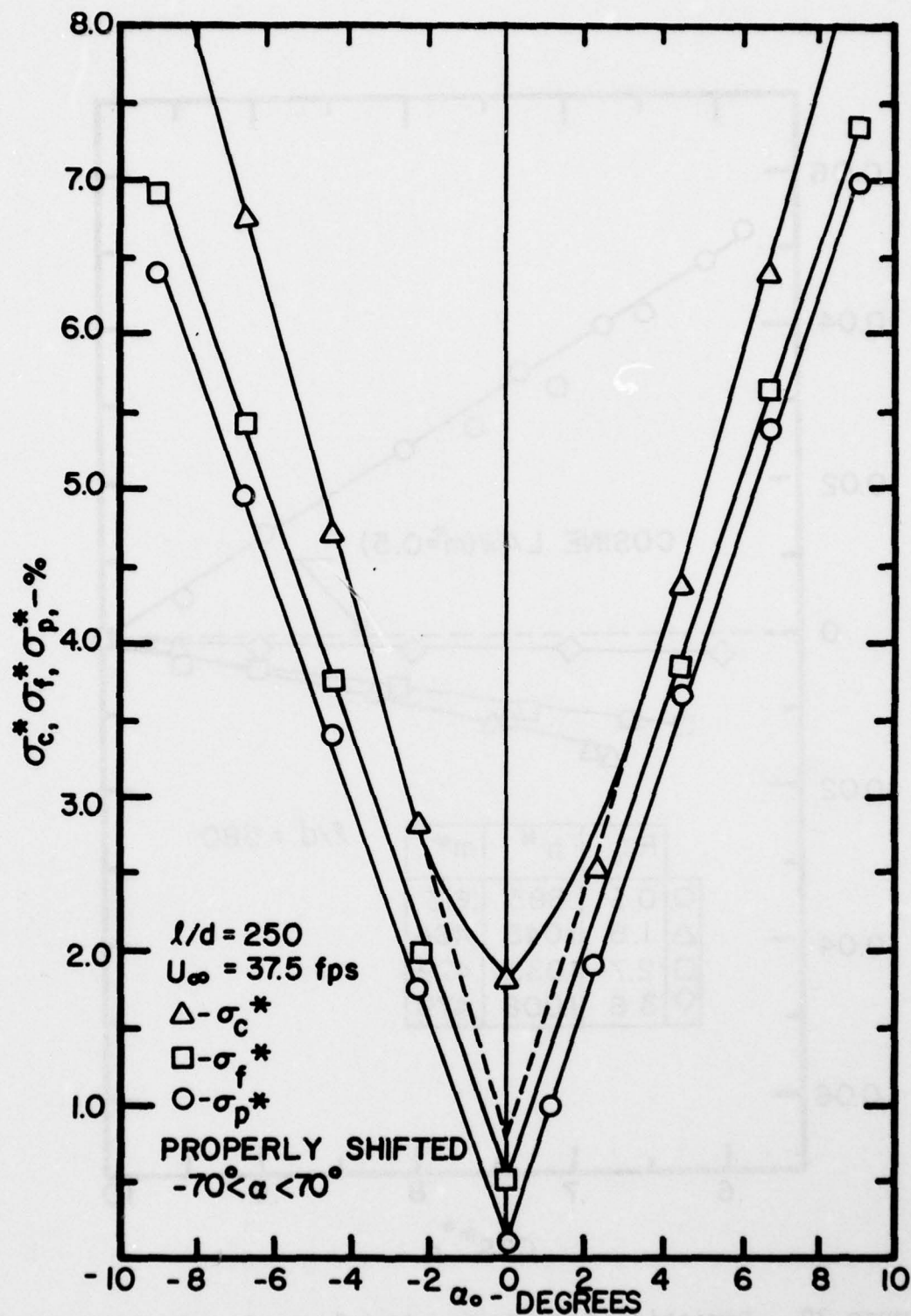


Figure 19. Typical Variation of Standard Deviation of Mean Yaw Calibration Data with Probe Misalignment Using Three Different Yaw Relations

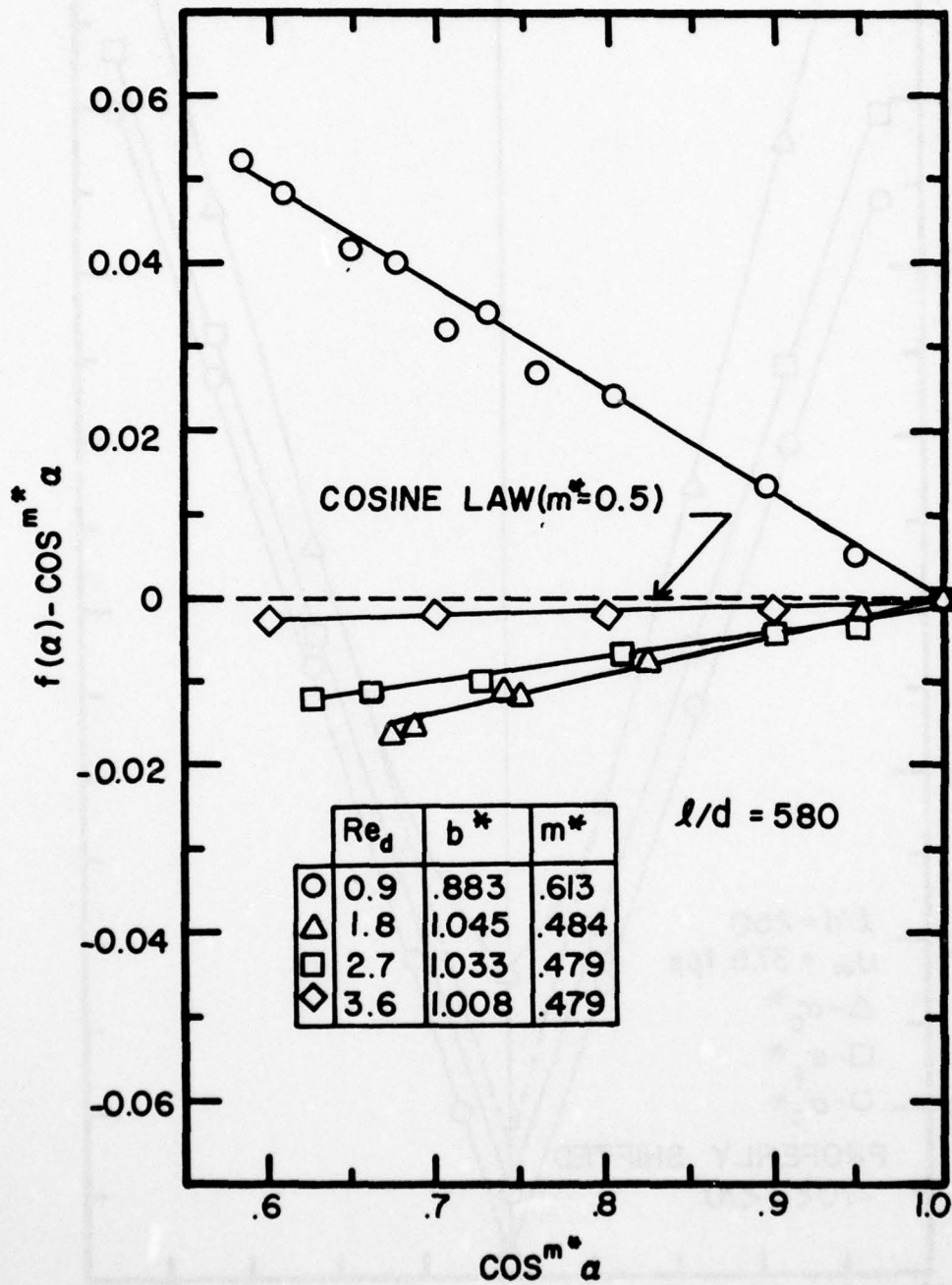


Figure 20. Deviation from Cosine Law for a Standard-length Single Wire Probe; $\ell/d=580$

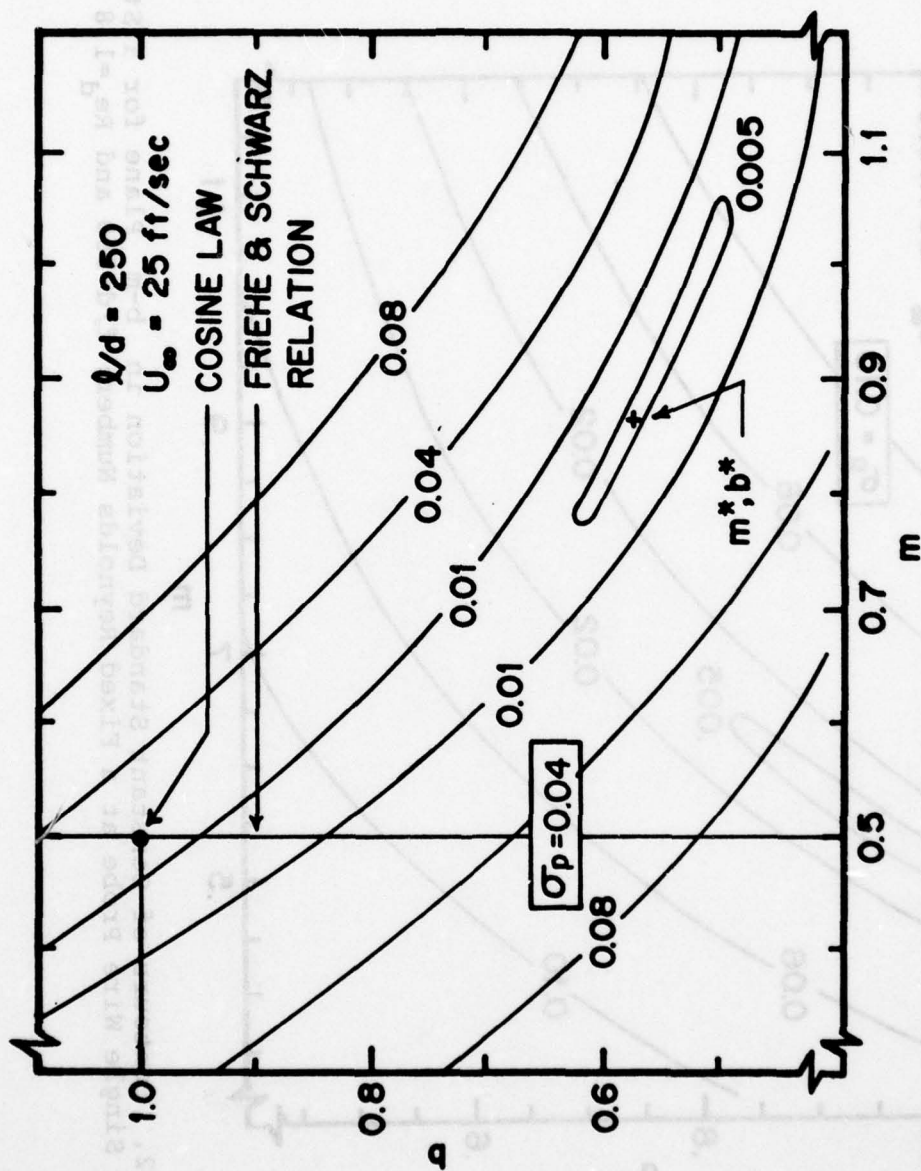


Figure 21. Contours of Constant Standard Deviation in b - m Plane for a Single Wire Probe at a Fixed Reynolds Number; $l/d=250$ and $Re_d=1.8$

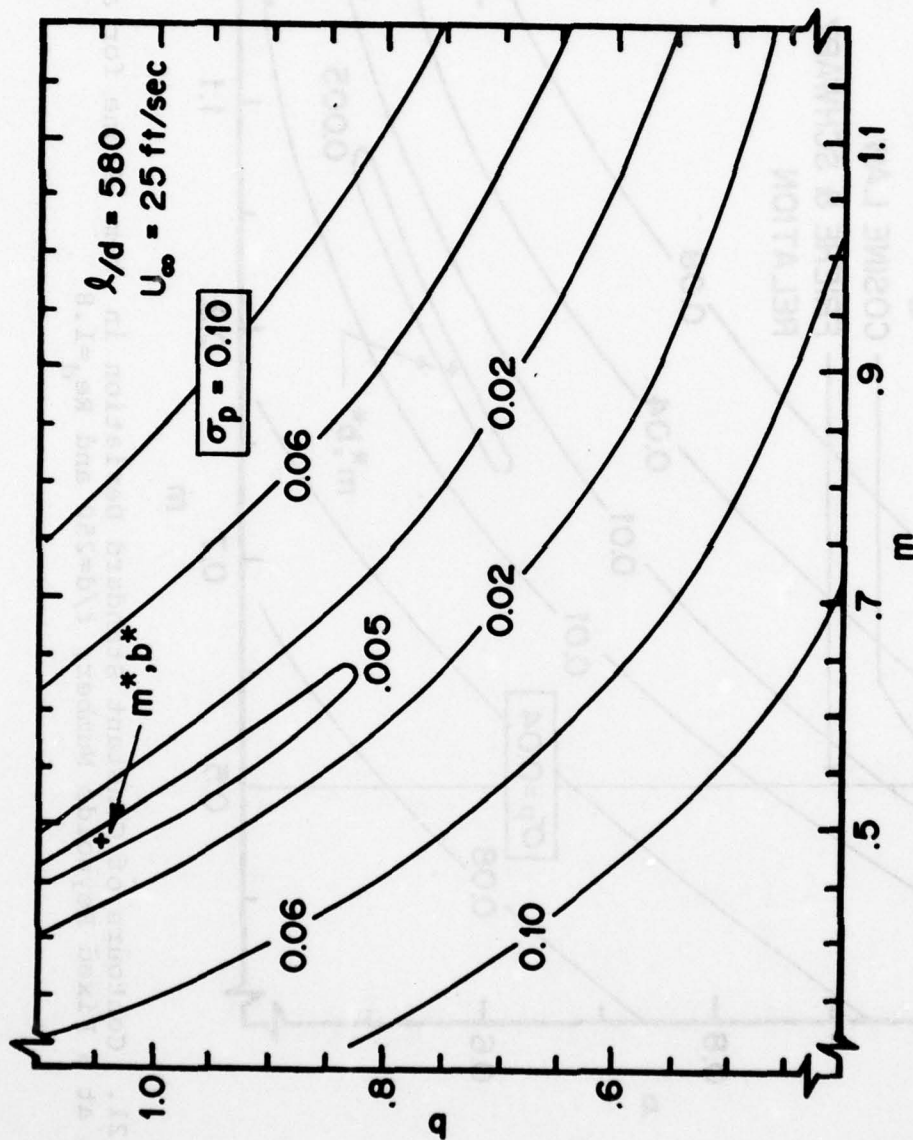


Figure 22. Contours of Constant Standard Deviation in b - m Plane for a Standard-length Single Wire Probe at a Fixed Reynolds Number; $l/d=580$ and $Re_d=1.8$

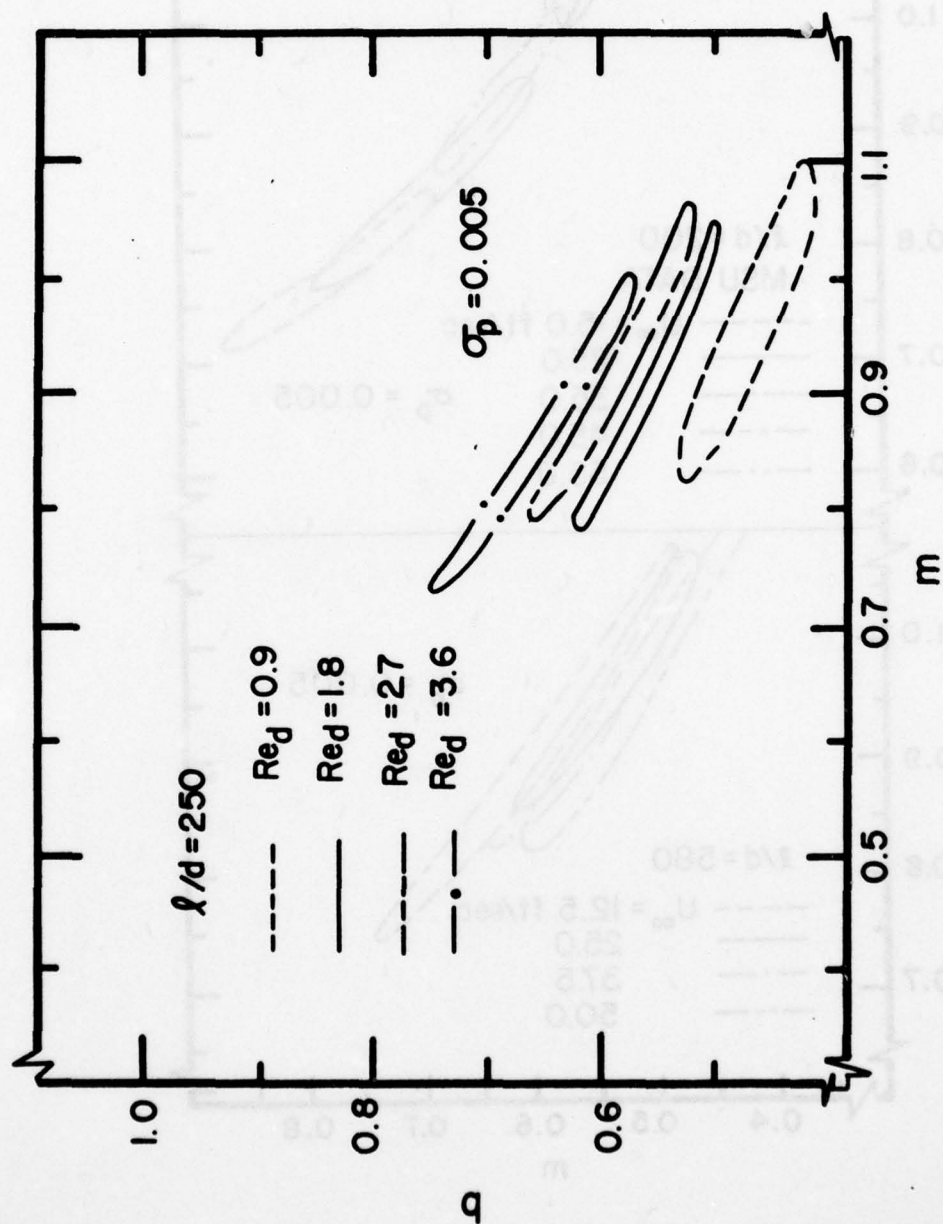


Figure 23. Variation with Reynolds Number of Region of a Minimum Standard Deviation in b - m Plane for a Single Wire Probe; $l/d=250$

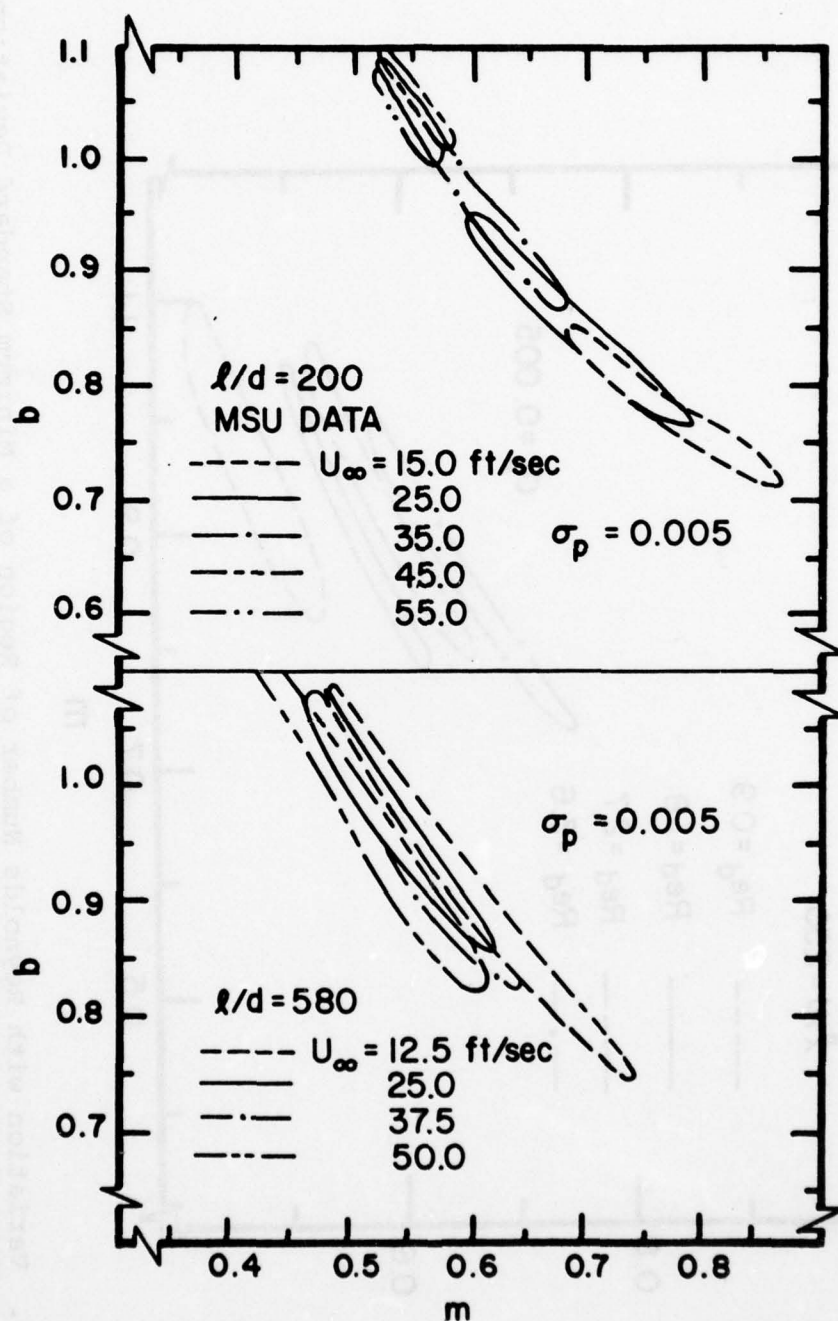


Figure 24. Variation with Free Stream Velocity of Region of Minimum Standard Deviation for X-Wire Data from MSU and a Standard-length Single Wire Probe

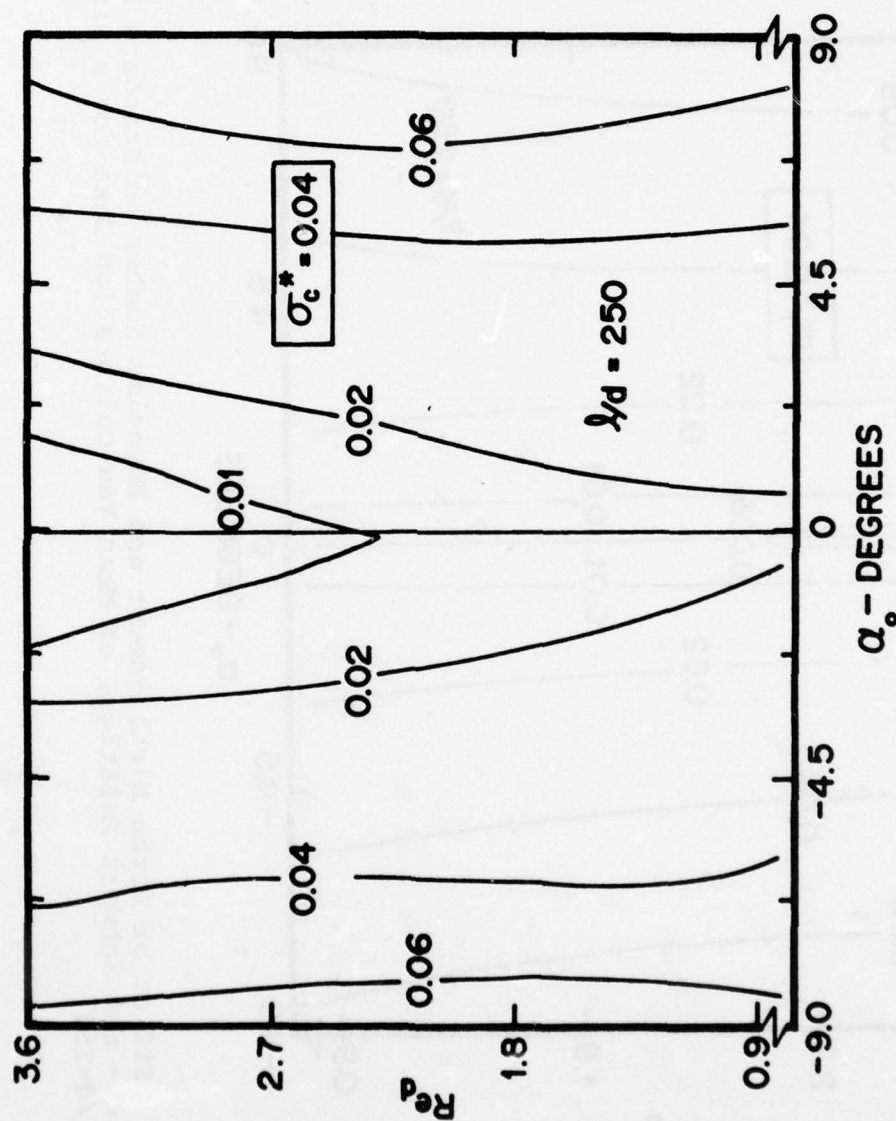


Figure 25. Effect of Probe Misalignment and Reynolds Number on Standard Deviation, from Cosine Law, of Mean Yaw Calibration Data for a Single Wire Probe; $l/d=250$

AD-A055 937

ILLINOIS INST OF TECH CHICAGO DEPT OF MECHANICS MECH--ETC F/G 14/2
ON TEMPERATURE AND YAW DEPENDENCE OF HOT-WIRES.(U)

AUG 77 R E DRUBKA, H M NAGIB, J TAN-ATICHAT F44620-76-C-0062

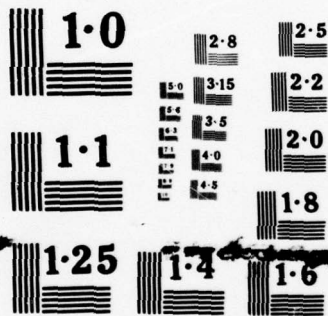
UNCLASSIFIED

IIT-FLUIDS/HEAT TRANS-R77 ARO-12290.9-E

NL

3 OF 3
ADA
065937





NATIONAL BUREAU OF STANDARDS
MICROCOPY RESOLUTION TEST CHART

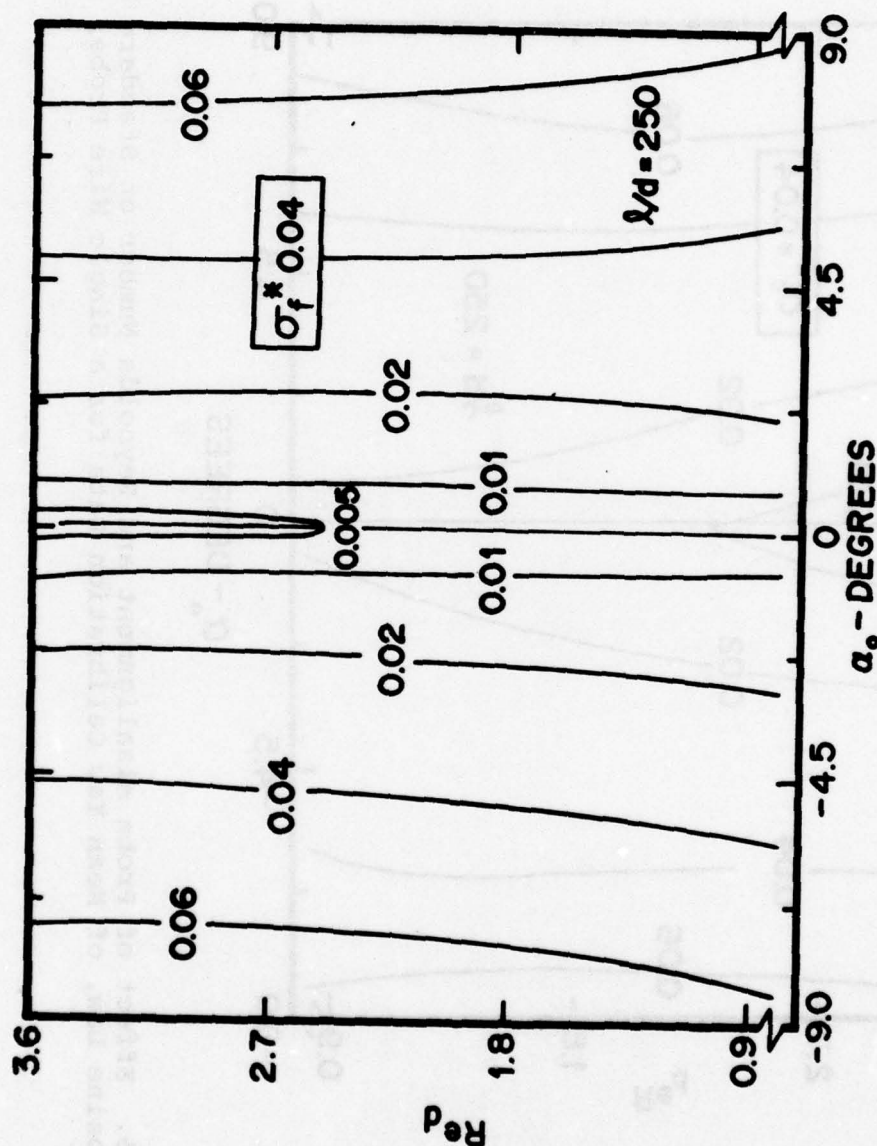


Figure 26. Effect of Probe Misalignment and Reynolds Number on Standard Deviation, from Friehe and Schwarz Relation, of Mean Yaw Calibration Data for a Single Wire Probe; $l/d=250$

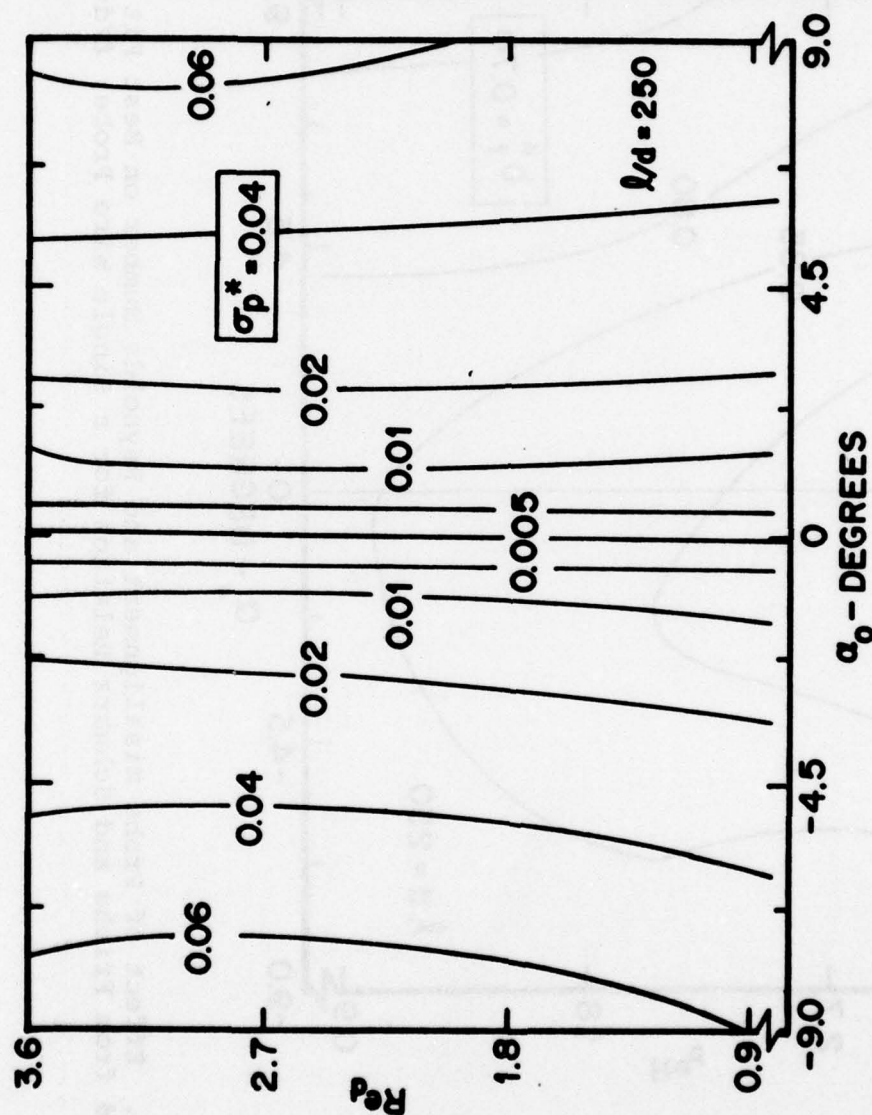


Figure 27. Effect of Probe Misalignment and Reynolds Number on Standard Deviation, from Present Relation, of Mean Yaw Calibration Data for a Single Wire Probe; $l/d=250$

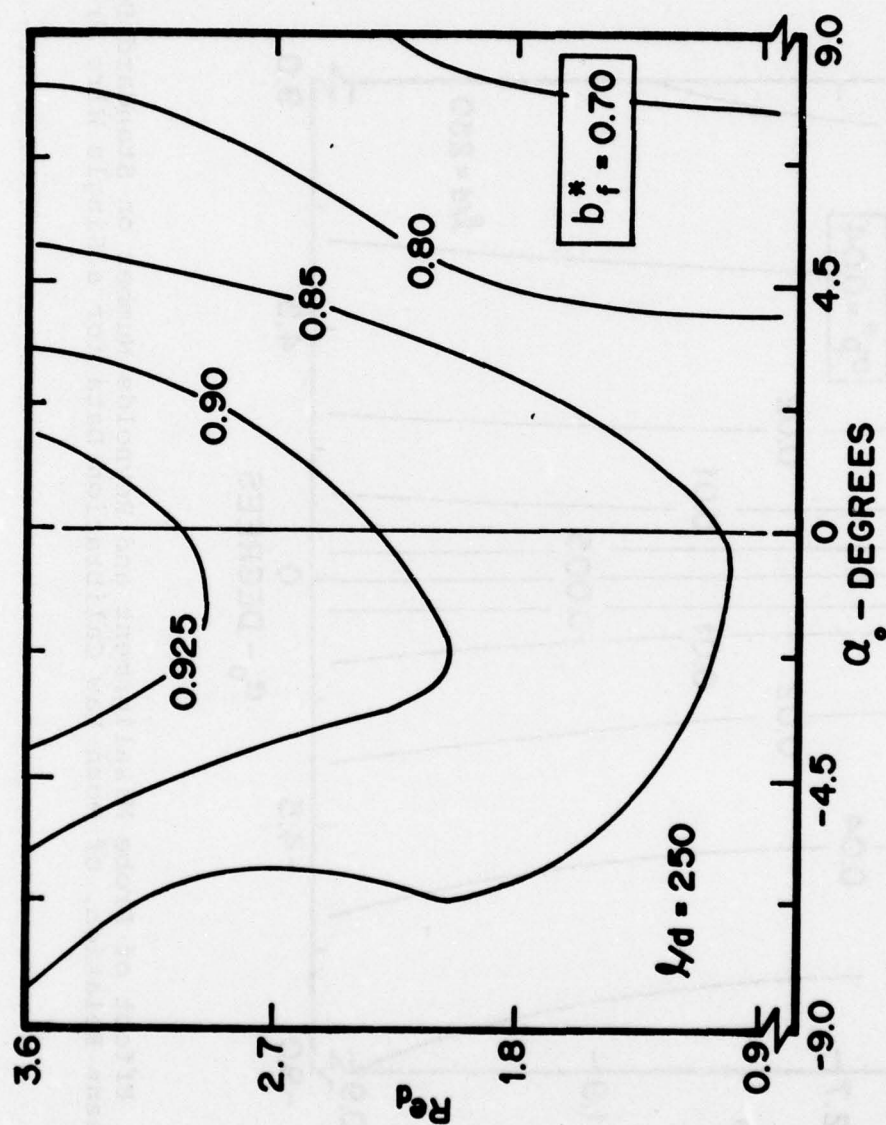


Figure 28. Effect of Probe Misalignment and Reynolds Number on Best Fit Coefficient Determined from Friehe and Schwarz Relation for a Single Wire Probe; $\lambda/d=250$

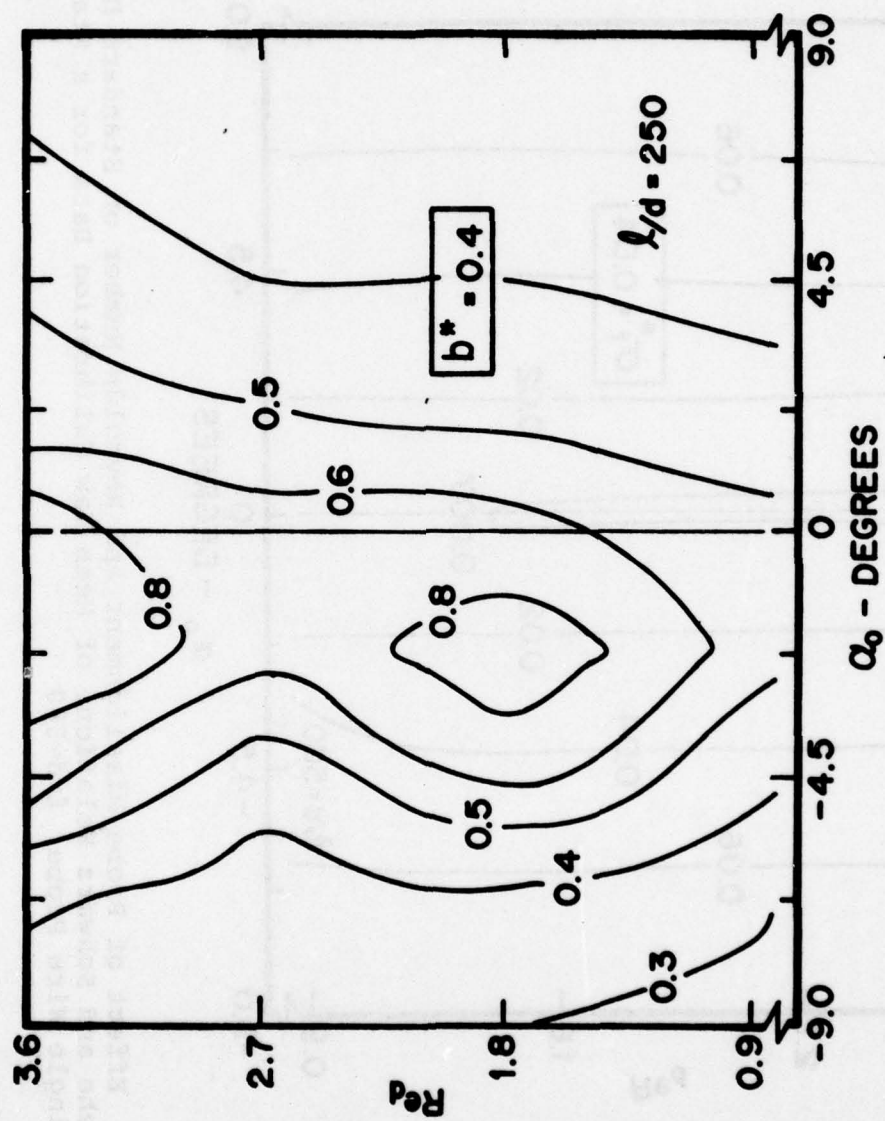


Figure 29. Effect of Probe Misalignment and Reynolds Number on Best Fit Coefficient Determined from Present Relation for a Single Wire Probe; $l/d=250$

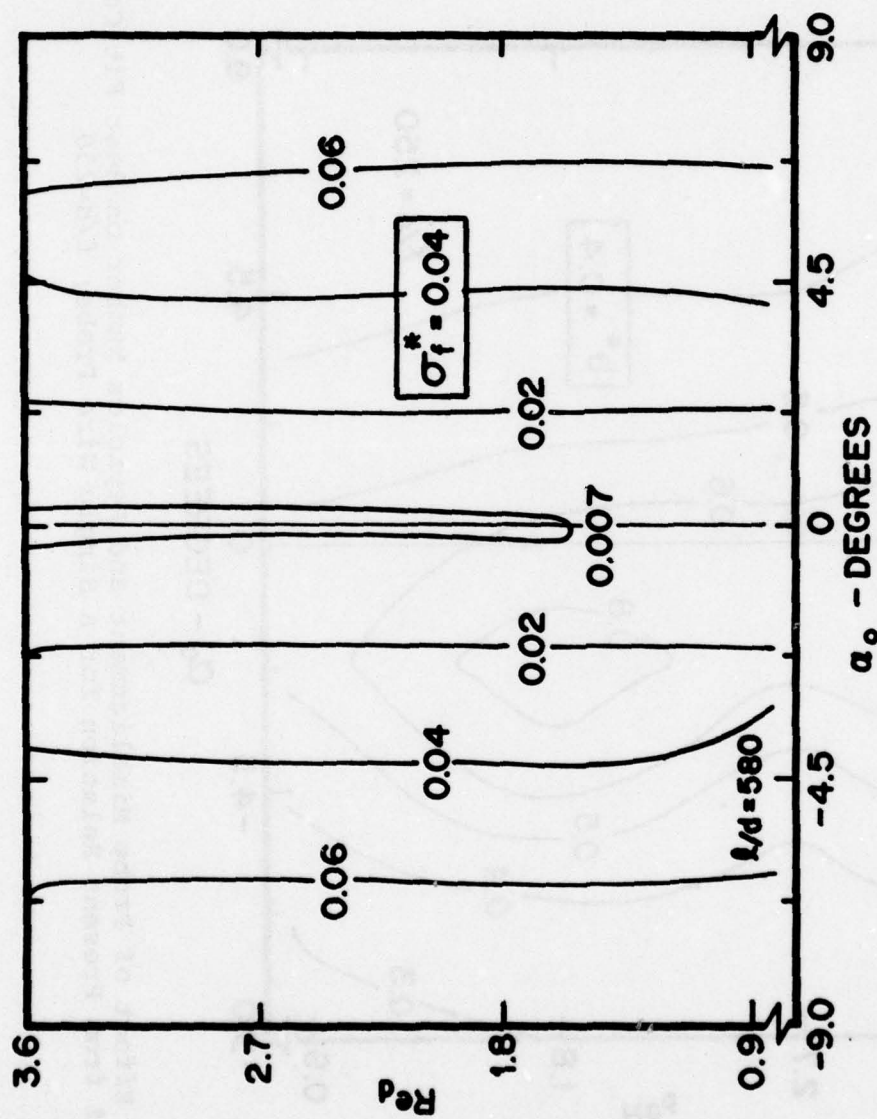


Figure 30. Effect of Probe Misalignment and Reynolds Number on Standard Deviation, from Friehe and Schwarz Relation, of Mean Yaw Calibration Data for a Standard-length Single Wire Probe; $l/d=580$

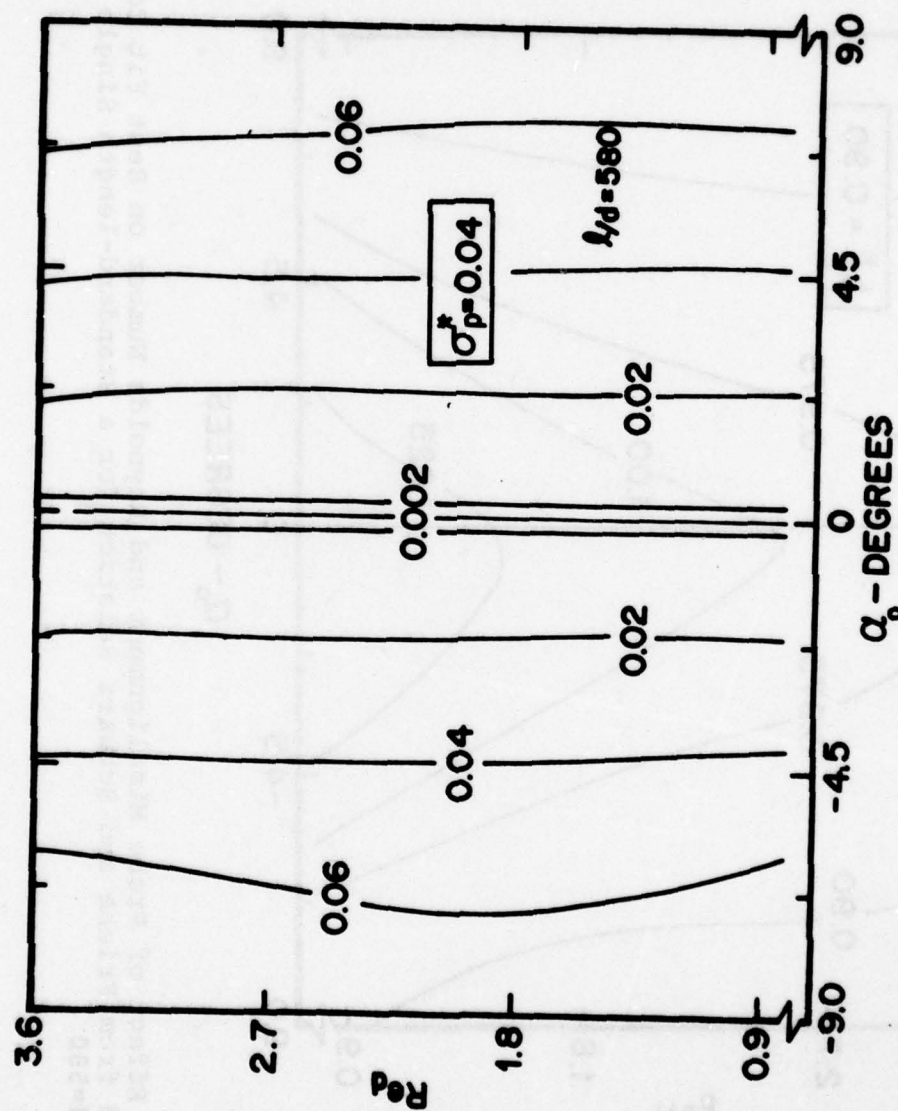


Figure 31. Effect of Probe Misalignment and Reynolds Number on Standard Deviation, from Present Relation, of Mean Yaw Calibration Data for a Standard-length Single Wire Probe; $l/d=580$

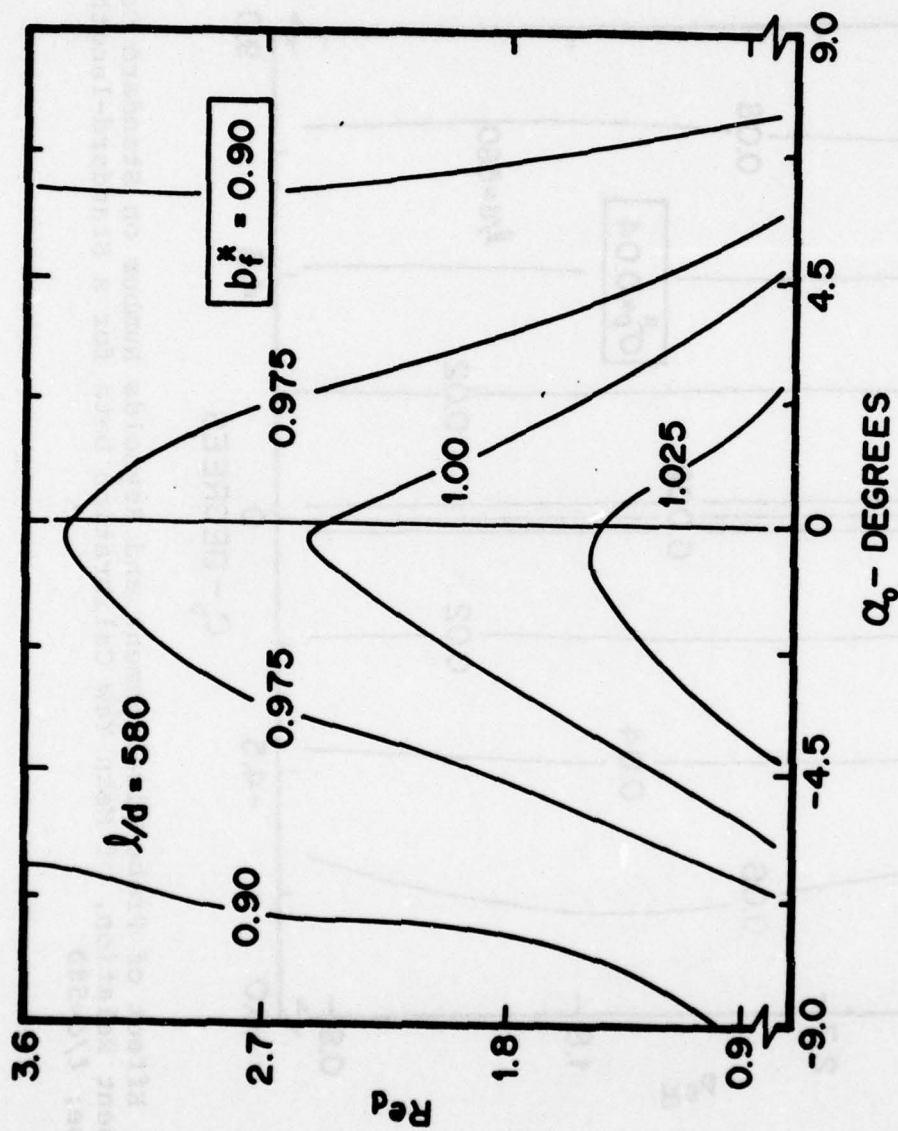


Figure 32. Effect of Probe Misalignment and Reynolds Number on Best Fit Coefficient Determined from Friehe and Schwarz Relation for a Standard-length Single Wire Probe; $l/d=580$

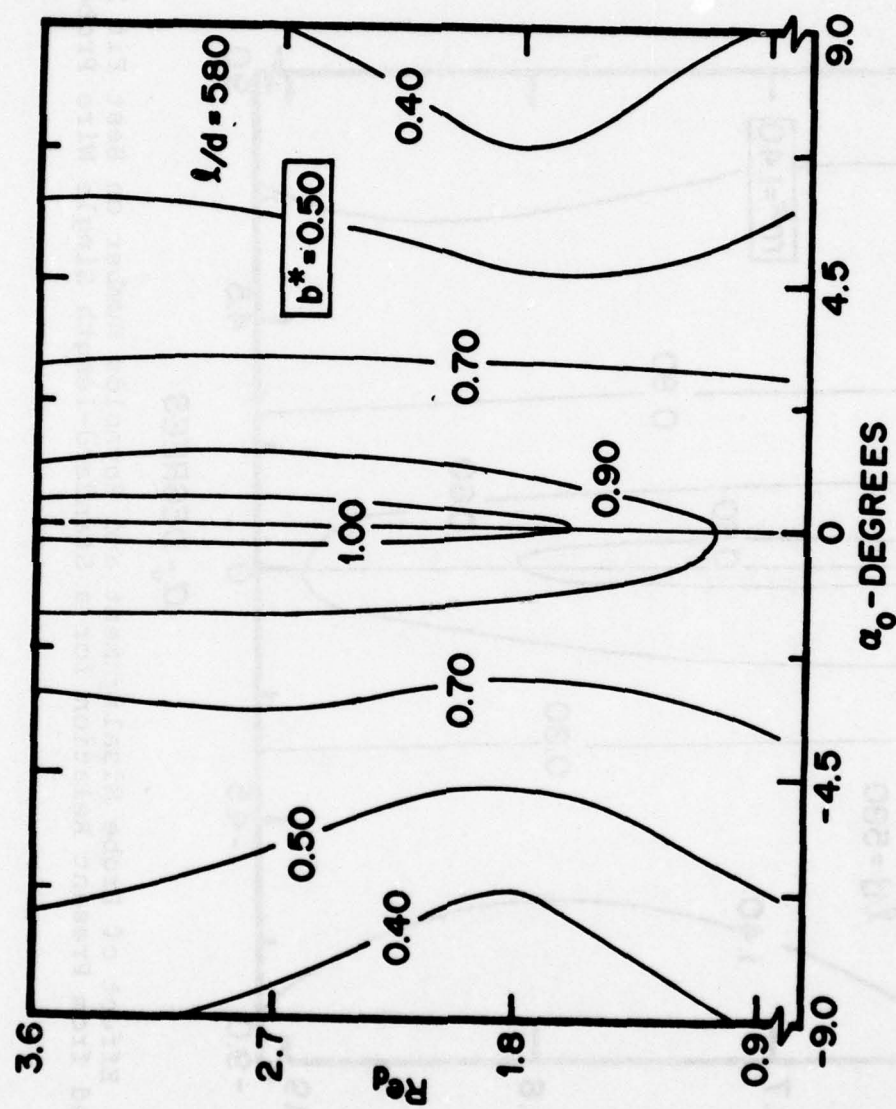


Figure 33. Effect of Probe Misalignment and Reynolds Number on Best Fit Coefficient Determined from Present Relation for a Standard-length Single Wire Probe; $l/d=580$

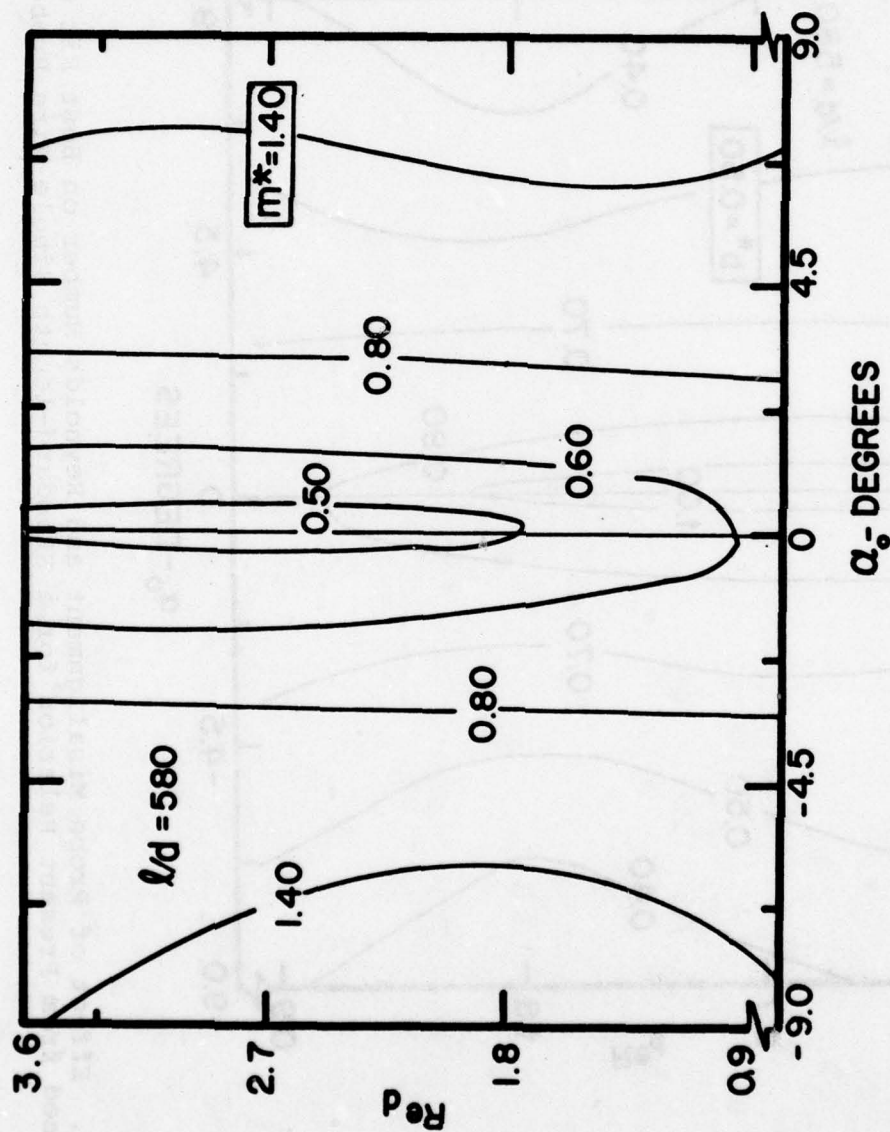


Figure 34. Effect of Probe Misalignment and Reynolds Number on Best Fit Exponent Determined from Present Relation for a Standard-length Single Wire Probe; $l/d=580$

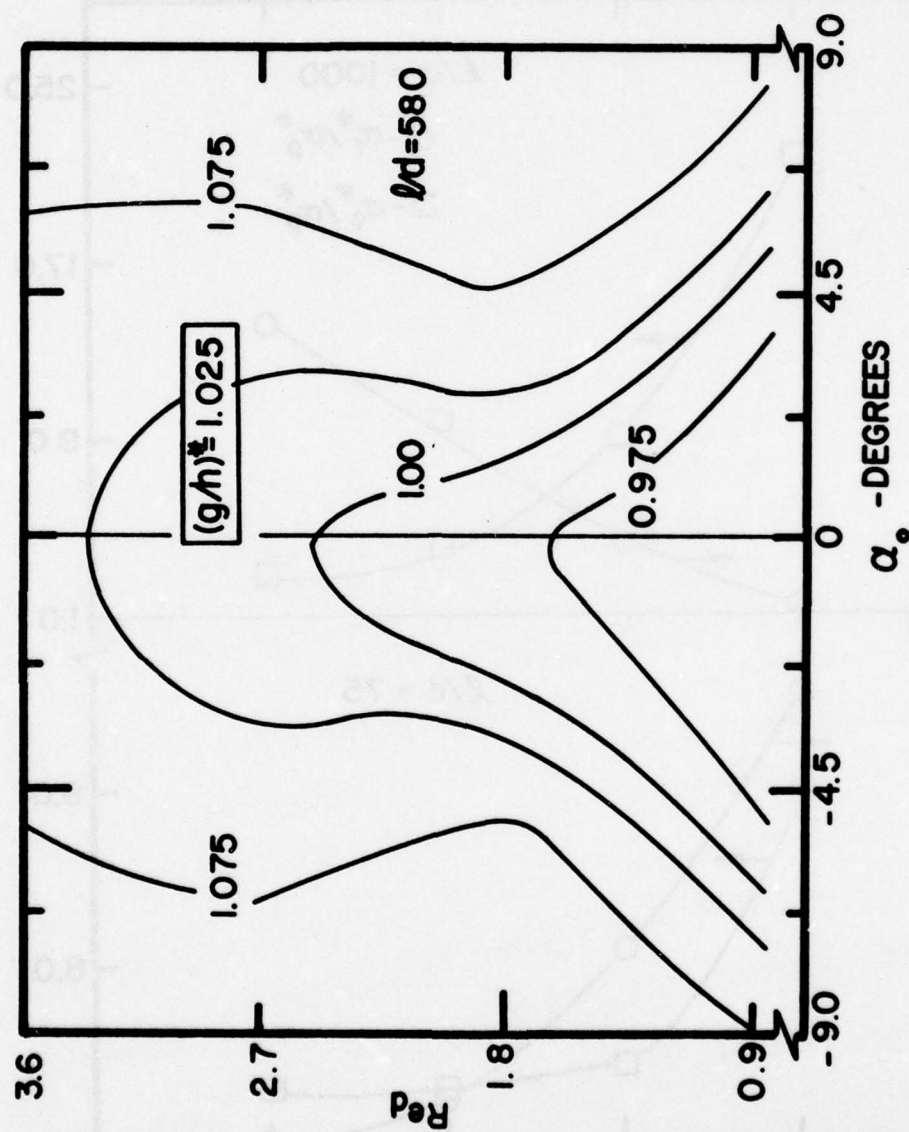


Figure 35. Effect of Probe Misalignment and Reynolds Number on Turbulence Correction Factor Determined from Present Relation for a Standard-length Single Wire Probe; $l/d=580$

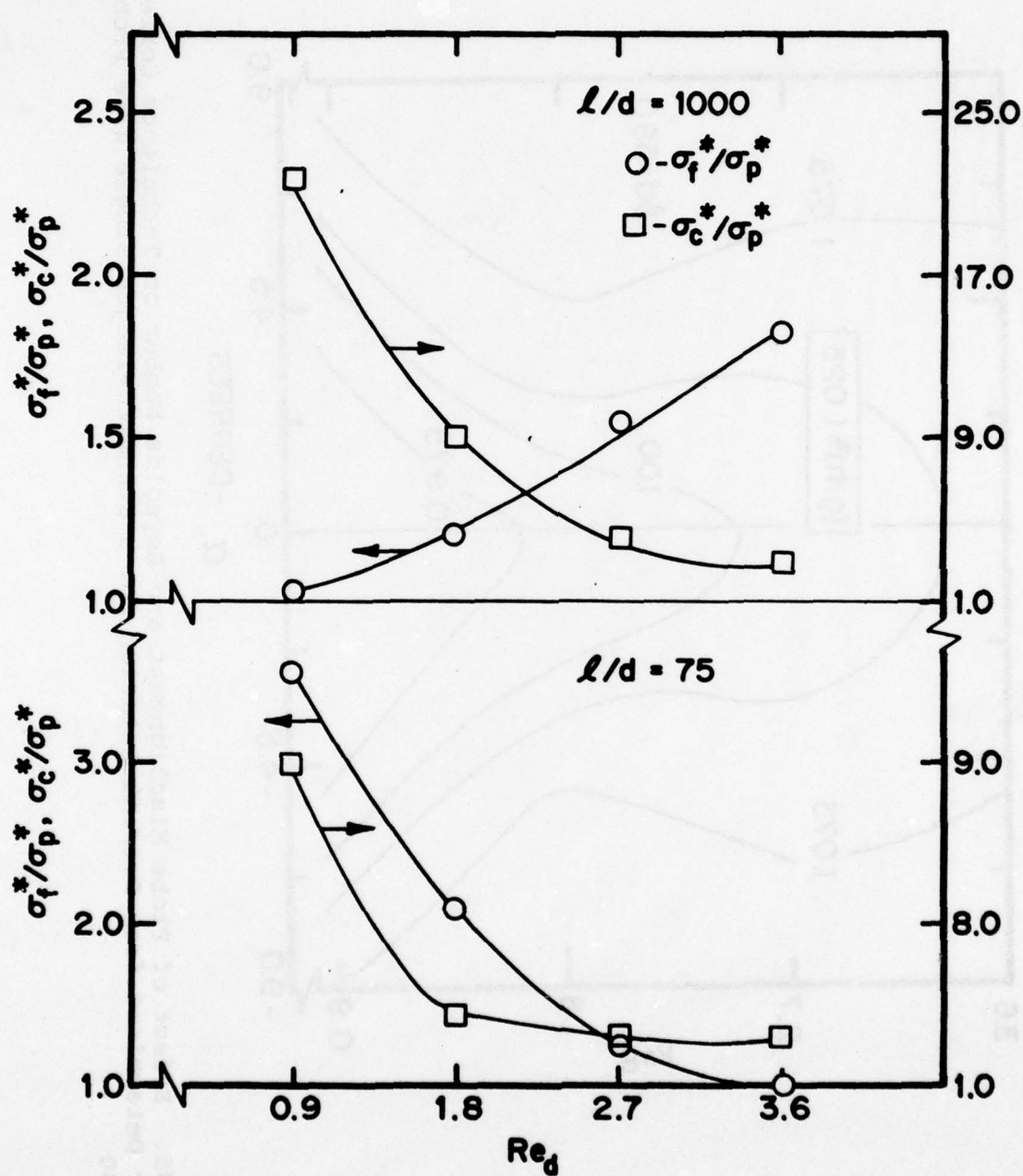


Figure 36. Effect of Reynolds Number on Ratio of Standard Deviation Improvement Between Cosine, Friehe and Schwarz and Present Relations for $l/d=75$ and 1000

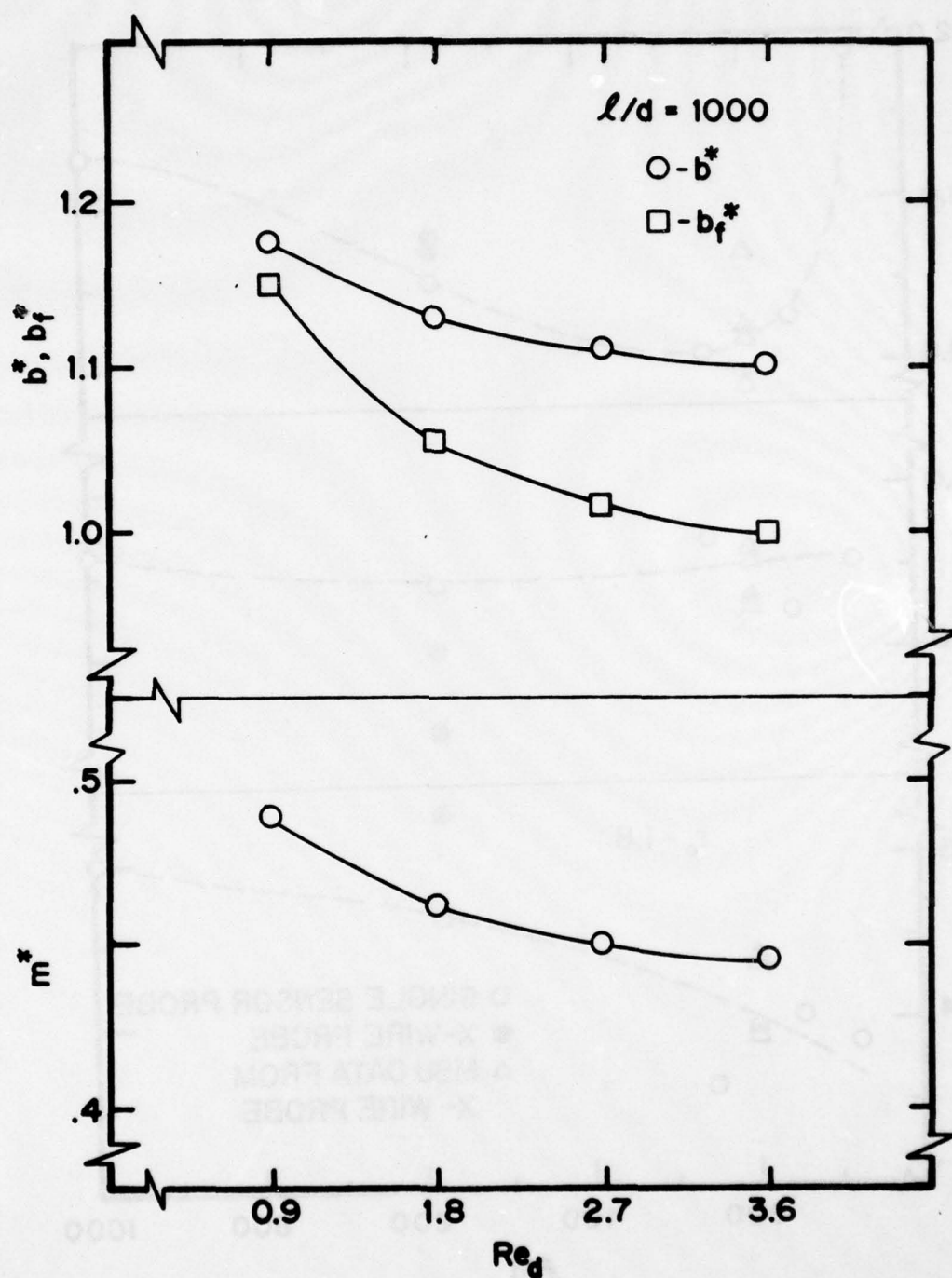


Figure 37. Variation with Reynolds Number of Best Fit Coefficients Determined from Friehe and Schwarz and Present Relations for $l/d=1000$

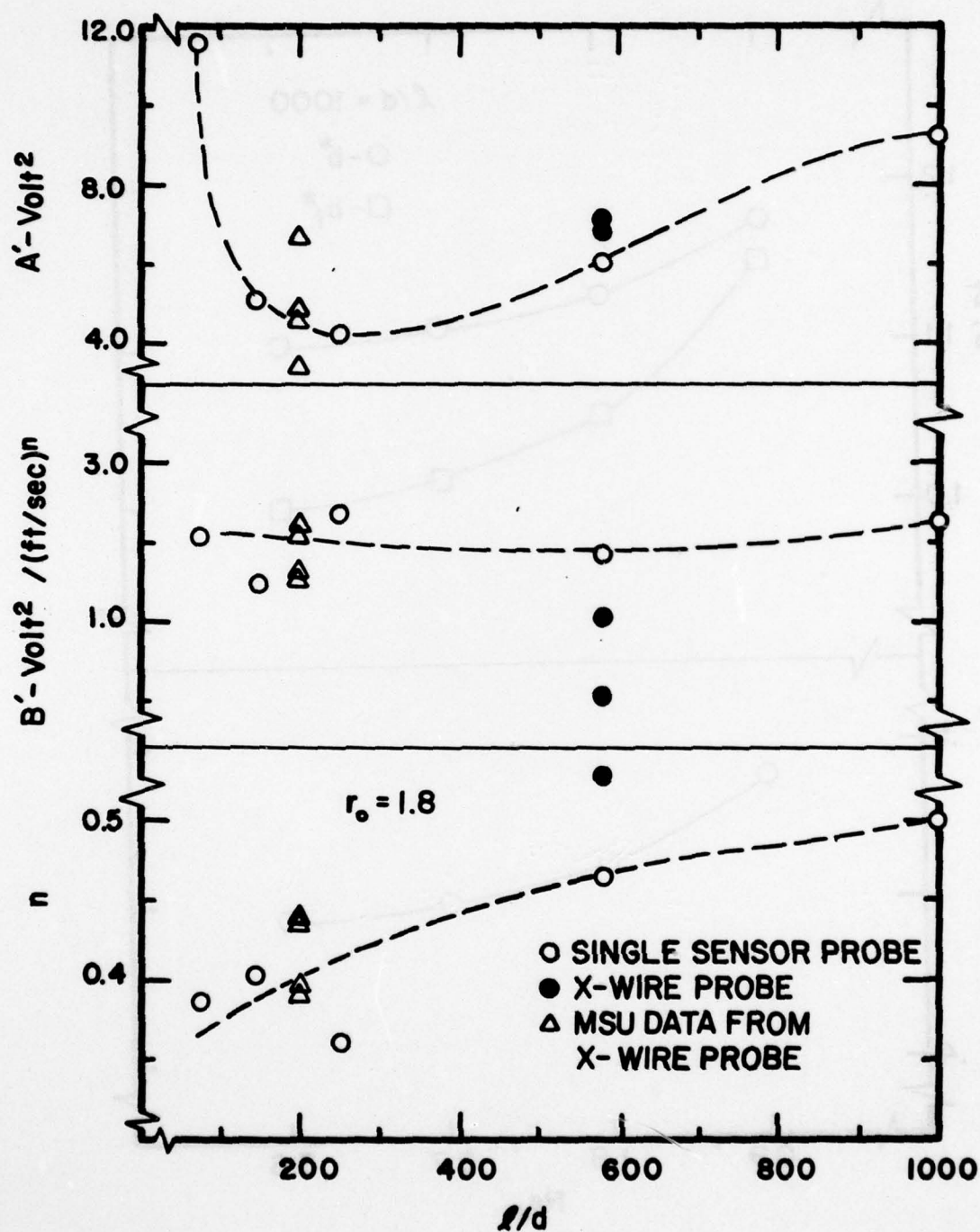


Figure 38. Variation of Hot-Wire Velocity Calibration Constants with l/d

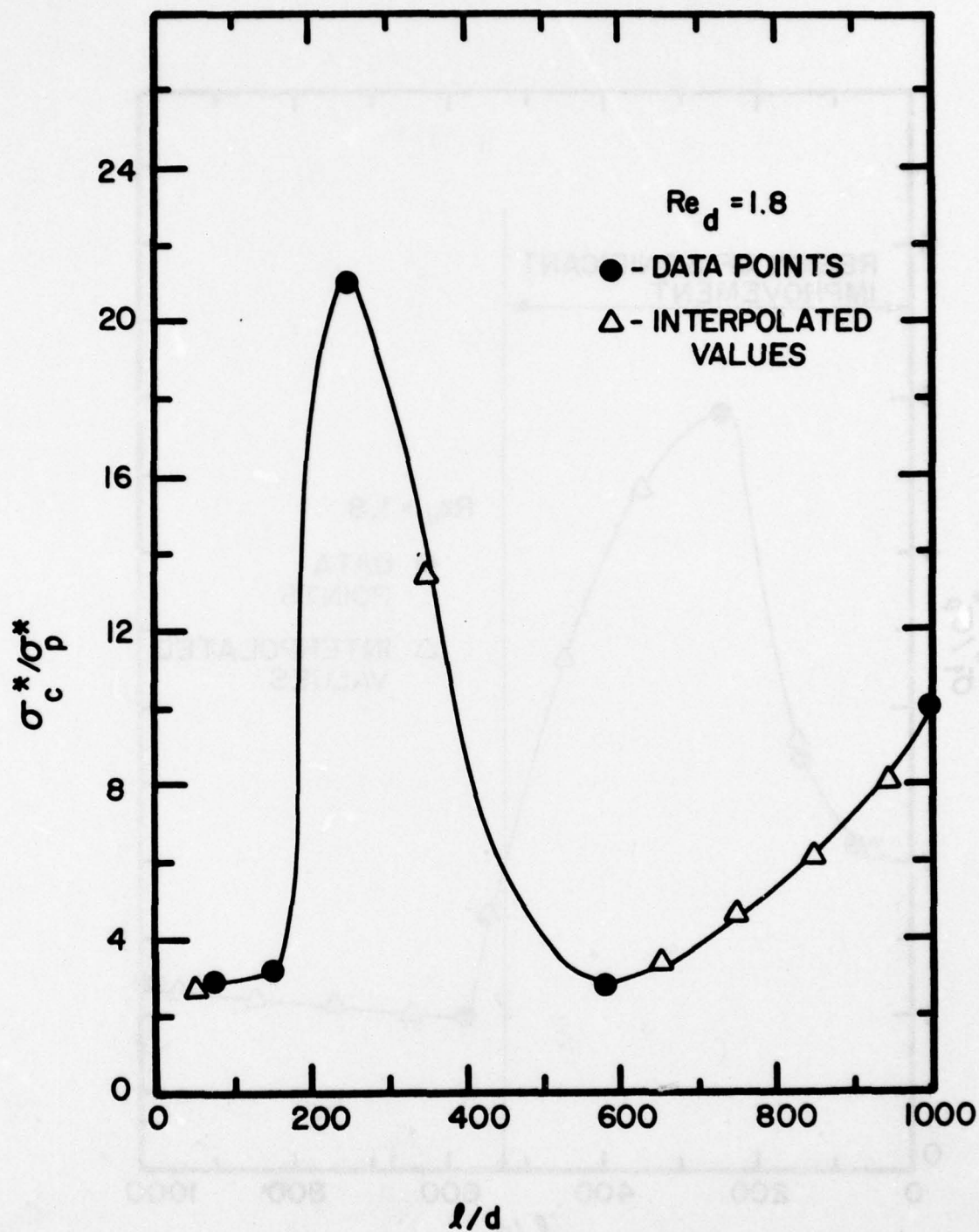


Figure 39. Variation of Ratio of Standard Deviation Improvement Between Cosine and Present Relations with Sensor l/d at a Fixed Reynolds Number; $Re_d = 1.8$

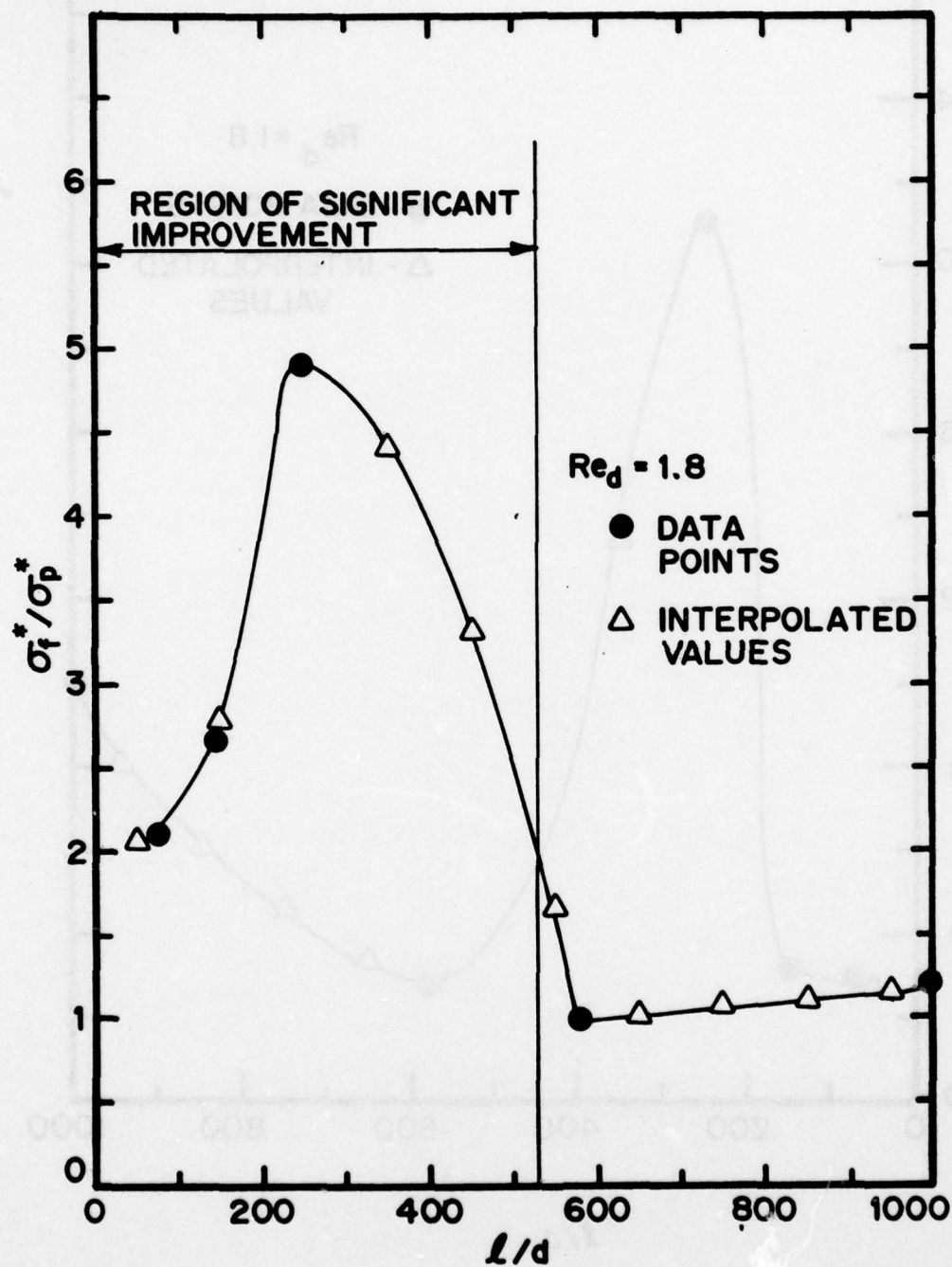


Figure 40. Variation of Ratio of Standard Deviation Improvement Between Friehe and Schwarz and Present Relations with Sensor l/d at a Fixed Reynolds Number; $Re_d = 1.8$

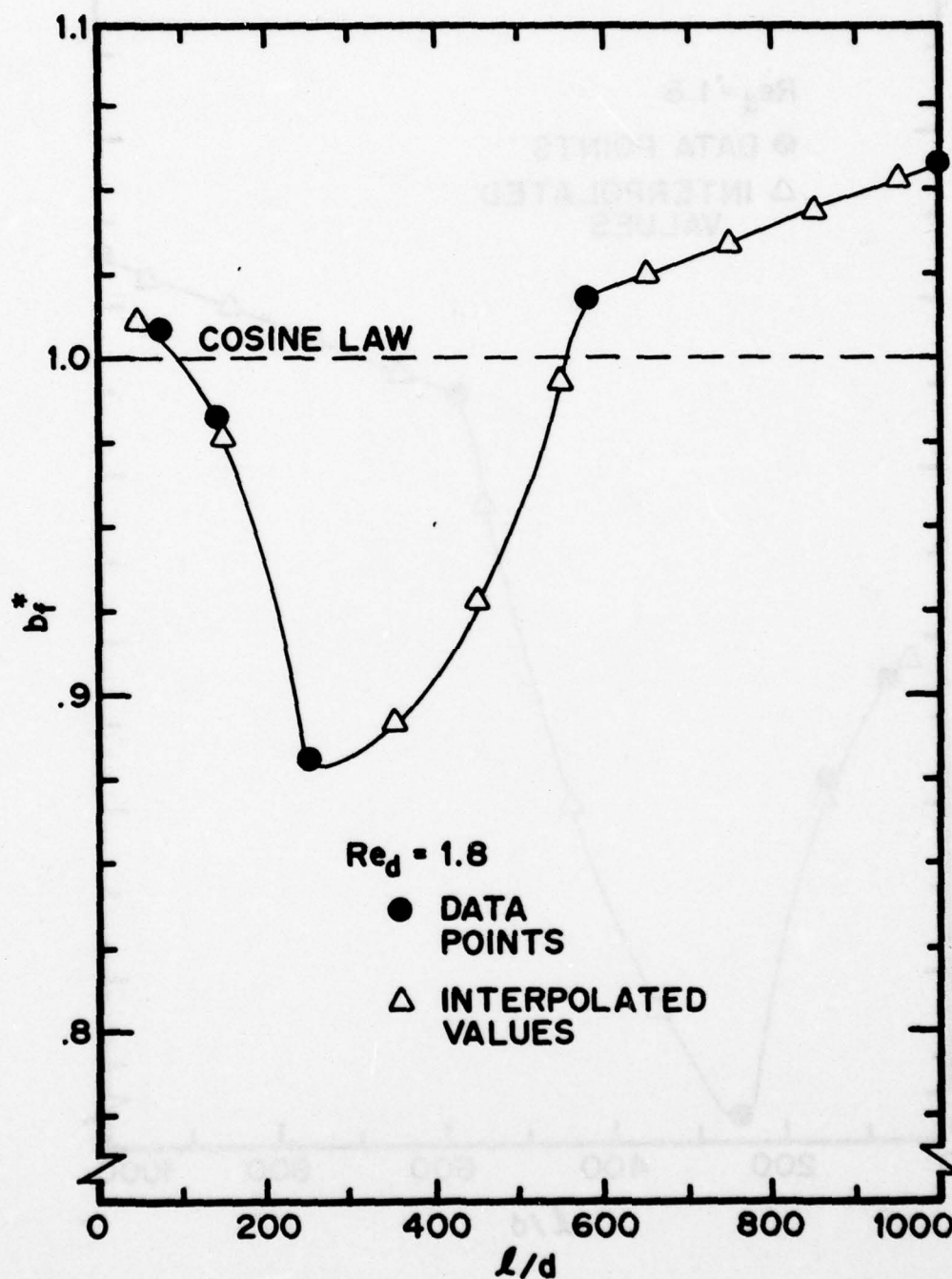


Figure 41. Variation of Best Fit Coefficient Determined from Friehe and Schwarz Relation with Sensor l/d at a Fixed Reynolds Number; $Re_d = 1.8$

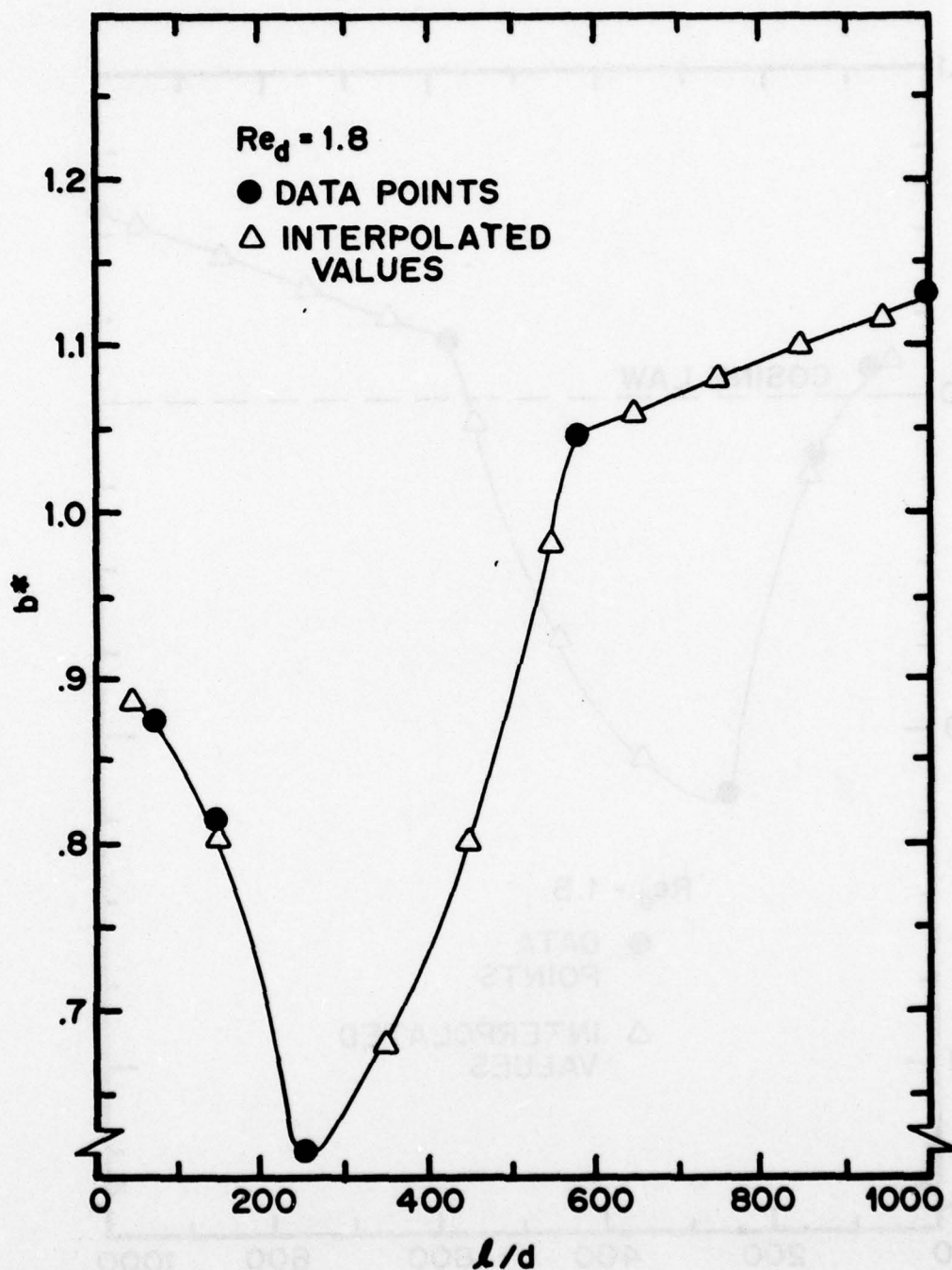


Figure 42. Variation of Best Fit Coefficient Determined from Present Relation with Sensor l/d at a Fixed Reynolds Number; $Re_d=1.8$

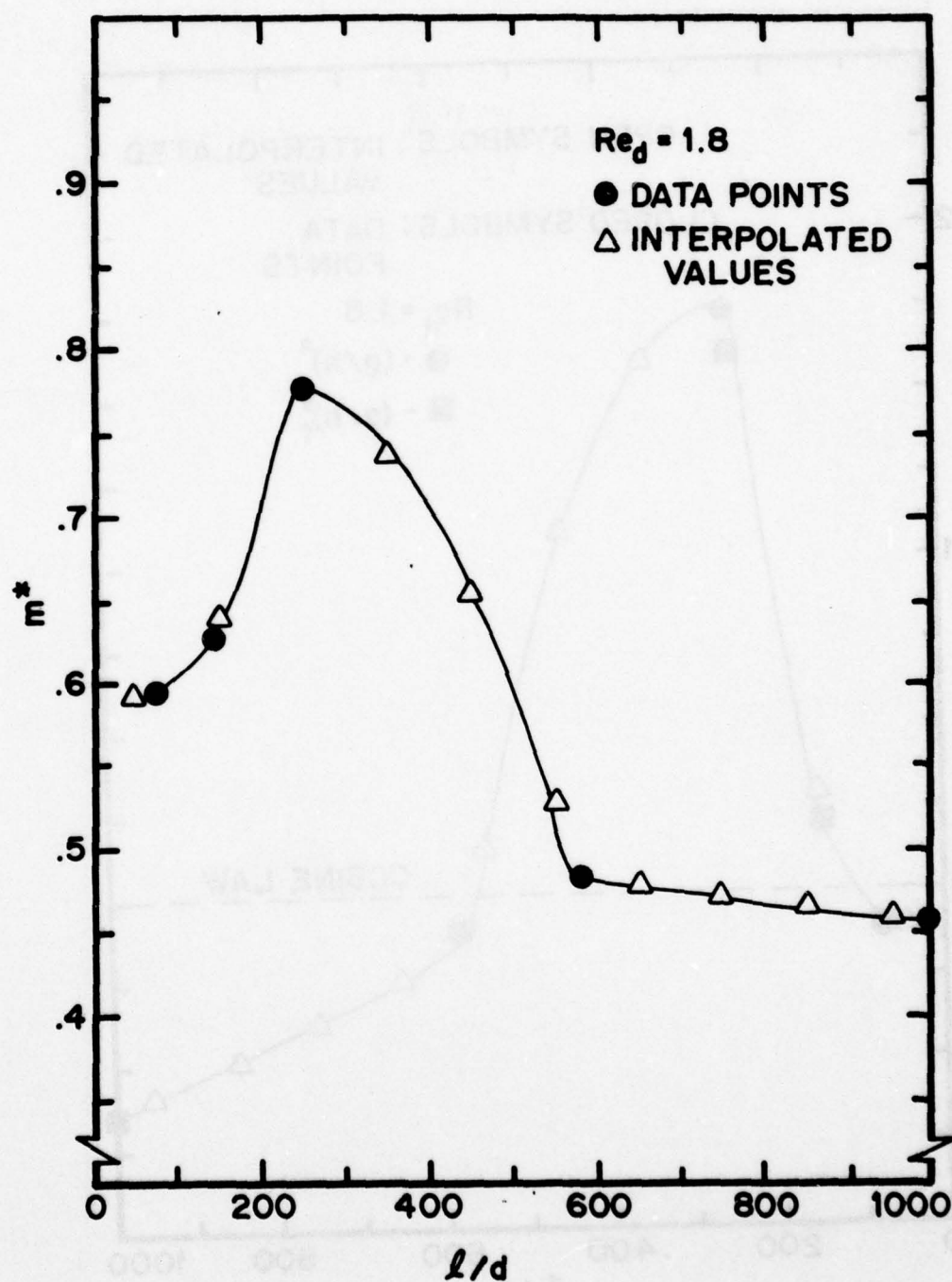


Figure 43. Variation of Best Fit Exponent Determined from Present Relation with Sensor l/d at a Fixed Reynolds Number; $Re_d = 1.8$

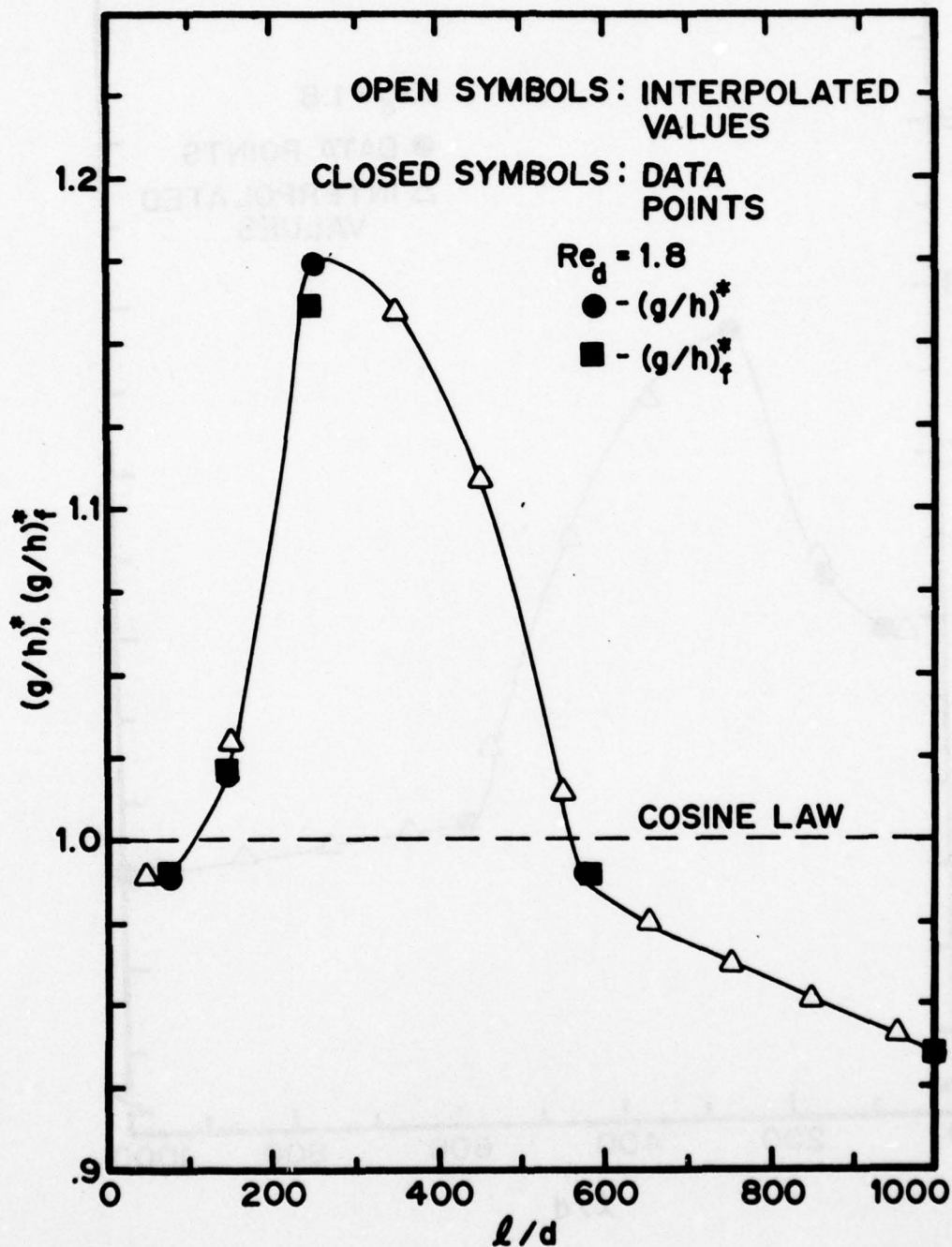


Figure 44. Variation of Turbulence Correction Factors, as Determined from Friehe and Schwarz and Present Relations, with Sensor l/d at a Fixed Reynolds Number; $Re_d=1.8$

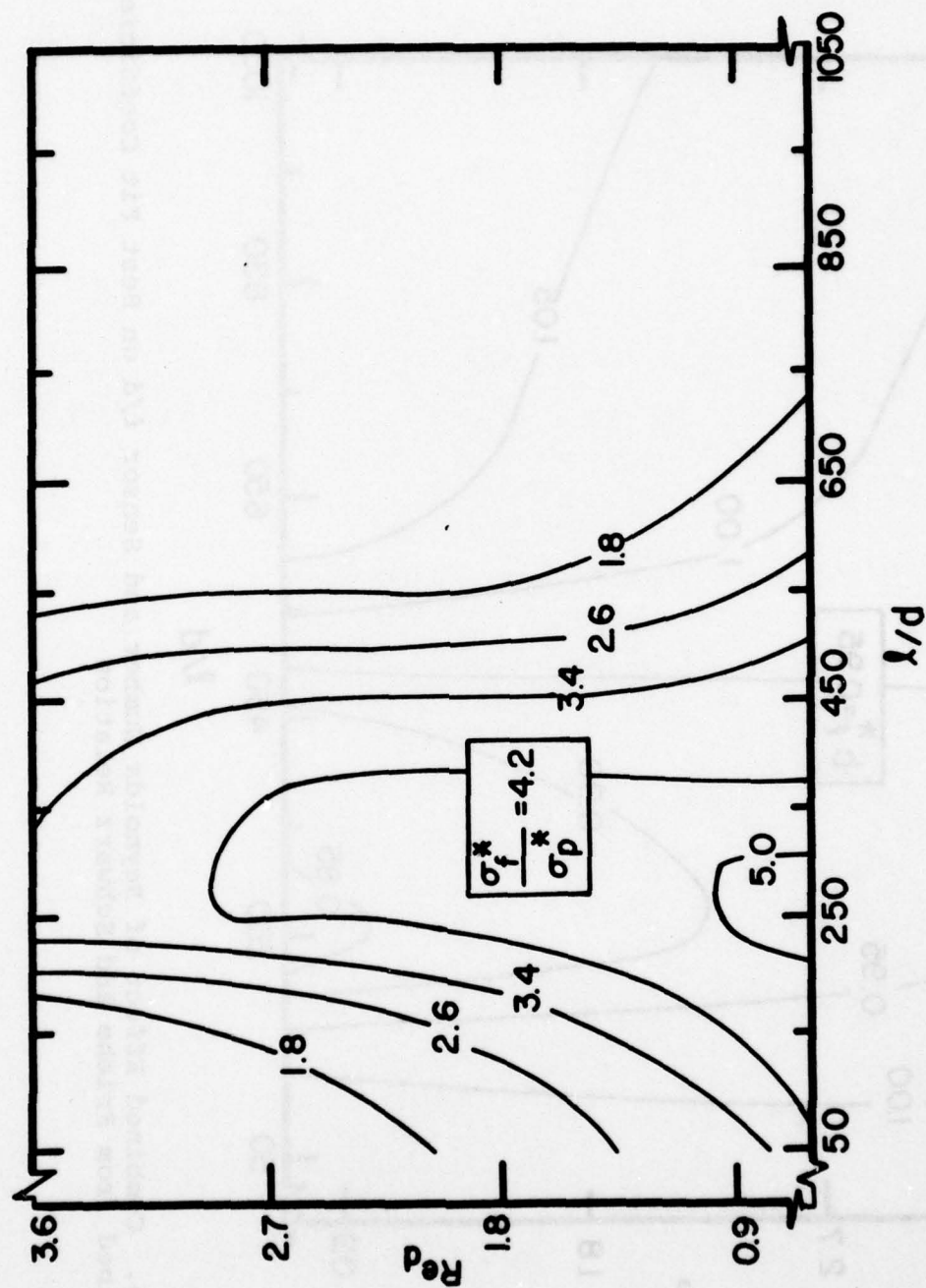


Figure 45. Combined Effect of Reynolds Number and Sensor l/d on Ratio of Standard Deviation Improvement Between Friehe and Schwarz and Present Relations

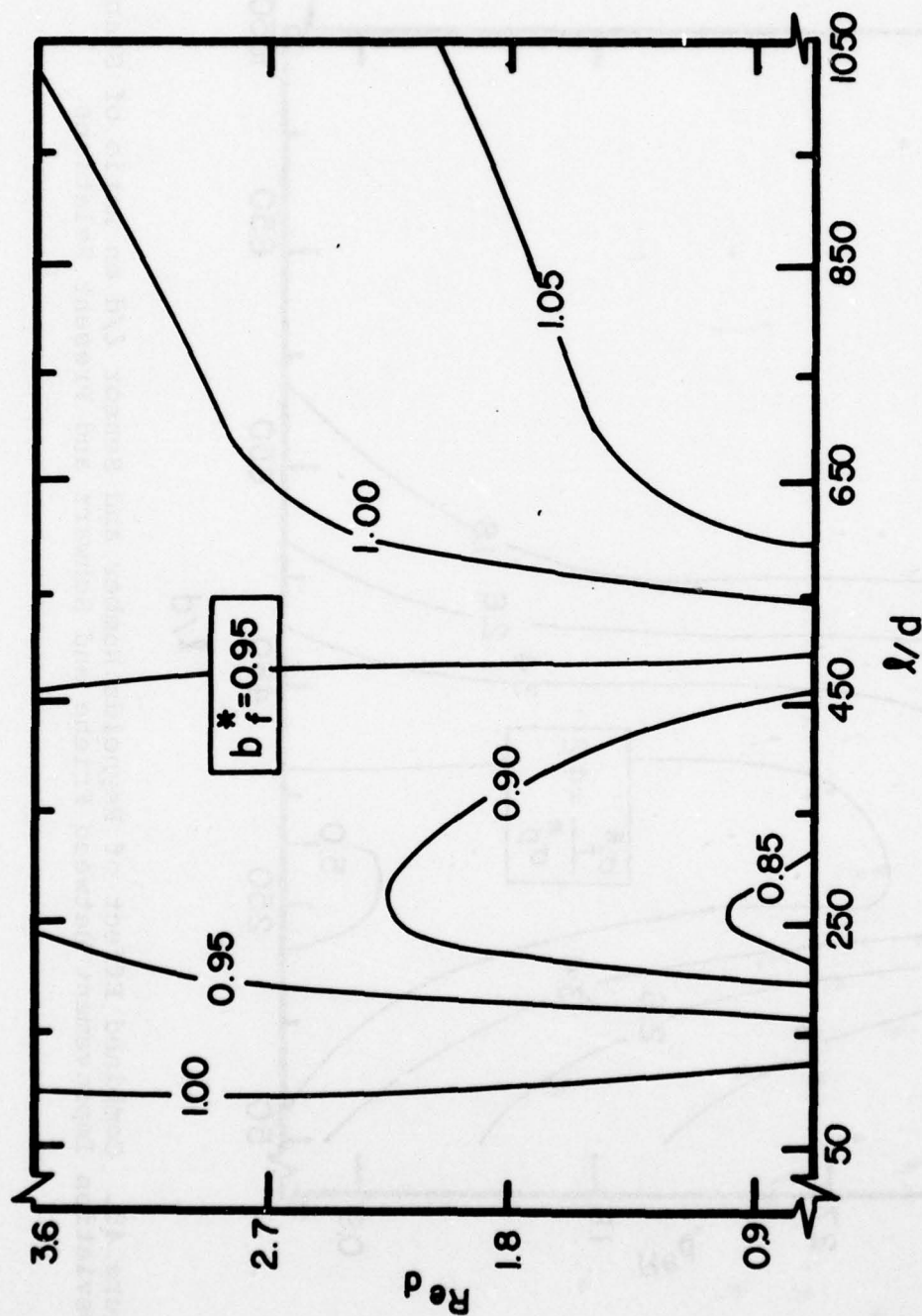


Figure 46. Combined Effect of Reynolds Number and Sensor l/d on Best Fit Coefficient Determined from Friehe and Schwarz Relation

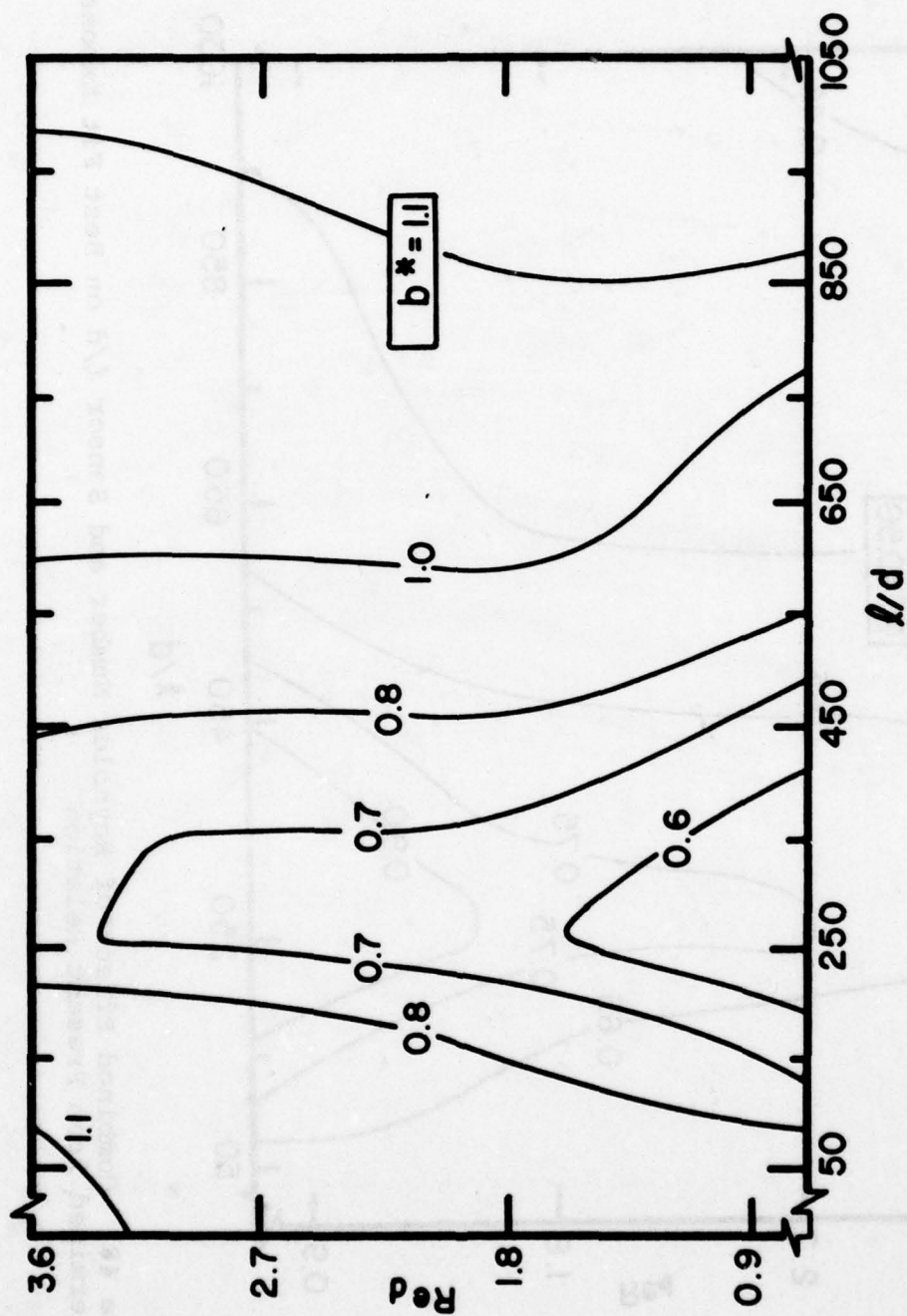


Figure 47. Combined Effect of Reynolds Number and Sensor l/d on Best Fit Coefficient Determined from Present Relation

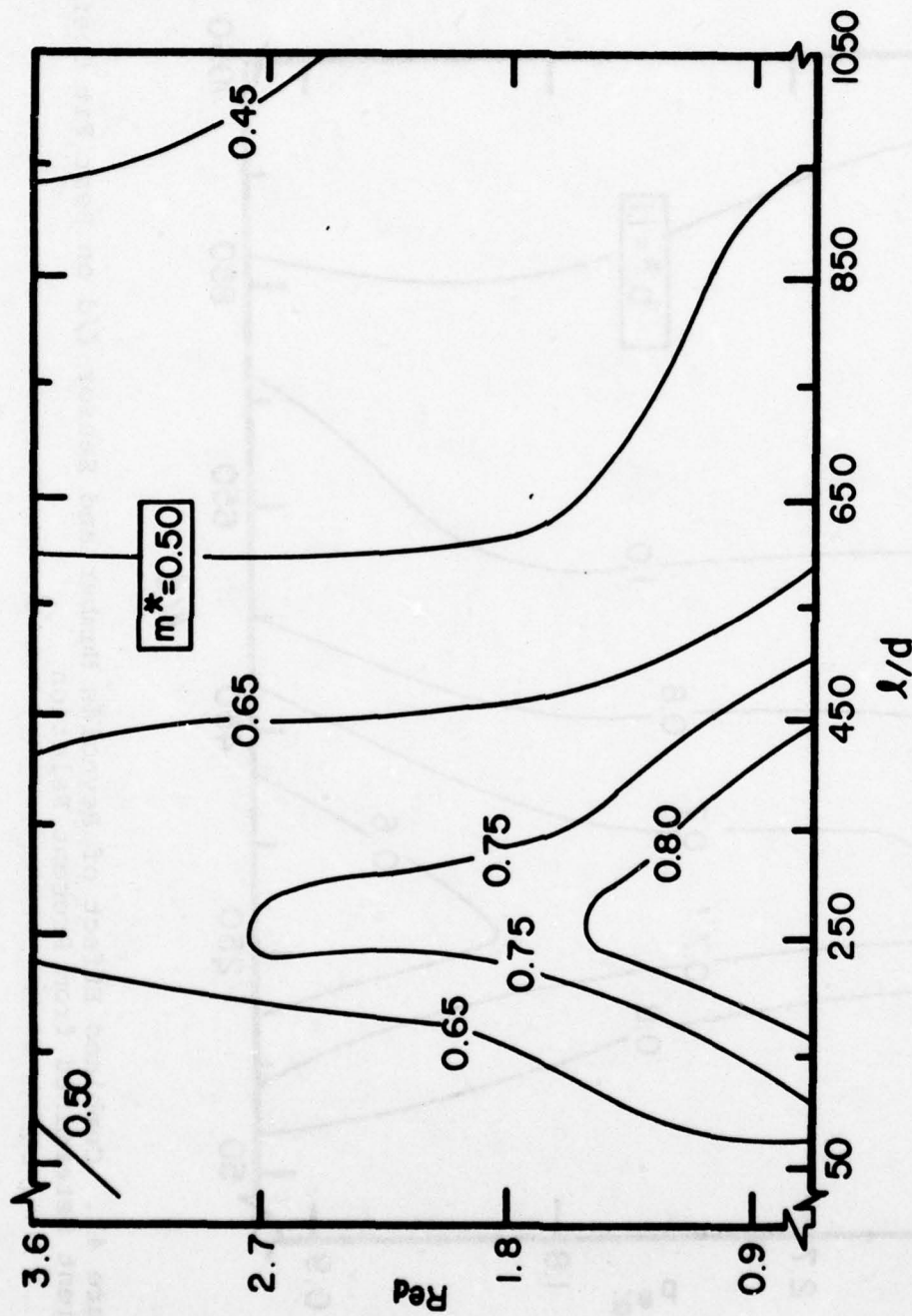


Figure 48. Combined Effect of Reynolds Number and Sensor l/d on Best Fit Exponent Determined from Present Relation

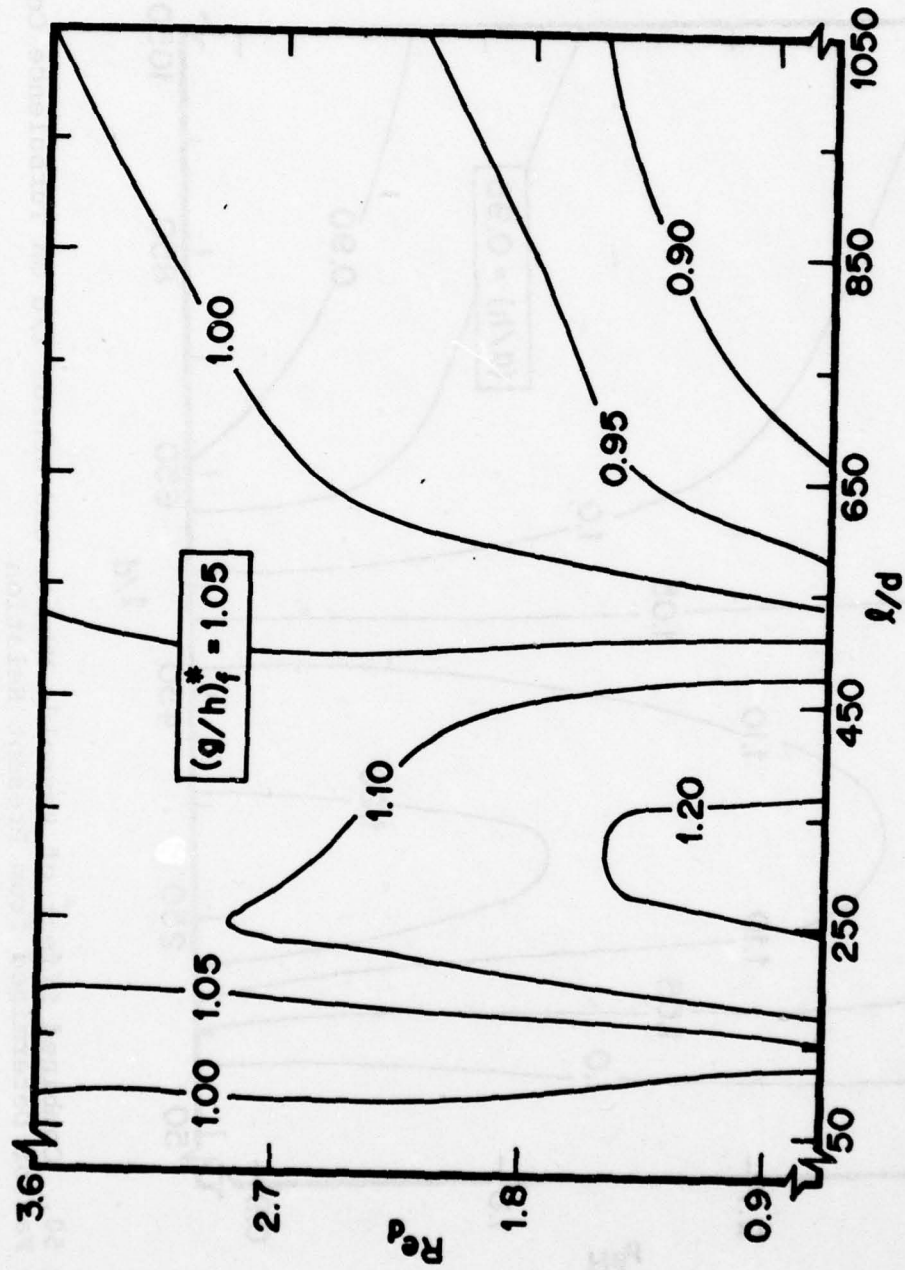


Figure 49. Combined Effect of Reynolds Number and Sensor l/d on Turbulence Correction Factor Determined from Friehe and Schwarz Relation

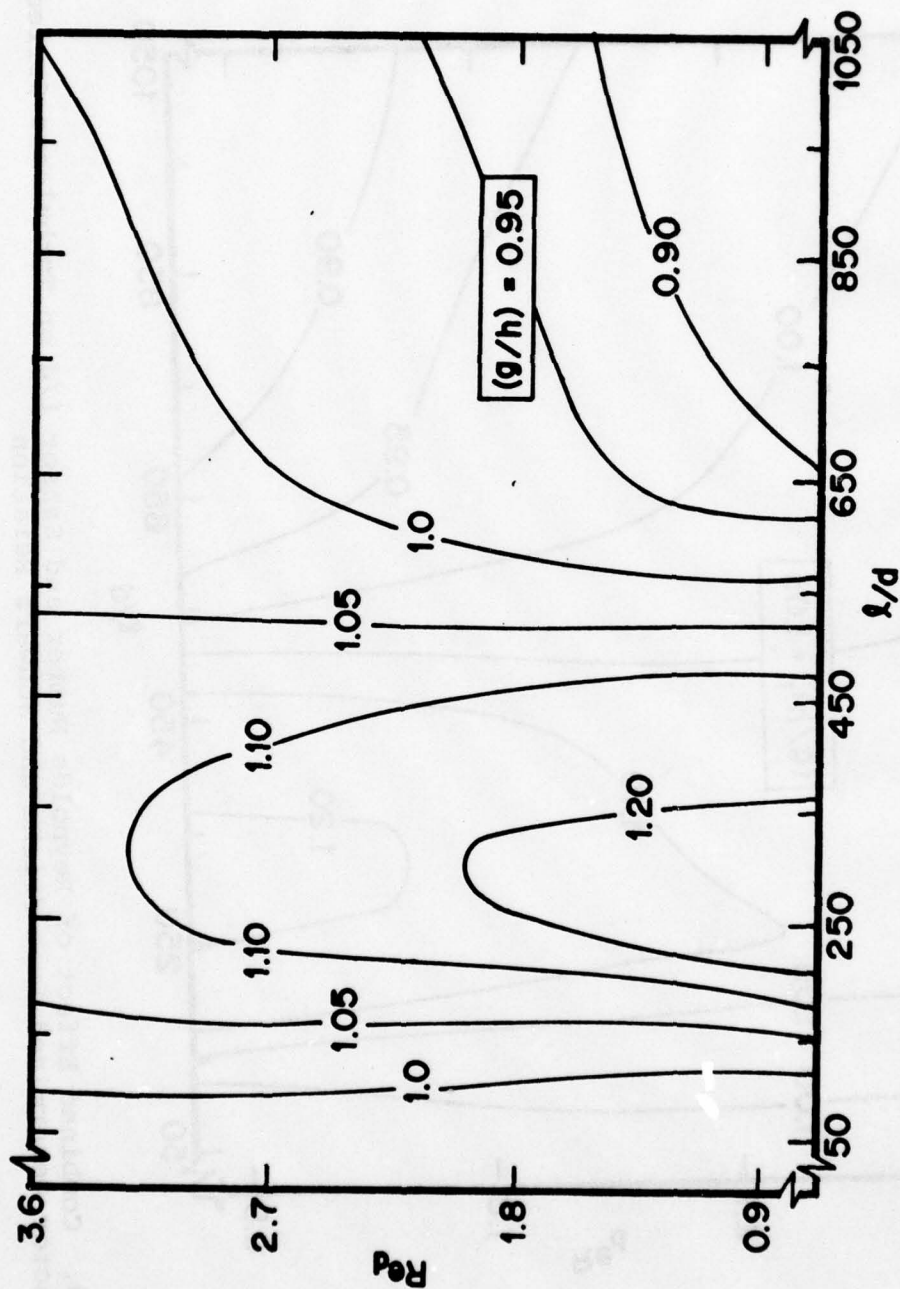


Figure 50. Combined Effect of Reynolds Number and Sensor l/d on Turbulence Correction Factor Determined from Present Relation

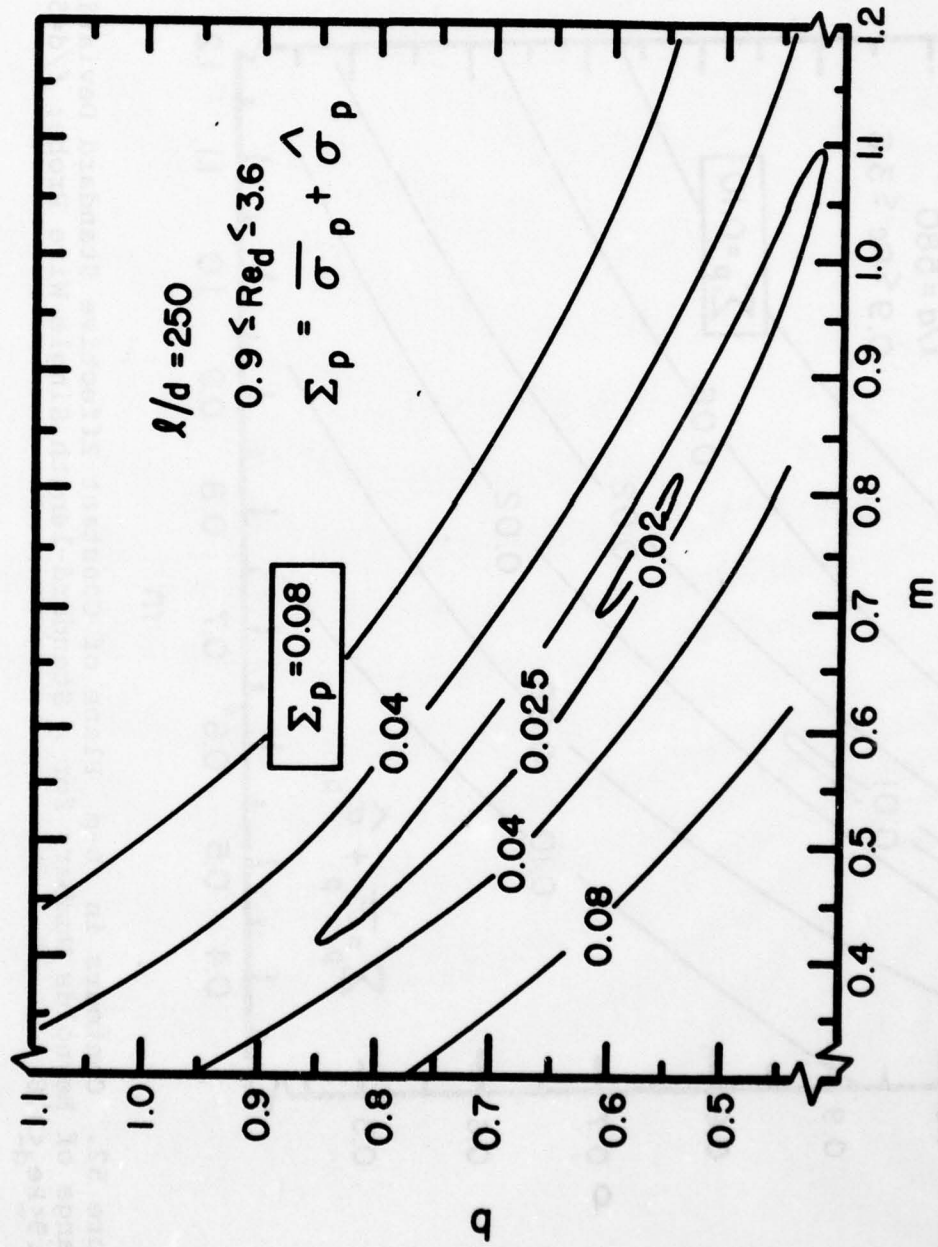


Figure 51. Contours in b - m Plane of Constant Effective Standard Deviation Over Range of Reynolds Numbers for a Single Wire Probe; $l/d=250$, $0.9 \leq Re_d \leq 3.6$

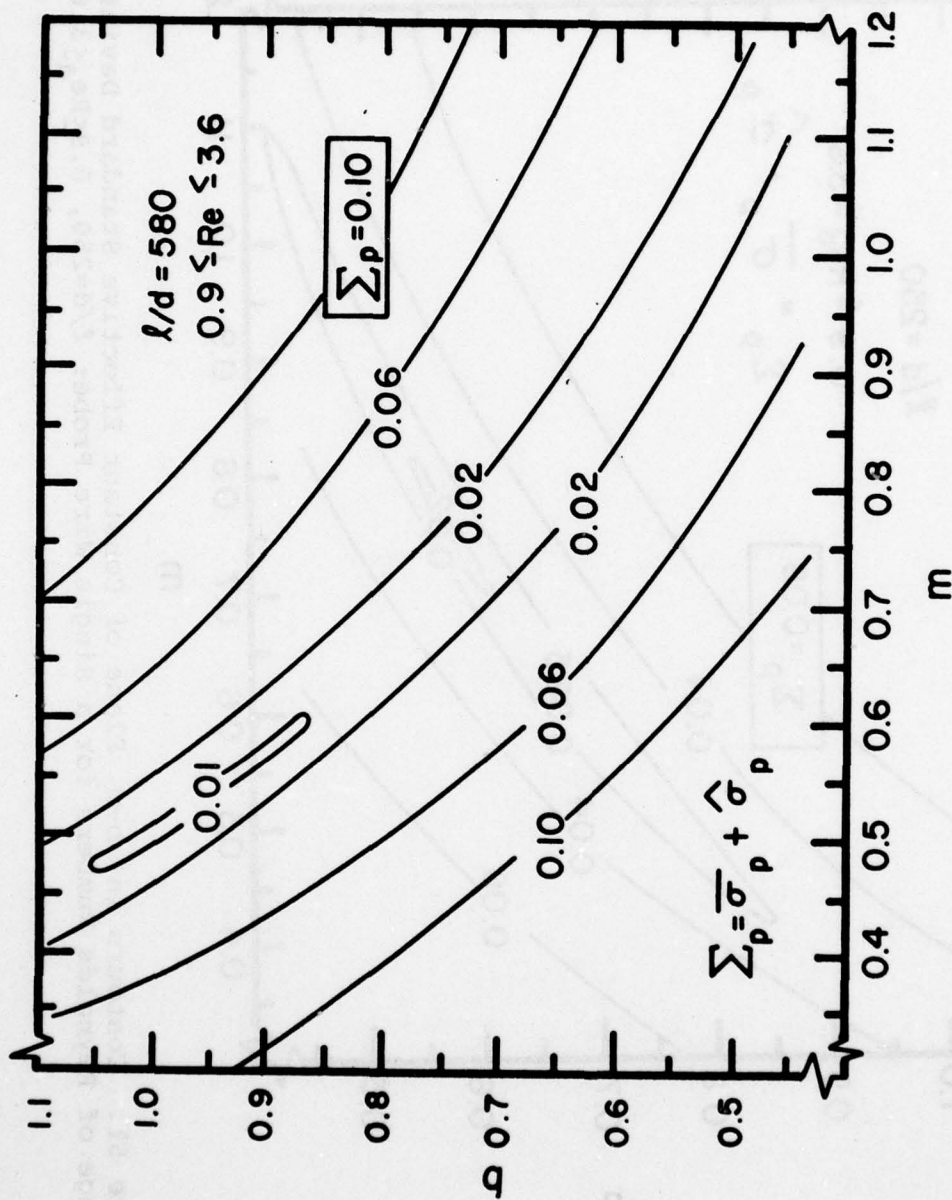


Figure 52. Contours in b - m Plane of Constant Effective Standard Deviation Over Range of Reynolds Numbers for a Standard-length Single Wire Probe; $l/d=580$, $0.9 \le Re_d \le 3.6$

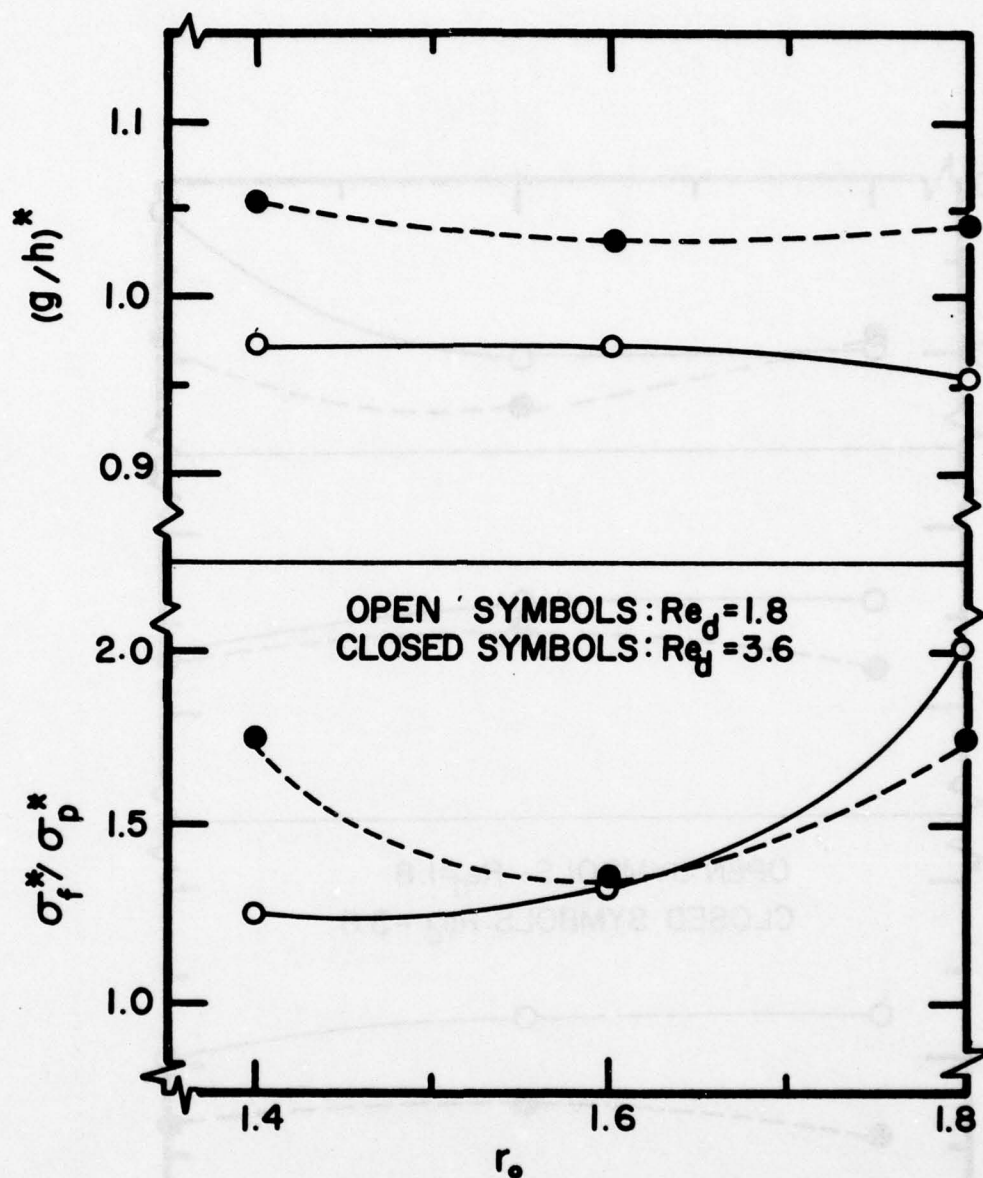


Figure 53. Variation with Overheat Ratio of Turbulence Correction Factor and Ratio of Standard Deviation Improvement Between Friehe and Schwarz and Present Relations for a Standard-length Probe; $l/d=580$

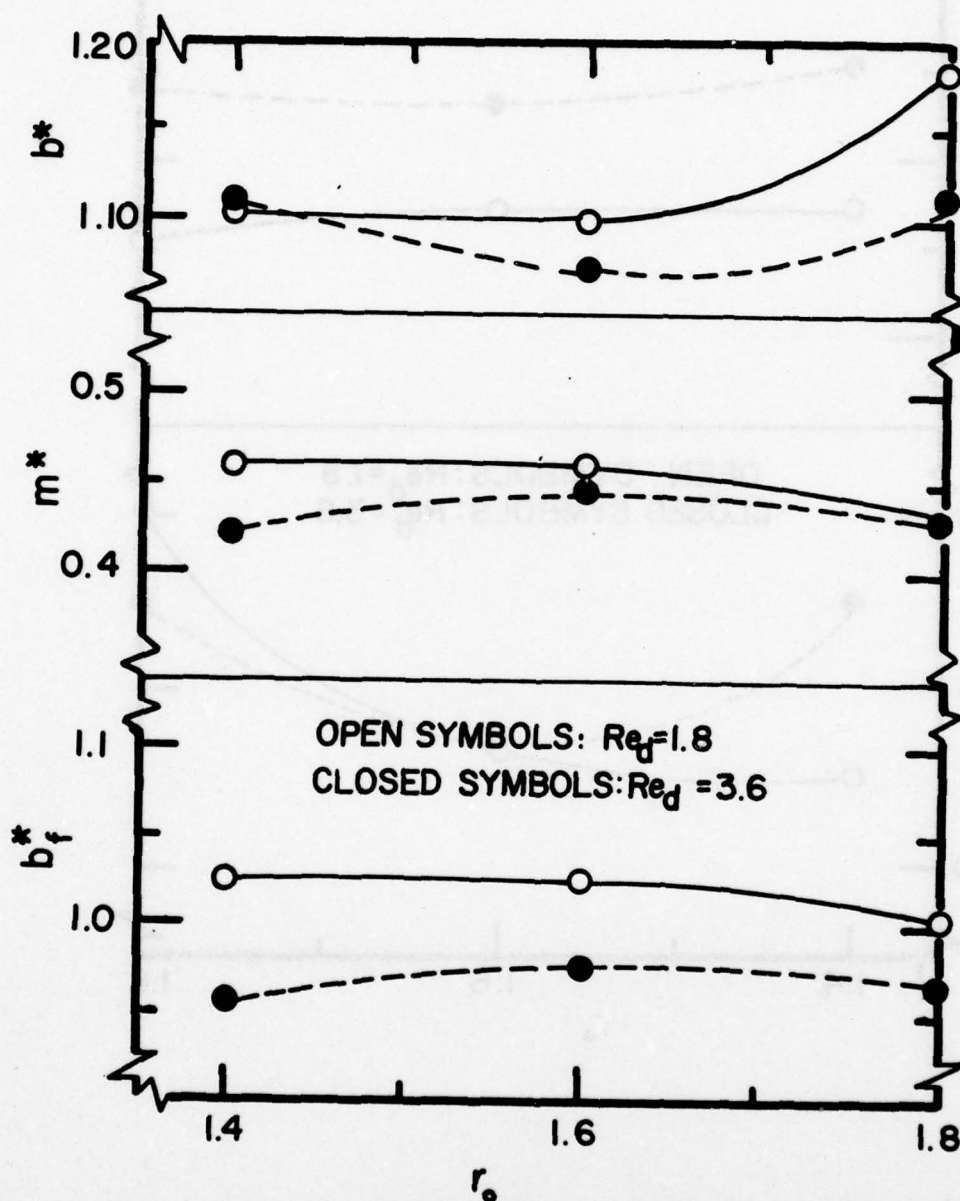


Figure 54. Variation of Best Fit Coefficients and Exponent Determined from Friehe and Schwarz and Present Relations with Overheat Ratios for a Standard-length Probe; $l/d=580$

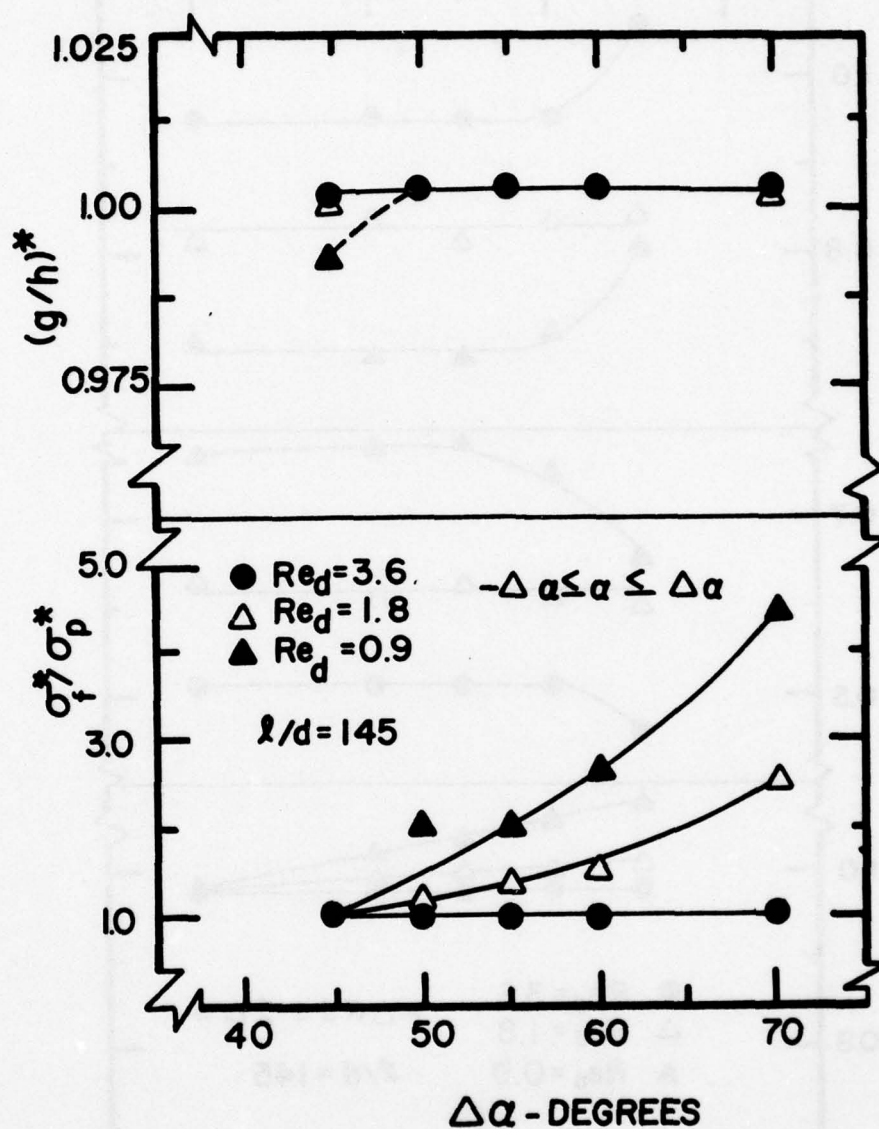


Figure 55. Variation of Turbulence Correction Factor and Ratio of Standard Deviation Improvement Between Friehe and Schwarz and Present Relations with Angular Range of Calibration; $l/d=145$

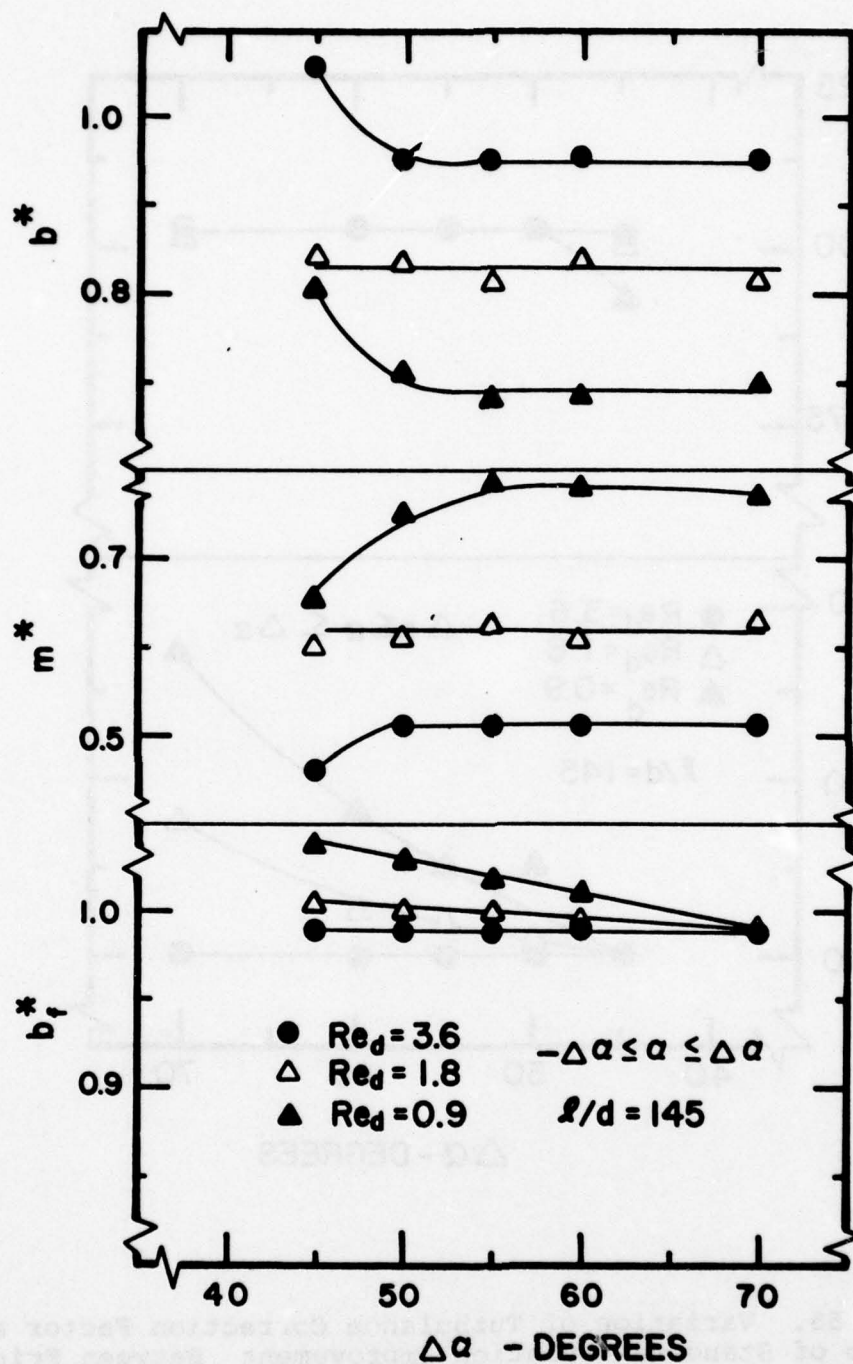


Figure 56. Variation of Best Fit Coefficients and Exponent Determined from Friehe and Schwarz and Present Relations with Angular Range of Calibration; $l/d=145$

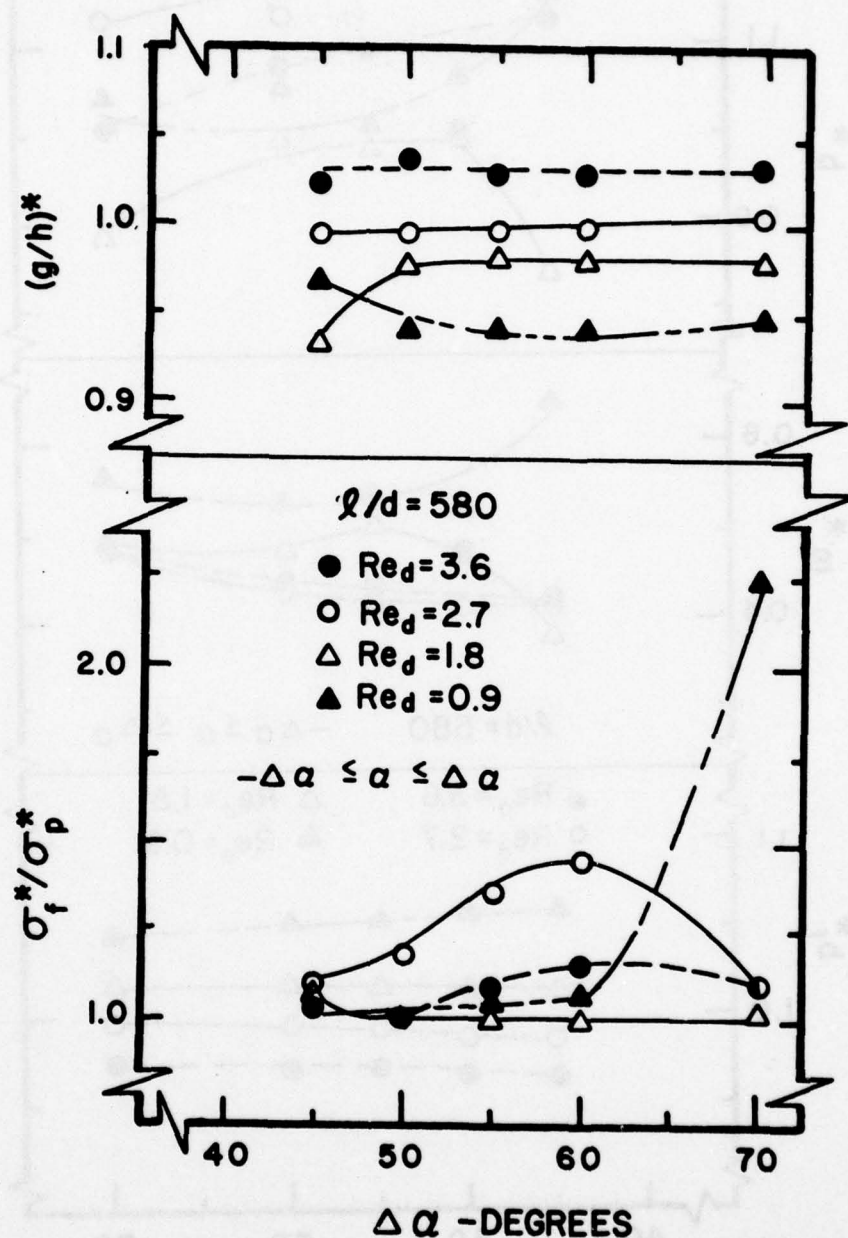


Figure 57. Variation of Turbulence Correction Factor and Ratio of Standard Deviation Improvement, Between Friehe and Schwarz and Present Relations, with Angular Range of Calibration for a Standard-length Single Wire Probe; $l/d=580$

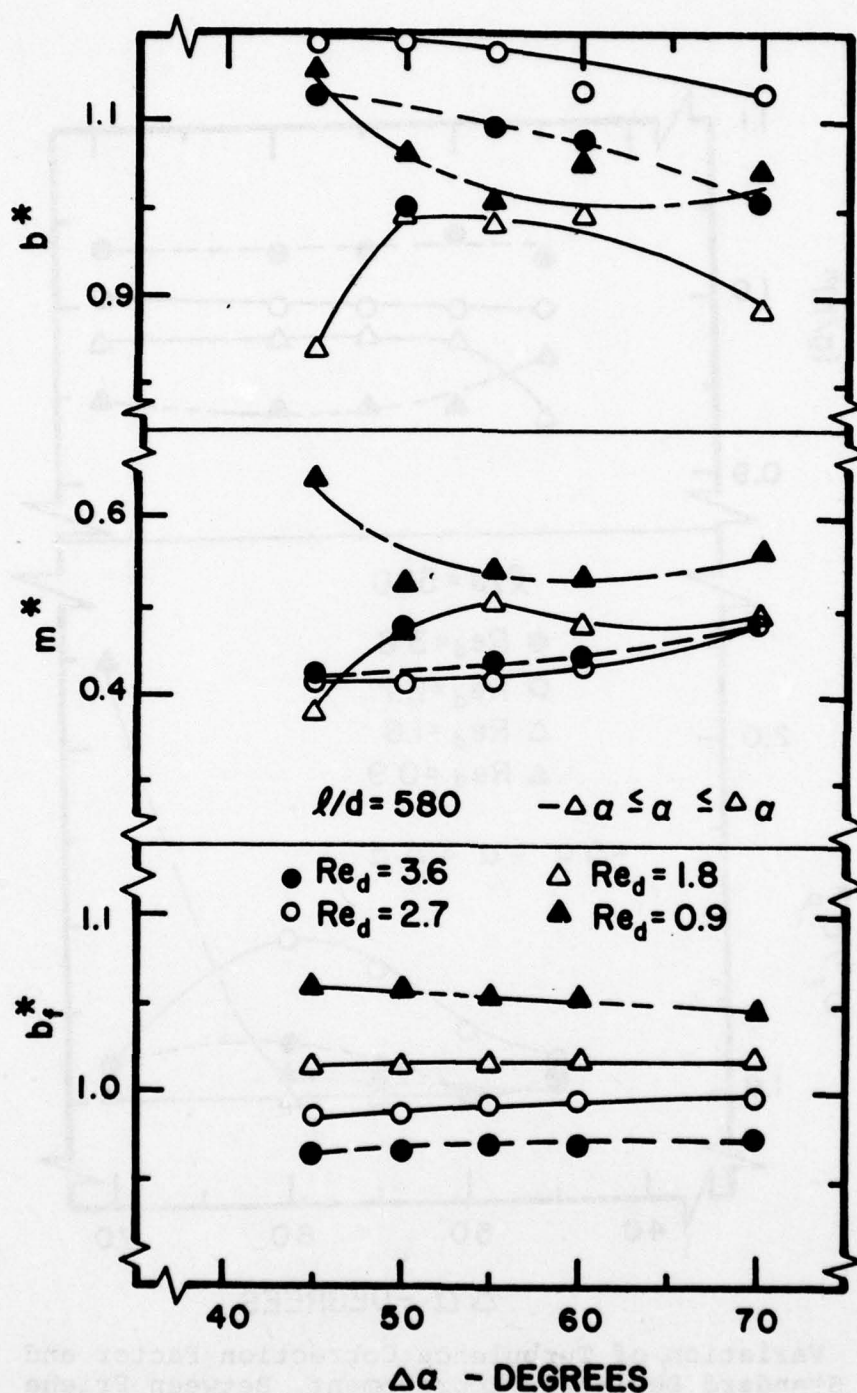


Figure 58. Variation of Best Fit Coefficients and Exponent Determined from Friehe and Schwarz and Present Relations with Angular Range of Calibration for a Standard-length Single Wire Probe; $l/d=580$

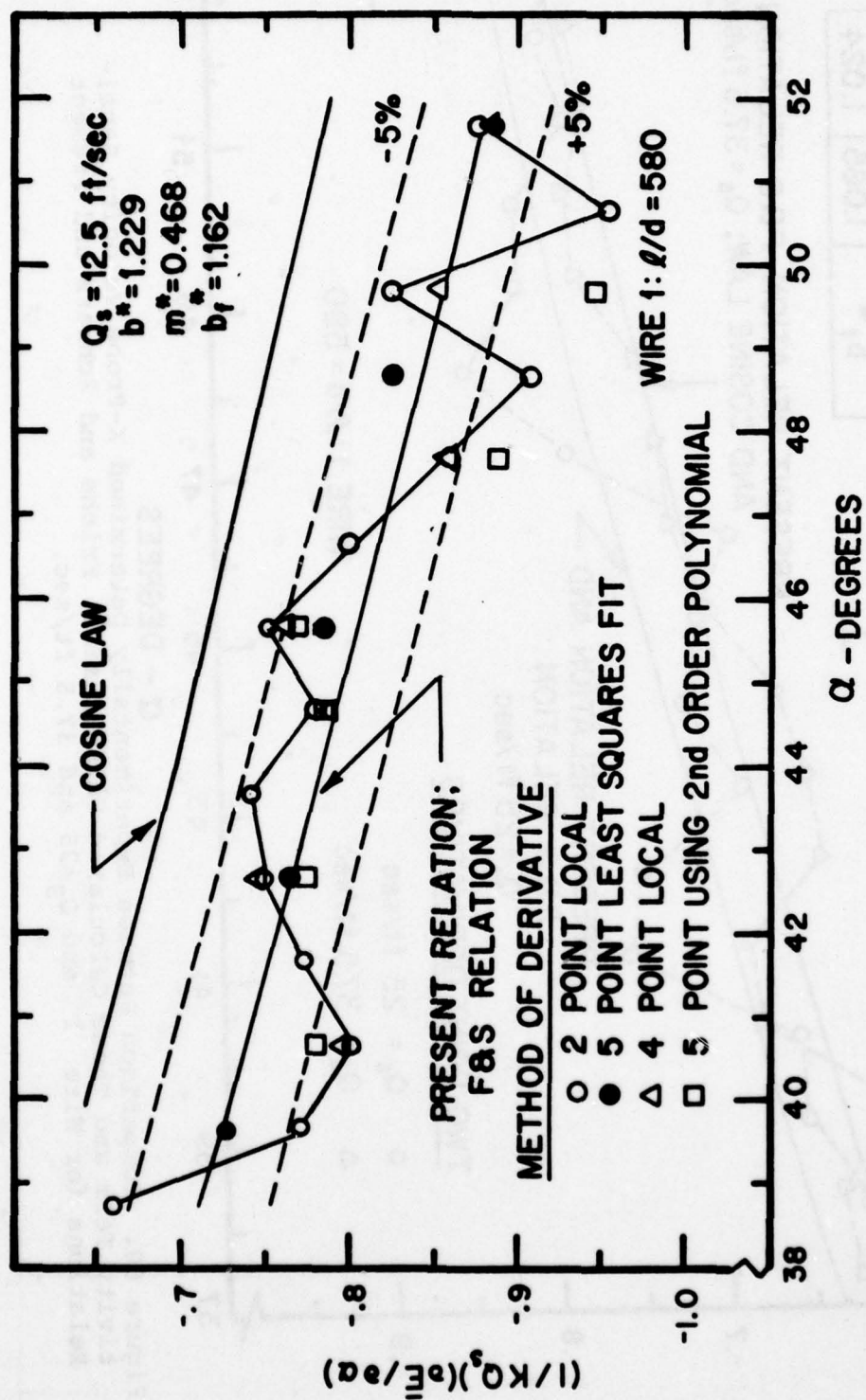


Figure 59. Comparison Between Experimentally Determined X-Probe Sensitivity Term and Those Calculated Using Cosine, Friehe and Schwarz and Present Relations for Wire 1 and $Q_s = 12.5 \text{ ft/sec}$.

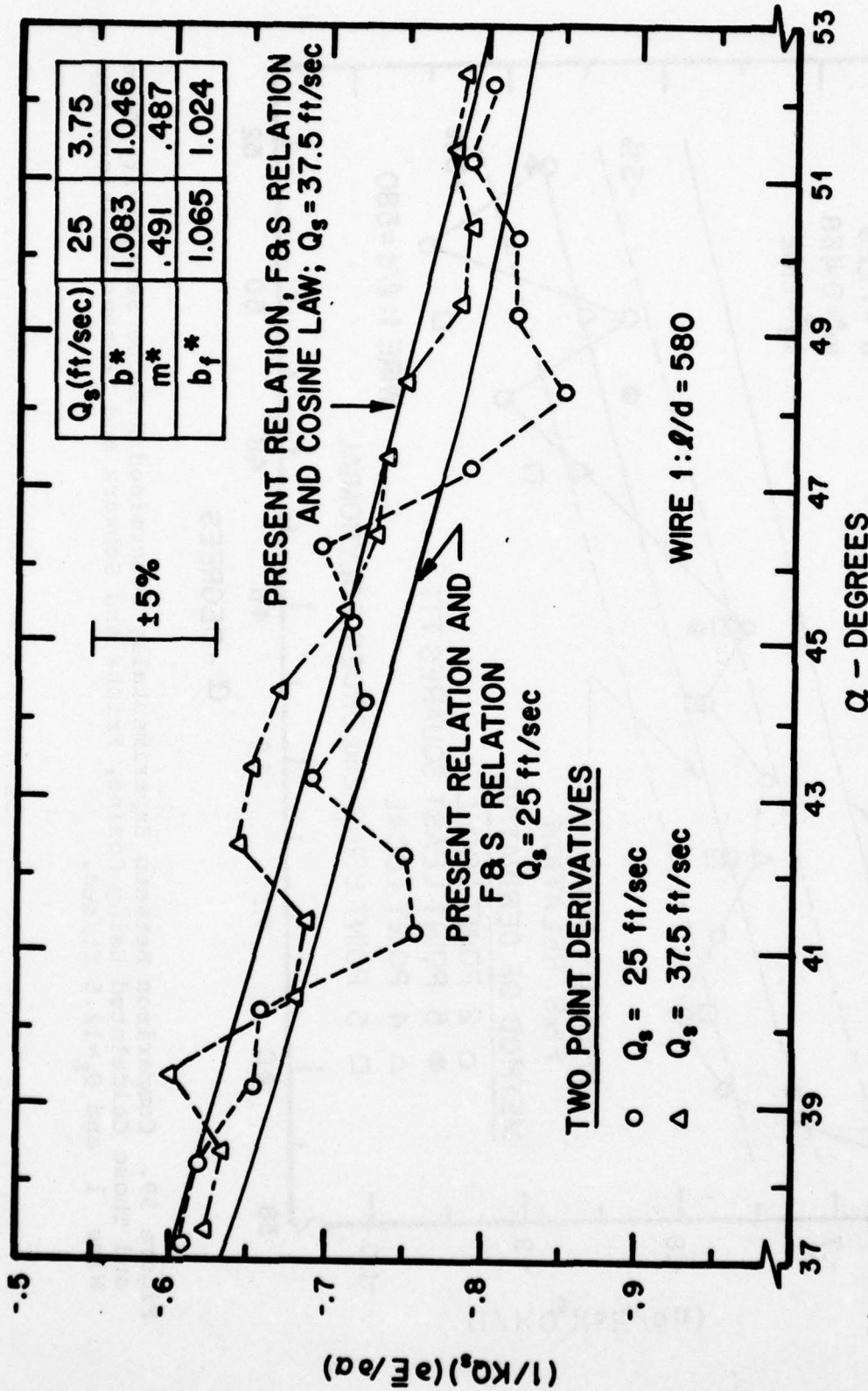


Figure 60. Comparison Between Experimentally Determined X-Probe Velocity Sensitivity Term and Those Calculated Using Cosine, Friehe and Schwarz and Present Relations for Wire 1 and $Q_s = 25$ and 37.5 ft/sec.

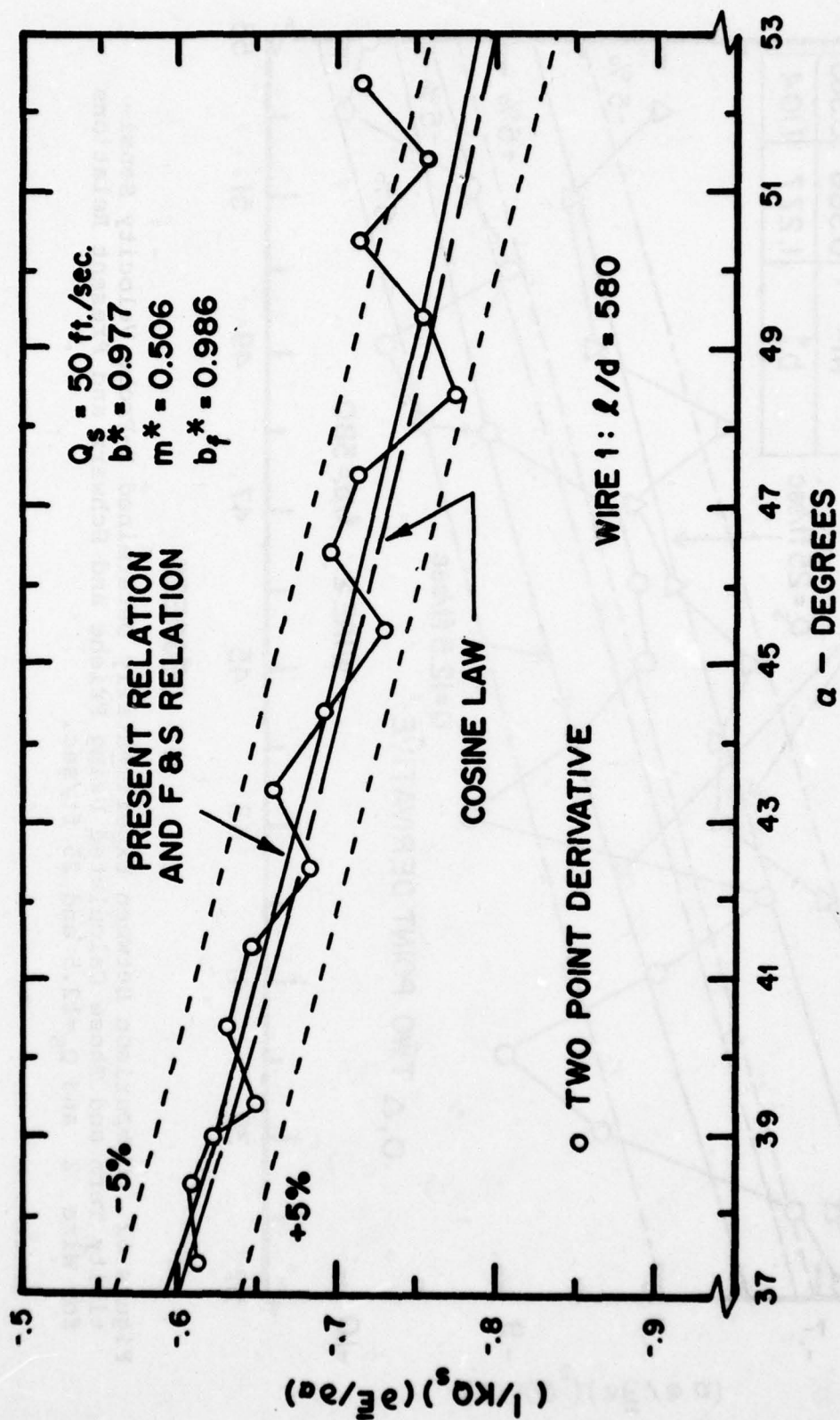


Figure 61. Comparison Between Experimentally Determined X-Probe Velocity Sensitivity Term and Those Calculated Using Cosine, Friehe and Schwarz and Present Relations for Wire 1 and $Q_s = 50 \text{ ft./sec.}$

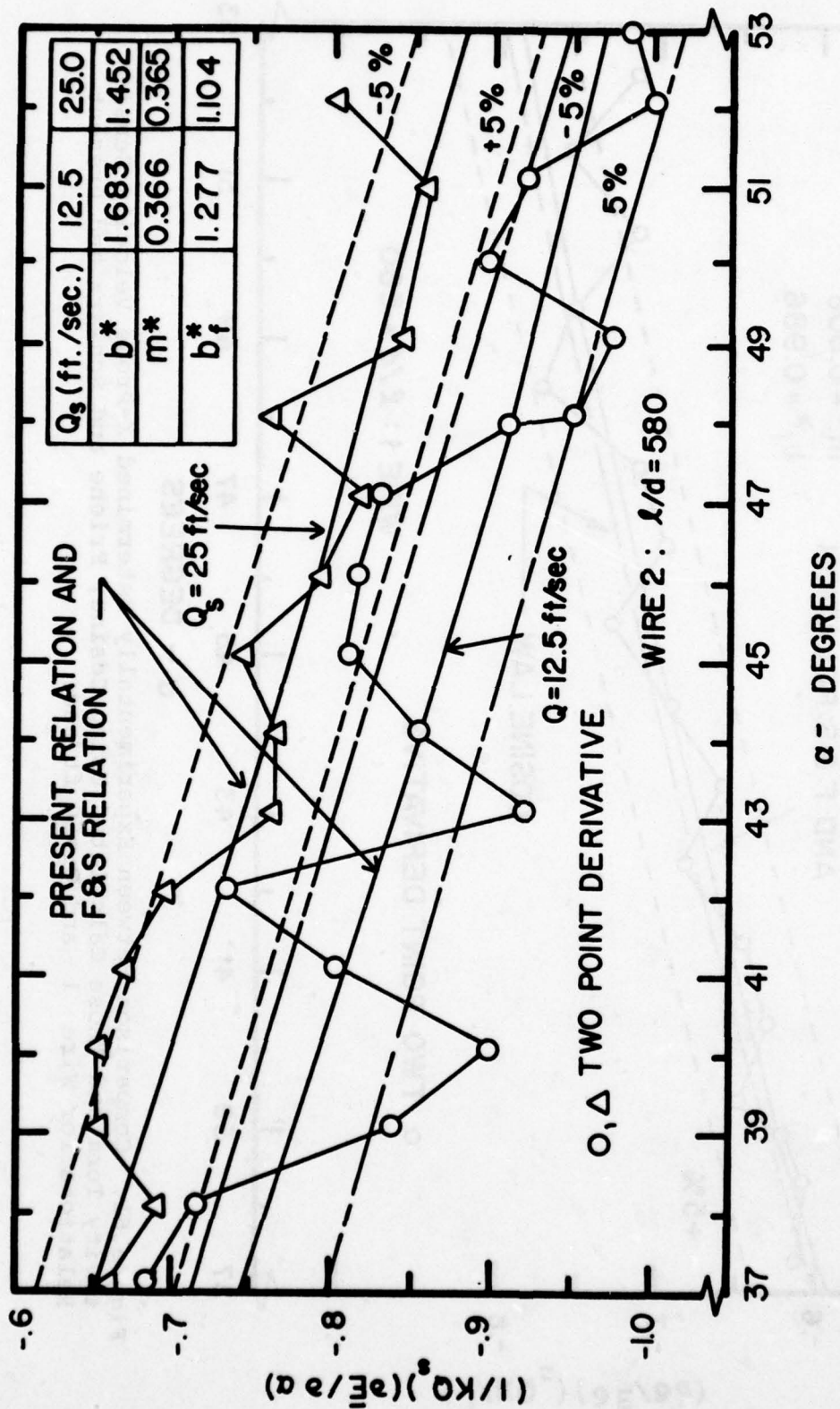


Figure 62. Comparison Between Experimentally Determined X-Probe Velocity Sensitivity Term and Those Calculated Using Friehe and Schwarz and Present Relations for Wire 2 and $Q_s = 12.5$ and 25 ft/sec.

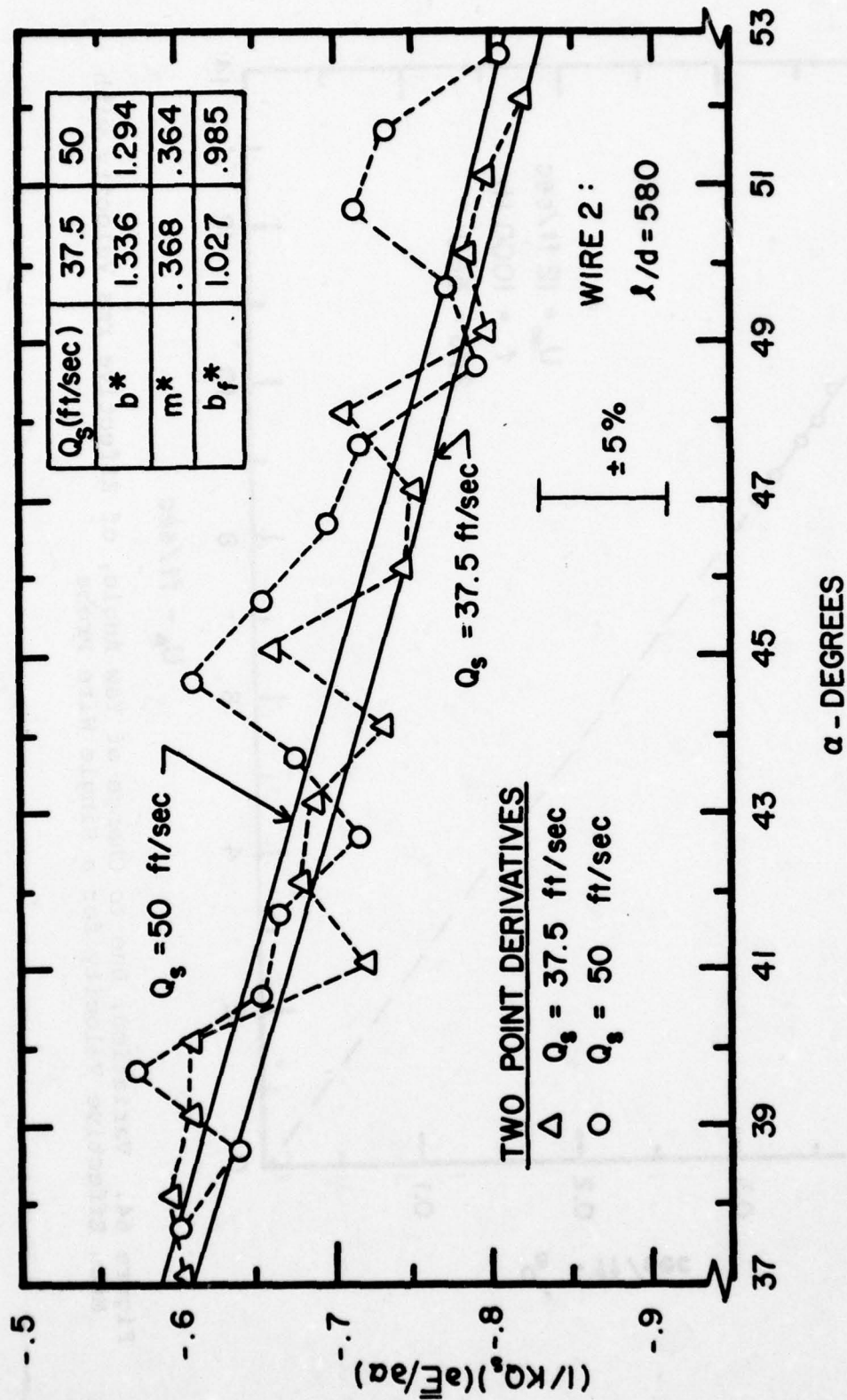


Figure 63. Comparison Between Experimentally Determined X-Probe Velocity Sensitivity Term and Those Calculated Using Friehe and Schwarz and Present Relations for Wire 2 and $Q_s = 37.5$ and 50 ft/sec .

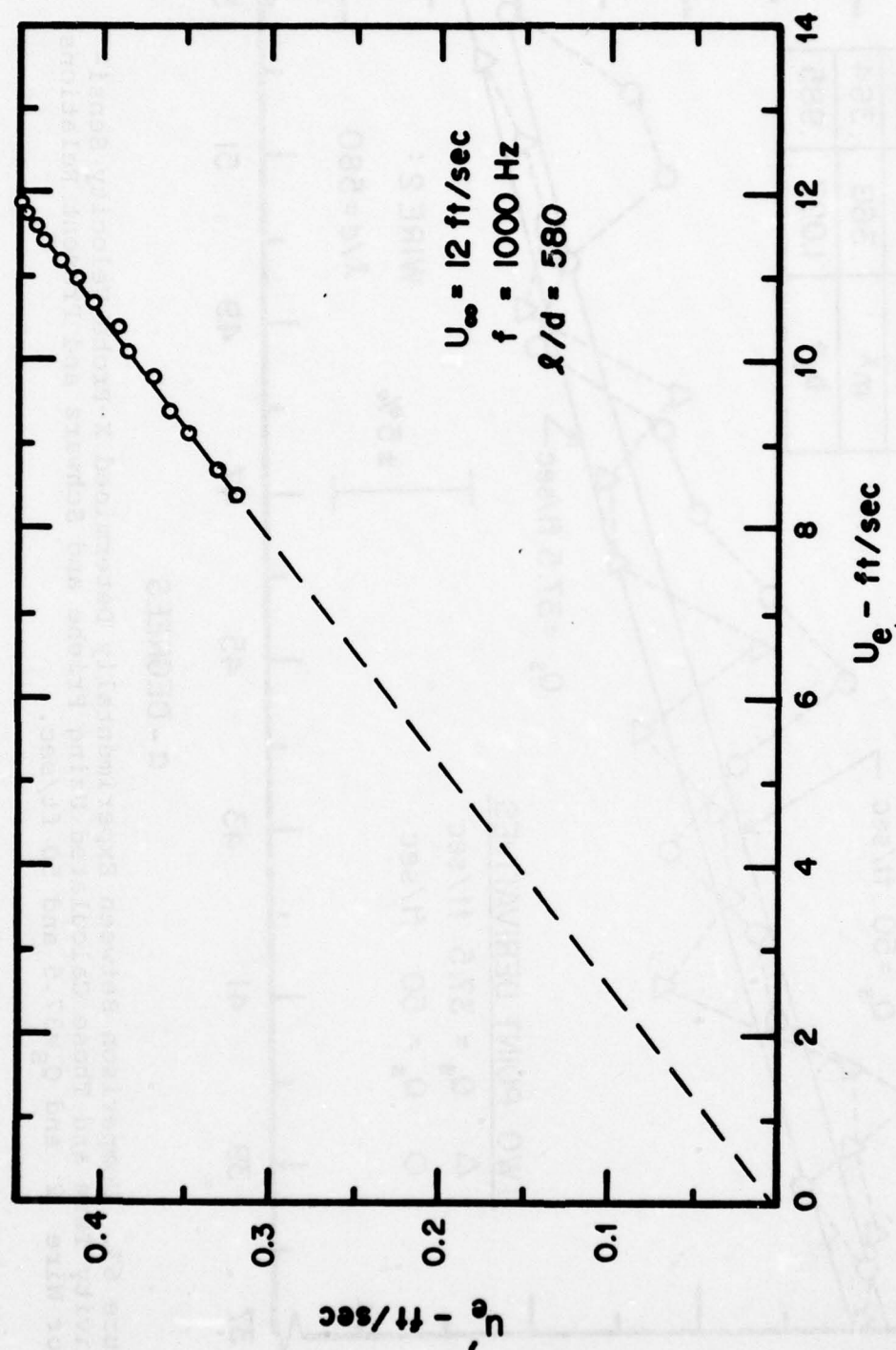


Figure 64. Variation, Due to Change of Yaw Angle, of Effective rms Velocity with Mean Effective Velocity for a Single Wire Probe

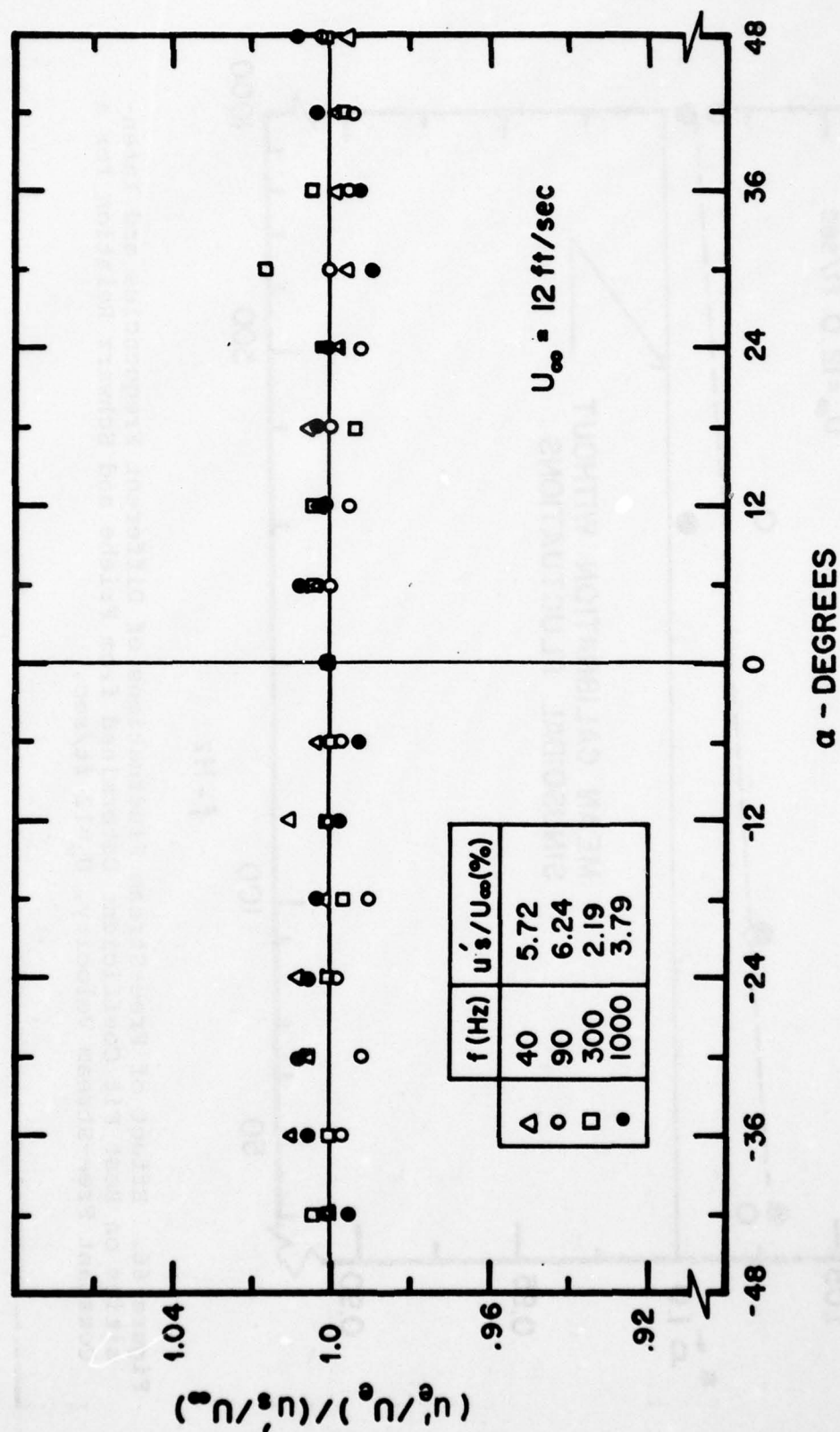


Figure 65. Variation of Normalized Effective Turbulence Intensity with Angle of Yaw for Single Wire Probe

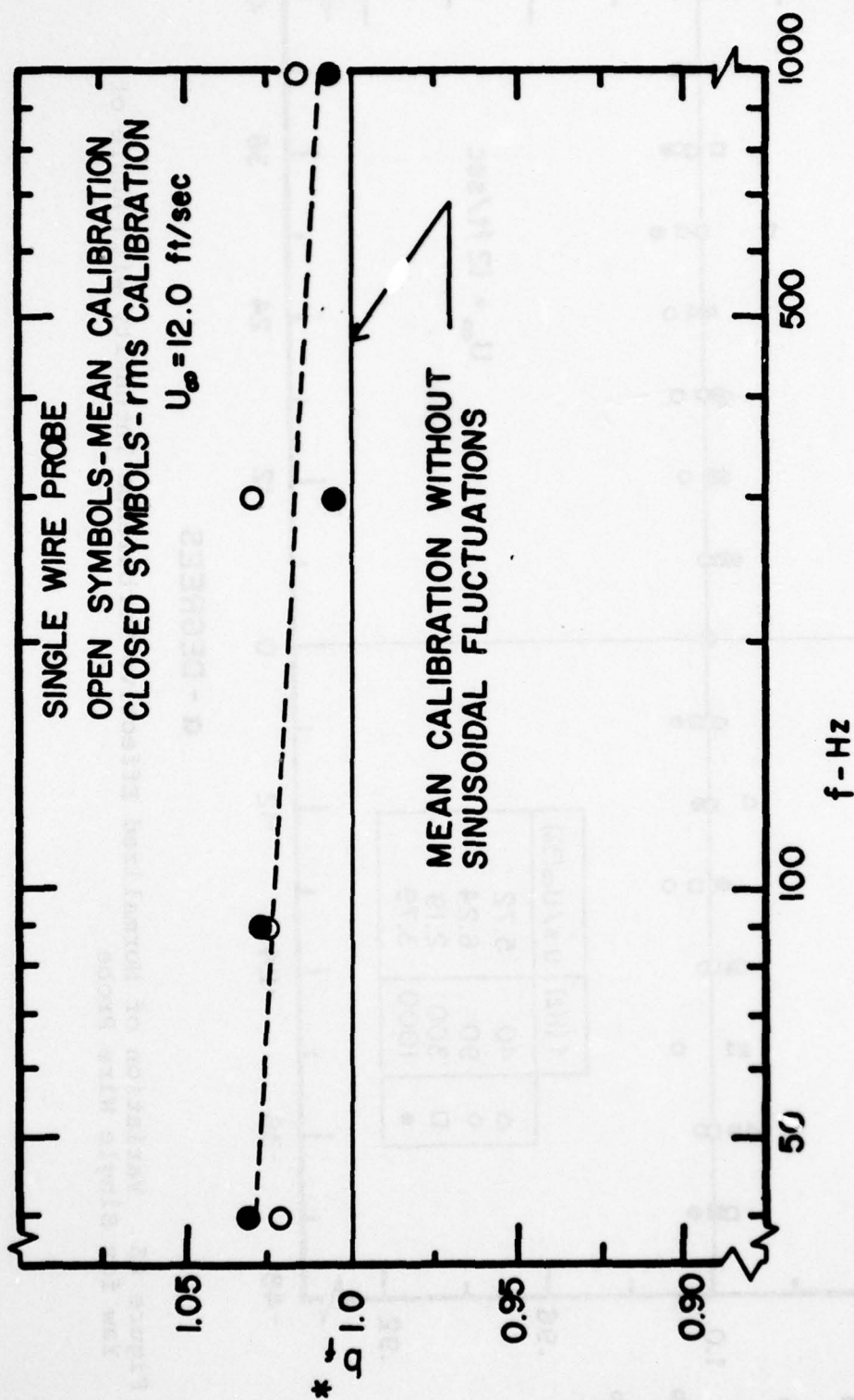


Figure 66. Effect of Free-Stream Fluctuations of Different Frequencies and Intensities on Best Fit Coefficient Determined from Friehe and Schwarz Relation for a Constant Free-Stream Velocity, $U_\infty = 12 \text{ ft/sec}$.

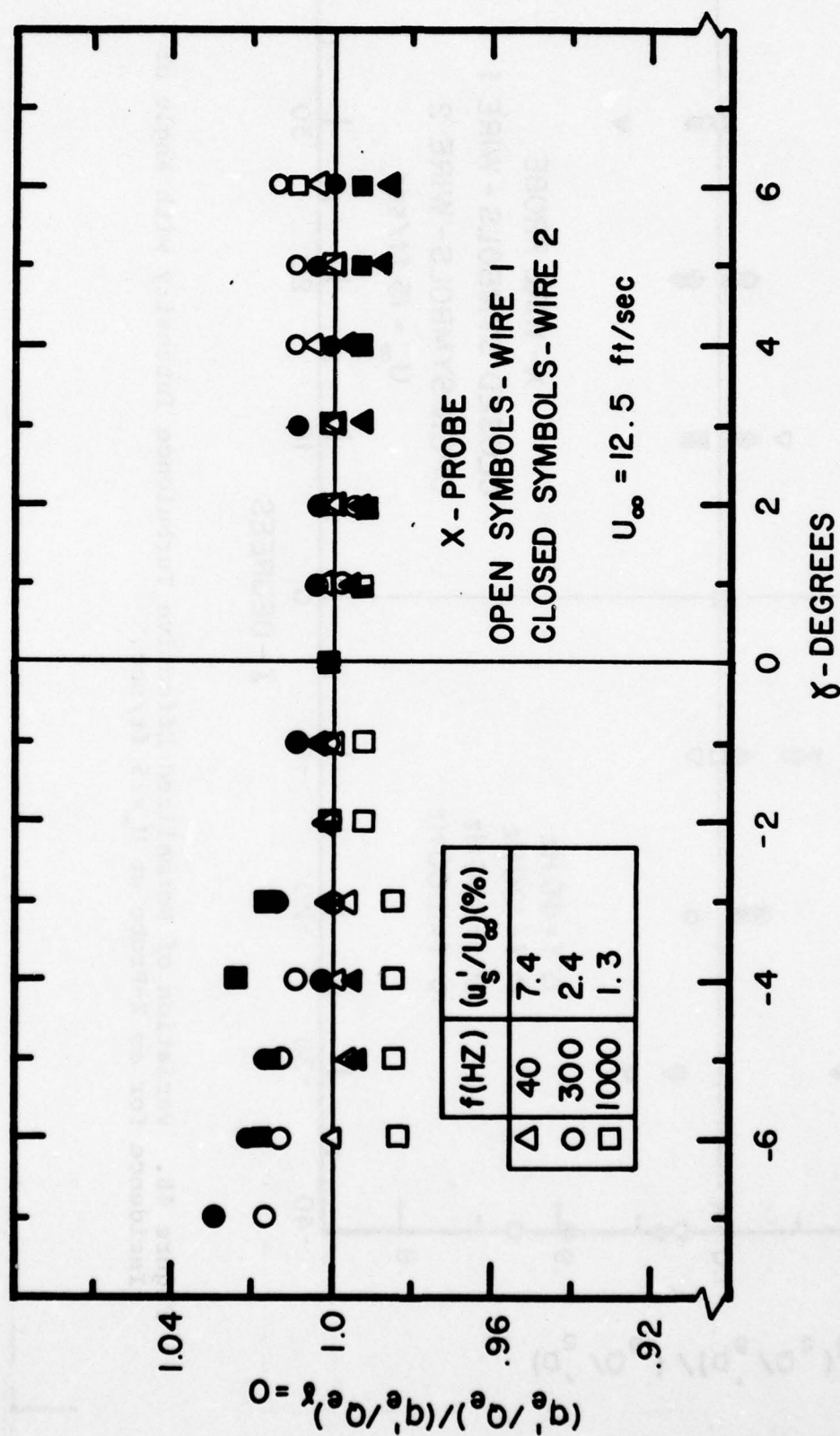


Figure 67. Variation of Normalized Effective Turbulence Intensity with Angle of Incidence for an X-Probe at $U_{\infty} = 12.5 \text{ ft/sec}$.

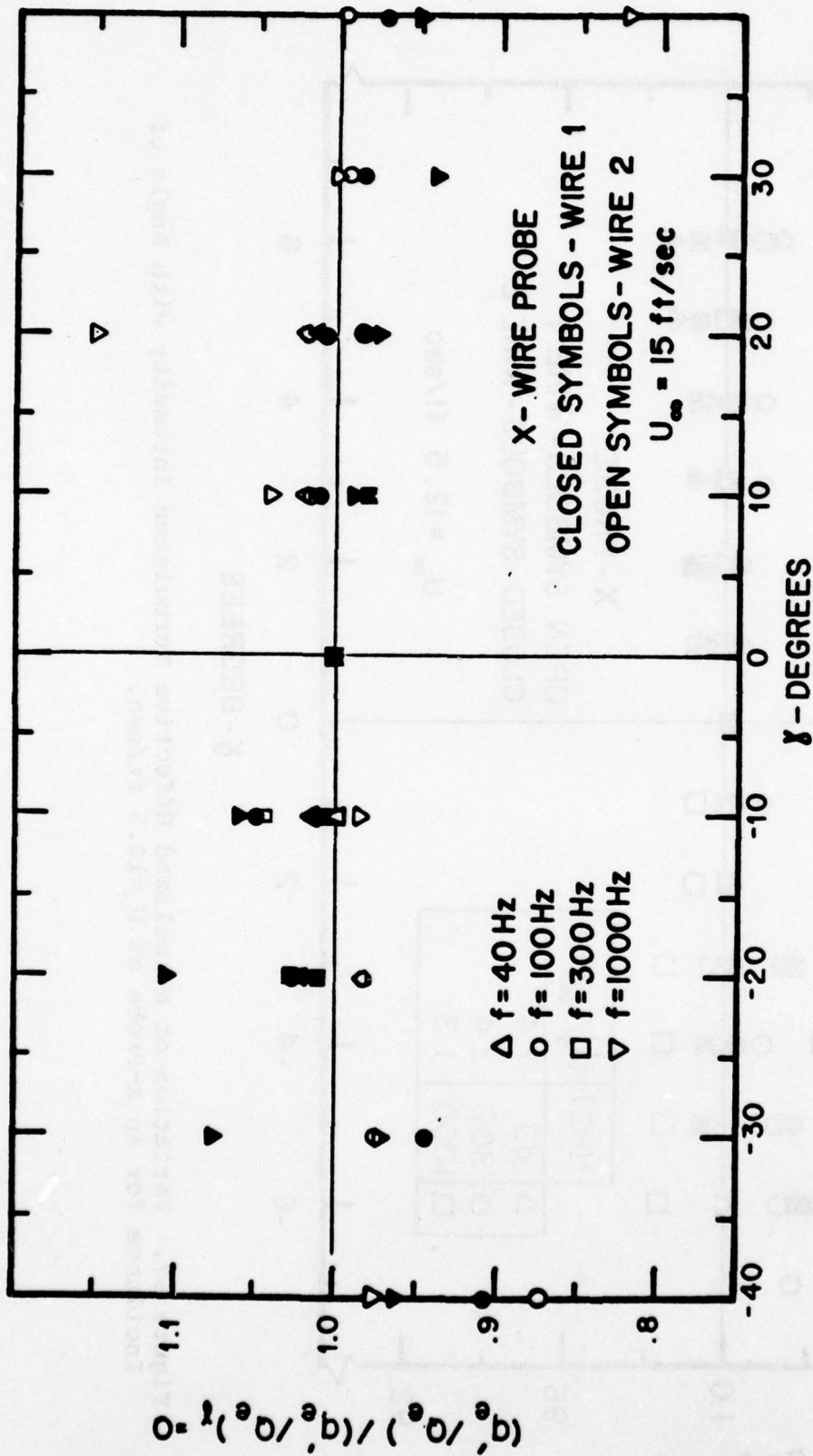


Figure 68. Variation of Normalized Effective Turbulence Intensity with Angle of Incidence for an X-Probe at $U_\infty = 15$ ft/sec.

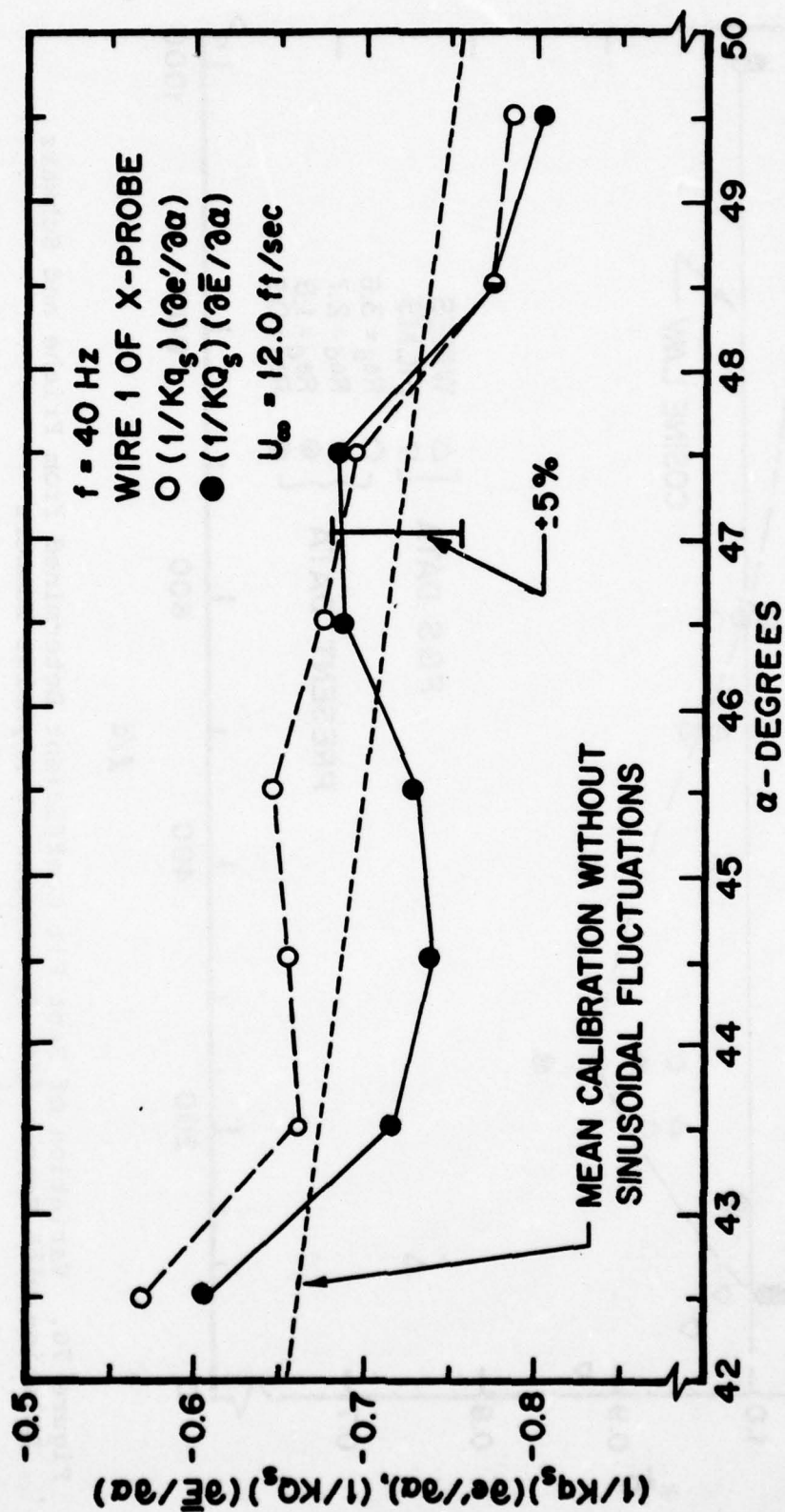


Figure 69. Comparison of X-Probe Velocity Sensitivity Term Calculated from Mean Velocity Yaw Calibration Data with that Calculated from Fluctuating Velocity Yaw Calibration Data

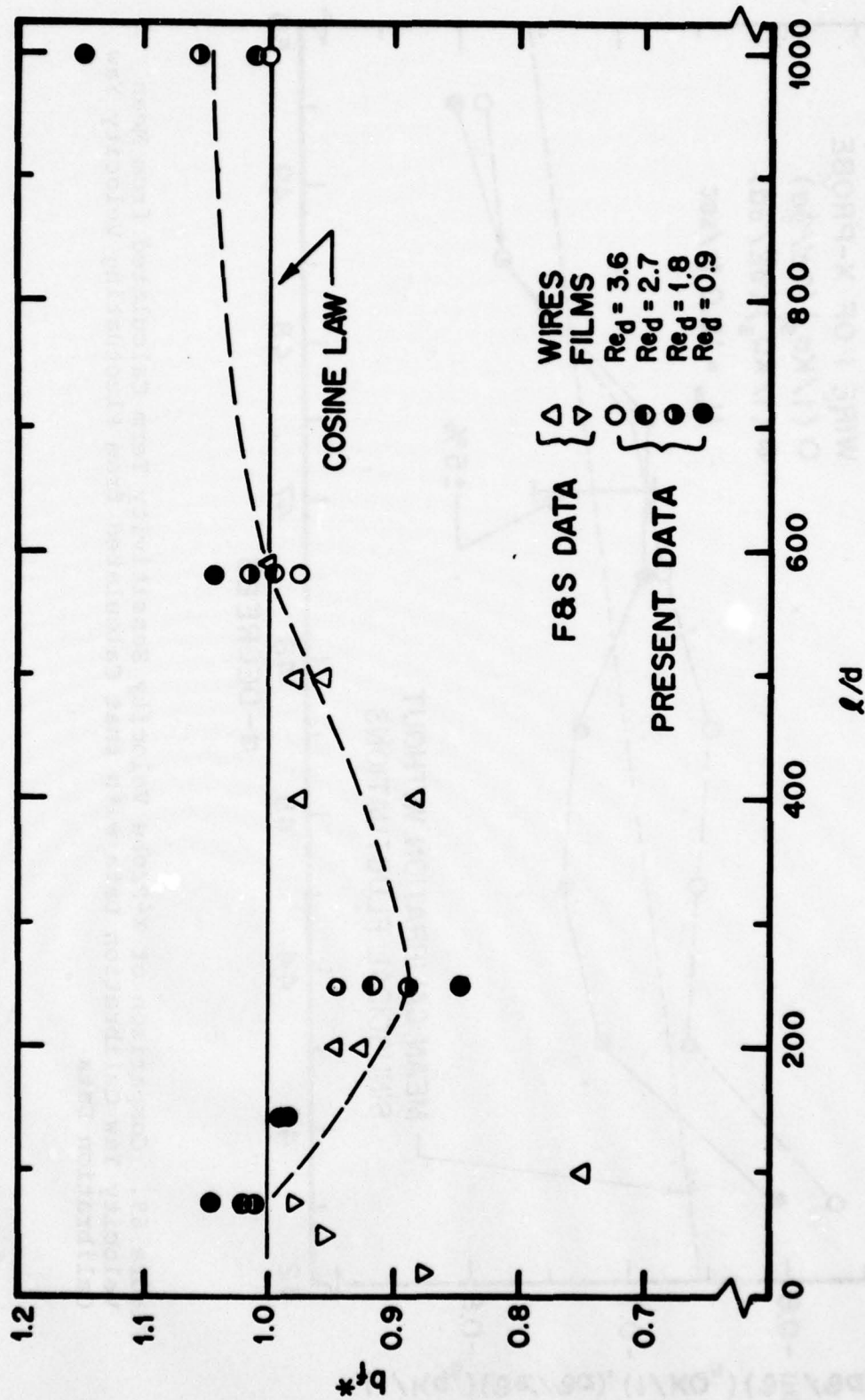


Figure 70. Variation of Best Fit Coefficient Determined from Friehe and Schwarz Relation with Sensor l/d for Different Reynolds Numbers

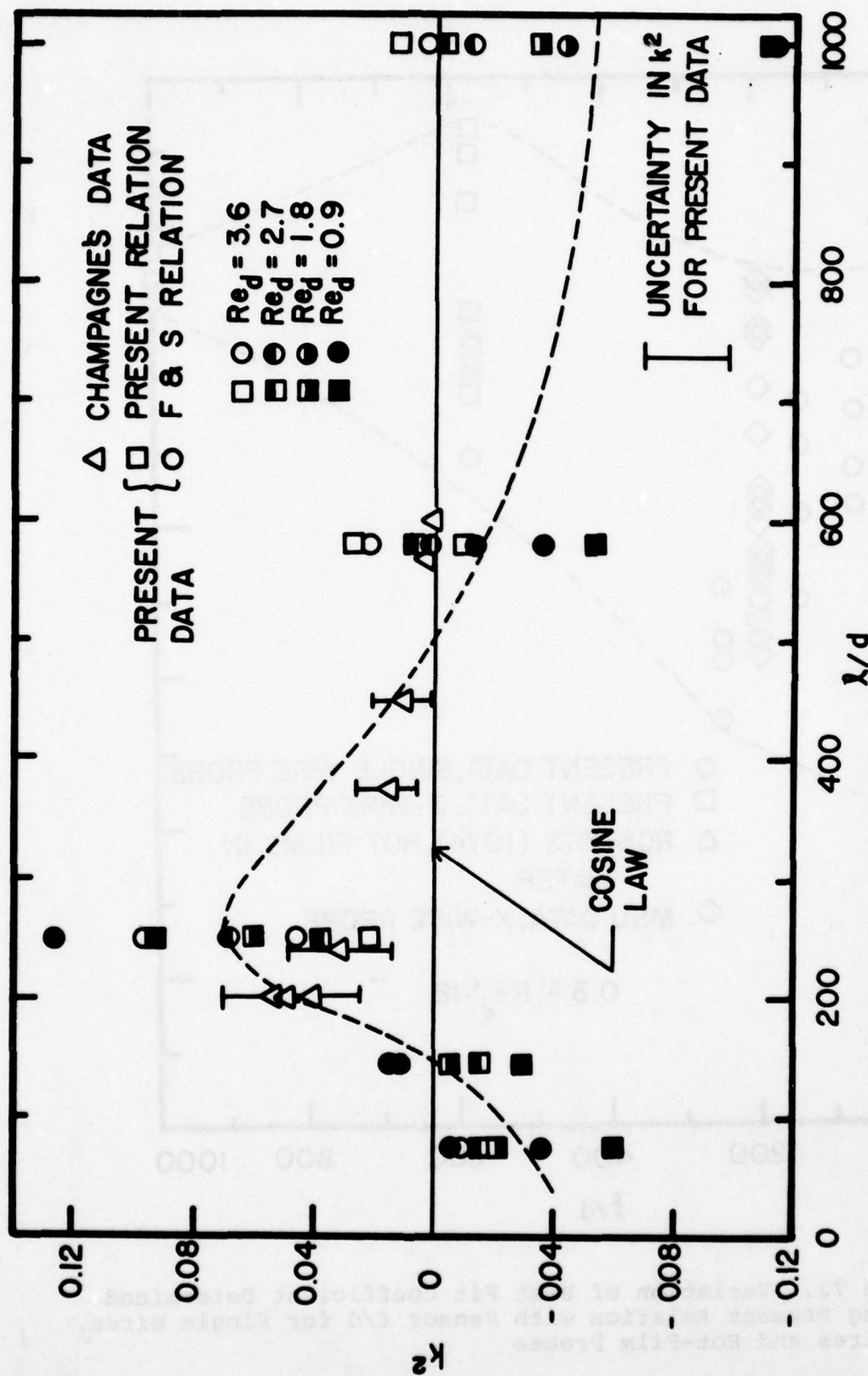


Figure 71. Variation of Equivalent Coefficient Determined from Hinze-Champagne Relation with Sensor λ/d , for Different Reynolds Numbers

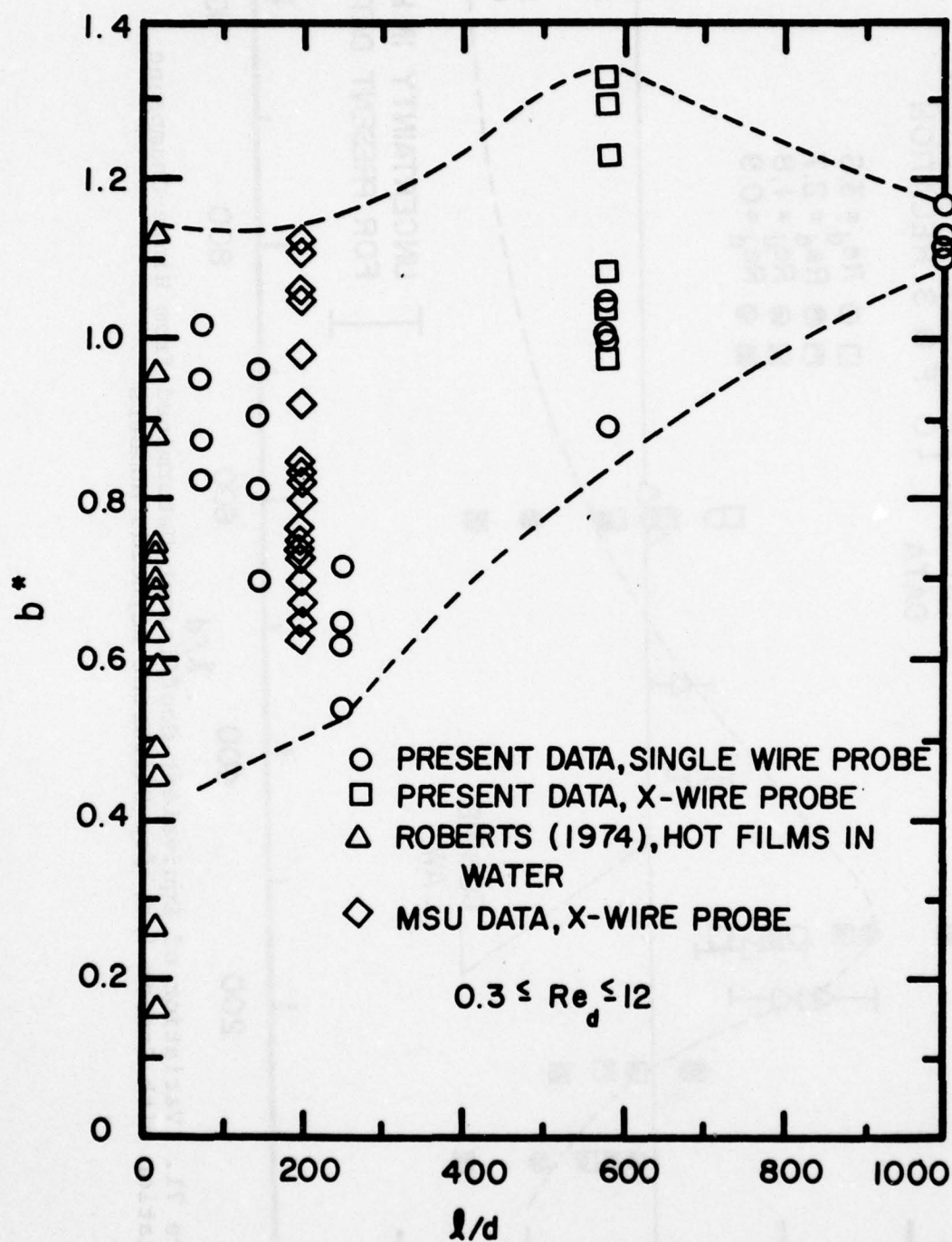


Figure 72. Variation of Best Fit Coefficient Determined Using Present Relation with Sensor l/d for Single Wires, X-Wires and Hot-Film Probes

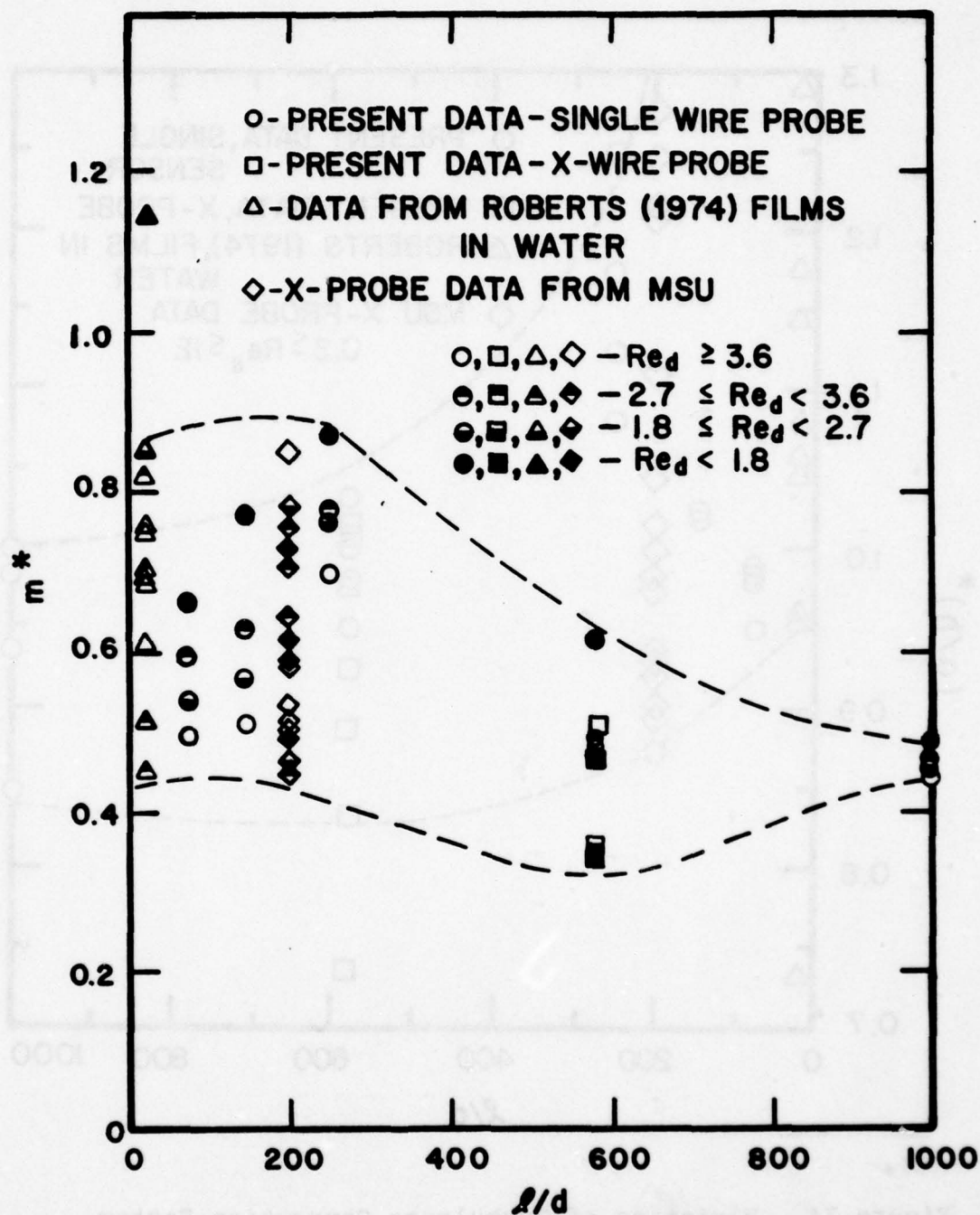


Figure 73. Variation of Best Fit Exponent Determined Using Present Relation with Sensor for Single Wires, X-Wires and Hot-Film Probes

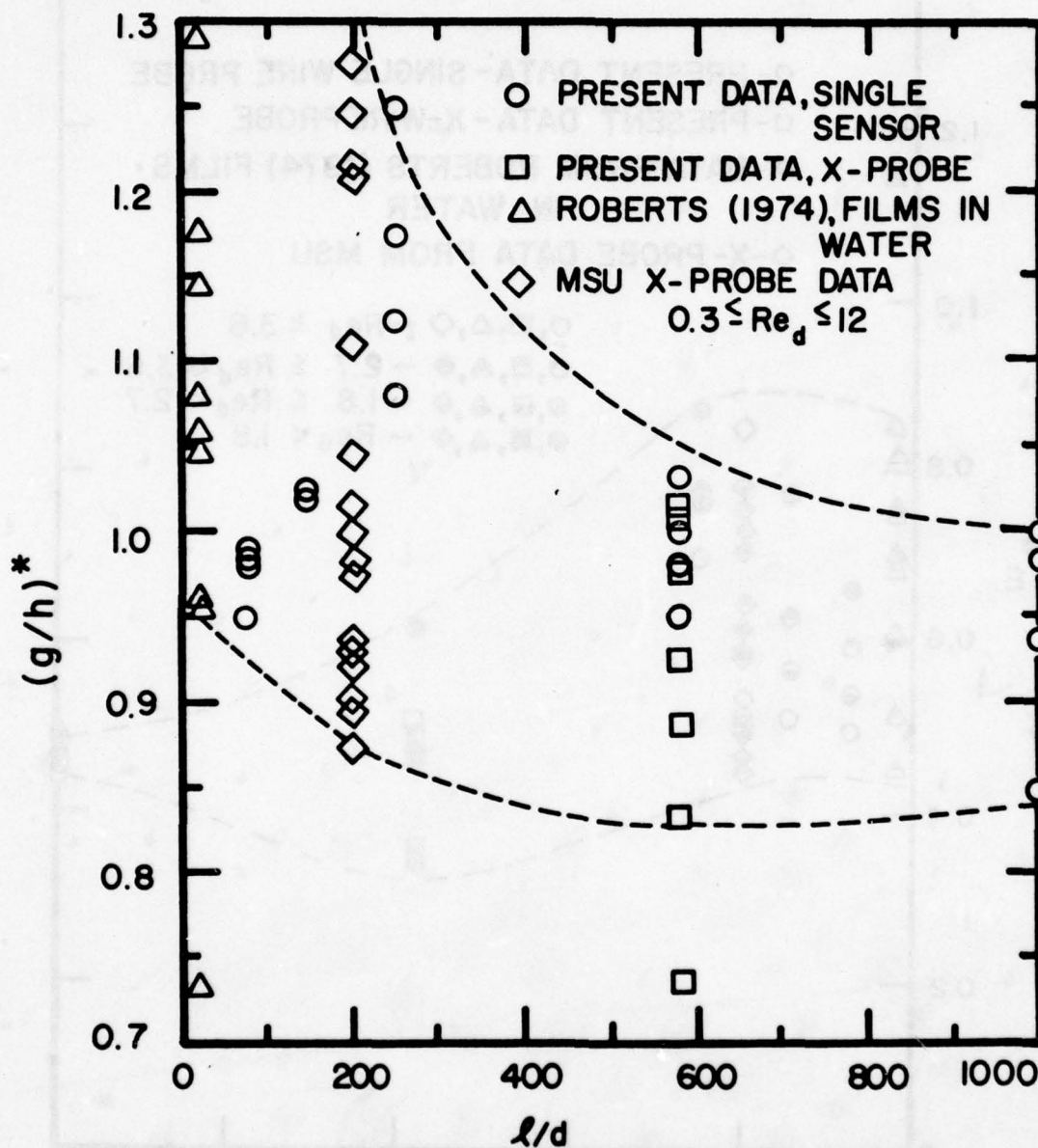


Figure 74. Variation of Turbulence Correction Factor Determined Using Present Relation with Sensor l/d for Single Wires, X-Wires and Hot-Film Probes

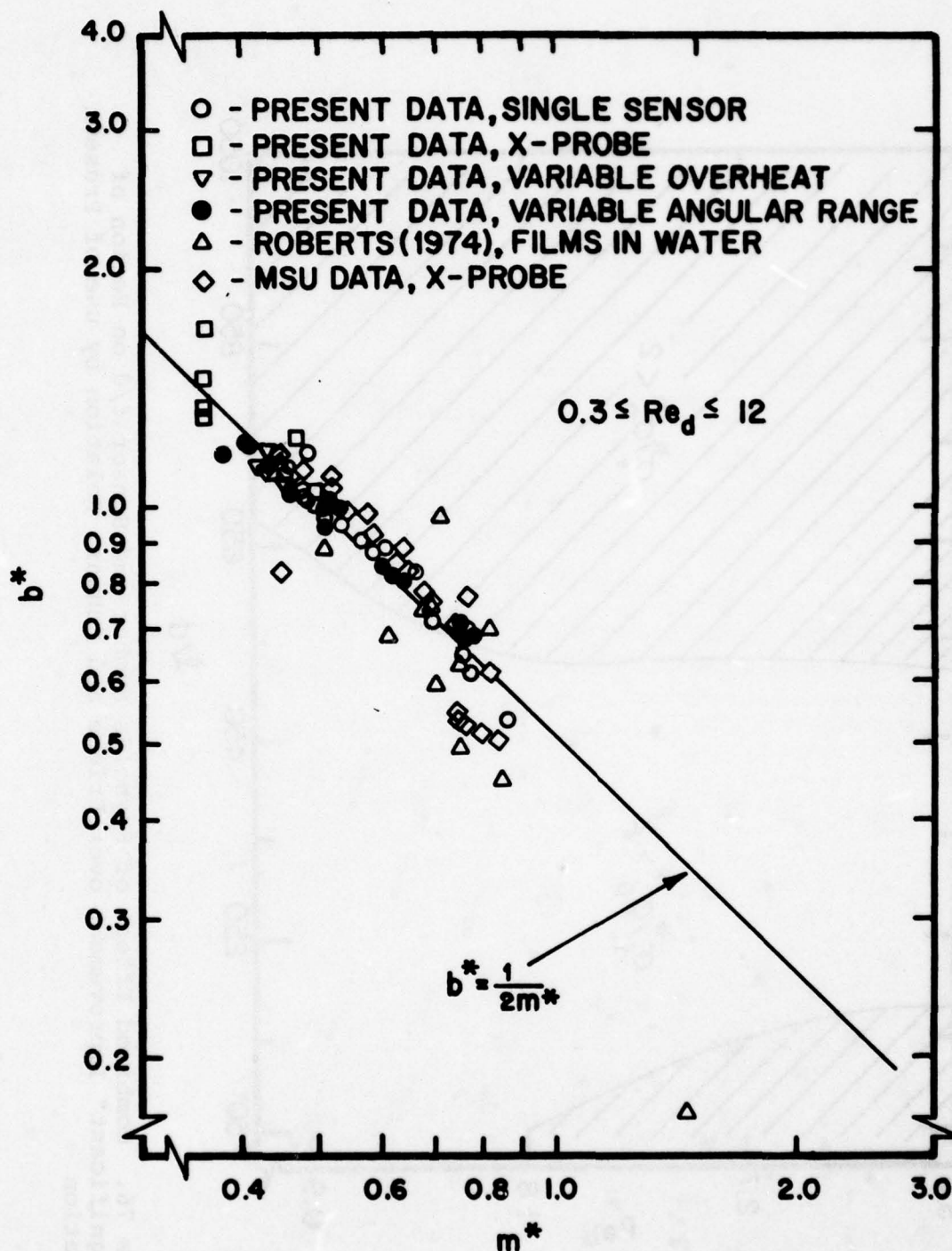


Figure 75. Correlation Between Best Fit Coefficients and Exponents Determined Using Present Relation for Single Wires, X-Wires and Hot-Film Probes

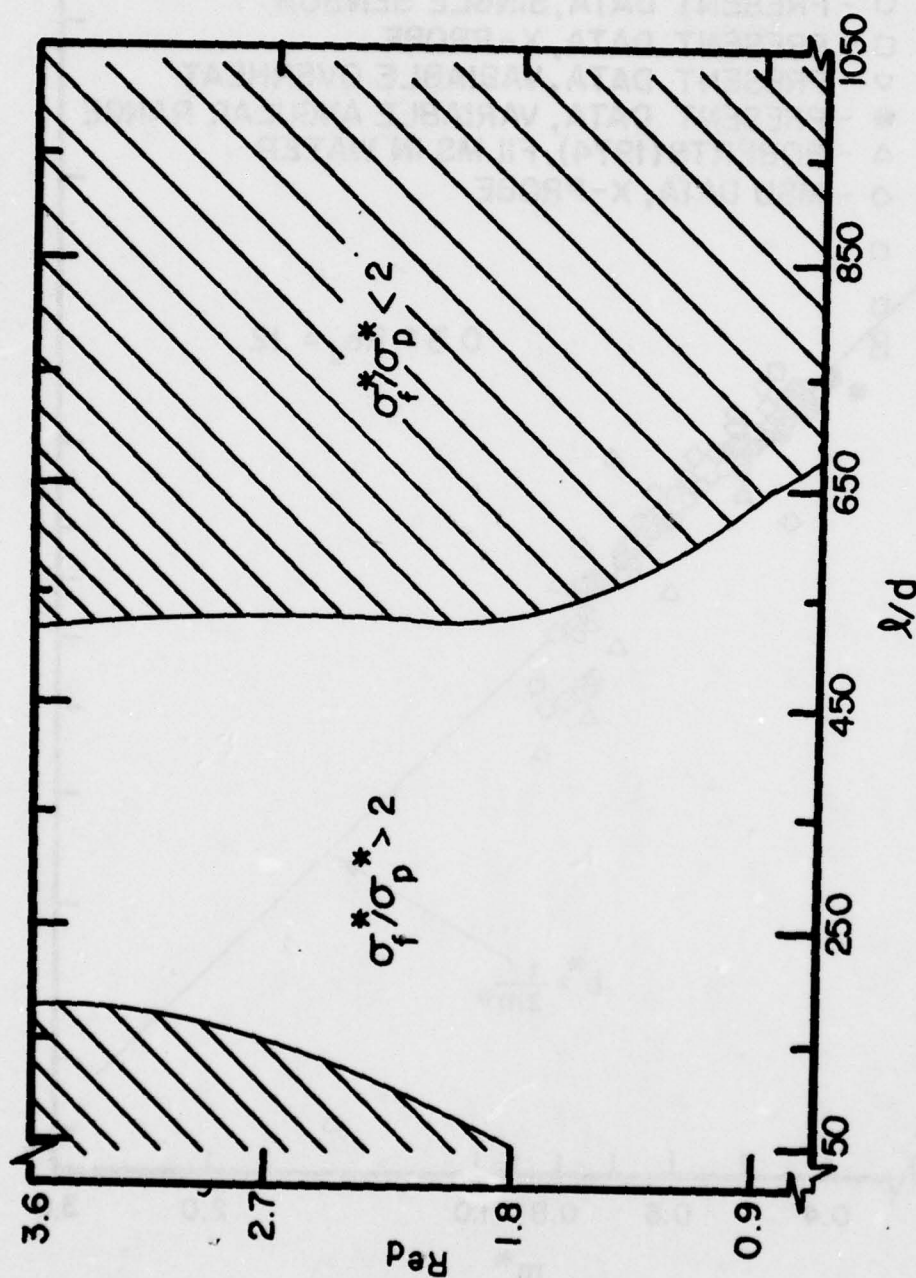


Figure 76. Combined Effect of Reynolds Number and Sensor l/d on Region of "Significant" Improvement over Friehe and Schwarz Relation by use of Present Relation

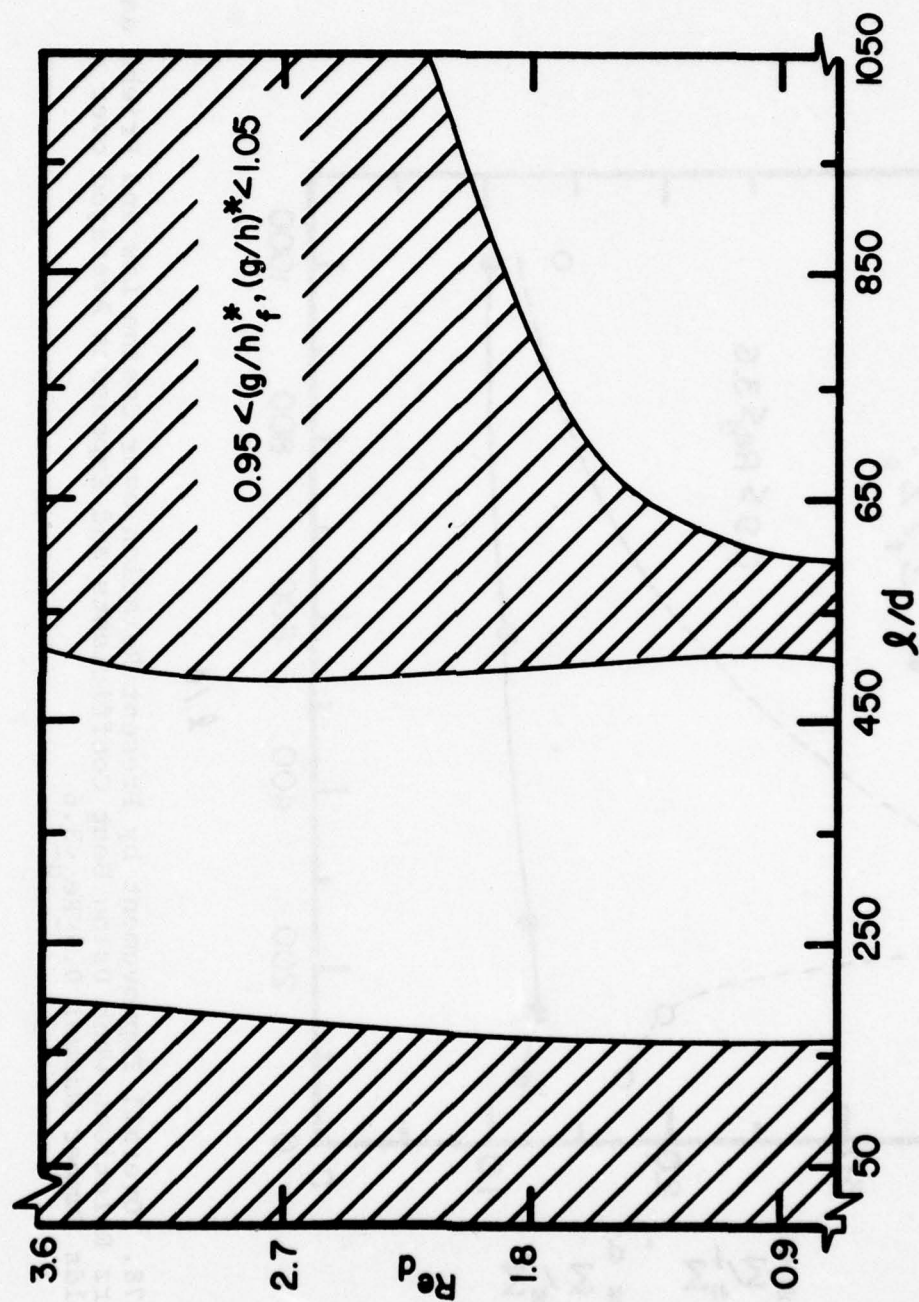


Figure 77. Combined Effect of Reynolds Number and Sensor l/d on Regions Where Turbulence Correction Factor Follows "Cosine-Like" Behavior

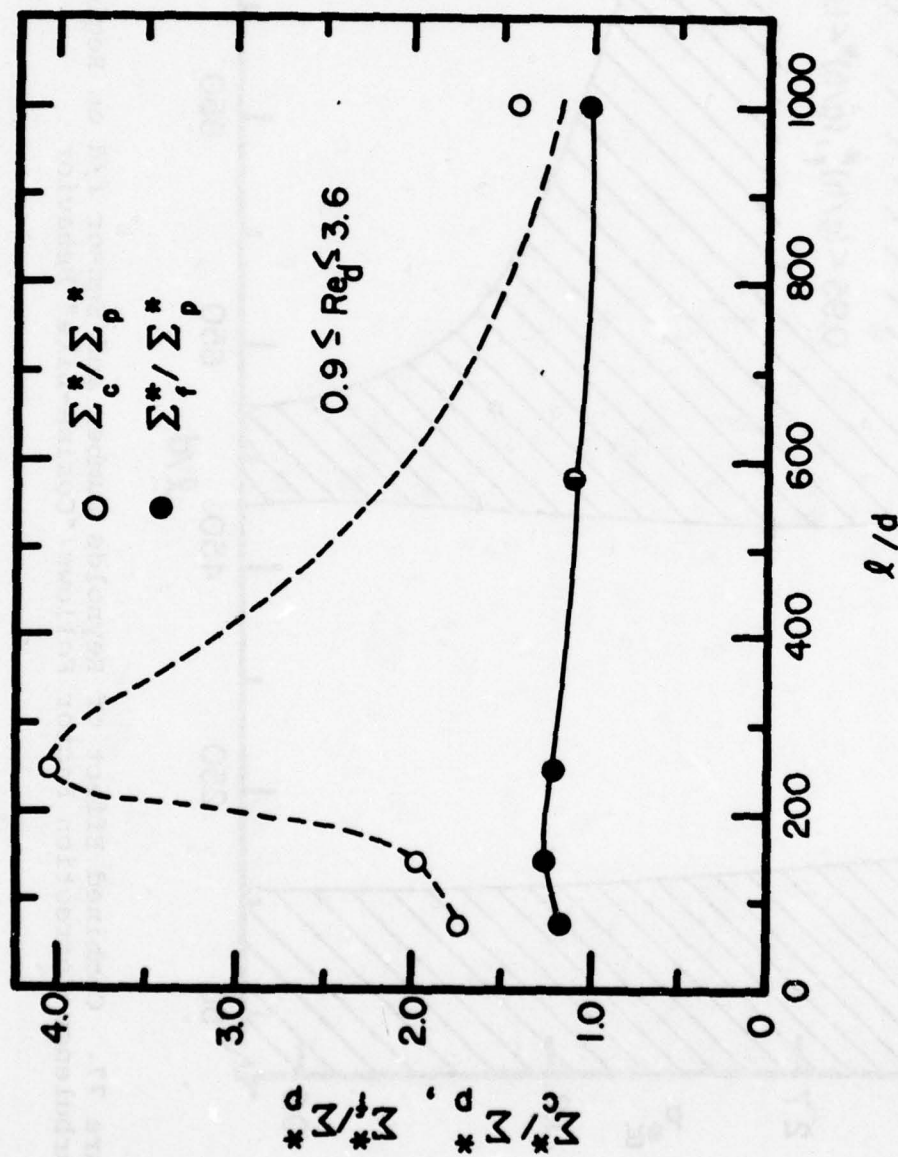


Figure 78. Overall Improvement by Present Relation over Cosine Law and Friehe and Schwarz Relations when Using Best Coefficients and Exponents Averaged over a Reynolds Number Range; $0.9 \leq Re_d \leq 3.6$

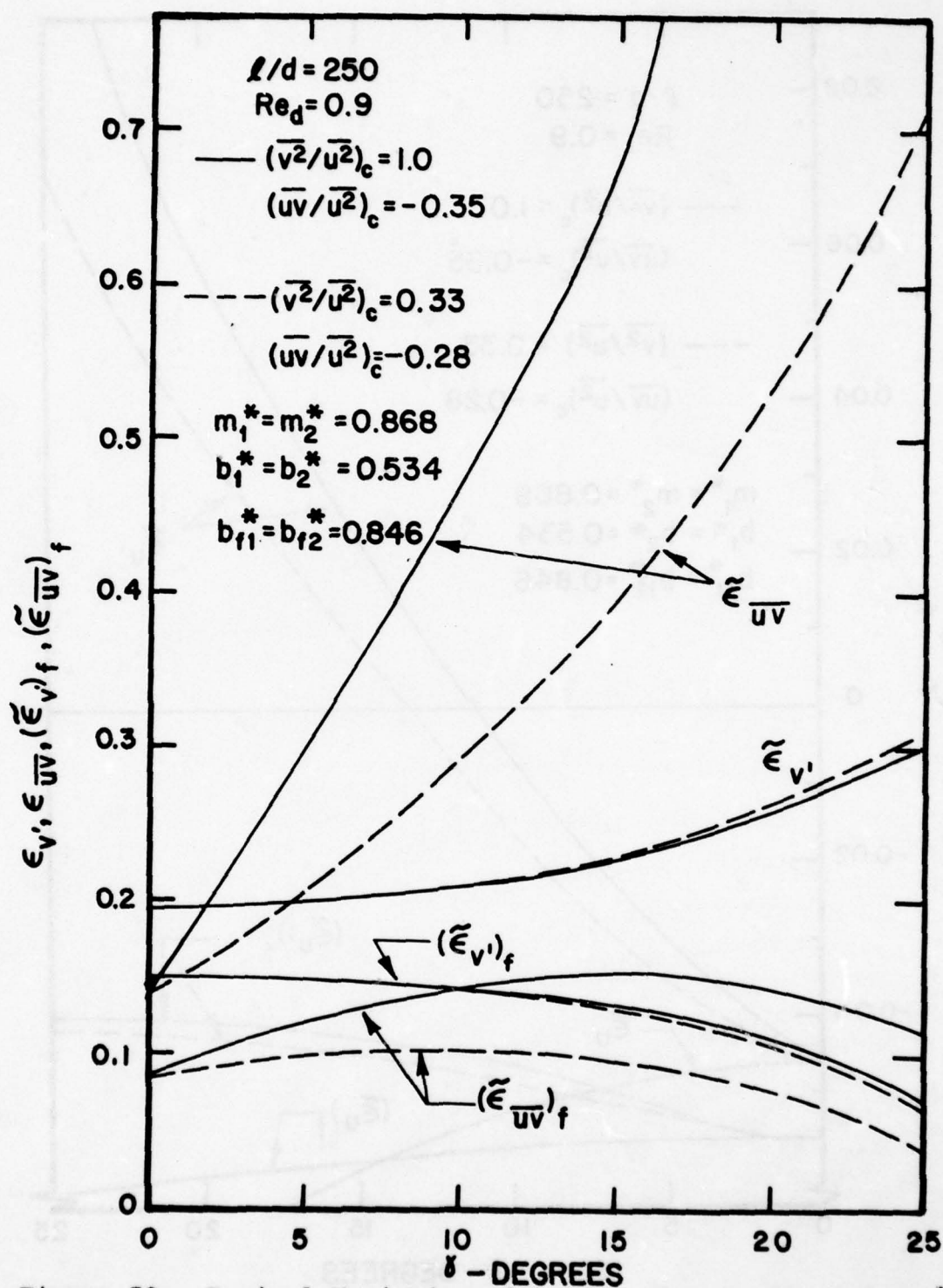


Figure 79. Typical Variation with Mean Flow Angle of Computed Differences in v' and \bar{uv} Obtained Using Different Yaw Relations for a Sensor with Large Deviations from Cosine Law

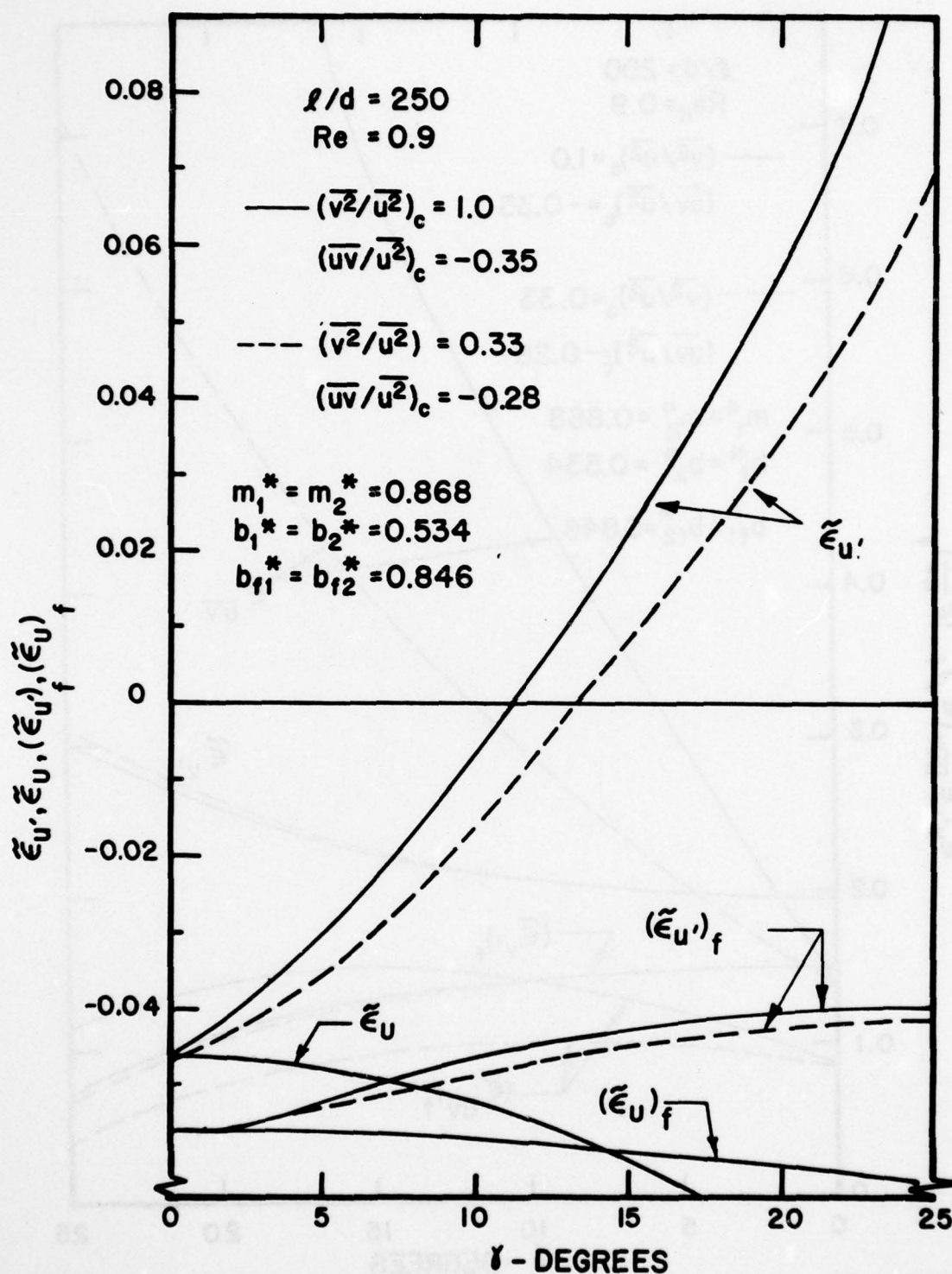


Figure 80. Typical Variation with Mean Flow Angle of Computed Differences in U and u' Intensity Obtained Using Different Yaw Relations for a Sensor with Large Deviation from Cosine Law

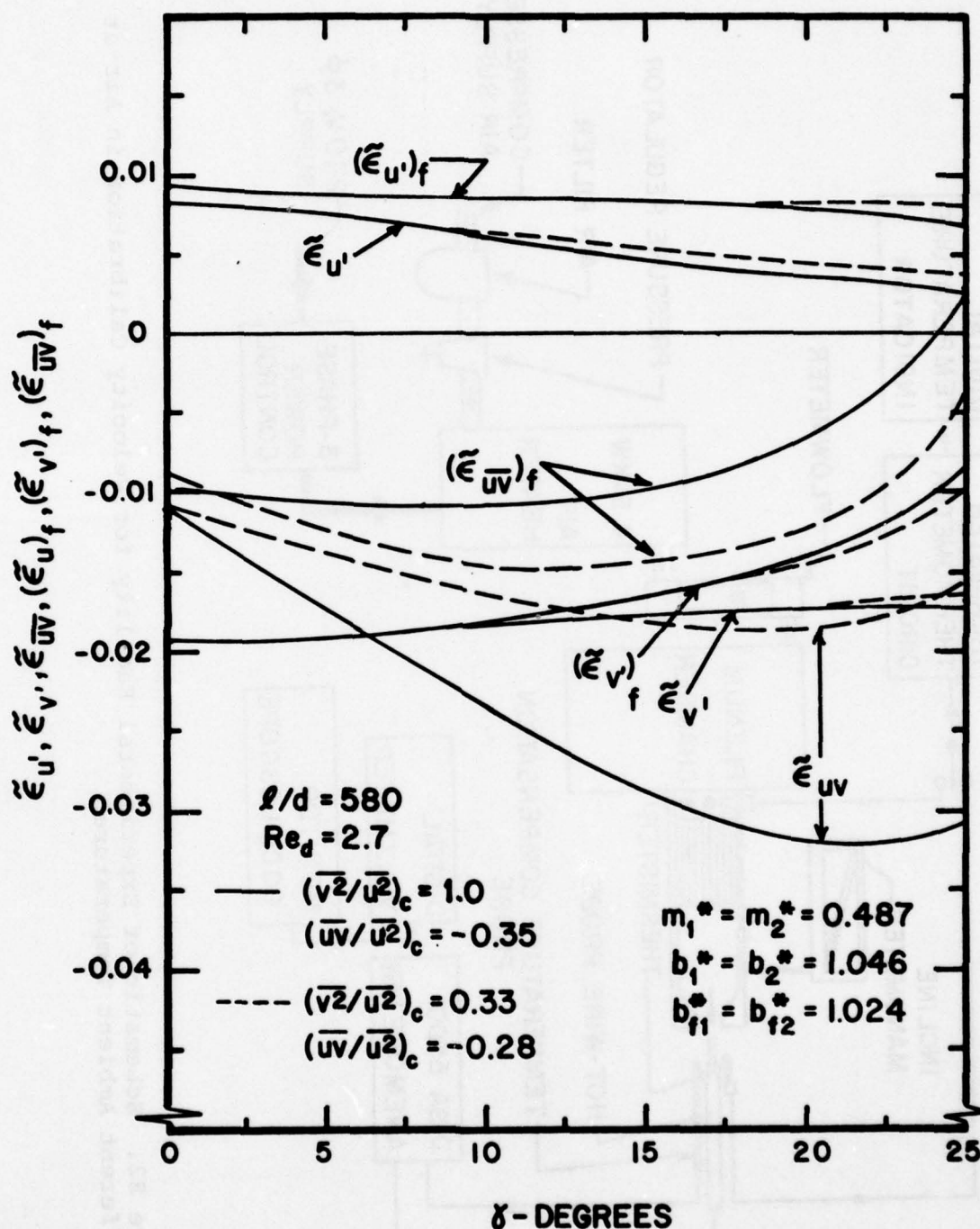


Figure 81. Typical Variation with Mean Flow Angle of Computed Turbulence Velocities Obtained Using Different Yaw Relations for a Standard-length Single Wire Probe

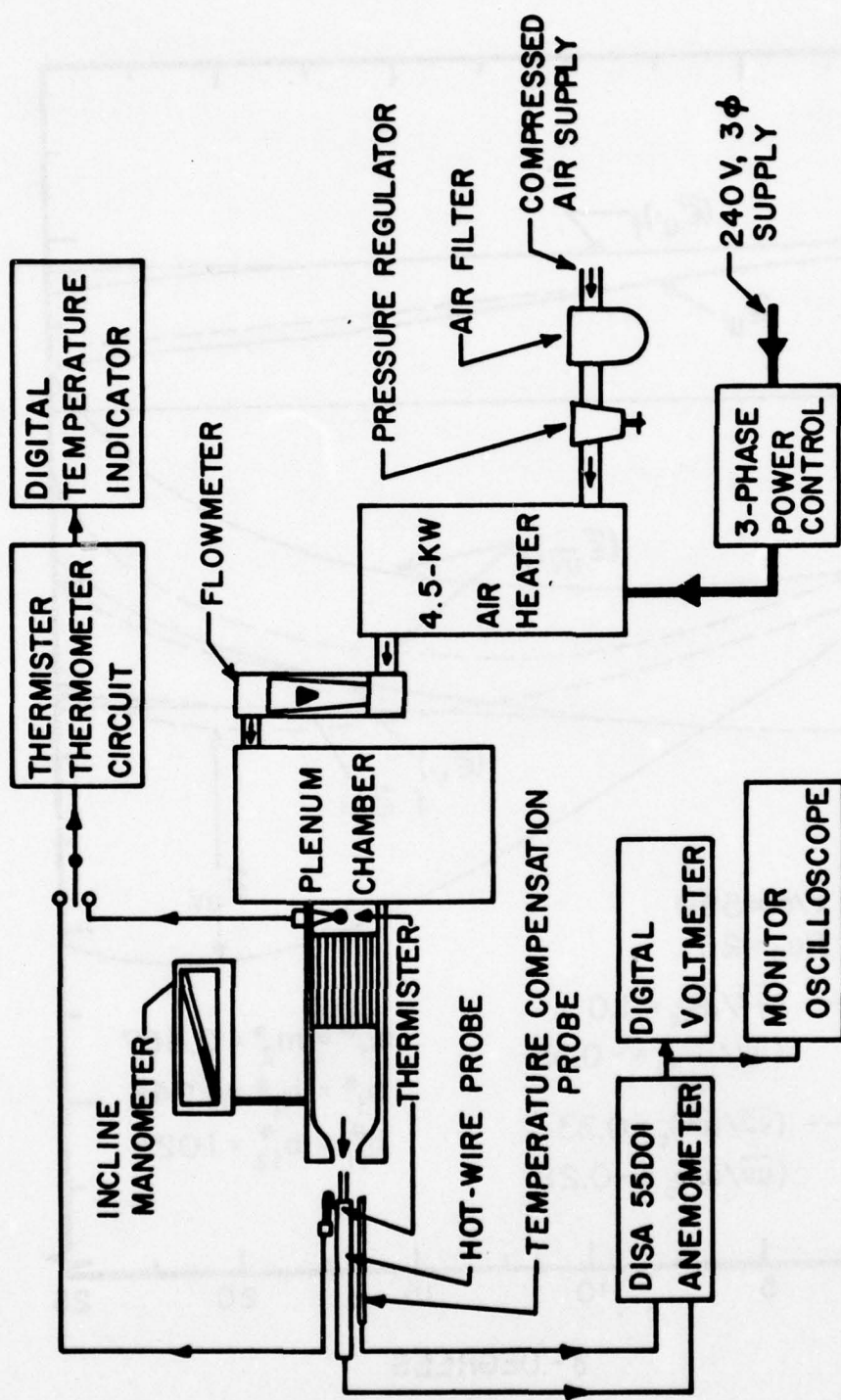


Figure 82. Schematic of Experimental Facility for Velocity Calibration in Air at Different Ambient Temperatures

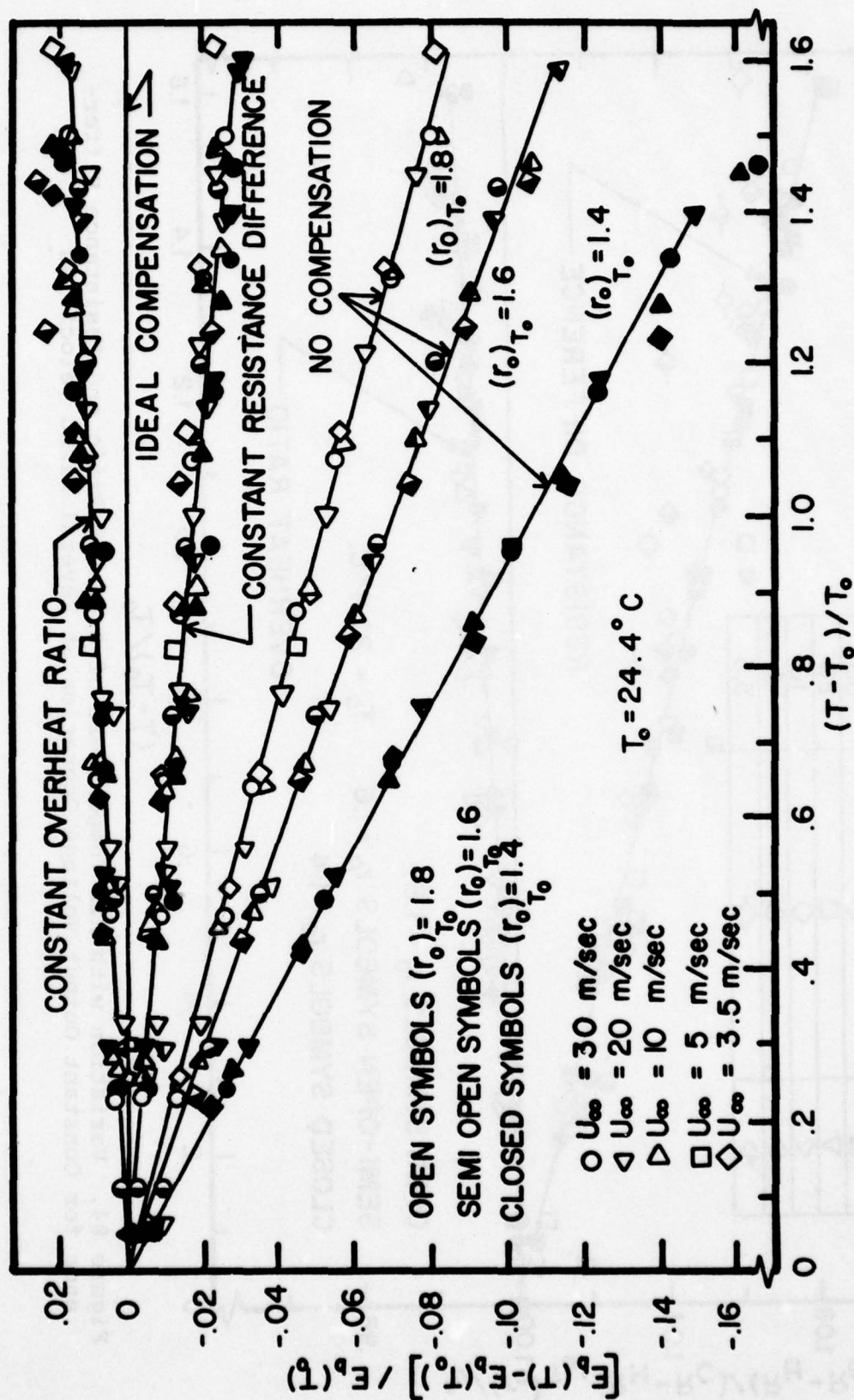


Figure 83. Effect of Air Temperature on Output of Anemometer for Different Overheat Ratios Including Operation in Constant Overheat Ratio and Constant Resistance Difference Modes at Several Fixed Velocities

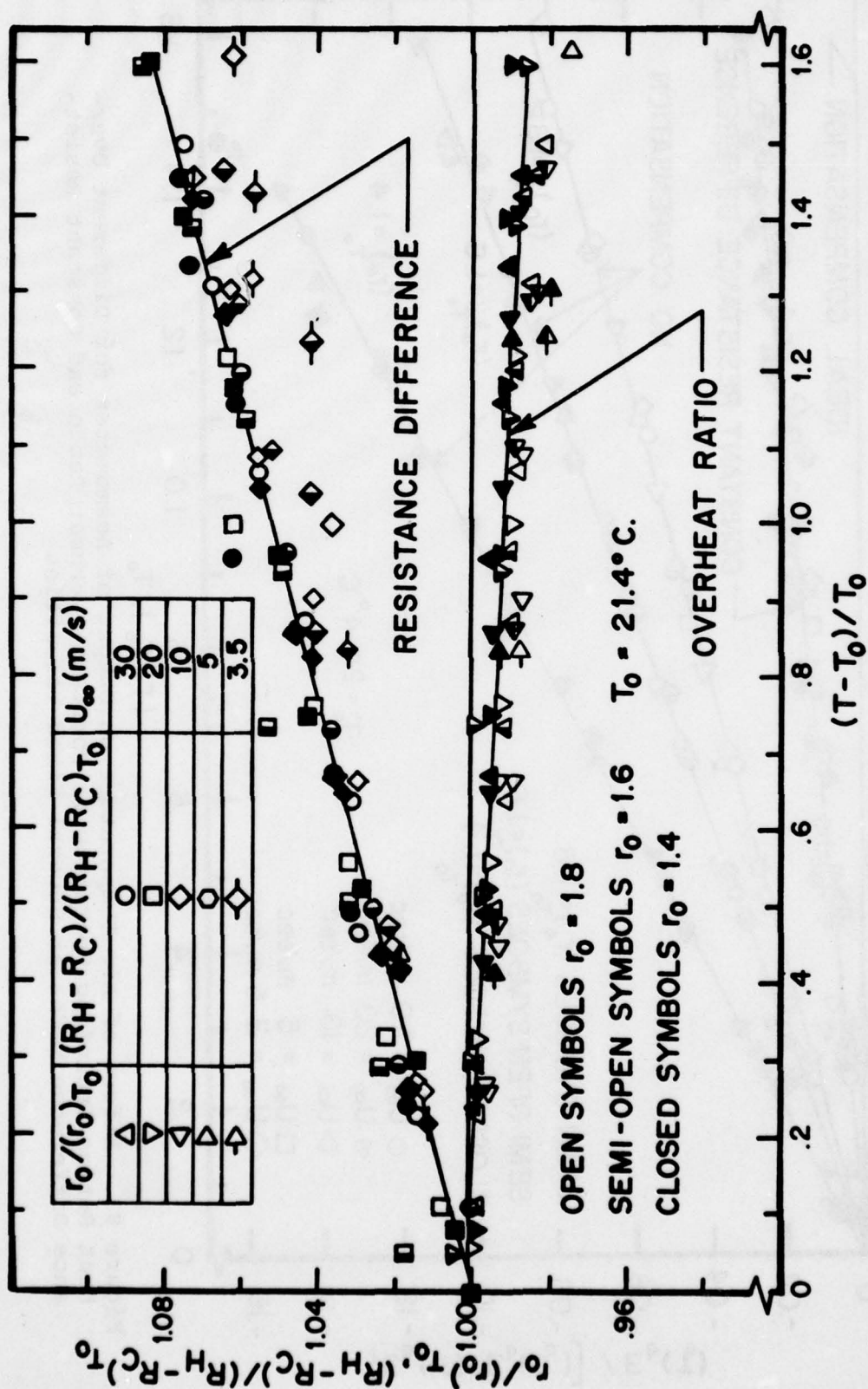


Figure 84. Variation with Air Temperature of Overheat Ratio and Resistance Difference for Constant Output Voltage Operation at Several Fixed Velocities

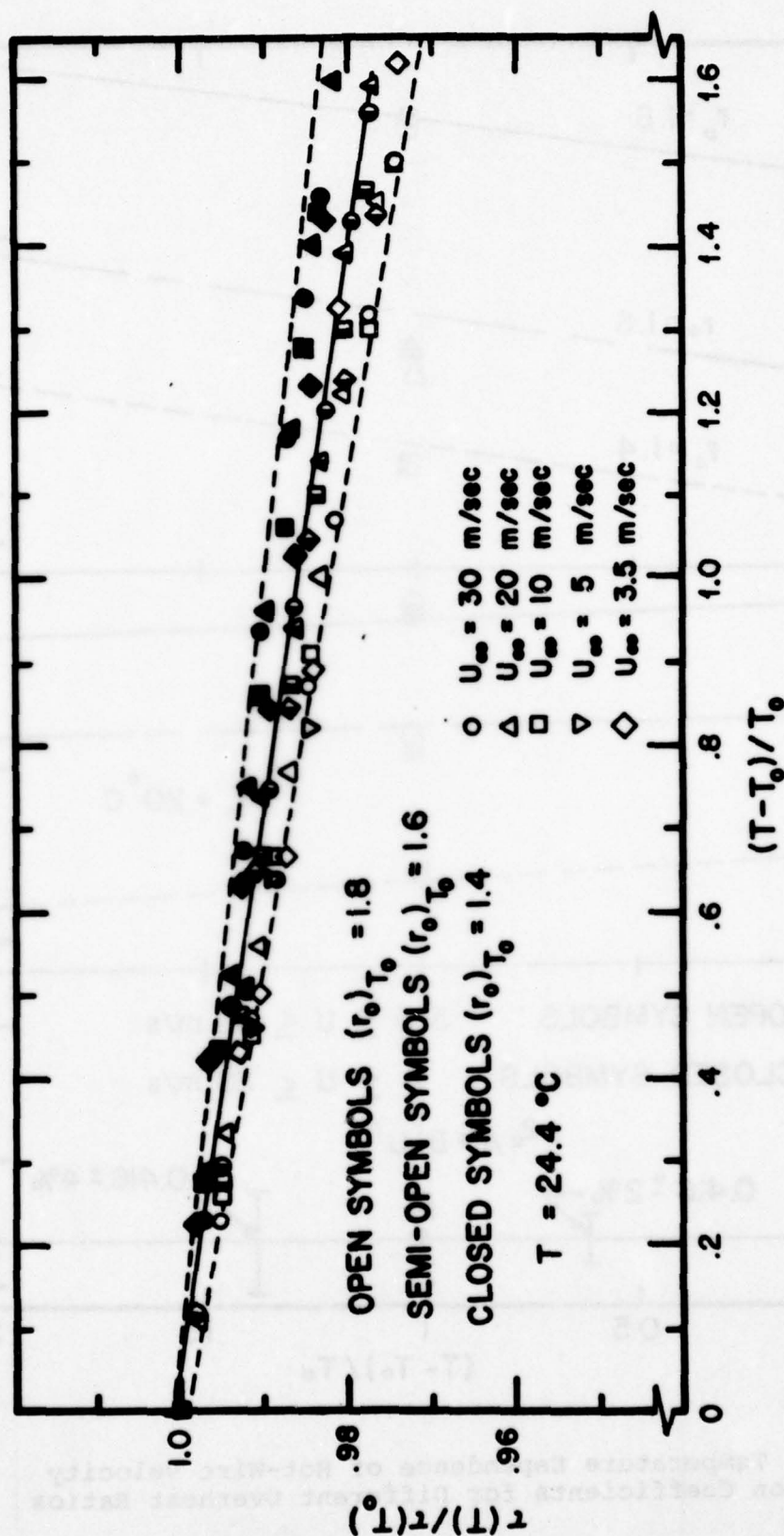


Figure 85. Typical Temperature Dependence of Resistances Ratio r for Hot-Wires in Air at Several Fixed Velocities

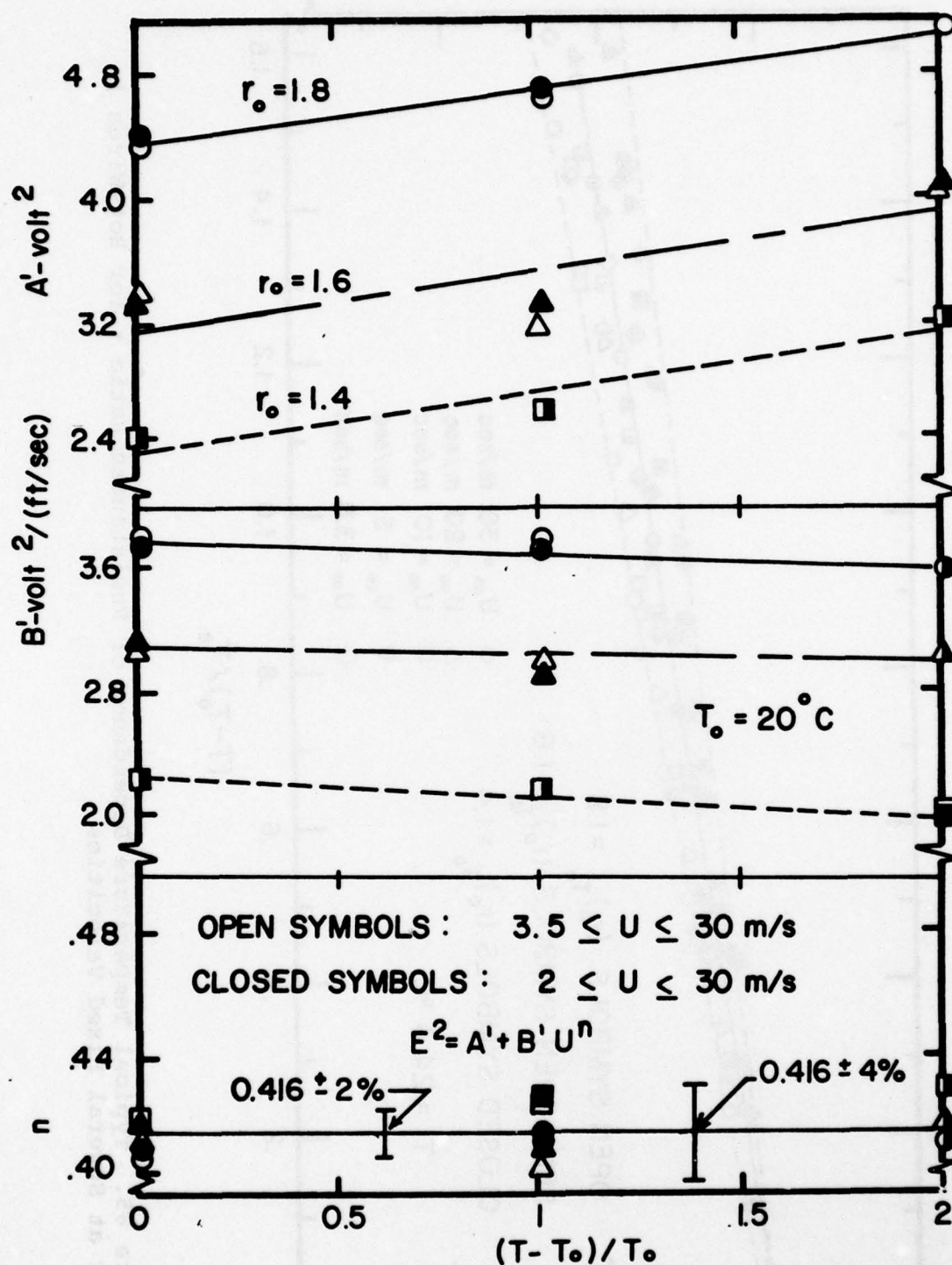


Figure 86. Temperature Dependence of Hot-Wire Velocity Calibration Coefficients for Different Overheat Ratios

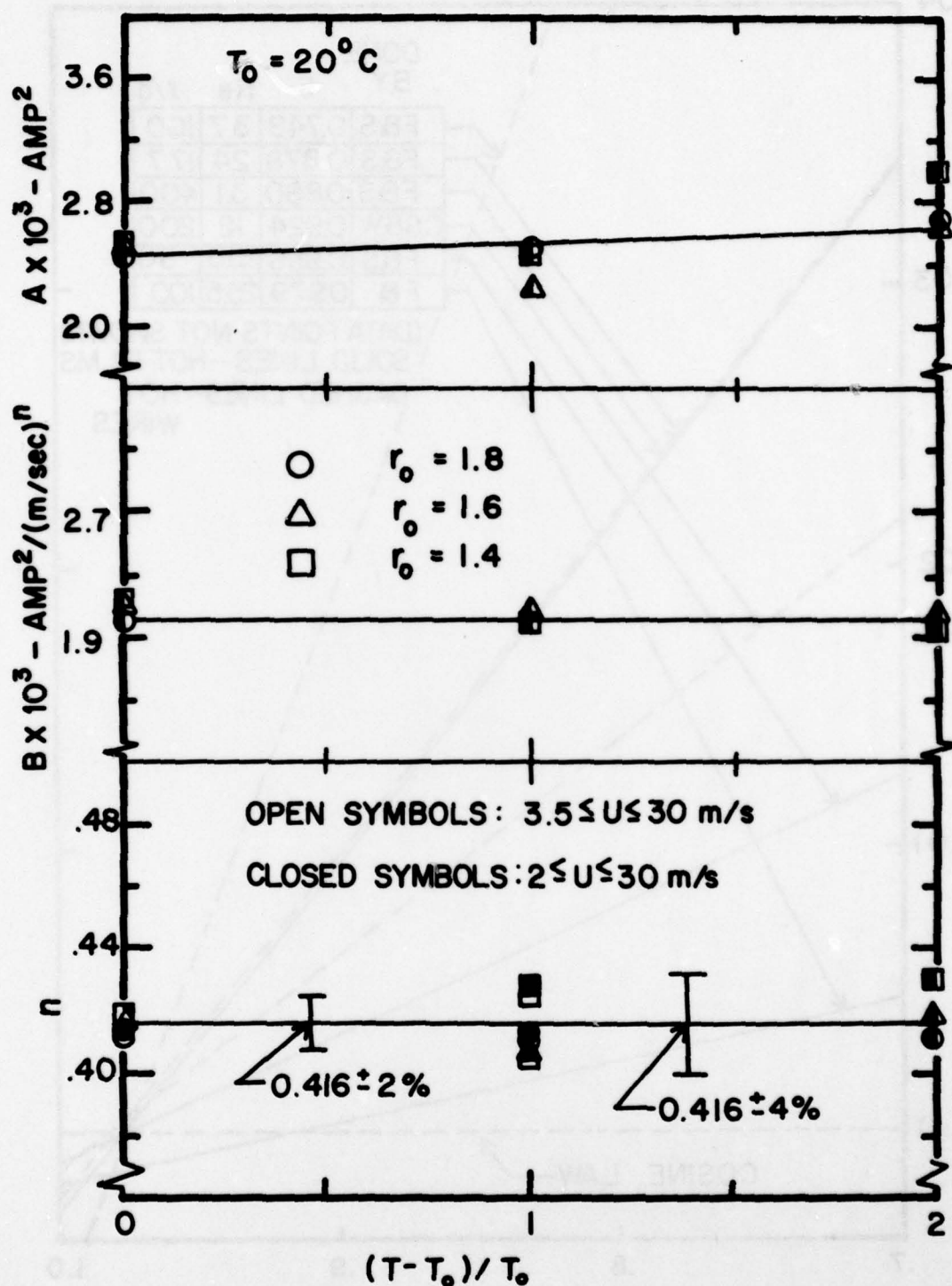


Figure 87. Temperature Dependence of King's Law Coefficients for Different Overheat Ratios

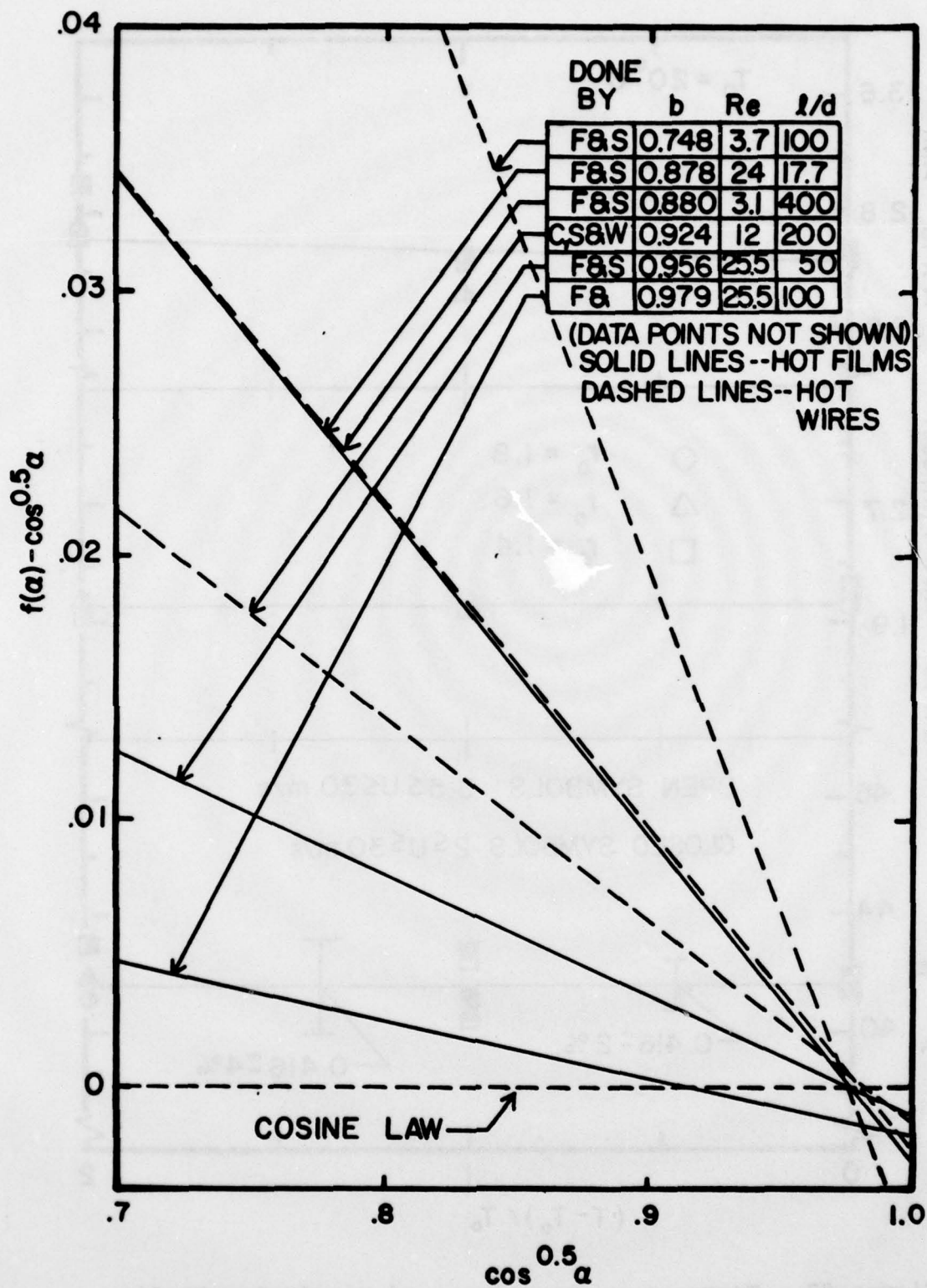


Figure 88. Deviations from Cosine Law as Determined by Friehe and Schwarz

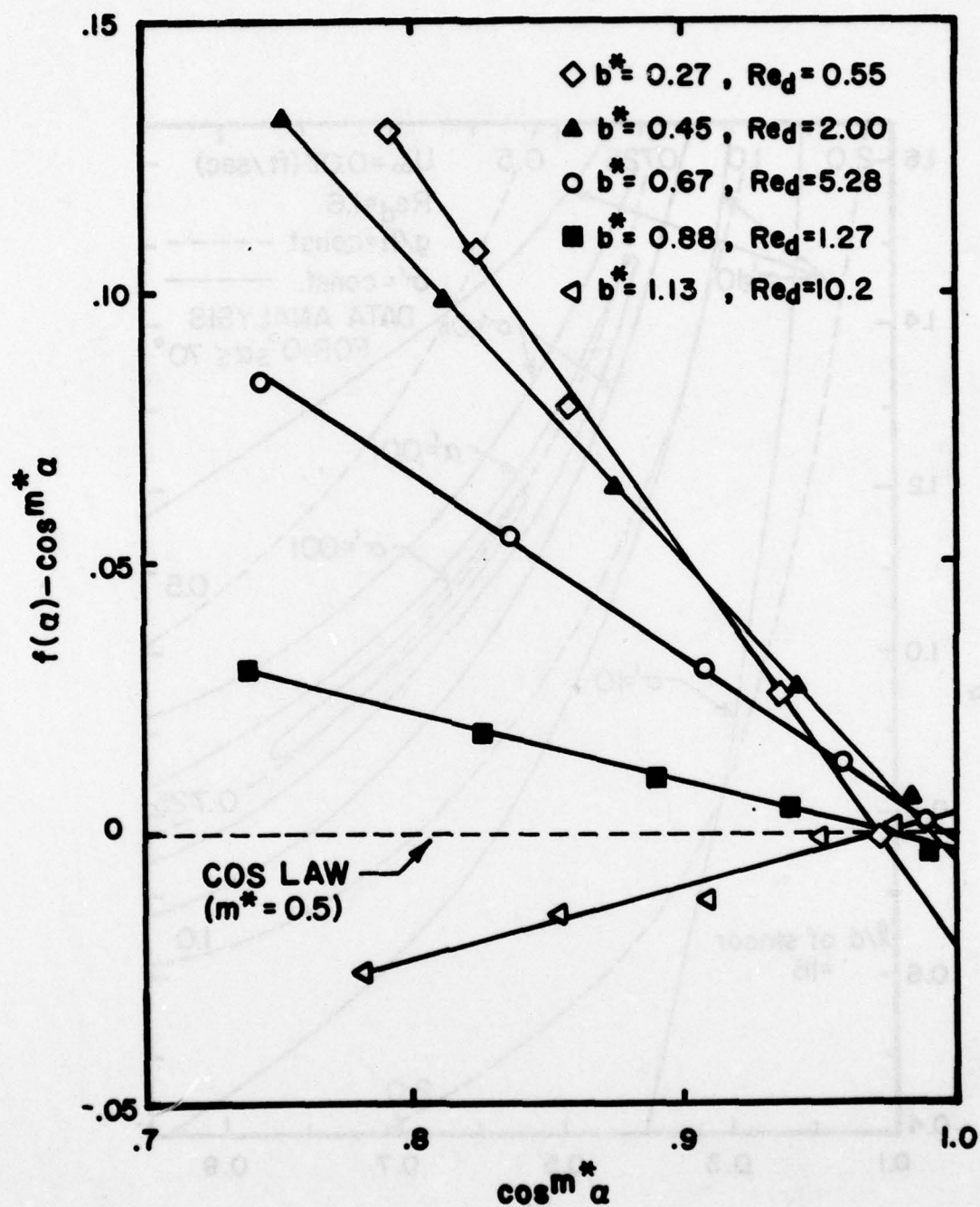


Figure 89. Deviations from Cosine Law for Hot-Films in Water

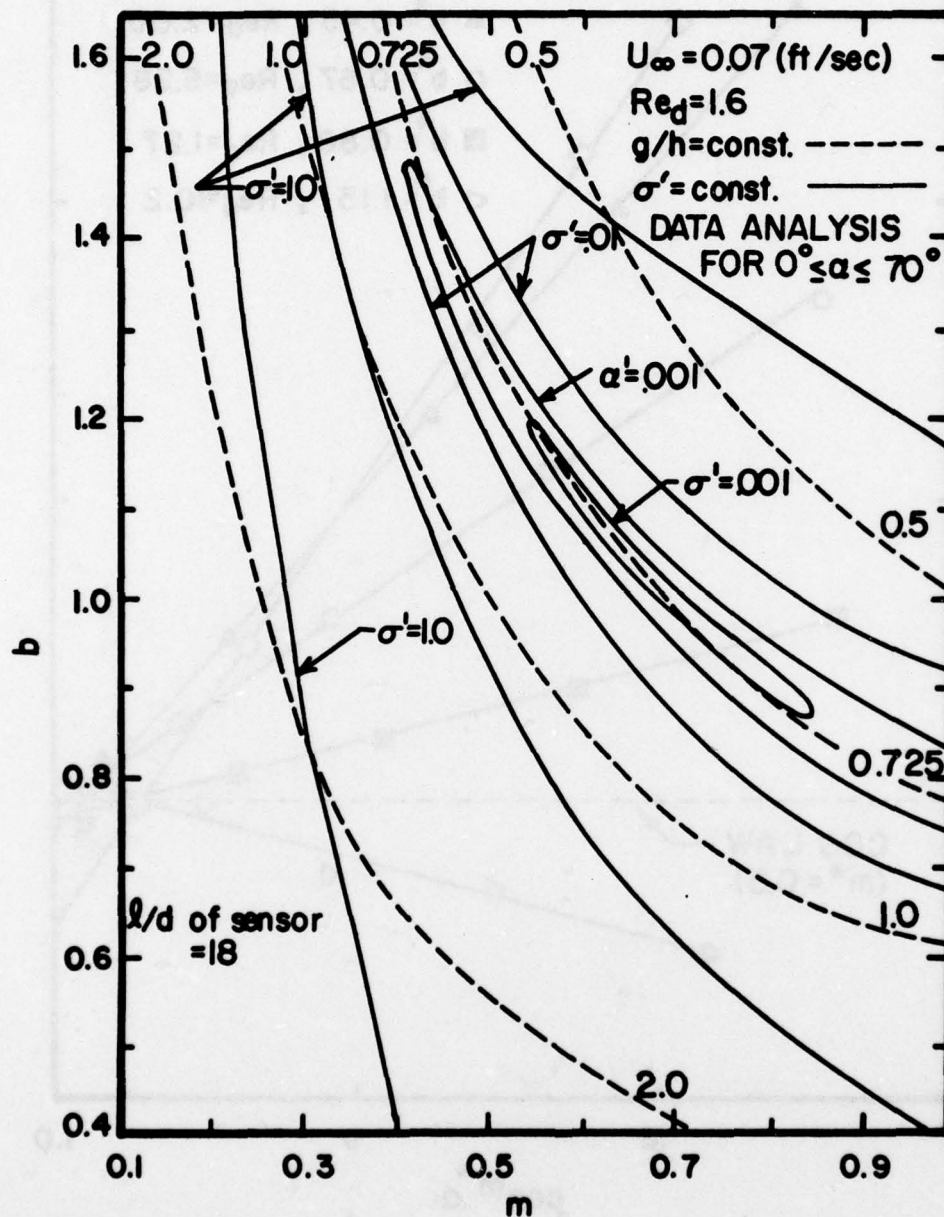


Figure 90. Contours of Constant Standard Deviation of $f(\alpha)$ in b - m Plane for a Hot-Film in Water at $U_{\infty} = 0.07 \text{ ft/sec}$.

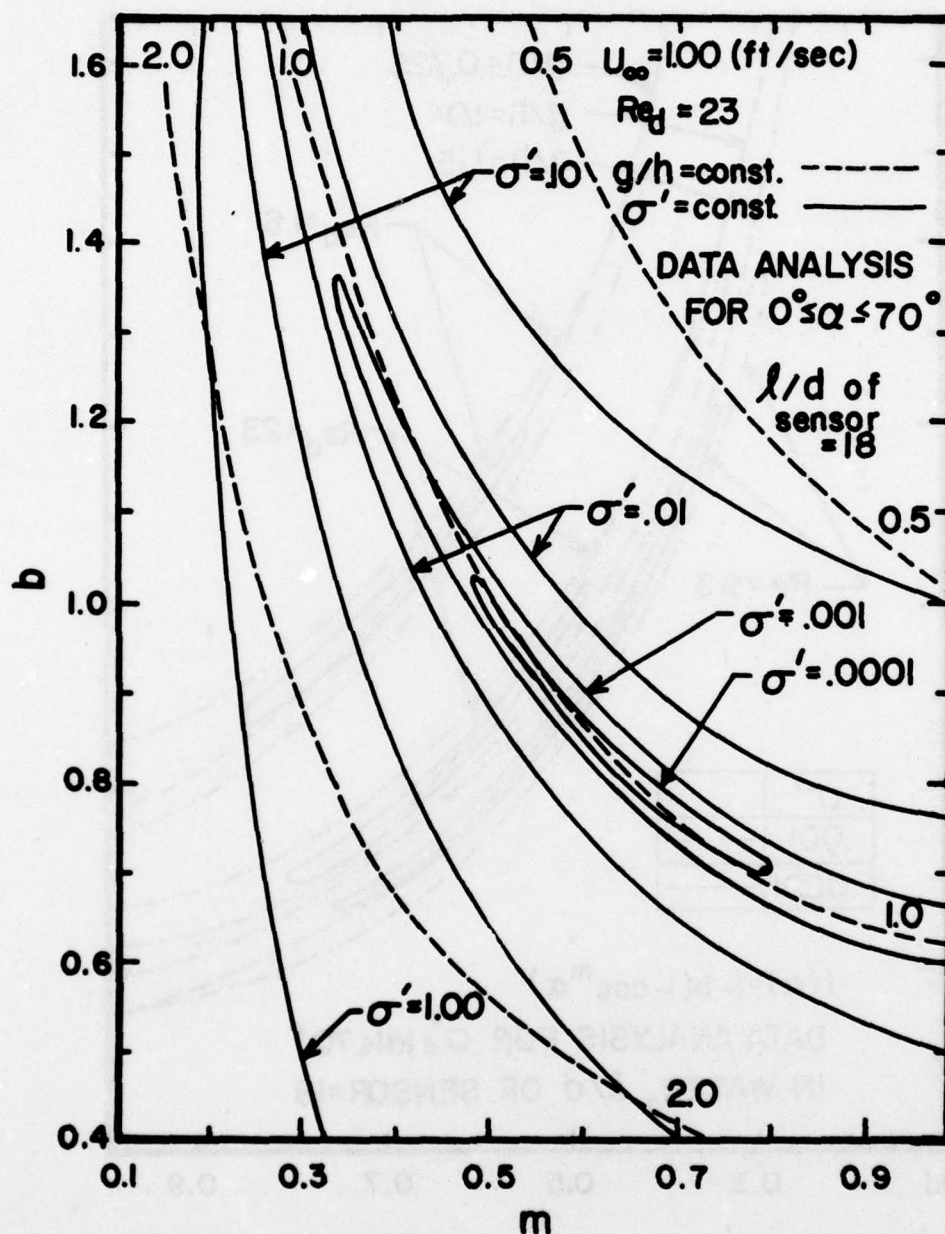


Figure 91. Contours of Constant Standard Deviation of $f(\alpha)$ in b - m Plane for a Hot-Film in Water at $U_\infty = 1.0$ ft/sec.

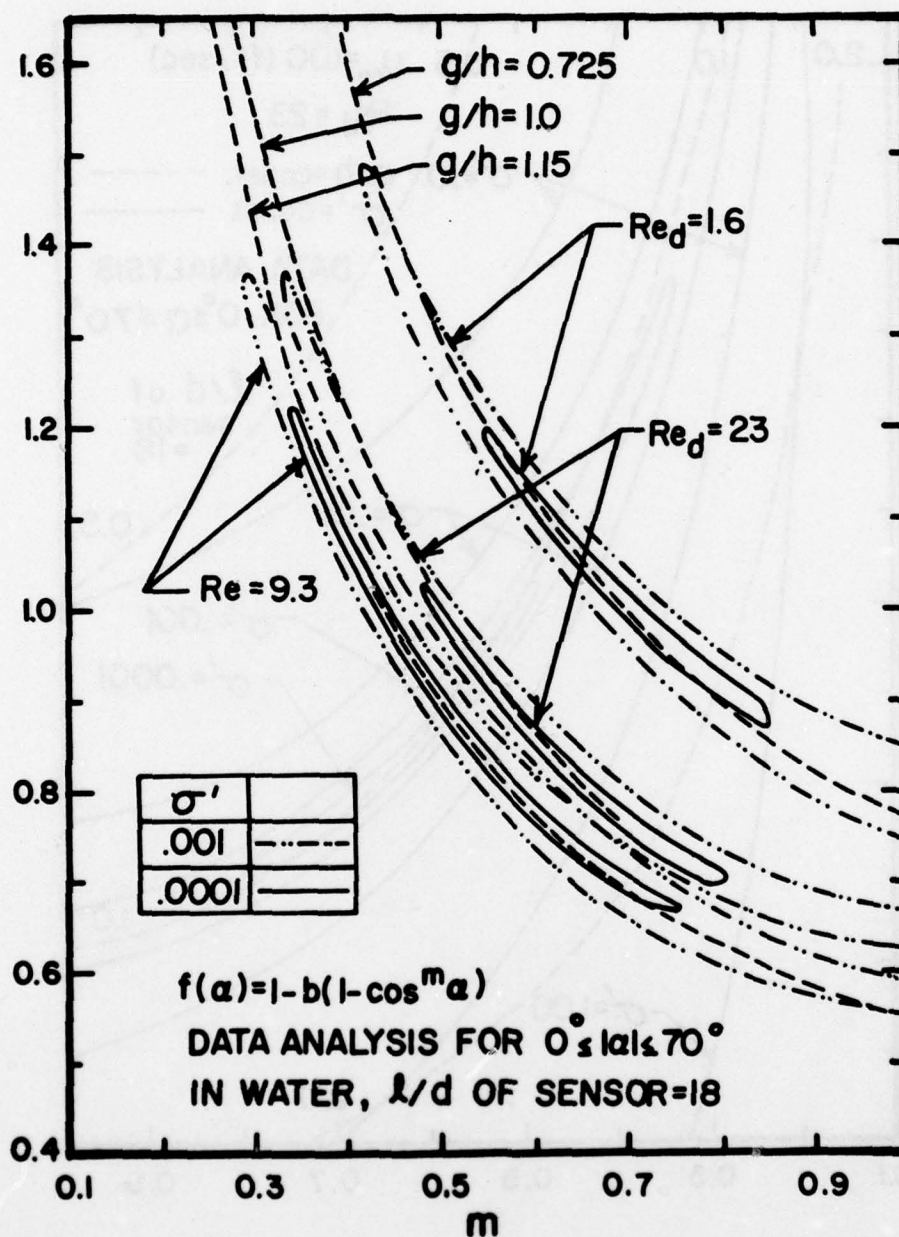


Figure 92. Dependence of Region of Minimum Standard Deviation in b - m Plane on Reynolds Number for Hot-Films in Water

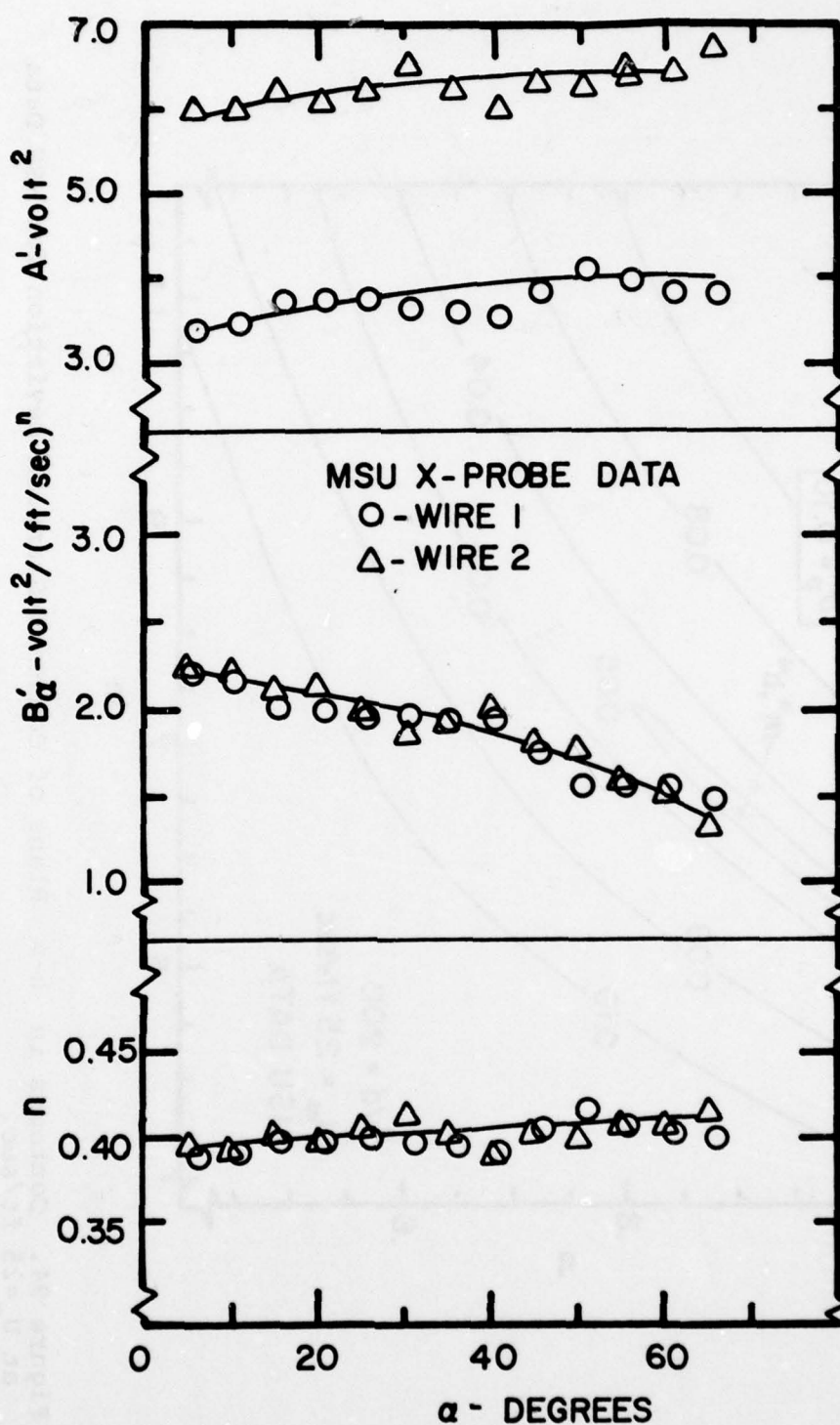


Figure 93. Variation of Hot-Wire Velocity Calibration Coefficients with Yaw Angle for an X-Probe

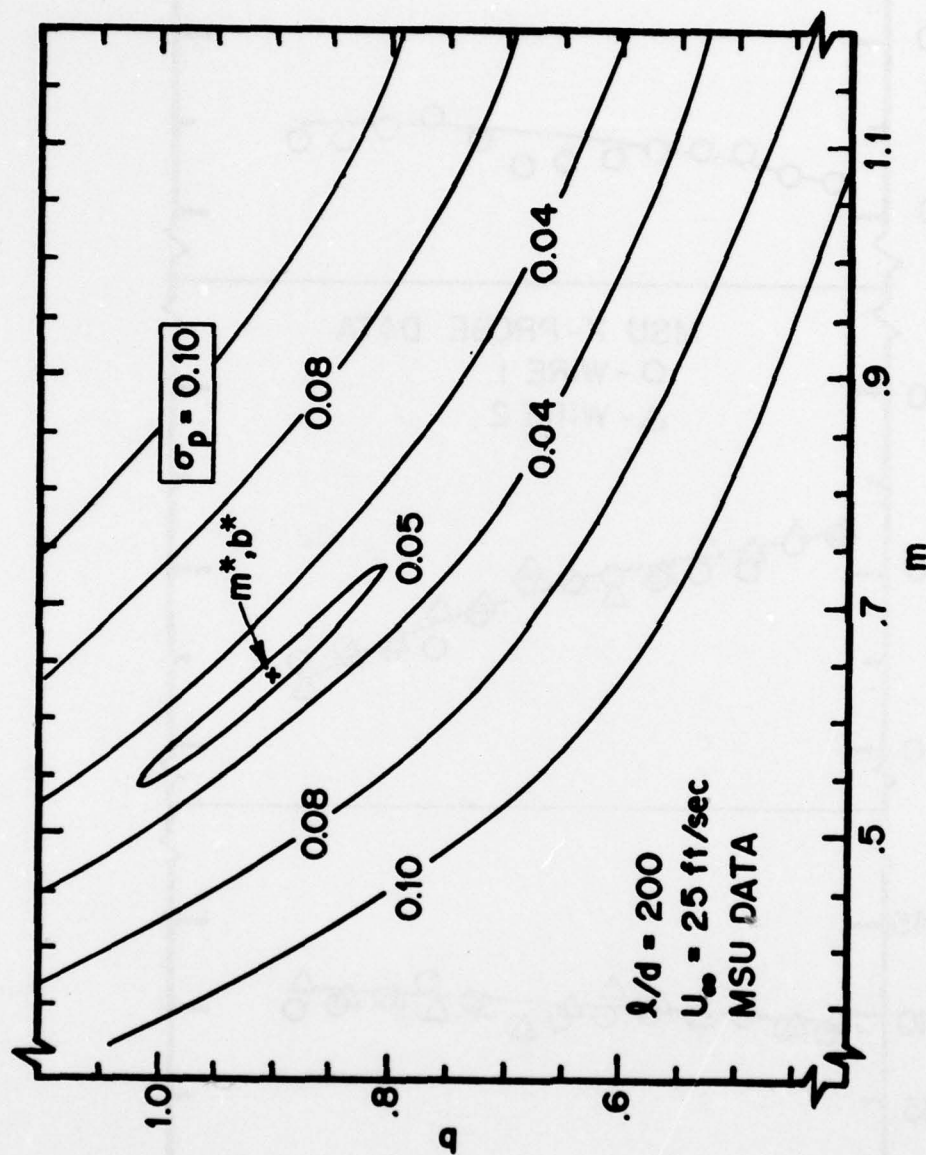


Figure 94. Contours in b - m Plane of Constant Standard Deviation for MSU Data at $U_\infty = 25 \text{ ft/sec}$.

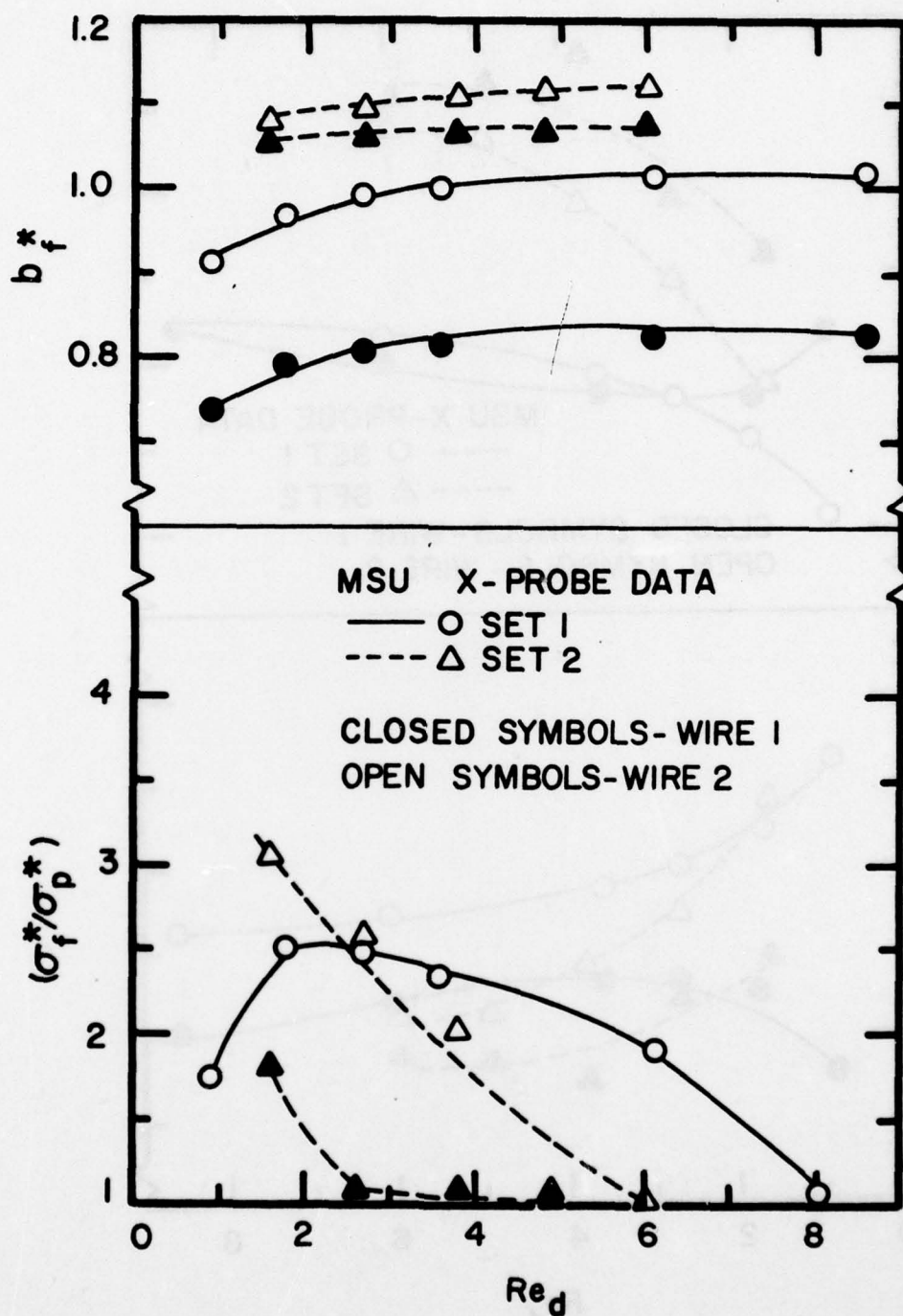


Figure 95. Variation with Reynolds Number of Best Fit Coefficient Determined from Friehe and Schwarz Relation, and Ratio of Standard Deviation Improvement Between Friehe and Schwarz and Present Relations for MSU Data

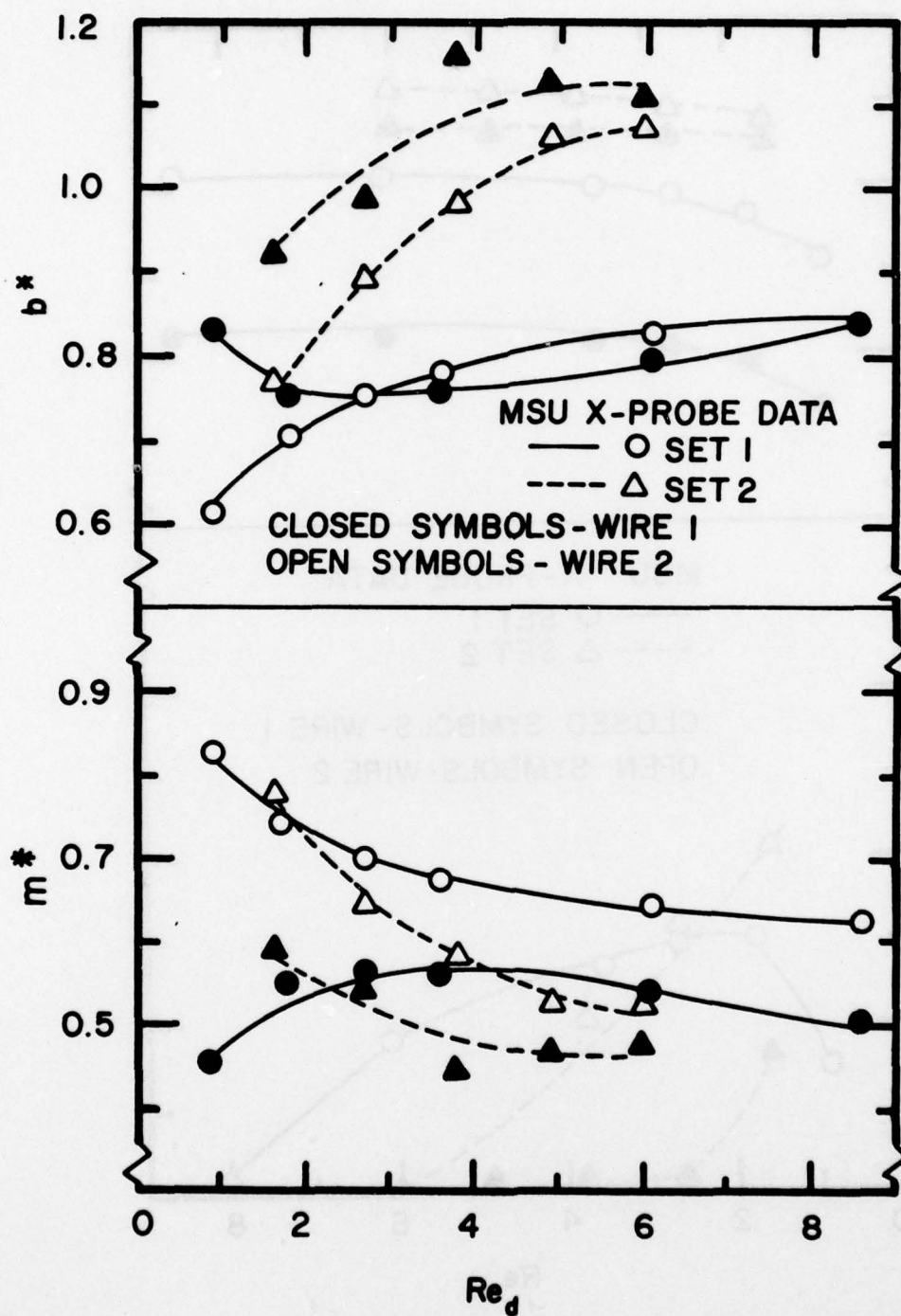


Figure 96. Variation with Reynolds Number of Best Fit Coefficient and Exponent Determined From Present Relation for MSU Data

BIBLIOGRAPHY

- [1] Nagib, H. M. 1972. "On Instabilities and Secondary Motions in Swirling Flows Through Annuli," Ph.D. Thesis, Illinois Institute of Technology.
- [2] Wigeland, R. A., Ahmed, M. and Nagib, H. M. 1977. "Management of Swirling Flows with Application to Wind-Tunnel Design and V/STOL Testing," AIAA Paper No. 77-585, AIAA/NASA Ames V/STOL Conference, Palo Alto, California.
- [3] Wigeland, R. A., Ahmed, M. and Nagib, H. M. 1977. "Vorticity Measurements Using Calibrated Vane-Vorticity Indicators and Comparison with X-Wire Data," AIAA Paper No. 77-720, AIAA 10th Fluid and Plasma Dynamics Conference, Albuquerque, New Mexico.
- [4] Collis, D. C. and Williams, M. J. 1959. "Two-Dimensional Convection from Heated Wires at Low Reynolds Numbers," Journal of Fluid Mechanics, Vol. 6, p. 357.
- [5] Davies, P.O.A.L. and Fisher, M. J. 1964. "Heat Transfer from Electrically Heated Cylinders," Proc. Roy. Soc. A, 280, p. 486.
- [6] Bradbury, L.J.S. and Castro, I. P. 1972. "Some Comments on Heat Transfer Laws for Fine Wires," Journal of Fluid Mechanics, Vol. 51, Part 3, p. 487.
- [7] Burchill, W. E. and Jones, B. G. 1971. "Interpretation of Hot-Film Anemometer Response," Proceedings Second Symposium on Turbulence Measurements in Liquids, Rolla, Missouri.
- [8] Chevray, R. and Tutu, N. K. 1971. "On Velocity Measurements in Non-Isothermal Turbulent Flows," Proceedings Second Symposium on Turbulence Measurements in Liquids, Rolla, Missouri.
- [9] Ali, S. F. 1976. "Hot-Wire Anemometry in Moderately Heated Flow," Private Communication, John Hopkins University.
- [10] Rose, W. G. 1962. "Some Corrections to the Linearized Response of a Constant-Temperature Hot-Wire Anemometer Operated in a Low-Speed Flow," Journal of Applied Mechanics, Vol. 29, P. 554, Trans. ASME, Series E.

- [11] Tan-atichat, J., Nagib, H. M. and Pluister, J. W. 1973. "On the Interpretation of the Output of Hot-Film Anemometers and a Scheme of Dynamic Compensation for Water Temperature Variation," I.I.T. Fluids and Heat Transfer Report R73-7, or U.S. Air Force Office of Scientific Research 74-1343 also Proceedings of Symposium on Turbulence in Liquids, Rolla, Missouri.
- [12] Prandtl, L. 1946. Ministry of Aircraft Production Völkenrode, Rep. and Trans. N. 64.
- [13] Struminsky, V. V. 1946. C. R. Acad. Sci. USSR, Vol. 54, p. 765.
- [14] Jones, R. T. 1947. NACA Tech. Note 1402.
- [15] Hinze, J. O. 1959. Turbulence, McGraw-Hill, New York.
- [16] Webster, C.A.G. 1962. "A Note on the Sensitivity to Yaw of a Hot-Wire Anemometer," Journal of Fluid Mechanics, Vol. 13.
- [17] Champagne, F. H. 1965. "Turbulence Measurements with Inclined Hot-Wires," Ph.D. Thesis, University of Washington.
- [18] Bruun, H. H. 1971. "Interpretation of a Hot Wire Signal Using a Universal Calibration Law," J. Phys., E., Sci. Instrum., 4, p. 225.
- [19] Kjellström, B. and Hedberg, S. 1970. "Calibration of a DISA Hot-Wire Anemometer and Measurements in a Circular Channel for Confirmation of the Calibration," DISA Information, No. 9, p. 8.
- [20] Horvatin, M. 1970. "A Contribution to the Calibration of Hot-Wire Dual Probes," DISA Information, No. 10, p. 22.
- [21] Fujita, H. and Kovasznay, L.S.G. 1967. "Measurement of Reynolds Stress by a Single Rotated Hot Wire Anemometer," presented at the 20th meeting of the Division of Fluid Dynamics, American Physical Society, Lehigh University.
- [22] Friehe, C. A. and Schwarz, W. H. 1968. "Deviations from the Cosine Law for Yawed Cylindrical Anemometer Sensors," Trans. AM. Soc. Mech. Engrs., No. 35. p. 655.

- [23] Roberts, F. A. 1974. "Turbulence Measurements in Water with Inclined Cylindrical Film Sensors," B.S. Thesis, Illinois Institute of Technology.
- [24] Roberts, F. A., Tan-atichat, J. and Nagib, H. M. 1975. "A Further Generalization of the Cosine Relation for Cylindrical Anemometer Sensors Leading to Improved Turbulence Measurements," Presented at 28th Fluid Dynamics Meeting of the American Physical Society, College Park, Maryland.
- [25] Champagne, F. H., Sleicher, C. A. 1967. "Turbulence Measurements with Inclined Hot Wires, Part 2," Journal of Fluid Mechanics, Vol. 28, p. 177.
- [26] Morrison, G. L., Perry, A. E. and Samuel, A. E. 1972. "Dynamic Calibration of Inclined and Crossed Hot Wires," Journal of Fluid Mechanics, Vol. 52, Part 3, p. 465.
- [27] Bruun, H. H. 1976. "A Note on Static and Dynamic Calibration of Constant-Temperature Hot-Wire Probes," Journal of Fluid Mechanics, Vol. 76, Part 1, p. 145.
- [28] Loehrke, R. I. and Nagib, H. M. 1972. "Experiments on Management of Free-Stream Turbulence," AGARD-R-598, AD-749-891.
- [29] Tan-atichat, J. and Nagib, H. M. 1974. "Measurements Near Bluff Bodies in Turbulent Boundary Layers Intended to Simulate Atmospheric Surface Layers," I.I.T. Fluids and Heat Transfer Report R74-2, or U.S. Air Force Office of Scientific Research 74-0964.
- [30] Marcichow, M. E. and Way, J. L., "Dynamic Response of Hot-Film Constant Temperature Anemometer Systems in Air Using Direct Testing," In publication, Journal of Fluid Engineering, ASME.
- [31] Comte-Bellot, G., Strohl, A. and Alcaraz, E. 1971. "On Aerodynamic Disturbances Caused by Single Hot-Wire Probes," Journal of Applied Mechanics, Vol. 38, Trans. ASME, Vol. 93. Series E, p. 767.
- [32] Strohl, A. and Comte-Bellot, G. 1973. "Aerodynamic Effects Due to Configuration of X-Wire Anemometers," Journal of Applied Mechanics, September, p. 661.

- [33] Corke, T. C. and Nagib, H. M. 1976. "Sensitivity of Flow Around and Pressures on a Building Model to Changes in Simulated Atmospheric Surface Layer Characteristics," I.I.T. Fluids and Heat Transfer Report R76-1.
- [34] Way, J. L. 1975. "Applications in Fluid Mechanics Research of a Portable Data Acquisition and Processing System," Proceedings 5th Annual ICIASF, Ottawa, Canada.
- [35] Sanborn, V. A. 1972. Resistance Temperature Transducers, Meteorology Press, Fort Collins, Colorado.
- [36] Horvatin, M. 1969. "Some Problems Concerning the Analytical Evaluation of the Characteristics of Hot-Wires Immersed in a Fluid of Variable Pressures and Temperatures," DISA Information, No. 8, p. 23.
- [37] Sandborn, V. A., Haberstroh, R. D. and Sek, K. S. 1975. "Prediction of Temperature Distribution Along a Thin Heated Wire of Finite Length," Letters in Heat and Mass Transfer, Vol. 2, pp. 461-472.
- [38] Gessner, F. B. and Moller, G. L. 1971. "Response Behavior of Hot Wires in Shear Flow," Journal of Fluid Mechanics, Vol. 47, Part 3, p. 449.
- [39] Frenkiel, F. N. 1954. "Effects of Wire Length in Turbulence Investigations with a Hot-Wire Anemometer," The Aeronautical Quarterly, Vol. 5, p. 1.
- [40] Brunn, H. H. 1975. "Interpretation of X-hot-wire Signals," DISA Information, No. 18, p. 5.
- [41] Perry, A. E. and Morrison, G. L. 1971. "Static and Dynamic Calibrations of Constant-Temperature Hot-Wire Systems," Journal of Fluid Mechanics, Vol. 47, Part 4, p. 765.
- [42] Klebanoff, P. S. 1954. Natl. Advisory Comm. Aeronat. Tech. Notes No. 3178.
- [43] Foss, J. F. 1976. "The Vorcom, Part 1: Analytical Considerations," Second Annual Report, NASA, Langley Research Center, Grant NGR23-004-091.